COHERENCE, CHARGING, AND SPIN EFFECTS IN

QUANTUM DOTS AND POINT CONTACTS

A DISSERTATION

SUBMITTED TO THE DEPARTMENT OF PHYSICS

AND THE COMMITTEE ON GRADUATE STUDIES

OF STANFORD UNIVERSITY

IN PARTIAL FULFILLMENT OF THE REQUIREMENTS

FOR THE DEGREE OF

DOCTOR OF PHILOSOPHY

Sara Marie Cronenwett

December 2001

I certify that I have read this dissertation and that in my opinion it is fully adequate, in scope and quality, as a dissertation for the degree of Doctor of Philosophy.

_____

Charles M. Marcus
(Principal Adviser)

I certify that I have read this dissertation and that in my opinion it is fully adequate, in scope and quality, as a dissertation for the degree of Doctor of Philosophy.

_____

David Goldhaber-Gordon
(Co-Adviser)

I certify that I have read this dissertation and that in my opinion it is fully adequate, in scope and quality, as a dissertation for the degree of Doctor of Philosophy.

_____

Malcolm R. Beasley

Approved for the University Committee on Graduate Studies:

_____

Abstract

A series of experiments is presented on electron transport through quantum dots and quantum point contacts in the strong-tunneling regime where electron coherence, charging, and spin play significant roles. In the first experiment, transport measurements are presented for quantum dots in the strong-tunneling Coulomb blockade (CB) regime. Fluctuations of the conductance, evidence of quantum interference, show sensitivity to charging effects in the CB valleys where elastic cotunneling is the dominent transport mechanism. The effects of interactions are accounted for using a single parameter—the charging energy (the energy required to add an additional electron to the dot)—and are measured using the magnetic field correlation length of conductance fluctuations. The second experiment shows CB in a quantum dot with one fully-transmitting lead and one weak-tunneling lead. In this system, the CB appears only due to constructive interference of backscattered trajectories. The predominant effect of interactions, namely the Coulomb blockade, is turned on and off by quantum interference. The third and fourth experiments investigate the Kondo effect, a classic many-body problem where the effects of coherence and interactions cannot be trivially separated. Quantum dots are well suited to study the Kondo effect as many parameters can be varied in dots that cannot be changed in traditional bulk metal systems. The second observation of the Kondo effect in dots is presented here, including the first demonstration of a gate voltage controlled Kondo temperature. The last part of this dissertation describes quantum point contacts (QPCs) which show a number of remarkable similarities to the Kondo effect in dots. Transport measurements of the "0.7 structure", a robust extra plateau or shoulder-like feature in the lowest mode of a QPC, show evidence for a lifted spin-degeneracy. The formation of a zero-bias peak at low temperature, the collapse of the temperature-dependent conductance to a single curve when scaled by one parameter (the Kondo temperature), and the correspondence of this temperature scaling parameter to the source-drain bias voltage width of the zero-bias peak strongly suggest that a Kondo-like correlated many-electron state forms in the QPC at low temperatures. This suggestion is currently under discussion theoretically.

Acknowledgements

You know you've reached the end of this long road called a Ph.D. when the time to write the Acknowledgements comes. For me, it comes on an otherwise unremarkable December morning, the sun shining once again in a clear blue sky over Stanford, California. For most of the past nine and a half years, I have called this place home, and it is not without some nostalgia that I prepare to hand in this dissertation and become a Stanford alumnae instead of a Stanford student—finally.

I would like to begin this long list of thank you's back in my undergraduate sophomore year when I chose to major in physics. Sitting in Physics 70 (Introduction to Modern Physics) with Mark Kasevich, and Physics 110 (Classical Mechanics, of all things) with Mason Yearian, helped me make that difficult decision. Working with Roger Romani that summer gave me the first taste of the opportunities Stanford has to offer its undergrads in physics—the chance to do cutting-edge research with almost any faculty member you wish. Though I decided, after a year, that studying compact stellar objects wasn't for me, I enjoyed working for Roger a tremendous amount.

The summer after my junior year I was invited to join the Marcus group, marking the beginning of "recent history". I quickly learned that research in the Marcus group often progresses at lightening speed. I was fortunate to start my tenure in mesoscopics by working with Joshua Folk and Sam Patel on a new type of experiment for the Marcus group—Coulomb blockaded dots. I remember the first day we finally "found" Coulomb blockade peaks. What seemed like a miracle then is now among the most straightforward measurements we do (the infamous "wall-wall"). The long days and nights spent in lab that summer were punctuated by many good runs at the Dish (the most memorable at 2:00am ending with the bossman jumping the fence of the Pierce Mitchell pool complex), numerous renditions of Neil Young's "Unknown Legend" (aka, the motorcycle song), and a culminating trip to Ragged Peaks in Yosemite when it was all over.

Since that summer of 1995 a whole list of people have joined or passed through the Marcus group, contributing to the lively atmosphere—intense in both work and play. Andy Huibers, in addition to becoming a treasured friend, toiled for years in the cleanroom in order to develop reliable fabrication

processes, was the electronics guru of the lab, and could always be counted on for a little fun—aerial photography anyone? Sam Patel was my partner through two more years of experiments, providing the dots to measure and helping run the fridge when I was swamped with first-year classes. I can't thank him enough for the companionship and assistance over those years. Duncan Stewart, also around from the beginning, was a source of logical reasoning, mesoscopics knowledge, and wonderful pictures from around the world. His memory will forever live on in the form of "Duncan's ac + dc box", regardless of the misnomer he claims. It was wonderful to have David Sprinzak, a graduate student at the Weizmann Institute in Israel, visit our lab for a year. He made many key suggestions during my elastic cotunneling experiment. Of the old guard, last but not least is Mike Switkes who joined the group the same year as I and became a good friend with whom to commiserate or celebrate as each day warranted.

A slew of undergrads joined the lab during my first few years (as I myself did). I was happy to see Lukasz Zelinski again this past year at Harvard, though he's turned traitor and become a theorist. Randy True became like a brother to me after surviving as his TA, his project partner in a VLSI design class, and finally as his housemate. Stuck on the tragic super-semi project, Randy was among the many Marcusians to jump ship after graduation and work for Andy's startup, Reflectivity. Rob van der Hage made the most of his three month visit after finishing his masters thesis at Delft, though he never succeeded in teaching us to correctly pronounce his name. Kevin Birnbaum made lasting contributions to the lab in the form of a beautiful battery box as well as the first valiant attempts at parallel sample holders and homemade perpendicular field magnets. John Stockton, having passed the "make a dunker" test, succeeded Rob as Randy's partner in crime. He also succumbed, in the end, to the Reflectivity tractor beam, though not before joining many of our adventures in the Sierras. Steve Grossman gave us a fresh perspective on life in the lab with his SEAL training stories and reports that he was also a history major. Along with Randy, Sam, Andy and myself, Steve rounded out a full house of former or current Marcus group students—an experience I will never forget. Last in the list of Stanford undergrads I would like to thank is Pam Olson who made the parallel sample holder I used for several years.

The other graduate students who joined the Marcus group while we were at Stanford included Sebastian Maurer, Mark Peterman, Dominik Zumbuhl, and Laila Mattos. Sebastian helped me with the measurements for the mesoscopic Coulomb blockade experiment, in between evenings of circle-packing and before leaving us for others who shared his joy of simulations. Mark, despite being from Ohio State, turned out to be a pretty good guy. Unfortunately, he was the last casualty of the super-semi project, and is the only person I've known with the bad luck to have two advisors leave Stanford. Laila, it was great to have another woman join the lab after so many years. I was sorry to say goodbye when we headed off to Harvard. It has been a pleasure to get to know Dominik, with his Swiss accent and mannerisms, and particularly to see him come into his own as an experimentalist in the past year. Many thanks to Alberto Morpurgo who was a post-doc in our lab at Stanford. His ability to discuss anyone's project and his rational

method of thinking and working were a source of inspiration. Michael Janus and Linda Olofsson both spent a spring visiting our group, providing many excuses to go out for drinks or to the mountains. Finally, I would not have come as quickly or successfully to the point I am today if Josh Folk hadn't come back to the lab after three years in the Peace Corps. We once again shared the joys (working devices and successful experiments) and pains (endless photolithography sessions, leaky cryostats, noisy dots, and moving the lab—twice) that daily life in the Marcus group entails. I don't think I would have survived without his help, even though I hated to ask for it!

The group got a new burst of life when we moved the lab to Harvard in the summer of 2000. With five new grad students, the Marcus group officially entered a new era. Many thanks to Heather Lynch who worked with me the past year on the last spin filter attempts and then on the point contact Kondo experiment. After working by myself for several years, it was wonderful to have a companion again. Heather was a great help in running experiments as well as her unending efforts in the machine shop, the cleanroom, winding magnets, setting up cryostats, and keeping the lab organized. Alex Johnson has given new meaning to the term "stock-boy". I admire his laid-back personality and easy-going manner, particularly during the more tumultuous times of the past year. In his short tenure, Andrew Houck left a lasting impression on the Marcus group with his list of "device names that have to do with chicken", soda-can Christmas trees, magnetic screwdrivers, and nacho cheese. I will miss his smiling face and endless enthusiasm for learning. Jeff Miller has played a very important role in the past year as the group cheerleader. With an unending supply of impersonations, jokes, stories, and general comic demeanor, Jeff can put a smile on anyone's face almost anytime. I am grateful to Ron Potok for caring as much (if not more) about football and basketball as I do, for being a great desk neighbor and someone I can always count on to go share a beer with. I will only remind him one more time about the score of a certain game in the fall of 2000.

Susan Watson, a professor at Middlebury, spent the past year in our group, often working with me and Heather. Her unselfish work ethic was a great example for us all. I would like to thank her not only for the beautiful machining and the incredible wiring job she did setting up two new cryostats, but more importantly for listening, talking, and providing an experienced perspective throughout the year. It was also nice to have a short overlap with Douwe Monsma and Nayda Mason, two new post-docs in the group, as well as Leo di Carlo, the fastest man to ever have his own experiment and new cryostat dumped in his lap. Michelangelo D'Agostino, Nikki Dutta, Brandon McKenna, and Esteban Real are continuing the strong tradition of undergrads in the Marcus group. To all those that remain on the first floor of Gordon McKay, I wish you the very best of luck in the upcoming years.

Much of the credit for the body of work presented in this thesis goes to my advisor, Charlie Marcus. Over the past six and a half years, he has encouraged and inspired me, reignited my enthusiasm when it waned, and taught me to be a good experimental physicist. Charlie provides his students with many

opportunities to meet and talk with theorists and experimentalists in the mesoscopics community either at conferences or as they visit our lab. This overall integration into the field gives a sense of purpose and motivation that is harder to find within the lab alone. Charlie is also an excellent experimentalist in his own right. Though I wouldn't trust him to write my data acquisition programs, his ability to find leaks on the fridge, solve grounding and noise problems, and come up with creative solutions to challenging problems (even if they don't always work) never ceases to amaze me. I am thankful that I have been able to work along side him.

Beyond the confines of my own group, I have had many useful discussions, friendly trades, and good times with the neighboring research groups in the various locations we have inhabited. It is important to have a set of friends nearby whether you need a coffee break or a 7/8" wrench. At Stanford, in the Varian Physics building, I would like to thank Doug Osheroff and his group for providing low-temperature measurement advice, cryostat advice, and liquid helium. I particularly enjoyed the company of Doug Natelson, Barry Barker and Danna Rosenberg in the lab next door over the years. When we moved to McCullough we were situated between Kam Moler's group and the KGB group. A strong sense of camaraderie developed in the basement labs, strengthened by the challenge of setting up new lab space, dealing with a new (renovated) building, and the lack of sunlight. I would like to particularly thank Eric Straver, Brian Gardner, Janice Wynn, and Per Bjornsson in Kam's lab as well as Myles Steiner, Nadya Mason, Mike Rozler, and John Chiaverini in the KGB group. A number of excellent Sierra mountaineering trips originated in the McCullough basement, Shephard's Pass and the Palisades being among the most memorable. Upon arrival at Harvard, our group was welcomed by the Westervelt and Tinkam groups on the second floor of Gordon McKay. Mark Topinka, Lester Chen, Brian LeRoy, Ian Chan, Ania Bleszynski, and Nina Markovic are among the upstairs residents with whom I've enjoyed good discussions, coffee, beer, or shopping trips. I hope the Marcus versus Westervelt basketball tradition lives on.

I was fortunate enough to spend six months of my graduate career working with Leo Kouwenhoven in the Quantum Transport group headed by Hans Mooij at TUDelft in the Netherlands. My "time away from Stanford" far exceeded my highest hopes both in scientific progress and personal experience. I enjoyed working with and learning the ropes from Tjerk Oosterkamp. Nothing was better than the night you brought the "Kondo wine" to my Thanksgiving dinner. Benno Broer and Michael Janus helped significantly with the Kondo experiment and the never-explained "bunching" phenomenon. I am ever grateful to Michael for dinners at his house, many nights at the Corps, and teaching me how to answer the phone correctly. Many other people, both in and out of work, made my time in Delft as good as it was, particularly Pauline Lunning, Eelco van Vliet, Annet-Jantien Smit, Bego San Jose, Andrew Dunn, Jorg Janssen, and Pieter Heij. For many late nights in the computerkamer as well as all the afstudeer borels, I thank Michiel Uilenreef, Mathijs Robbens, Wilfred van der Wiel, Sander Groenteman, Hinne Temminck-Tuinstra, and Hans Cool. Hans has become a great friend with whom I've now enjoyed memorable trips to

Utah, Paris, and soon Barcelona. Lastly, I want to thank Caspar van der Wal for the many dinners, runs back in the polders, and the friendship we now share.

I was able to work closely with Leo Kouwenhoven again in this past year while he was on sabbatical at Harvard. In every respect he certainly became a second advisor to me. I have really enjoyed the daily interactions we have when working on an experiment together as well as the many late night conversations in the Beestemarkt, the Plough & Stars, or over a bottle of wine at home. As I know I've said many times before, Leo, thank you.

I would like to thank Kam Moler for the significant advisorly role she played in our lab at Stanford when Charlie moved to Harvard. I have appreciated getting to know her and having a female mentor, and wish her all the best with her new family. For similar contributions to our lab in the past year at Harvard, I am very thankful to David Goldhaber-Gordon. His clear answers and patience are exactly what I needed to understand a problem sometimes. I am glad to now call him a good friend, close colleague, and, technically, my co-advisor. I wish him well in his new position at Stanford.

Over the years, I have been lucky to have many fruitful discussions with other physicists in the field. I would particularly like to thank Igor Aleiner, Leonid Glazman, and Ned Wingreen who have been integrally involved in my experiments and have taken the time to explain their theories to me. Oded Agam, Yoram Alhassid, Boris Altshuler, Harold Baranger, Robert Blick, Henrik Bruus, Daniel Fisher, Bert Halperin, Moty Heiblum, Daniel Loss, Hans Mooij, Dan Ralph, Steve Simon, Boris Spivak, and Mike Stopa are among the many others with whom I've enjoyed good drinks and conversations.

A number of people have helped keep our group running smoothly on a daily basis in the past six years. For hundreds of purchase orders and thousands of liters of liquid helium, I would like to thank Linda Hubley, Roberta Edwards and Jim Reynolds. In the Ginzton cleanroom, I benefited greatly from the expert advice and assistance of Tom Carver. At CIS, Paul Jerebek and John Schott helped keep the ebeam running as best anyone could. Without those three, a miserable two years of constant fabrication would have likely been longer. I would also like to give special thanks to Mark Jackson of Oxford Instruments for taking my calls (even on vacation), giving advice, stopping by to help figure out why a cryostat was acting up, and always being a lot of fun.

Special thanks to the professors who sat on my defense and reading committees, Mac Beasley, Sandy Fetter, David Goldhaber-Gordon, Ted Geballe, and Charlie Marcus. I appreciate the time you have taken to participate in these crucial last steps of my Ph.D.

None of the research presented in this thesis could have been done without the collaborations with the groups who grew the GaAs/AlGaAs heterostructures. Many thanks to Ken Campman and Kevin Marinowski in Art Gossard's lab at UCSB, Cem Düroz in Jim Harris' lab at Stanford, C. T. Foxon at Philips Laboratories in the Netherlands, Vladimir Umansky at the Braun Center for Submicron Research at Israel's Weizman Institute of Science, and Mansour Shayegan and his group at Princeton. In addition to the

It takes a strong network of friends and family to keep one going through the many years required to finish a Ph.D. I am very thankful to have had the camaraderie and support of so many friends in so many places. Barrett Adams, Josh Burgel, Chris Donahue, Krista Fairbairn, Julie Farrell, Josh Folk, Rick Hardy, Adam Heaney, Andy Huibers, Rob Jenks, Nick Judson, Eva Kim, Jonathan Ledlie, Rob Linden, Sam Patel, Susannah Porter, Bryan Rollins, Steve Simon, Matt Stein, Myles Steiner, Eric Straver, Caspar van der Wal, and Glenn Wong, you have all helped keep me sane at various times in this long process. Andy and Josh, in particular, thank you for sharing your lives with me.

Lastly, I would like to thank my family for their twenty-eight years of unwavering love and support. Our family home in Ludington, Michigan, has always been a haven for summer fun and revelry. I am thankful for the close contact our extended family maintains and the frequency with which we gather. From my grandparents, J. Russell and Florence Mary Houk, and Jack and Marie Cronenwett, I have learned what is truly most important in life. Carol Anderson, Judy Emery, Shirley Tullar, and Debby Cronenwett, I am very glad for the years we have shared as family. My sister Molly Cronenwett has been a life-long friend and companion. She serves as a valuable reminder to me that not everything in the world has to be based on science and logic. I am happy that we can be so different and yet so similar at the same time. Finally, I would like to thank my mother Linda Cronenwett, and my father, Jack Cronenwett, for having instilled in me a strong desire to learn and the dedication to work towards my goals. They have been the best role models and supporters I could ask for.

Contents

xv

List of Tables

List of Figures

Chapter 1

Introduction

1.1 Introduction and Motivation

The beginning of the 21st century finds the science of small systems at a number of interesting crossroads. Transistors are more plentiful than lightbulbs, and "nanotechnology" is leading the charge toward new applications of ever smaller man-made systems. In addition, the boundaries between the traditional disciplines of physics, chemistry, biology, and even computer science are beginning to blur. Condensed matter physicists are trying to measure the conductivity of DNA [1-4], while biologists are starting to use lithography techniques to fabricate nano-scale devices that imitate or assist in their study of biological phenomena [5-9]. Chemists have started making transistors and circuits out of single molecules [10-14], computer scientists are using quantum mechanics to discover fundamentally new algorithms [15, 16], and physicists are using, among other things, nuclear magnetic resonance (NMR) techniques—a longstanding physics tool used in medical imaging (MRI)—to build the fundamentally new "quantum computer" [17-20].

In 1959, Richard Feynman gave a now-famous speech entitled "There's Plenty of Room at the Bottom" [21], in which he expounded the possibilities of manipulating and controlling things at a small scale. Four decades later, several of the goals that Feynman mentioned have been realized: transistors are *much* smaller than they were in the room-sized computers of the time, individual atoms can be imaged and manipulated using scanning tunneling and atomic force microscopy (STM & AFM), and the full sequence of the human genome has been mapped out (though not through a 100x improvement in the electron microscope as Feynman challenged). Other suggestions of Feynman have not yet come to pass but are

currently the subject of significant efforts. The field of micro-mechanical-electrical-systems (MEMS) or, more recently, nano-mechanical-electrical-systems (NEMS) is starting to create amazingly complicated miniature systems [22], though not yet at the self-replicating machine level that Feynman imagined. Looking from the other side, it is possible to assemble some extremely simple structures from the bottom-up, atom by atom [23, 24], but we are still a long way from the ability to synthesize objects from the atomic scale at will.

In general, as the push to create smaller and smaller objects continues, the limits of *macroscopic* behavior, governed by classical Newtonian mechanics, and *microscopic* (atomic-scale) phenomena, which require a full quantum mechanical description, are beginning to overlap. Within the physics community, this boundary area is known as *mesoscopics*. Mesoscopic devices are generally nanometers or microns in size, falling under the broad umbrella of "nanotechnology." They are well suited to explore the regime where both quantum mechanics and classical mechanics are relevant, for example at the density limits that silicon transistor chips are quickly approaching [25, 26]. Many large molecules, such as the carbon nanotubes [27-30], C_{60} molecules (buckyballs) [31], and DNA strands [1-4] that form the basis for a large number of experimental efforts, can also be considered mesoscopic. As well, many quantum computing proposals suggest the use of mesoscopic devices as the fundamental qubit [32-35].

The work I have done in this thesis falls under the heading mesoscopic physics and, in particular, explores confined electron systems—quantum dots and quantum point contacts—in the regime where both quantum and classical effects play important roles. A quantum dot is a small puddle of electrons, typically 10's to 1000's [36]. Electrons can enter and exit the dot through narrow constrictions which connect to large electron reservoirs. These constrictions are the quantum point contacts. I have investigated these devices by measuring their electrical resistance, looking for signatures of quantum interference, charging effects or electron-electron interactions, and electron spin.

Depending on your point of view, there are several motivations for this class of experiments. The first is a desire to understand the basic physics of small systems. Mesoscopic physics has become increasingly accessible over the past 15 years due to advances in micro- and nano-scale fabrication. Previously, experimental studies of quantum phenomena relied on atomic size systems. The physics of quantum dots with a small number of electrons is very similar to that of real atoms, earning them the oft-used name "artificial atoms" [37]. Unlike real atoms, however, a quantum dot is a tunable system with many parameters that can be varied to investigate its properties, including the breaking of time-reversal symmetry with an experimentally accessible magnetic field. In addition to atomic systems, transport phenomena in semiconductor quantum dots is remarkably similar to that observed in other small devices such as clean metallic nanoparticles [38, 39], C_{60} molecules [31], and carbon nanotubes [27-30]. Understanding the behavior of quantum dots has and will continue to aid the investigations of these less controllable systems.

In addition to helping us understand basic physics, mesoscopic systems may have many technological applications in the future. As mentioned above, the density of transistors on traditional CMOS silicon chips is approaching the classical limit [25, 26]. Thanks to continued improvements in fabrication techniques transistors have gotten smaller and smaller. They will eventually reach the mesoscopic scale where quantum effects influence their behavior, and the standard laws of digital computer architecture become unreliable. The study of semiconductor systems where quantum mechanics plays a significant role may provide insight into the future problems faced by the semiconductor chip industries as they continually strive to miniaturize their chips.

Another compelling reason to study small quantum systems has emerged during the years of my Ph.D.: a possible application to quantum computing. The field of quantum computing took off in 1994 with the discovery by Peter Shor [40] that a quantum computer could find the prime factors of an N-digit number in a time of order N^3, exponentially faster than could be achieved with a classical computer.[1] Other interesting applications for a quantum computer have been explored, including Grover's search algorithm [41], and the simulation of quantum systems. However, it is the importance of Shor's algorithm that is fueling this field—quite literally—because the factoring of large numbers is the key to modern cryptography systems. This means the various national funding agencies, especially the Department of Defense, are allocating large amounts of money to university scientists for research leading to the realization of a quantum bit (qubit) and eventually a quantum computer.

A useful quantum computer is a long-term goal, and one towards which many groups are now working. As a motivation for the continued study of small quantum systems, however, the excitement over quantum computing has been a watershed. Indeed, quantum dots are one of the primary candidates for making qubits from a solid state system.[2] The experiments described in this thesis can be viewed as providing some background study on the behavior of quantum dots and quantum point contacts in the interesting regimes where quantum coherence, charging effects, and electron spin all play important roles. It is these same regimes where current efforts to realize a qubit with quantum dots continue.

1.2   Coherence, Charging, and Spin

The study of semiconductor quantum dots began in the late '80s and early '90s and has since become an active research topic both experimentally and theoretically. The results of many initial experiments, particularly those in which the dot was well coupled to the reservoirs through the point contacts, could be

---

[1] The time for a classical factoring algorithm has not been proven, but is widely believed to increase with N faster than any power.

[2] Besides quantum dots and NMR techniques, other proposals for quantum computers include Josephson junction devices [35], single nuclear spins of dopant atoms in silicon [33], ion traps [42], and optics [43].

described reasonably well by considering quantum interference of non-interacting electrons [44, 45]. The next level of complexity consisted of taking interactions into account only through one parameter: the energy required to add an additional electron to the dot, known as the charging energy. The charging energy comes into play most significantly in the Coulomb blockade, a classical effect where current flow through an isolated quantum dot is forbidden because of this charging energy [44, 46]. Considering the nature of a quantum dot—a small region of confined electrons—and the strongly interacting nature of electrons, the success of theories which took interactions into account in such a simple way is somewhat remarkable. Nonetheless, beyond the Coulomb blockade, electron-electron interactions could be neglected in a number of experiments. The list of phenomena which are successfully explained with this type of non-interacting single-particle picture is long. For overall reviews of the field of electron transport in quantum dots, see Refs. [44, 46-48].

Not every aspect of quantum dot behavior could be explained so easily, however, and this thesis addresses some experiments which illustrate not only the coherent nature of these devices but also the roles of charging and electron spin. In the first experiment, described in Chapter 3, we find that charging effects control the conductance fluctuations of a Coulomb blockaded quantum dot when elastic cotunneling is the dominant transport mechanism [49]. Conductance fluctuations are the result of coherent interference of each possible electron trajectory leading from the entrance to the exit of the dot. This experiment confirmed that the effects of charging on coherent transport had to be included in a more sophisticated way. A second experiment, discussed in Chapter 4, describes a regime of quantum dots where the Coulomb blockade itself, the most basic effect of charging, occurs only because of coherent interference in the dot [50]. Both of these results show systems where the characteristic effect of one physical process (wavefunction coherence or charging) is controlled by the existence of the other.

The third and fourth experiments described in this thesis address the Kondo effect, first in quantum dots and second in quantum point contacts. Unlike the situations described above, in a Kondo system, the effects of coherence, charging and now spin cannot be trivially separated. The Kondo effect is intrinsically a many-body problem and is one of the classic many-body problems in condensed matter physics [51, 52]. Though the Kondo effect was originally discovered in bulk metals systems with magnetic impurities in the 1930's, quantum dots were identified as a more useful system for studying this physics because many of the relevant parameters in the problem can be easily varied. Our successful observation of the Kondo effect in quantum dots [53], described in Chapter 5, helped open a new experimental chapter of Kondo investigations [52].

One of the unexpected places the Kondo effect seems to occur is in quantum point contacts. Point contacts are narrow constrictions through which electrons are confined to travel. Historically, they have been very well described by a non-interacting theory. Recently, deviations from this simple model have been observed. In Chapter 6, we investigate one such deviation, the so-called "0.7 structure," and find

many remarkable similarities to the Kondo effect in quantum dots [54]. At this writing, a complete theoretical description of a Kondo-like state in a quantum point contact is still lacking. However, it seems certain that any full explanation will need to incorporate the effects of coherence, electron-electron interactions and spin into a new many-body state analogous to the Kondo effect in dots.

1.3   Organization of this Thesis

This chapter has given an introduction to and some motivation for the study of small quantum systems in the regimes where coherence, charging and spin effects are important.

Chapter 2 gives a more detailed introduction to quantum point contacts and quantum dots including the devices themselves as well as basic transport properties. Chapter 3 describes an experiment on mesoscopic fluctuations of cotunneling in the valleys of Coulomb blockaded quantum dots. Chapter 4 discusses the mesoscopic Coulomb blockade in one-channel quantum dots. Chapter 5 describes a tunable Kondo effect in quantum dots and discusses some of the more recent work in that field since that experiment. Chapter 6 presents measurements of a single quantum point contact which seem to demonstrate a type of Kondo effect, but now in an "open" quantum system. The results are summarized in Chapter 7 with a brief discussion of future work. Appendix A describes my attempts to make a spin filter from ferromagnetic QPCs. Appendix B contains a description of our fabrication processes. Appendix C is an inventory of devices. Appendix D is a compilation of useful measurement information. Finally, Appendix E contains some of the data acquisition programs for future reference.

Chapter 2

Basic Transport in Quantum Point Contacts and Quantum Dots

2.1   Introduction

A number of fortuitous properties make GaAs quantum dots (QDs) and quantum point contacts (QPCs) useful systems to study coherence, charging and spin effects [44, 55]. To begin with, mesoscopic devices are characterized by a size, L, which is much smaller than or comparable to the electron coherence length, L_φ. This means that electrons retain a definite phase relation during transport, allowing coherent processes such as quantum interference or multi-particle entanglement to occur. The coherence length is affected by the coupling of an electron to the environment. It increases rapidly as the temperature decreases and can reach lengths up to 10's of microns at temperatures below 100 mK [56]. It is now possible to meet the condition that $L < L_\varphi$ quite easily at the lowest temperatures because advances in lithography have made the fabrication of micron and sub-micron devices standard. Additionally, significant efforts in the growth of two-dimensional electron gases (2DEG) on GaAs/AlGaAs heterostructures have yielded high mobility samples with mean free paths up to 100 μm, meaning that transport in small devices is ballistic.

In addition to satisfying the condition $L < L_\varphi$, mesoscopic devices must also be larger than the Fermi wavelength of the electron, λ_F. This implies that a device contains many electrons and suggests that electron-electron interactions are likely to be important. One measure of the significance of interactions in an electron system is the ratio of the typical Coulomb interaction (potential) energy to the average kinetic

energy of the electrons at the Fermi level. This ratio, known as the dimensionless gas parameter r_s, is also the average inter-electron spacing in units of the effective Bohr radius, a_{Bohr}:

$$r_s = \frac{E_P}{E_K} = \frac{e^2 m^* r^2}{r\hbar^2} = \frac{r}{a_{Bohr}}, \tag{2.1}$$

where $m^* = 0.067 m_e$ is the effective mass of the electron in GaAs, and the inter-electron spacing, r, for a 2DEG can be taken from the electron sheet density, $r = n_s^{-1/2}$. For high density electron gases, the kinetic energy is large and $r_s \ll 1$. In these systems, interactions can generally be treated as a perturbation to the kinetic motion, yielding tractable perturbation theory calculations of a relatively complex many-body system. A low density electron gas, on the other hand, has small kinetic energy, so $r_s \gg 1$. Interactions dominate in these systems, which tend towards an electron lattice or Wigner crystal to minimize the Coulomb interaction energy [57]. This solid limit is also well described theoretically. In between these extremes is a range of r_s where the interaction and kinetic energies are comparable. Such systems have presented a wide array of surprising and complicated behavior including superconductivity and the quantum Hall effect. The 2DEGs which comprise our QDs and QPCs have $r_s \sim 1$ suggesting that these devices are well suited to the study of interactions in mesoscopic systems.

Finally, it is well known that electrons are fermions and have a spin of 1/2. In many cases, the electron spin is easily incorporated into non-interacting single-particle models. There are some instances, however, when the existence of an excess spin along with electron-electron interactions which involve a spin-flip fundamentally change the character of transport. Such is the case for the Kondo effect. As mentioned previously, quantum dots are viable candidates for studying the Kondo effect because they can be tuned to a regime where an excess spin on the dot interacts significantly with electrons in the leads [58-60].

For general introductions to the field of mesoscopic physics, the reader is advised to consult Refs. [55, 61]. The remainder of this chapter gives an overview of transport through QDs and QPCs. First, the heterostructures used to make the devices are described, along with the various measurement configurations. Then basic transport properties of the quantum point contact are introduced. Lastly, basic transport through quantum dots is discussed for both open and closed systems.

2.2   GaAs/AlGaAs 2DEG Devices

The quantum dots and point contacts described in this thesis are made in a two-dimensional electron gas (2DEG) which forms at the interface of a GaAs/$Al_x Ga_{1-x}$As heterostructure grown by molecular-beam-
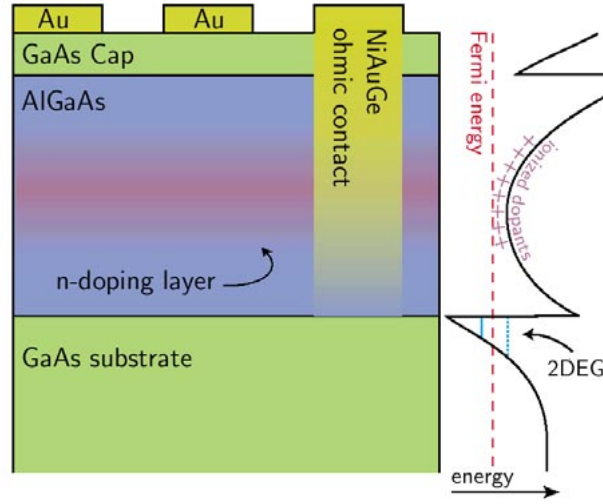
Figure 2-1. GaAs/AlGaAs heterostructure and band diagram. The GaAs/AlGaAs heterostructure is comprised of a bulk GaAs substrate, a layer (~ 50 – 200 nm thick) of $Al_xGa_{1-x}As$, and a plain GaAs cap (~ 10 nm). The AlGaAs layer is partially doped with n-type donors which contribute electrons to a two-dimensional electron gas (2DEG) that forms at the interface at low temperature. Gold (Au) gates and Ni-Au-Ge ohmic contacts are patterned on the surface during device fabrication. The ohmic contacts are annealed so that their metal diffuses down and makes electrical contact with the 2DEG. The band diagram of the GaAs/AlGaAs wafer is shown on the right with energy on the horizontal axis. At low temperature, electrons fill the triangular potential well at the GaAs/AlGaAs interface up to the Fermi energy, forming the 2DEG. (Figure courtesy of M. Switkes).

epitaxy [44]. The heterostructure layering, seen in Fig. 2-1, starts with a bulk GaAs substrate, then a layer of AlGaAs (typically 50 – 200 nm thick), and finally a thin (~ 10 nm) GaAs cap to prevent oxidation. The AlGaAs layer contains a region of n-type dopants which contributes free electrons to the 2DEG. The band diagram of this heterostructure is shown on the right of Fig. 2-1. At the interface between the GaAs and AlGaAs, a triangular potential well is formed. At low temperatures, electrons exist only where the conduction band dips below the Fermi energy. As a result, the free electrons in the system are confined to the potential well in the interface plane. At typical electron densities, only the first subband of this well is populated, localizing electrons in the z-direction to ~ 10 nm from the interface. The second subband is ~ 150 meV above the first. As this is much larger than either the typical Fermi energy, E_F ~ 10 meV, the measurement temperature, T < 1K ~ 86 μeV, or the source-drain bias voltage, eV_{sd} ~ 1meV, the second subband is unoccupied, and the electron gas can be considered two-dimensional. The number of interfacial defects in the 2DEG plane is low because GaAs and AlGaAs have only a slight lattice mismatch. In addition, the n-type dopants in the AlGaAs layer are separated from the interface by 20 – 40 nm of plain AlGaAs to prevent defects near the 2DEG plane. The result is a high mobility 2DEG with a mean free path (the distance an electron can travel before scattering off an impurity) in the 10's of microns. Typical values for the parameters of a 2DEG formed in a GaAs/AlGaAs heterostructure are given in Table 2-1.

2DEG Property	Symbol	Value	Units
Effective mass	m^*	0.067	$m_e = 9.1 \times 10^{-28}$ g
Spin degeneracy	g_s	2	
Valley degeneracy	g_v	1	
Dielectric constant	ε	13.1	$\varepsilon_0 = 8.9 \times 10^{-12}$ Fm^{-1}
Effective Lande g-factor	g^*	–0.44	
Density of states	$\rho(E) = g_s g_v (m^*/2\pi\hbar^2)$	2.8×10^{10}	cm^{-2}meV^{-1}
Level spacing	$1/\rho(E)$	3.57	μeVμm^2
Fermi wave vector	$k_F = (4\pi n_s/g_s g_v)^{1/2}$	1.1×10^6	cm^{-1}
Fermi energy	$E_F = (\hbar k_F)^2/2m^*$	7.0	meV
		81	K
Fermi wavelength	$\lambda_F = 2\pi/k_F$	56	nm
Fermi velocity	$v_F = \hbar k_F/m^*$	1.9×10^7	cm/s
Scattering time	$\tau = m^*\mu_e/e$	40	ps
Mean free path	$l = v_F\tau$	10	μm
Resistivity	$\rho = (n_s e \mu_e)^{-1}$	30	Ω per square
Diffusion constant	$D = v_F^2\tau/2$	7×10^4	cm^2/s
Thermal diffusion length	$l_T = (\hbar D/kT)^{1/2}$	5×10^3	nm/$\sqrt{T}$
Cyclotron energy	$\hbar\omega_c$	1.73	meV/B
		20	K/B
Cyclotron radius	$l_c = \hbar k_F/eB$	70	nm/B
Magnetic length	$l_m = (\hbar/eB)^{1/2}$	26	nm/$\sqrt{B}$
Zeeman energy	$g^*\mu_B B$	25.5	μeV/B
		296	mK/B

Table 2-1. Typical parameters of a 2DEG formed in a GaAs/AlGaAs heterostructure. The 2DEG sheet density and mobility are taken as $n_s = 2 \times 10^{11}$ cm^{-2} and $\mu_e = 1 \times 10^6$ cm^2/Vs, respectively. The units of B are tesla, and the units for T are kelvin. (Adapted from Ref. [44]).

(a)

(b)
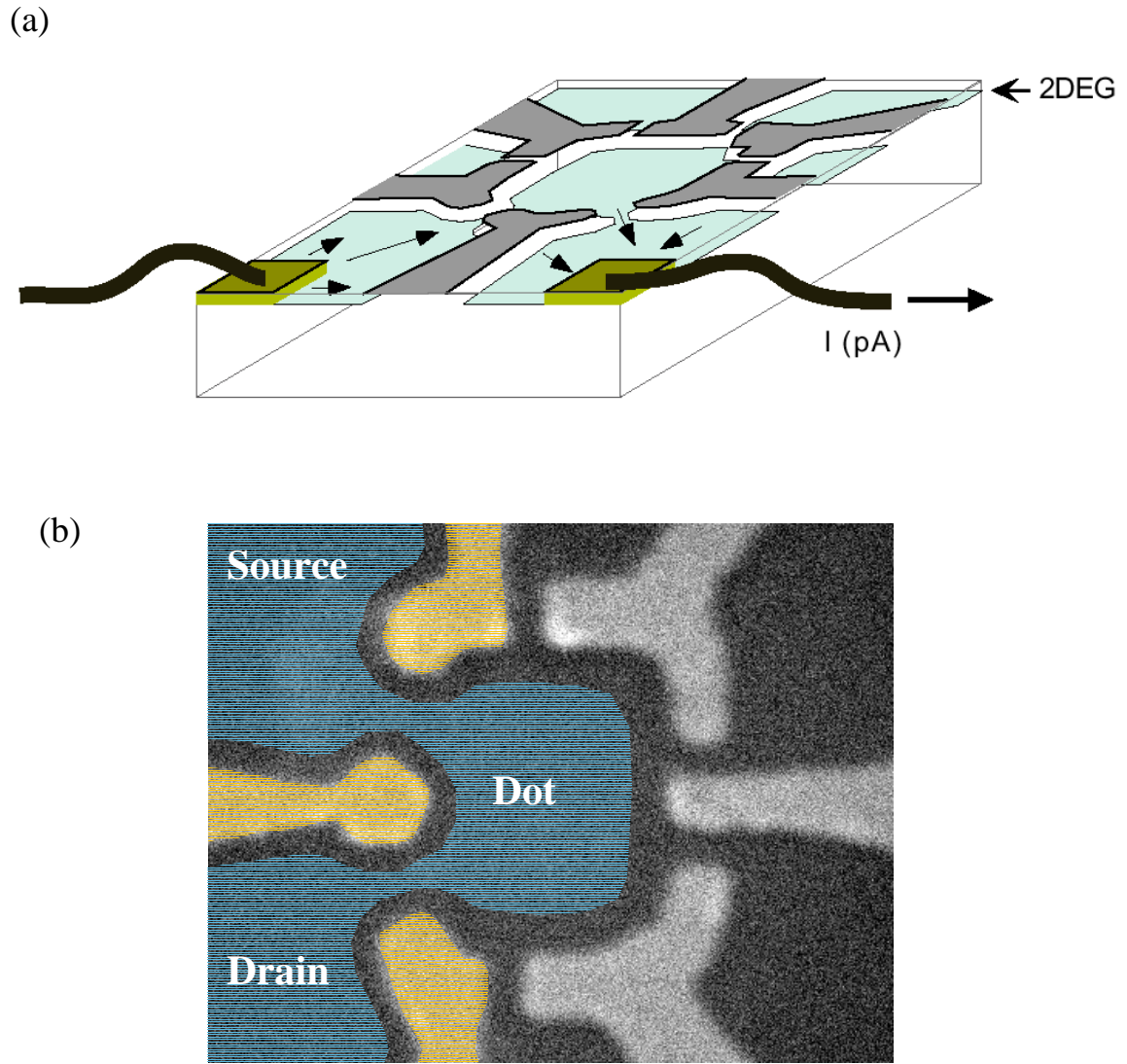
Figure 2-2. **(a)** Schematic 3D view of a quantum dot formed by six gates (gray) on the surface of a GaAs/AlGaAs wafer. The 2DEG, shown in blue, exists slightly below the surface at the interface plane except immediately beneath the negatively biased depletion gates. A current can be passed through the device via the ohmic contacts (gold). Current flows only through the two openings indicated with the black arrows; all the other spaces between gates are fully depleted. **(b)** A scanning electron micrograph (SEM) of a quantum dot. The gates forming the QPCs are colored gold. The 2DEG regions forming the source, drain, and dot are colored in blue.

To create small devices, electrons in the 2DEG must be confined to prescribed regions. This is accomplished by "gating" the heterostructure with thin films of patterned metal defined with an electron beam lithography system. Fabrication techniques are described fully in Appendix B. The metal forms a Schottky barrier at the surface so that a negative voltage of ~ 0.5 V applied to the gates depletes electrons in the 2DEG below without leaking charge into the sample. Further applied voltage extends the region of depletion, giving control of the size and shape of devices. Figure 2-2a shows a perspective view of a QD formed by six gates (gray) on the wafer surface. The 2DEG is shown in blue and exists everywhere except immediately under the negatively biased gates. These depleted regions confine electrons to be either inside the small "dot," or outside, in the macroscopic source and drain reservoirs. Electrons can enter and exit the dot through the QPCs, as illustrated with the black arrows. A scanning electron microscope (SEM) image of the surface gates which form a similar QD is shown in Fig. 2-2b. This colorized image highlights the electron gas which forms the dot and the source and drain reservoirs as well as the gates which define the entrance and exit QPCs. Additional SEM images of other QD designs, as well as single QPCs, are shown in Fig. 2-3.

Electrical contact is made to the 2DEG through "ohmic contacts" (see Fig. 2-1). These contacts are composed of metals which, when heated, diffuse into the heterostructure forming electrical connection to the 2DEG. I have experimented with both Ni-Au-Ge and Pt-Au-Ge ohmics as described further in Appendix B. Using the ohmics, we can pass a current, I, through the small entrance and exit slits in the device, as seen in Fig. 2-2a, and measure the voltage drop, ΔV, across the device. Many of the interesting properties of quantum devices can be directly probed by measuring the resistance, $R = V/I$, or conductance, $G = I/V$, of the device in this way.

2.3   Measurement Set-ups

We commonly use two different set-ups to measure the conductance through a device depending on its average resistance. As mentioned above, we access the 2DEG—to pass a current and measure the voltage, or vice-versa—via the ohmic contacts. For most measurements, it is important to keep the current and voltage across the device relatively small. In particular, the voltage drop across the device, V_{sd}, should not exceed the temperature of electrons or higher energy states in the device may become accessible; that is $eV_{sd} < kT$, where k is Boltzman's constant. For high resistance samples it is easiest to apply a constant bias voltage, V_{sd}, chosen to meet the above condition, and measure the current through the sample. In the opposite limit, for low resistance samples, a more reliable measurement comes from sourcing a constant current through the device and measuring the voltage drop in a 4-wire configuration. Both of these set-ups will be discussed below.

(a)

(b)
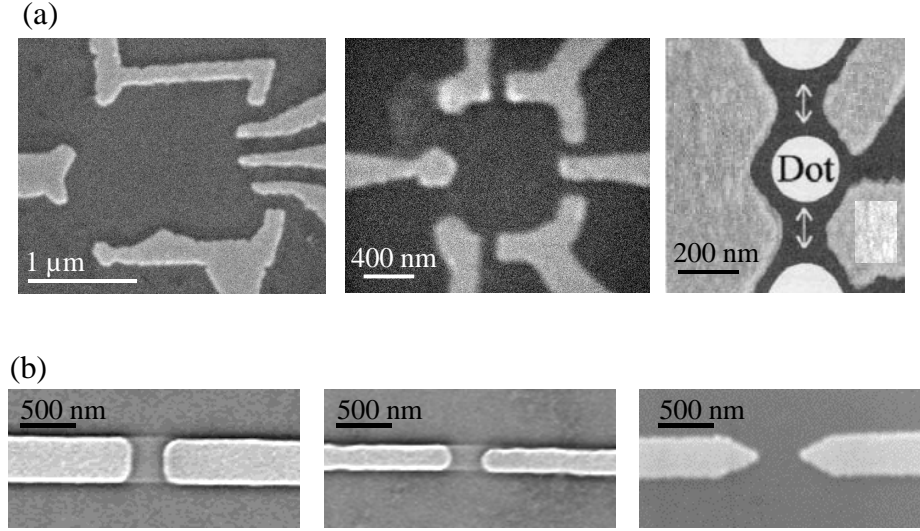
Figure 2-3. Quantum dot and quantum point contact images. **(a)** SEM images of several quantum dot designs. From left to right, these devices are measured in Chapters 3, 4, and 5 and have estimated areas (assuming a depletion region of ~ 100 – 150 nm) of 0.81 μm^2, 0.5 μm^2, and 0.03 μm^2, respectively. **(b)** SEM images of quantum point contacts of different shapes and sizes. The two leftmost were used for the measurements in Chapter 6.

2.3.1   4-Wire Current Bias Measurements

Current bias measurements are most often used when the sample resistance is of order 25 kΩ or less, or equivalently, the conductance is larger than e^2/h. A 4-wire current bias measurement requires two ohmic contacts in both of the source and drain reservoirs, as seen in the SEM image of Fig. 2-4 and illustrated schematically in Fig. 2-5. In general, we measure the differential conductance, $g = dI/dV_{sd}$, using standard ac lockin techniques.[3] A constant ac current is sourced from a PAR-124 lockin amplifier using an rms voltage (typically 0.1 – 5 V) through a large in-line resistor (typically 100 MΩ – 1 GΩ). The voltage drop across the device using the other two ohmic contacts, ΔV, is fed back into the lockin through a PAR-116 current pre-amp. Because no current flows through the voltage probe leads, the measured voltage drop is due only to the resistance of the device (plus a small contribution from the wide 2DEG regions). One

---

[3] We usually measure the linear differential conductance $g = dI/dV_{sd}$. In Chapter 5, however, we also measure the dc conductance, $G = I/V_{sd}$. In the limit of small source-drain voltage, the differential conductance is equal to the linear conductance. In most cases, a lowercase 'g' is used for the differential conductance and an uppercase 'G' for the linear conductance. The known exception will be in Chapter 3 where uppercase $G = dI/dV$.
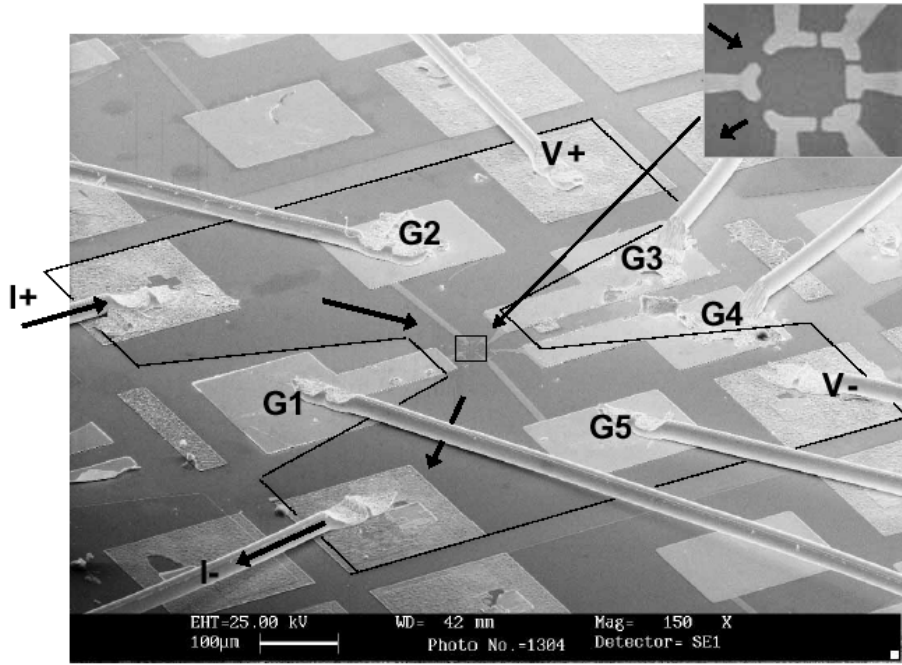
Figure 2-4. Perspective SEM image of a bonded QD device. The black hourglass outline indicates the mesa of 2DEG associated with a single device. The large square films of metal in the corners of the hourglass are the ohmic contacts. The metal pads labeled G1 to G5 are the gatepads. Each small gate which confines a dot (shown in the upper right inset) extends out to one of these macroscopic pads. Wirebonds attached to each pad connect to a chip carrier outside the picture and carry currents or voltages to the ohmics and gates. This picture depicts a 4-wire measurement where current flows from the ohmic labeled I+ through the dot and out the ohmic labeled I-. The voltage across the dot is measured via the V+ and V-ohmics. (Images courtesy of A. Huibers).

caution which must be taken in the current bias set-up is to ensure that the voltage across the device ($V_{sd} = \Delta V = R * I_{rms}$) does not become too large if the sample resistance grows significantly. Excessive voltage loads can be prevented by placing a voltage divider on the lockin output, before the in-line GΩ resistor. This is a useful trick for samples of intermediate resistance or where the resistance may vary widely over the course of a measurement.

The depletion gates are negatively biased with respect to the ohmic at current "low" (labeled I- in Fig. 2-4 and 2-5) using individual channels of a potentiometer-controlled battery box. An additional gate voltage can be added in series with the battery box from a computer controlled analog-digital (A/D) board. This allows the relevant gate voltages to be smoothly varied by the computer as data is taken. A circuit diagram of the battery boxes we use can be found in Appendix D, along with other details and tricks regarding the measurement set-up.
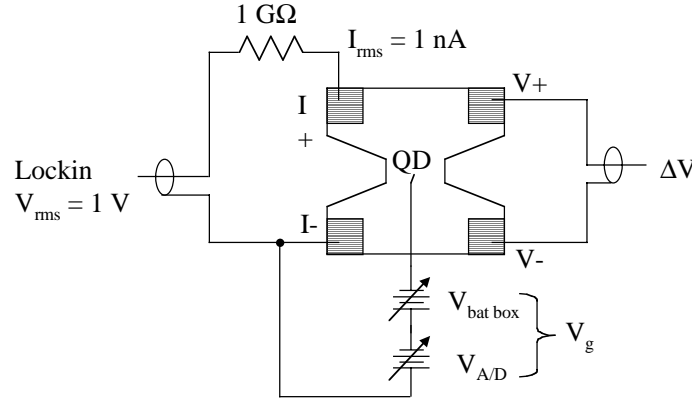
Figure 2-5. Circuit diagram of a 4-wire ac current bias measurement. The lockin sources an ac voltage V_{rms} which is converted into a constant ac current source, I_{rms}, via a 1 GΩ resistor. Two ohmics are used for the current path and two are used to measure the voltage drop, ΔV, across the device (fed back into the lockin, not shown). The gates are biased with negative voltages from the computer driven A/D converter and the battery box, $V_g = V_{A/D} + V_{bat box}$, which are referenced to the 2DEG via the I- ohmic.

2.3.2   2- and 4-Wire Voltage Bias Measurements

Voltage bias measurements are usually used when the average sample resistance is greater than 25 kΩ, or for conductances $g < e^2/h$. The simplest voltage bias set-up is a 2-wire measurement where a constant ac voltage, V_{sd}, is applied across the source-drain reservoirs and the resulting current in the circuit is measured to determine the conductance (Fig. 2-6a). The ohmic contacts typically have resistances of ~ 1 kΩ, and the sample wiring of the cryostat may also be of order kΩ's. These resistances add in series with the sample to determine the current measured: $I = V_{sd}/(R_{dev} + R_{ohmics} + R_{wires})$. Therefore, it is necessary that the sample resistance be much larger than the other in-line resistances in order for a 2-wire voltage bias measurement to be useful.

As seen in Fig. 2-6a, a voltage bias is applied across the device using the output of the lockin amplifier divided down to the desired voltage (to keep $eV_{sd} < kT$). The high voltage is connected to an ohmic contact in the source reservoir. An ohmic in the drain reservoir is connected to an Ithaco 1211 current pre-amp which feeds into the lockin to measure the current. Small 50 Ω resistors are put in series with both the high and low voltage outputs on the lockin because we have found that lockin low (the shield of the output voltage) floats up and down by a few μV's. The gates are again biased relative to the low ohmics in the drain, with the same battery box plus computer controlled voltages described above.

A 4-wire voltage bias set-up can be used for measurements when the sample resistance is not always much larger than the other series resistances in the set-up. Such a circuit is shown in Fig. 2-6b and

(a)

(b)
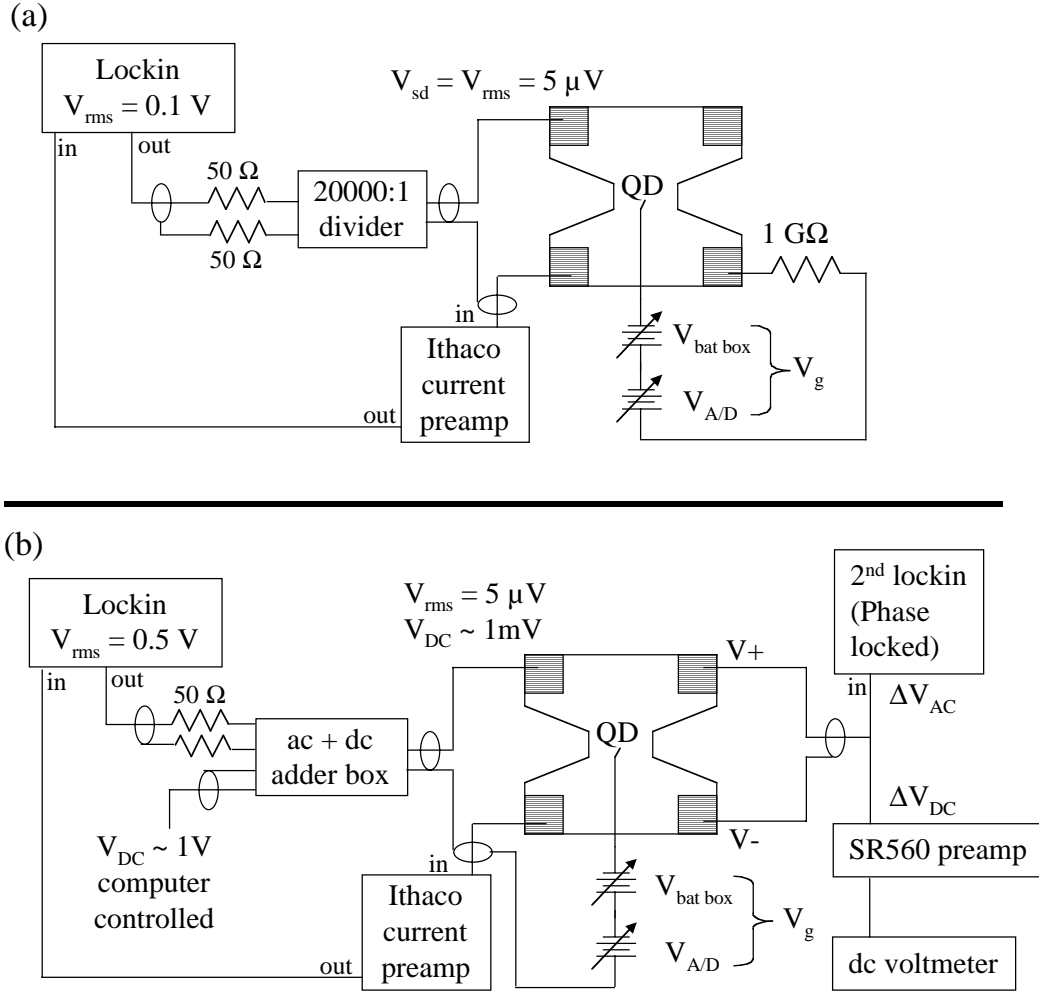
Figure 2-6.   Circuit diagram of 2- and 4-wire voltage bias measurements.   **(a)** A simple 2-wire measurement consists of a lockin sourced ac voltage, divided down to the desired $V_{sd} \sim \mu V$'s. The circuit is completed with an Ithaco 1211 current preamp connected to an ohmic in the drain. The output of the Ithaco feeds into the lockin to measure the current. The gates are biased relative to the drain ohmic contacts, through a GΩ resistor to prevent current leakage. **(b)** The 4-wire voltage bias measurement includes separate voltage sensing lines which feed into a second lockin, phase locked to the first, and an optional dc voltmeter. This circuit also shows a finite dc source-drain bias voltage added to the ac voltage. At a frequency of 13 Hz, the ac + dc adder box contains voltage dividers of 100,000:1 and 1000:1 for the ac and dc components respectively. A circuit diagram of the ac + dc box can be found in Appendix D.

consists primarily of an additional set of voltage probes to determine the voltage drop across the device itself, $V_{sd} = \Delta V$, using a second lockin frequency-locked to the first. This gives an accurate measure of the device resistance, $R_{dev} = \Delta V/I$. The circuit in Fig. 2-6b also includes a dc component to the applied source-drain bias voltage. The voltage measured across the device also contains a dc component, $V_{sd} = \Delta V_{ac} + \Delta V_{dc}$, read using a dc voltmeter. The applied dc voltage is produced by the computer using the A/D converter. The ac + dc adder box combines and divides the two voltage components; the box has a 100,000:1 divider for the ac voltage and a 1000:1 divider for the dc voltage, at 13 Hz. The circuit diagram of the adder box can be found in Appendix D.

2.4   Quantum Point Contacts

Having introduced GaAs/AlGaAs devices in general, and the various measurement schemes, we are ready to begin a more specific discussion of basic transport through quantum point contacts. Quantum point contacts (QPCs) are short one-dimensional (1D) channels connected adiabatically to large source and drain reservoirs. The devices we use are all formed by two surface depletion gates (Fig. 2-3b) which, when negatively biased, force the electrons to flow through a narrow constriction in the 2DEG. The width of the channel is controlled by the gate voltage and can be made comparable to the Fermi wavelength (~ 40 nm in a typical 2DEG). An excellent overall review of QPCs can be found in Ref. [62].

The conductance through a QPC shows steps in units of $2e^2/h$ as the negative gate voltage is increased (Fig. 2-7). This quantization was first discovered in 1988 by van Wees and collaborators at Delft University of Technology in the Netherlands [63] and by Wharam and collaborators at Cambridge University in England [64]. The quantization of conductance was understood, even in the first papers, as indicating the full transmission of one-dimensional (1D) modes of the constriction with the factor of two reflecting spin-degeneracy. Figure 2-8 shows a cartoon QPC with the first and second modes—corresponding to a half and full wavelength in a waveguide picture—illustrated.

Following Ref [65], the quantization of conductance in a QPC can be calculated in a simple model starting from the Hamiltonian

$$H = \frac{p_x^{\,2}}{2m^*} + eV(x) + \frac{p_y^{\,2}}{2m^*}, \tag{2.2}$$

where $V(x)$ is the confining potential from the gates in the lateral direction. We do not include the potential $V(y)$ in the longitudinal direction which describes the transition from the wide 2DEG reservoirs to the constriction. Glazman *et al.* [66, 67] have shown that the potentials $V(x)$ and $V(y)$ can be decoupled if the transition to the wide 2DEG regions is sufficiently smooth. The Hamiltonian in Eq. 2.2 then describes the
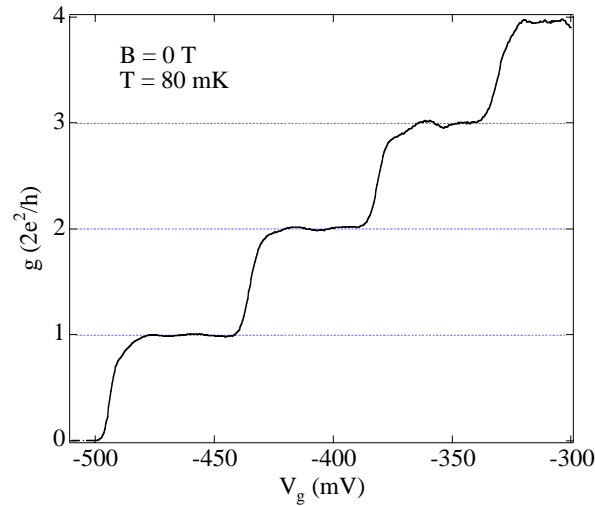
Figure 2-7. Quantized conductance in a quantum point contact. The linear differential conductance, g, through a QPC as a function of gate voltage shows steps, quantized in units of $2e^2/h$ at B = 0, corresponding to the full transmission of spin-degenerate modes through the constriction. This data from QPC 4, described in Chapter 6.
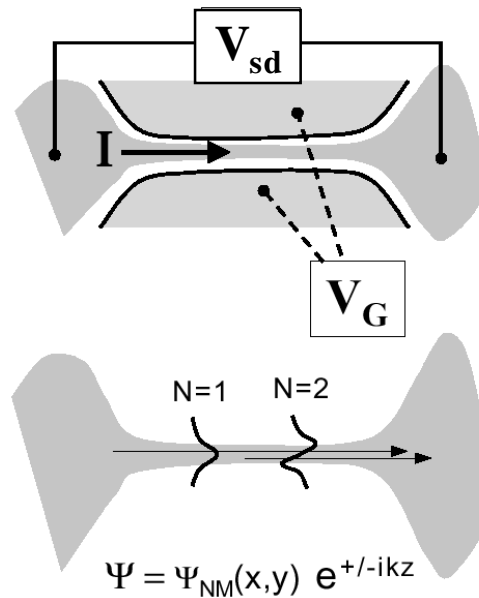
Figure 2-8. Cartoon QPC showing quantized modes. The top drawing shows the two gates of the QPC with applied gate voltage V_g. Current is restricted to flow through the constriction. The lower drawing indicates the lowest two transport modes, occurring when the width of the constriction is approximately one half and one full Fermi wavelength wide, respectively. (Figure courtesy of A. Huibers).
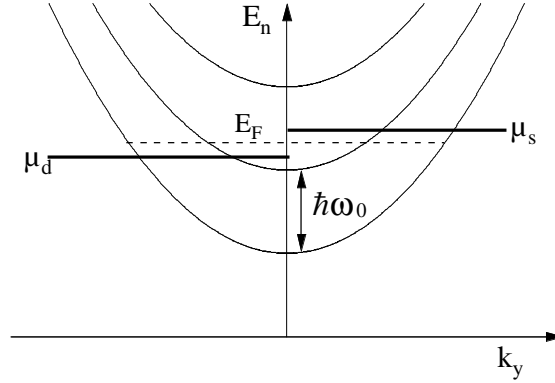
Figure 2-9. Energy dispersions for 1D channel. Energy E_n (for n = 1,2,3) vs. longitudinal wavevector k_y from Eq. 2.3 at the bottleneck of a QPC assuming parabolic confinement in the lateral direction. Electrons in the source and drain fill the available states up to the chemical potentials μ_s and μ_d, respectively. When a finite source-drain voltage is applied, a net current results from the uncompensated occupied electron states in the interval between μ_s and μ_d.

narrowest point of the QPC, which determines the transport properties. We take a parabolic confining potential in the lateral direction, $V(x) = 1/2 \, m^* \omega_0^2 x^2$, in accord with Refs. [68, 69]. Solutions to the Schrodinger equation using this Hamiltonian can be written in the form of a harmonic oscillator with energy eigenvalues

$$E_n = (n - \tfrac{1}{2})\hbar\omega_0 + \frac{\hbar^2 k_y^2}{2m^*}, \quad (n = 1, 2, \ldots). \tag{2.3}$$

These energies describe 1-D subbands because electrons are free to move in the y-direction (described by the free-electron kinetic energy dispersion) but quantized in the x-direction. Figure 2-9 shows these 1-D subband dispersions versus the longitudinal wave vector k_y. Electrons in the source and drain leads fill up states in the Fermi sea to the respective chemical potentials, μ_s and μ_d. Considering the orientation of the QPC shown in Fig. 2-8, electrons moving to the right come from the source and those moving to the left come from the drain. The velocity of the electrons in each subband is given by $v_n = (dE_n/dk_y)/\hbar$.

When a voltage V_{sd} is applied between the source and drain reservoirs, the chemical potentials on each side of the QPC are related as $eV_{sd} = \mu_s - \mu_d$. The resulting current, I, through the QPC is carried by the uncompensated states in this energy interval. At zero temperature, the net current is

$$I = e \sum_{n=1}^{N} \int_{\mu_d}^{\mu_s} dE \, \tfrac{1}{2} \rho_n(E) \, v_n(E) \, T_n(E), \tag{2.4}$$

where $\rho_n(E)$ is the 1D density of states and $T_n(E)$ is the transmission probability of the nth subband. For small values of V_{sd}, we can approximate $T_n(E) = T_n(E_F)$. The sum over n counts the number of occupied subbands, where the last (N^{th}) occupied subband is determined by the condition $E_N (k_y = 0) < E_F$. The 1D density of states is $\rho_n(E) = 2/\pi (dE_n/dk_y)^{-1}$. Herein lies the key to the quantization of the QPC: *The energy dependence of the 1D density of states exactly cancels that of the velocity*, leaving the current carried by each subband the same, independent of energy. Substituting these relations into Eq. 2.4 and calculating the conductance, $G = I/V_{sd} = eI/(\mu_s - \mu_d)$ one finds:

$$G = \frac{2e^2}{h} \sum_{n=1}^{N} T_n (E_F).$$ (2.5)

Equation 2.5 is known as the 2-terminal Landauer formula. In the limit of no backscattering, $\Sigma T_n = N$, so

$$G = \frac{2e^2}{h} N.$$ (2.6)

Therefore, each occupied subband contributes $2e^2/h$ to the conductance (in the absence of a magnetic field). Finite temperature smears what would otherwise be sharp steps in the conductance by convolving this zero-temperature limit with the derivative of the Fermi-Dirac distribution, resulting in quantized conductance plateaus like those seen in Fig. 2-7.

The above description applies to spin-degenerate 1D subbands in the QPC. The application of a large magnetic field in the plane of the sample splits the spin degenerate modes by the Zeeman energy, $g^*\mu_B B$, where $g^* = -0.44$ is the effective g-factor in GaAs. The resulting spin-resolved subbands can each carry a conductance of e^2/h. Plateaus in the conductance as a function of gate voltage reflect this quantization, as seen in Fig. 2-10. A magnetic field perpendicular to the 2DEG not only causes spin-splitting of the 1D subbands, but also affects the wide 2D source-drain regions via the quantum Hall effect. A review of the quantum Hall effect and QPCs can be found in Ref [62]. We are not interested in the quantum Hall regime, so the measurements on QPCs presented in Chapter 6 are all taken with an in-plane, parallel magnetic field.

2.5   Quantum Dots

Quantum dots (QDs) are formed by placing two quantum point contacts in series between the source and drain reservoirs and confining electrons in between to a small area characterized by $\lambda_F < L < L_\phi$. In ballistic dots, such as the ones studied here, this dimension must also be smaller than the mean free path. Because electron motion is restricted in all three dimensions, QDs are often considered zero-dimensional systems.
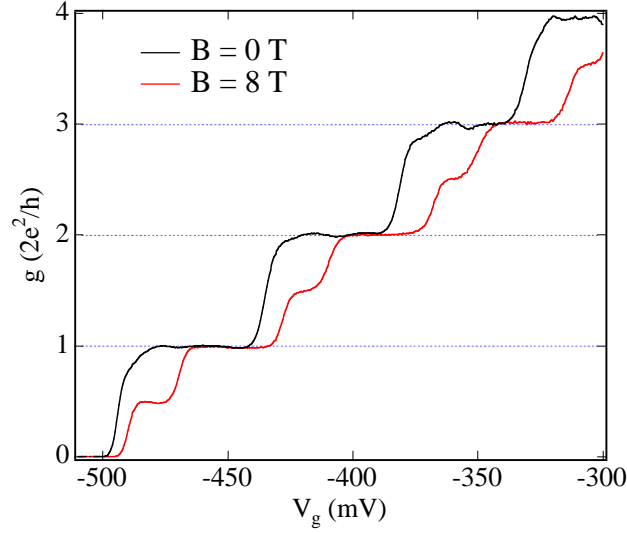
Figure 2-10. Quantized conductance of a QPC at $B_{\parallel} = 0$ and $B_{\parallel} = 8$ T. In a large in-plane magnetic field, the spin-degenerate conductance plateaus at multiples of $2e^2/h$ split into plateaus quantized in units of e^2/h. This data is from QPC 4, described in Chapter 6.

The electron confinement for dots is accomplished by gating a GaAs/AlGaAs heterostructure in the same way described above for QPCs. Several examples of multi-gate QDs were shown already in Fig. 2-3a. In these devices, the gates which form the entrance and exit point contacts control the coupling of the dot to the source and drain leads while the remaining gate voltages control the size and shape of the dot. Multiple gates allow measurements of the dot in a number of statistically different configurations (shape and size) without changing the coupling to the leads [70, 71]. This technique has been imperative to the successful investigation of quantum dot behavior which is often revealed only in statistical ensembles [48, 72].

2.5.1   Transport in "Open" Dots

Transport through quantum dots is typically divided into two regimes, "open" and "closed," based on the strength of the coupling between the dot and the leads. For strong coupling, where each QPC passes one or more modes, the conductance $g > e^2/h$, and the dot is considered "open." In this regime, electrons are classically allowed to travel through the dot, from the source to the drain.

The conductance of open QDs at low temperature is characterized by fluctuations which can be understood as the interference of phase-coherent electrons traversing the dot via a number of interfering paths [45, 70]. Though interference clearly requires a wave description of the electron, transport in open

QDs is often discussed using particle-like trajectories with phase. The conductance through the dot is determined by the relative probability of an electron which enters the dot from the source QPC exiting into the drain versus returning to the source QPC where it started. These probabilities, in turn, depend on the constructive or destructive interference of all possible trajectories which either make it through the dot or return to the entrance. Figure 2-11 shows a QD with two possible through-trajectories illustrated. Any change to the dot system which affects the accumulation of the trajectory phase, such as changing the shape with a gate voltage or changing a perpendicular magnetic field, will alter the interference pattern, resulting in random but repeatable conductance fluctuations as a function of the external parameter. A perpendicular magnetic field affects the interference because trajectories accrue an Aharonov-Bohm phase from the flux they encircle, $\Phi = BA_{traj}$, where A_{traj} is the area swept out by a given trajectory. Conductance fluctuations are shown in Fig. 2-12a as a function of gate voltage, and in 2-12b as a function of perpendicular magnetic field.

The fluctuations described above have been given the name "universal conductance fluctuations" (UCF) because they exhibit universal statistical properties [70, 73-78]. One such universal property is that the magnitude of UCF is always of order e^2/h regardless of the average conductance through the device. These universalities apply whenever the QD has an irregular (non-integrable) shape such that chaotic scattering occurs. Put another way, trajectories through the dot must cover the available phase space evenly. Practically speaking, this chaotic-shape condition is easily met at low magnetic fields. Not only can we design dots with arbitrarily shaped cavities, but the walls of any man-made device will contain irregularities which lead to non-specular scattering.

Significant theoretical efforts over the past two decades have shown that universal aspects of mesoscopic phenomena, such as UCF, are associated with the universal spectral properties of random matrices [72, 79-81] and the universal properties of the quantum manifestations of classical chaos [79, 80, 82]. A review of this remarkable field is beyond the scope of this thesis, but the reader is referred to Refs. [55, 61, 82] for discussions on this subject.

Besides UCF, another characteristic of transport through open QDs which will be relevant later in this work is "weak localization." In QDs, weak localization refers to the increase in constructive backscattering which occurs in the presence of time-reversal symmetry [70, 83-85]. For a given dot configuration, a certain number of trajectories will backscatter, or return to the same point contact where they began. These paths have time-reversed pairs which paths that travel *through* the dot (exiting at the other QPC) do not. At zero magnetic field, time-reversed paths accumulate the same phase because they share the same length and no magnetic flux is encircled. This ensures constructive interference of time-reversed pairs back at the entrance QPC which in turn enhances the probability that electrons will backscatter rather than conduct *through* the dot. When time-reversal symmetry is broken with a perpendicular magnetic field, each path accumulates a different Aharonov-Bohm phase, killing the
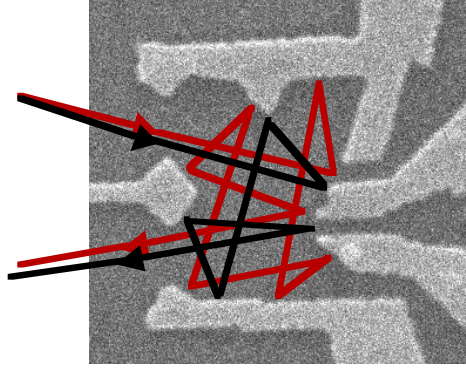
Figure 2-11. Interfering paths in a quantum dot. Two possible trajectories for an electron traversing the QD interfere at the exit point contact. The paths accumulate phase based on the pathlength and the magnetic flux enclosed. The interference of these and all other paths through the dot determine the conductance.
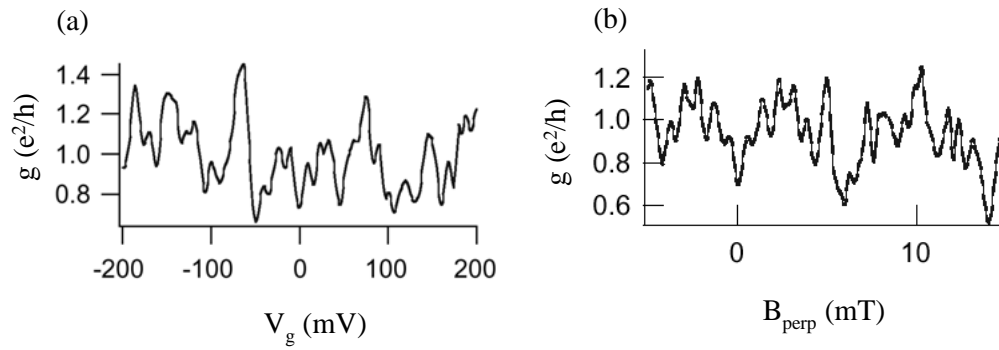
Figure 2-12. Conductance fluctuations in an open quantum dot. The conductance as a function of gate voltage **(a)** and perpendicular magnetic field **(b)** shows random but repeatable fluctuations. (Data taken by A. Huibers in the Marcus Group).

enhanced constructive interference and the enhanced backscattering. The overall result is a decrease in the conductance *through* the dot around zero magnetic field as seen in the traces of Fig. 2-13. Random fluctuations still determine the particular conductance of a QD even at B = 0, but when averaged over a large number of configurations, the conductance exhibits a prominent dip around B = 0 compared to the average for B ≠ 0 (see the average of 47 traces in Fig. 2-13). Weak localization in open QD systems is important because it can be used to measure decoherence leading to experimental estimations of the coherence time and length in these devices. Reviews of weak localization can be found in [55, 61].

2.5.2   Transport in "Closed" Dots

Quantum dots are considered "closed," or isolated, when the coupling between the dot and the leads is small such that the conductance $g < e^2/h$. This occurs when the number of modes through each point contact is less than one. Classically, transport through closed dots is forbidden, but quantum mechanics allows electrons to tunnel on and off the dot through the QPC barriers. In this regime, it is convenient to consider the dot as an island of charge with three nearby terminals: the source, drain, and gate. The source and drain each have a resistive and capacitive element connecting them to the dot, while the gate is coupled only capacitively. This representation is shown in the circuit diagram of Fig. 2-14.

Classically, if we view the dot as one electrode of the gate capacitor, the charge on the dot should be a simple function of the voltage V_g applied to the gate, $Q = C_g V_g$, where C_g is the capacitance to the gate (Fig. 2-15a). This is a good approximation for dots containing a large number of electrons, or for open dots where fractional equivalent charge can occur because electrons are allowed to flow easily on and off the dot. For small closed dots, however, charge cannot flow freely, the dot contains a discrete number of electrons, and the linear Q versus V relationship breaks down. In particular, the charge on the dot is always an integer (in units of e) and increases in a step-like manner as the gate voltage is increased (Fig. 2-15b).

For the isolated dot, the number of electrons at a certain gate voltage is always fixed, either N or N+1 for example, except at the vertical steps in the Q staircase. At these "charge degeneracy" points, the number of electrons can fluctuate by one—an additional electron can tunnel onto the dot, then tunnel off again, repeatedly changing the number of electrons from N to N + 1 and back to N [67]. This results in current flow through the dot. Away from the degeneracy points, the number of electrons on the dot is fixed and no current flows. A measurement of current through the dot as a function of gate voltage shows evenly spaced peaks aligned with the degeneracy points, as illustrated in Fig. 2-15c. This behavior, and in particular the regions where no current flows, is known as the Coulomb blockade [46, 47, 86].

The periodicity of the Coulomb blockade (CB) peaks as a function of gate voltage is determined by the capacitive coupling to the dot, $\Delta V_g = e/C_g$. In terms of the dot energy, $\Delta E_{dot} = e^2/C_g$, which can be interpreted as the energy required to add one more electron to the collection of negative charge on the dot.
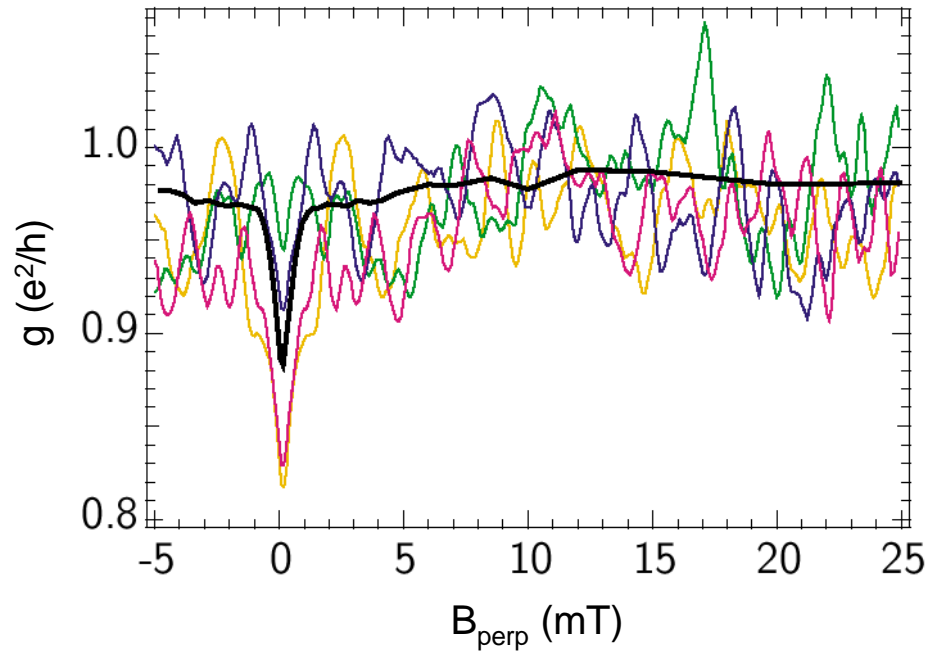
Figure 2-13. Weak localization in open dots. Conductance as a function of perpendicular magnetic field shows universal conductance fluctuations (UCF) and weak localization for several different gate configurations (colored traces). The average of 47 individual traces (thick black line) shows that UCF average to zero but the weak localization correction around $B_{perp} = 0$ does not. (Data taken by A. Huibers and M. Switkes in the Marcus Group).
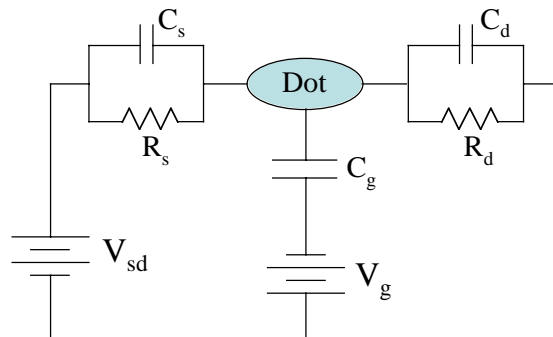
Figure 2-14. Schematic circuit diagram of a "closed" quantum dot. The dot is connected to the source and drain terminals capacitively and resistively. The gate(s) couple only capacitively to the dot.
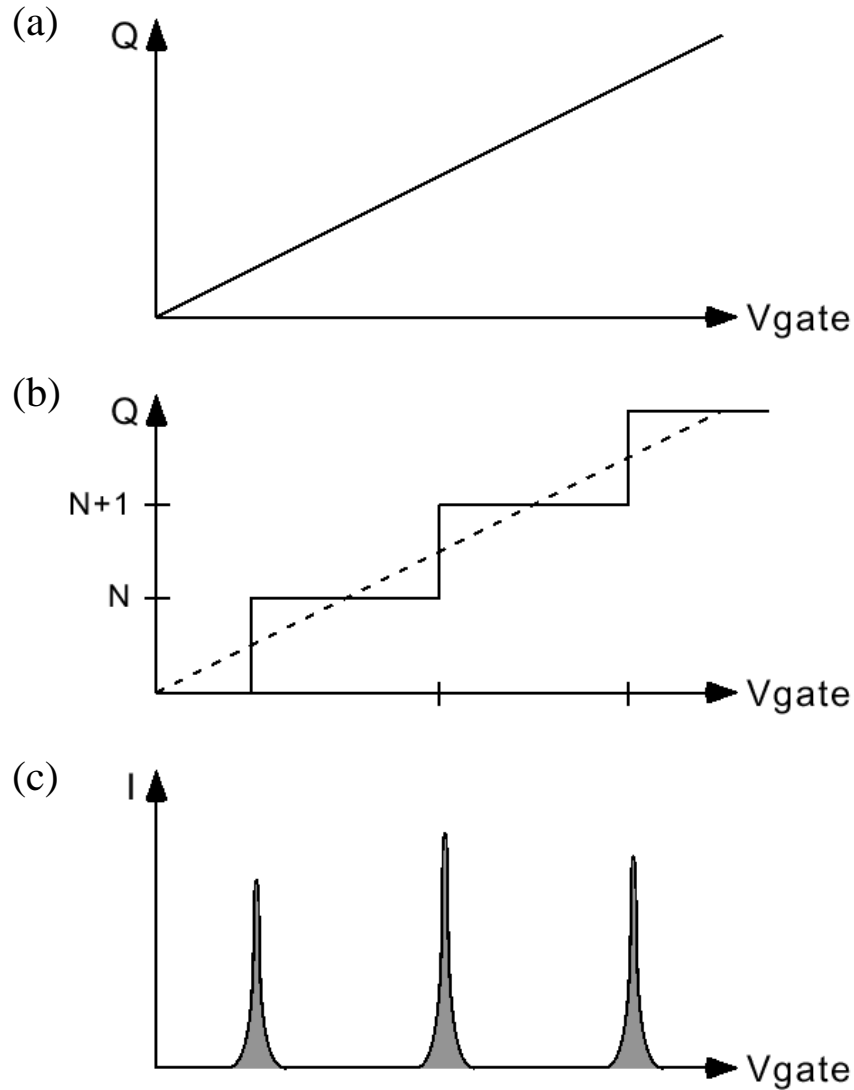
Figure 2-15. Quantized charge and the Coulomb blockade. **(a)** The linear Q vs. V relation for classical capacitors describes the charge of a closed QD for a large number N of electrons or for open dots. **(b)** For a countable number of electrons in a closed QD, the charge Q increases in steps with each electron added to the dot. **(c)** At the vertical steps where the charge on the dot can fluctuate by one, current can flow through the dot. In between, where Q is fixed, current is blocked by the Coulomb blockade. The signature of the Coulomb blockade is periodic peaks in current (conductance) as a function of V_{gate}. (Figure courtesy of D. Stewart).

As described in the first chapter, this is the charging energy, U. Technically speaking, the spacing between CB peaks is not exactly equivalent to the charging energy because the dot is capacitively coupled to more than just the single gate. Taking all the capacitances into account, $C_{tot} = C_s + C_d + C_g$, where $C_{s(d)}$ is the capacitance to the source (drain) lead, the charging energy is defined as $U = e^2/C_{tot}$. The peak spacing can be written as $\Delta V_g = e/C_g = (1/\eta)U/e$, where $\eta = C_g/C_{tot}$ is the conversion factor between the applied gate voltage and the actual change in the island energy. (So far, the finite energy spacing between levels, which also contributes to the peak spacing, has been neglected).

To observe the charging effects of the Coulomb blockade, two conditions must be met. The first is that the temperature must be less than the charging energy; that is $kT < U$. The second condition requires that the QPC barriers be sufficiently high that electrons are firmly located either on the dot or in the source or drain leads. This translates into a lower bound for the tunnel resistance of the barriers, R_t. To determine this bound, consider the typical time to charge or discharge the dot, $\Delta t = R_t C_{tot}$. Electrons move on and off the dot, changing the dot energy by U, via classically forbidden tunneling which is regulated by the Heisenberg uncertainty relation: $\Delta E \Delta t = (e^2/C_{tot})(R_t C_{tot}) > h$. This implies that $R_t > h/e^2 = 25813 \; \Omega$, or equivalently the conductance $g = 1/R < e^2/h$, which is precisely the weakly coupled condition for "closed" dots presented at the beginning of this section.

The discussion above describes how charge on an isolated dot builds up in discrete steps and leads to the Coulomb blockade. The Coulomb blockade can also be easily understood using the types of energy diagrams shown in Fig. 2-16. These diagrams show the potential landscape in the transport direction where the dot is modeled as a set of discrete energy levels between two tunnel barriers. Outside the dot, electrons fill up the states of the source and drain leads to the chemical potentials μ_s, μ_d, which are related by the applied bias voltage $eV_{sd} = \mu_s - \mu_d$. Particles confined to a finite system can only exist at certain allowed energies which are the eigenvalue solutions to the Schrodinger equation for the particular confining potential. For a small 2D system of area A, these energy levels have a constant average spacing given by $\Delta = \hbar^2 \pi/m^*A$ for the spin-degenerate case and $\Delta = 2\hbar^2 \pi/m^*A$ if there is no spin-degeneracy. A lifetime broadening is associated with the energy states, $\Gamma = \Gamma_L + \Gamma_R$, where $\Gamma_{L,R}$ are the couplings of the dot to the "left" and "right" (or source and drain) leads.

In a simple picture, the energy states of the dot are filled sequentially with two electrons of opposite spin occupying each spin-degenerate level. The number of electrons allowed on the dot at a given gate voltage is such that the chemical potential of the dot, indicated by the last filled state, is less than that of the source or drain leads. A gap exists between the last filled state and the next available unoccupied state (Fig. 2-16). This is, again, the charging energy U—now easily seen as the energy required to add the

next electron to the dot.[4] Within this energy diagram picture, transport through the dot (at zero temperature) follows a simple rule: *the current is (non) zero when the number of available states in the energy window between μ_s and μ_d is (non) zero*. In Fig. 2-16a, there is an unoccupied state aligned between the source and drain leads. An electron from the source is free to tunnel onto the dot, then back off into the drain, repeatedly. This process, known as *single electron tunneling*, transfers one electron through the dot while oscillating the number of electrons on the dot from $N \rightarrow N + 1 \rightarrow N$. When the dot is tuned with the gate voltage, such that no states exist in the source-drain bias window, tunneling through the dot via first-order processes is forbidden, and little or no current flows (Fig. 2-16b). This is the Coulomb blockade. As a function of gate voltage, energy states are continually moved into then out of the source-drain bias window resulting in nearly periodic peaks in the current or conductance of the dot.

It is worth briefly discussing the temperature dependence of the Coulomb blockade peaks. For very high temperatures, $kT > U$, the quantization of charge indicated by the Coulomb blockade cannot be observed. For $(\Gamma, \Delta) < kT < U$, dots exhibit classical Coulomb blockade [94-98], so called because a number of states ($\sim kT/\Delta$) are available for transport on each peak due to the thermal width of the Fermi function in the source and drain leads. In this regime, the heights of CB peaks are roughly constant and equal to half of the high temperature conductance. The low temperature quantum Coulomb blockade regime occurs for $\Gamma < kT < \Delta < U$ [86]. Here, transport occurs only through one level (assuming $eV_{sd} < \Delta$), and the height of each CB peak reflects the coupling of its particular energy eigenfunction to the source and drain leads (Fig. 2-17). The average peak height, given by Random Matrix Theory (RMT) [99], is

$$\langle g_{max} \rangle = \frac{e^2}{h} \frac{\pi}{2kT} \left(\frac{\Gamma_L \Gamma_R}{\Gamma_L + \Gamma_R} \right). \tag{2.7}$$

The full distribution of peak heights in the "resonant tunneling" regime has also been calculated with RMT [99] and experimentally verified [100, 101], and is one of the remarkable properties of quantum dots that is well-described by a theory of non-interacting electrons.

The lineshape of CB peaks is the same in both the quantum and classical Coulomb blockade regimes, roughly a $\cosh^{-2}$ form [94, 102]. Additionally, the width of the $\cosh^{-2}$ peak is proportional to temperature in both cases (as long as $\Gamma < kT$ so that the peaks are broadened by temperature). The exact dependence is different, however, with the CB peak width $\sim 3.5kT$ in the quantum regime and $\sim 4.3kT$ in

---

[4] In the simple picture of spin-degenerate levels, the energy to add an electron to the dot depends on the parity of the dot. For an even number of electrons, the next electron will occupy a new energy level, so the addition energy is equal to $U + \Delta$. When the dot contains an odd number of electrons, the next electron will fill the remaining state of the last energy level, so the addition energy is simply U. Experimentally, this simple picture of even-odd spacings between CB peaks is often not borne out, presumably due to interactions. Theoretical predictions and experiments on CB peak spacings can be found in Refs. [87-93].
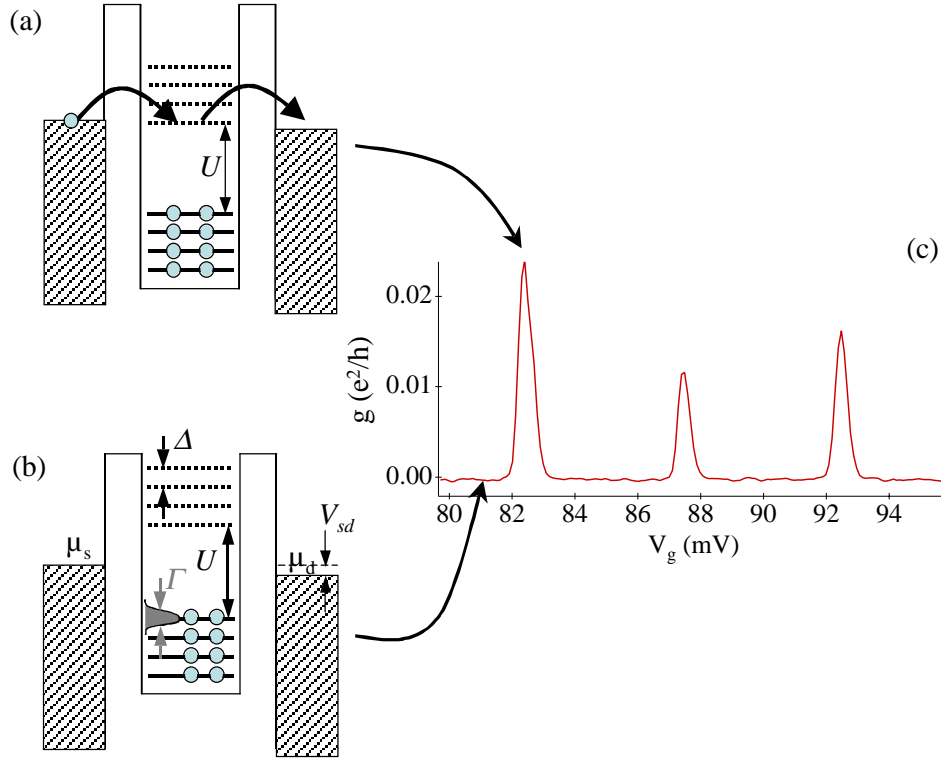
Figure 2-16. Coulomb blockade energy diagrams. **(a,b)** The dot is made of discrete energy levels with broadening, Γ, separated by the level spacing, Δ. The charging energy, U, separates the last filled from the next unoccupied state. Electrons in the source and drain leads are filled up to the chemical potentials μ_s, μ_d, related by $eV_{sd} = \mu_s - \mu_d$. In **(a)**, finite current flows as electrons tunnel on and off the dot via the single state that lies between μ_s and μ_d. In **(b)**, the chemical potential of the dot has been shifted up by the gate voltage. Now there is no state available for first order tunneling processes and transport through the dot is blocked. **(c)** Changing V_g to shift the levels of the dot up further will result in a new state entering the source-drain window, leading to peaks in the conductance as a function of V_g.

the classical regime [94, 102]. Though the exact line shape of the CB peaks is not relevant for the experiments described in this thesis, the dependence of the peak width is the general method by which both the electron temperature and the capacitive conversion factor η are determined experimentally. Specifically, we measure CB peak widths, the full-width at half-max (FWHM), as a function of the cryostat temperature, as shown in Fig. 2-18. At low T, the peak widths deviate from the linear relation, indicating a saturation of the electron temperature. We report this saturation value as the base electron temperature. The slope of the peak widths in Fig. 2-18 gives the conversion factor η between gate voltage and dot energy as $e\eta$(FWHM) = 3.5kT or 4.3kT, as appropriate. This allows an experimental determination of the charging energy U, described previously.
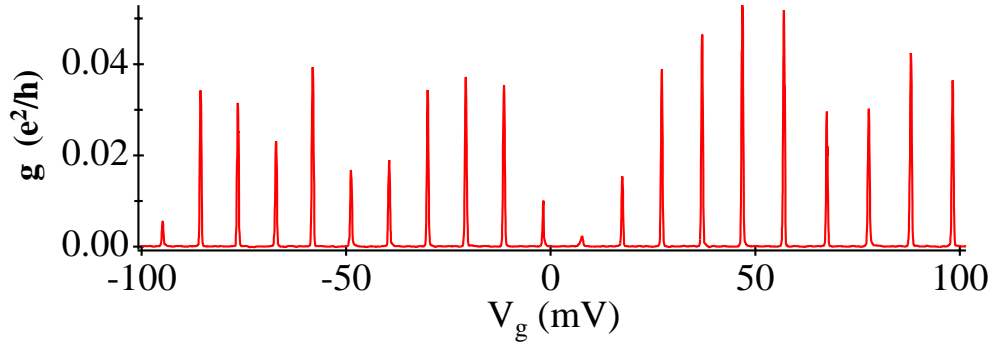
Figure 2-17. Resonant tunneling Coulomb blockade peaks. For $\Gamma < kT < \Delta$, transport on CB peaks occurs through only one energy state. Peak heights show mesoscopic fluctuations which reflect the coupling of a particular state to the leads. From Ref [100].
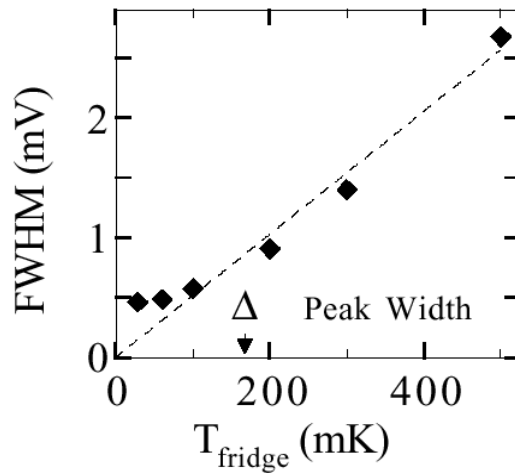
Figure 2-18. CB peak width vs. cryostat temperature. The linear dependence of the CB peak width on temperature determines the conversion factor between gate voltage and dot energy, as discussed in the text. The low temperature saturation of the peak width indicates the saturation of the electron temperature. From Ref [100].

The final topic in the discussion of basic transport through closed, Coulomb blockaded quantum dots is the effect of a perpendicular magnetic field on the CB peaks. Just as for open dots, a perpendicular magnetic field affects the wavefunctions of a closed dot. This means that peak heights, which reflect the coupling of a certain state (or the average over several states), will fluctuate as a magnetic field perturbs those wavefunctions. The conductance fluctuations of CB peaks are analogous to UCF in open dots and have also been calculated, along with their correlation functions, within non-interacting models for the quantum CB regime [99, 103, 104]. In addition, the position of a CB peak in gate voltage will fluctuate with magnetic field, reflecting the changes in the eigenenergy of its particular state. The fluctuations of height and position for one CB peak are shown in Fig. 2-19a as a function of perpendicular magnetic field and gate voltage. In Fig. 2-19b, the same data is shown in a grayscale image. The exact character of CB peak height and position fluctuations in the quantum tunneling regime is often considered a magneto-fingerprint of the particular quantum energy state. These fingerprints have been studied extensively in efforts to understand the energy spectrum of QDs and, in particular, how and where the spectrum deviates from a simple non-interacting picture [105, 106].

For the interested reader, there are a number of reviews on transport phenomena in quantum dots. For an introduction, historical context, and review of experimental work on QD transport (focusing on the Coulomb blockade regime), see Ref. [47]. Theoretical reviews of QD transport can be found in Refs. [96] (detailed transport theory), Ref. [48] (statistical theory of QDs), Ref. [86] (single electron theory of QDs), and Ref. [107] (CB regime, including cotunneling and Kondo effects).

The above description of the Coulomb blockade in quantum dots has assumed a level broadening $\Gamma \ll (kT, \Delta)$. As will be seen in the upcoming chapters, however, this is not an intrinsic requirement for the CB. Indeed, as the coupling to the leads increases such that $\Gamma \sim \Delta$, some interesting behaviors emerge. Most noticeably, the conductance in between CB peaks, in the *CB valleys*, becomes measurable. Transport in CB valleys requires second order processes known as *cotunneling* [108], where electrons traverse the dot through high energy "virtual" states. Though more difficult to treat theoretically, transport through an isolated but strongly coupled quantum dot shows a number of characteristics which illustrate the importance of coherence, charging and spin in these systems. The experiments in the following chapters explore a few of these behaviors in detail.
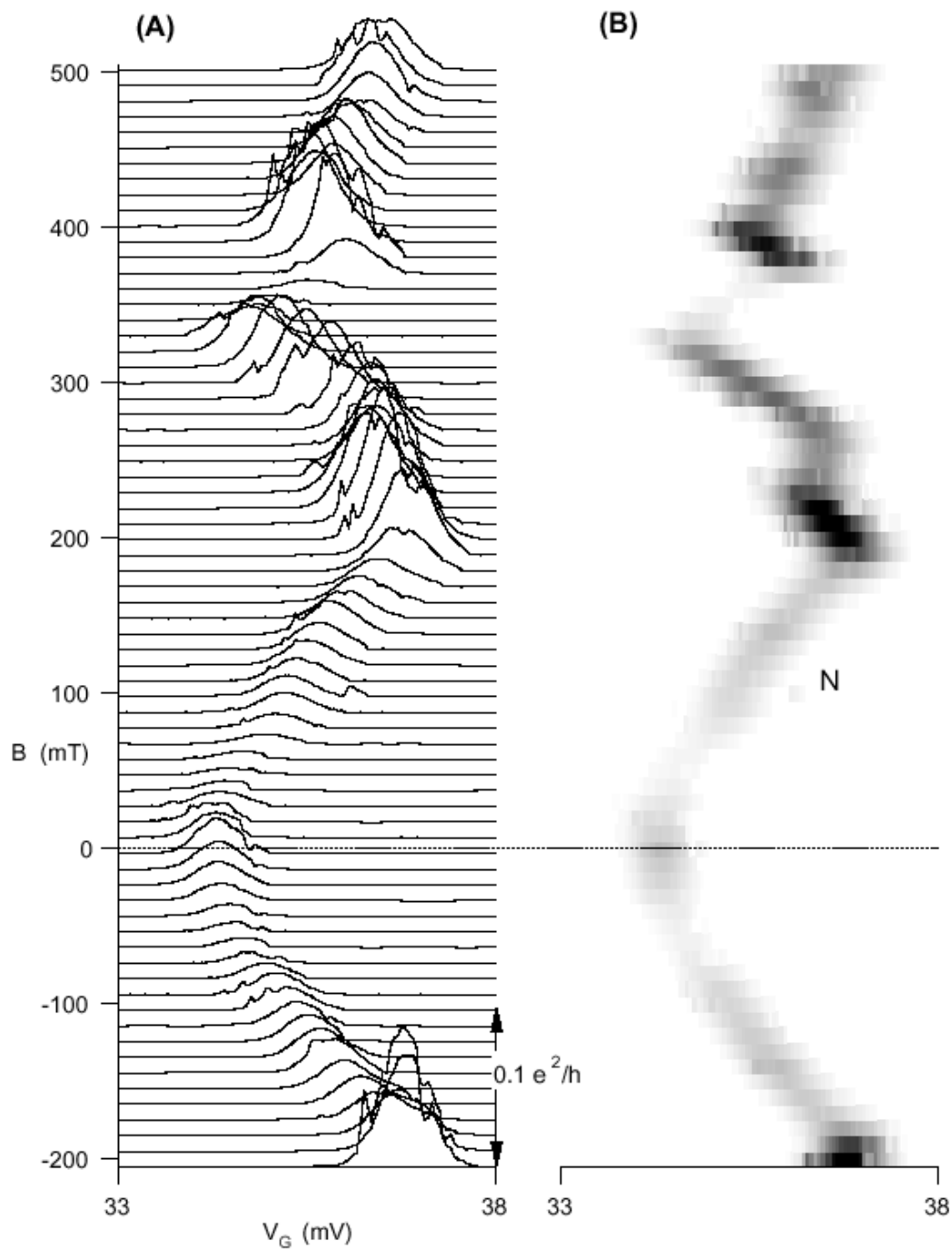
Figure 2-19. Magnetic field dependence of a CB peak. **(a)** Conductance as a function of V_g at discrete values of the perpendicular magnetic field, B. The CB peak fluctuates in both position and height as a function of B. **(b)** The same data shown with conductance in grayscale as a function of V_g and B. (Data courtesy of D. Stewart, Ref. [105]).

Chapter 3

Mesoscopic Fluctuations of Elastic Cotunneling in Coulomb Blockaded Quantum Dots

3.1   Introduction

The Coulomb blockade (CB) in small metallic and semiconductor structures provides a system in which transport is dominated by the effects of electron-electron interactions [46, 96]. At low temperature, transport in small systems is also influenced by quantum interference, leading to mesoscopic fluctuations with universal statistical features [74, 75, 109-111]. Theoretical work has provided a detailed understanding of mesoscopic fluctuations for the case of noninteracting electrons and has called attention to the connection between the universal statistics and quantum chaos [72, 77-79, 112-114]. Coulomb blockaded quantum dots provide a useful system to move beyond the noninteracting picture, yet remain relatively simple: interactions can often be treated in terms of a single charging energy, U.

This chapter presents measurements of elastic cotunneling in Coulomb blockade valleys where electron-electron interactions, through the charging energy, play a significant role in determining transport properties. The behavior of the CB valleys is compared to the behavior of the CB peaks, which are insensitive to charging effects. The conductance of both peaks and valleys show mesoscopic fluctuations due to quantum interference which provide the statistical tool used to investigate the effects of electron-electron interactions in this system. We observe an increase in the characteristic magnetic field scale of

conductance fluctuations in CB valleys compared to fluctuations of CB peaks, and find that valleys do not exhibit the decrease in average conductance at B = 0 (the "weak localization" introduced in Chapter 2) that is seen in peaks. We also compare the cross correlations of the magneto-conductance of neighboring peaks and valleys, finding longer correlations among the valleys. This effect is explained in terms of the number of quantum levels participating in transport.

3.2   Cotunneling in quantum dots: Theory

The dominant experimental signature of the Coulomb blockade is the appearance of narrow peaks in conductance as an external gate voltage is swept, changing the potential of the dot. As introduced in Chapter 2, conduction is suppressed between peaks when the temperature T and voltage bias V_{sd} are less than the energy $U = e^2/C$ required to add one electron to the dot. In the quantum regime $\Gamma \ll (kT, V_{sd}) < \Delta \ll U$ (where $\Gamma = \Gamma_L + \Gamma_R$ is the coupling of energy states in the dot to the left and right leads, $\Delta = 2\pi\hbar^2/m^*A$ is the mean level spacing, and A is the dot area), transport on CB peaks is mediated by resonant tunneling where electrons traverse a single energy level aligned with the source and drain leads (Fig. 3-1a). Resonant tunneling, also known as "weak-tunneling", is insensitive to charging effects as can be inferred from the average conductance of CB peaks [99],

$$\langle G_{res} \rangle = \frac{e^2}{h} \frac{\pi}{2kT} \frac{\Gamma_L \Gamma_R}{(\Gamma_L + \Gamma_R)}, \tag{3.1}$$

which has no dependence on the charging energy U. Additionally, the insensitivity to charging has been demonstrated, for instance, in measurements of peak height statistics [100, 101] which gave excellent agreement with the single-particle random matrix theory (RMT) [99, 103, 104].

Resonant tunneling has another identifying characteristic which is a decrease in average conductance when time-reversal symmetry is obeyed (i.e. around zero perpendicular magnetic field) [48, 99, 115, 116], analogous to weak localization in open dots [48, 70, 83-85] and 1D and 2D disordered conductors [117]. RMT predicts that the average conductance of CB peaks (normalized to the average away from B = 0) will be smaller at B = 0 than at B >> 0 by a factor of 1/4 [99, 115].

The measurements presented in this chapter (and most of the thesis), do not fall strictly in the resonant, or weak-tunneling regime. Instead of closing the point contact leads such that the coupling Γ between the dot and the leads is very small ($\Gamma \ll \Delta$), we tune the coupling so that $\Gamma < \sim\Delta$, known as the "strong-tunneling" regime. Experimentally, this results in CB peaks with higher conductance and, if $\Gamma > \sim kT$, broadened by Γ instead of kT. Additionally, transport on CB peaks in the strong-tunneling regime may take place through several energy levels in parallel, as the broadened tails of neighboring levels

overlap. This reduces conductance fluctuations and increases correlations between neighboring peaks somewhat, but does not change the overall character of the CB and, in particular, does not change the insensitivity of CB peaks to charging effects.

The move to the strong-tunneling regime, where $\Gamma < \sim\Delta$, is very important in the CB valleys. In the weak-tunneling regime, the valley conductance is immeasurably small (as seen in Chapter 2, Fig. 2-16). The increased coupling to the leads in the strong-tunneling regime gives a measurable conductance in the CB valleys, thereby providing the necessary tool to investigate this system. In the valleys between CB peaks, first-order (resonant) tunneling is blocked because there is no energy state aligned with the leads. Conduction in the CB valleys is instead mediated by so-called cotunneling [118-121]. These are second-order processes where an electron tunnels through the dot via a high energy "virtual" state. Figure 3-1 illustrates the two forms of cotunneling processes: elastic and inelastic [120]. During inelastic cotunneling (Fig. 3-1b), imagine that one electron tunnels onto the dot and a different electron tunnels off. This leaves an electron-hole excitation and is not a *coherent* process—that is, the electron which is transported from the source to the drain does not show quantum interference. Elastic cotunneling, on the other hand, is coherent. Here, a single electron tunnels onto the dot and back off through a virtual state (Fig. 3-1c), so quantum interference can occur. At low temperatures, $kT < \sqrt{U\Delta}$, the dominant cotunneling process is elastic and, like the peaks, exhibits interference effects in the form of random but repeatable conductance fluctuations [122].

In contrast to resonant tunneling on CB peaks, cotunneling in CB valleys is sensitive to charging. This sensitivity is immediately obvious from the average conductance contribution of both cotunneling mechanisms [120]:

$$\langle G_{el} \rangle = \frac{\hbar G_L G_R \Delta}{4\pi e^2}\left(\frac{1}{E_e} + \frac{1}{E_h}\right), \ \langle G_{in} \rangle = \frac{\hbar G_L G_R \pi}{3e^2}(kT)^2\left(\frac{1}{E_e} + \frac{1}{E_h}\right)^2, \tag{3.2}$$

where $G_{L,R}$ is the conductance of the point contact to each lead, and $E_{e(h)}$ is the difference between the Fermi energy in the leads and the next available state for electron (hole) tunneling (i.e. $E_e + E_h = U$, and $E_e = E_h = U/2$ in the middle of the valley, see Fig. 3-1c). At low temperatures, conductance is dominated by the elastic mechanism, consisting of virtual tunneling of charge over an energy barrier of height $\sim E$, the smaller of (E_e, E_h). Near the valley center, where $E \sim U/2 >> \Delta$, virtual tunneling takes place through a large number $\sim E/\Delta$ of levels. Conduction through each level fluctuates randomly with external parameters, resulting in mesoscopic cotunneling fluctuations that do not average away even for large E/Δ [122]. Fluctuations of both CB peaks and CB valleys can be seen in the surface plot of Fig. 3-2. The direct dependence of the cotunneling conductance on U (through $E_{e,h}$) leads to characteristic signatures of cotunneling fluctuations which are distinctly different than those of resonant tunneling.
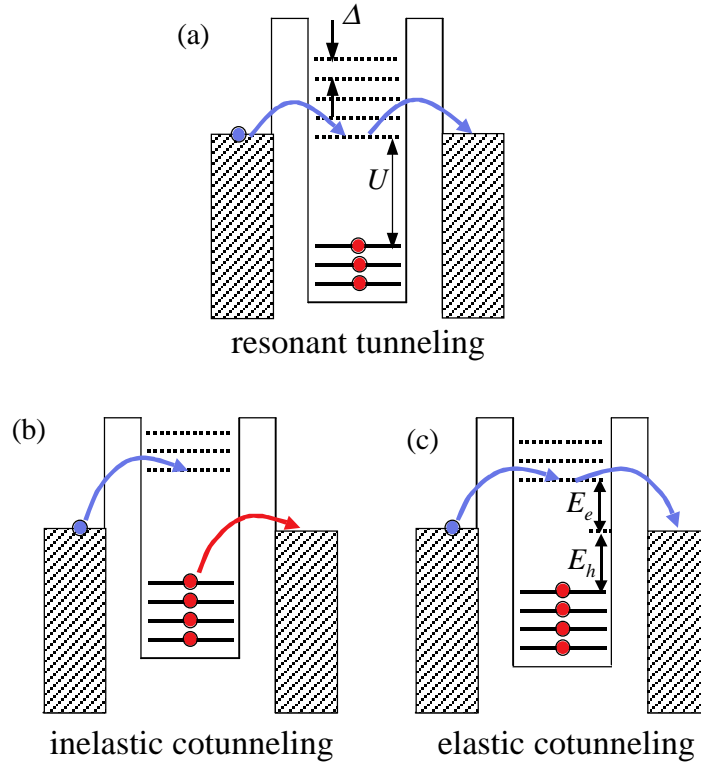
Figure 3-1. Resonant tunneling, inelastic and elastic cotunneling. **(a)** Energy diagram picture of resonant tunneling through a quantum dot in the Coulomb blockade regime. An electron tunnels through a single energy state aligned with the source and drain leads. This coherent process leads to mesoscopic fluctuations of peak position and height which reflect the particular transport state. **(b)** Inelastic cotunneling in CB valleys involves one electron tunneling onto the dot and a different electron tunneling off. This process is not phase coherent and cannot show quantum interference. **(c)** Elastic cotunneling, where a single particle tunnels though the dot via a "virtual" state (classically forbidden), is coherent. The definition of $E_{e(h)}$, the energy required for an electron (hole) to tunnel, is indicated.
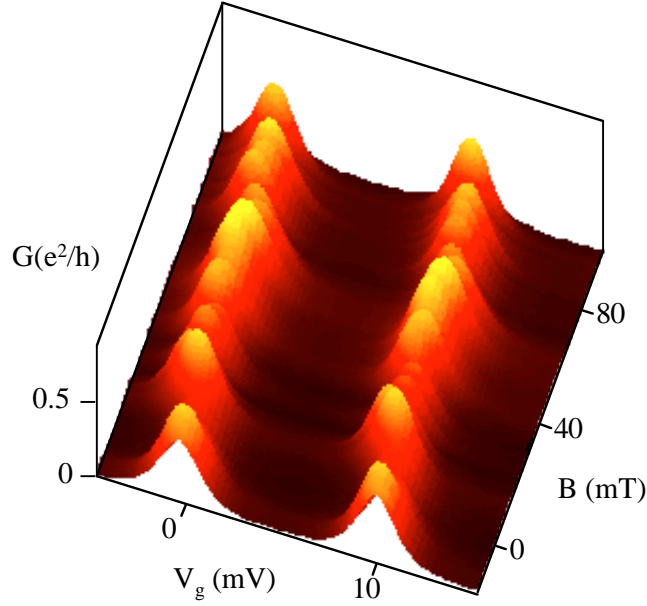
Figure 3-2. Conductance fluctuations of CB peaks and valleys. The differential conductance G as a function of gate voltage V_g and perpendicular magnetic field B shows two CB peaks and the valley between in the strong tunneling regime (note the height of the peaks, ~ 0.5 e^2/h). Mesoscopic fluctuations can be seen in the conductance of the peaks and of the valley. This data is from dot 1.

Experimentally, one can distinguish resonant tunneling fluctuations (on peaks) from cotunneling fluctuations (in valleys) by the characteristic scale, in perpendicular magnetic field, of fluctuations in the differential conductance G = dI/dV.[5] The characteristic magnetic field scale, B_c, of conductance fluctuations, G(B), is defined as the width of the autocorrelation function $C_{i,i}(\Delta B)$, where the correlation function

$$C_{i,j}(\Delta B) = \left\langle \tilde{g}_i(B)\, \tilde{g}_j(B + \Delta B)\right\rangle_B \Big/ \left(\sqrt{\mathrm{var}\,\tilde{g}_i}\,\sqrt{\mathrm{var}\,\tilde{g}_j}\right), \tag{3.3}$$

and $\tilde{g} = G - \langle G\rangle_B$ give the fluctuations in conductance around the average. The $\langle\ \rangle_B$ notation refers to an average over the perpendicular magnetic field B. The correlation function is a measure of the similarity between two functions (in this case the conductance fluctuations $\tilde{g}_i(B)$ and $\tilde{g}_j(B)$) as they are offset from

---

[5] Note that we use a capital 'G' for the differential conductance in this chapter, for lack of enough lowercase 'g' options. Also note that the magnetic field, B, is perpendicular to the sample.

each other by the relevant variable (ΔB in this example). The autocorrelation function compares $\tilde{g}_i$(B) to $\tilde{g}_i$(B + ΔB) and is normalized to 1 at ΔB = 0. Note that the autocorrelation $C_{i,i}(\Delta B)$ is symmetric about ΔB = 0 because the functions being correlated are the same, while the cross-correlation $C_{i,j}(\Delta B)$ is generally not.

Generally speaking, conductance fluctuations in magnetic field occur on a scale determined by the field required to pass one flux quantum ϕ_0 = h/e through a typical area difference accumulated by chaotic trajectories passing through the dot: $B_c A_{traj} \sim \phi_0$. In chaotic quantum dots the area swept out by a trajectory is diffusive, so $A_{traj} \propto \sqrt{\tau}$, where τ is the typical time an electron spends in the dot. For CB valleys, this time is limited by the Heisenberg uncertainty relation, $\Delta\tau\Delta E \sim \hbar$, because cotunneling occurs via classically forbidden (virtual) states at an energy $\sim$ E above the Fermi energy of the leads. Taking $\tau \sim \hbar/E$, the characteristic magnetic field scale for CB valley fluctuations has been calculated as:

$$B_c^{valley} = \kappa(\phi_0/A)\sqrt{E/E_T} \,, \tag{3.4}$$

where $E_T = \hbar v_F/A^{1/2}$ is the ballistic Thouless energy (related, inversely, to the time to cross the dot), A is the dot area, and κ is a device-dependent geometrical factor [122]. Equation 3.4 applies when most trajectories are fully chaotic, E < E_T. In the opposite case, for E > E_T, then E_T replaces E in Eq. 3.4, giving $B_c^{valley} \sim \kappa\phi_0/A$.

For comparison, the typical time spent in the dot during resonant tunneling on CB peaks is given by the Heisenberg time, $\tau_H \sim \hbar/\Delta$. For transport through open quantum dots, this timescale is $\tau \sim \hbar/\Gamma_{tot}$, controlled by the total broadening $\Gamma_{tot} = \Gamma_L + \Gamma_R + \Gamma_\varphi$ due to both escape from the dot [$\Gamma_{L,R} = (h\Delta/\pi e^2)G_{L,R}$] and dephasing [114, 123, 124]. This yields equivalent characteristic field scales for fluctuations of CB peaks and in open dots:

$$B_c^{peak} = \kappa(\phi_0/A)\sqrt{\Delta/E_T} \,, \tag{3.5}$$

$$B_c^{open} = \kappa(\phi_0/A)\sqrt{\Gamma_{tot}/E_T} \,. \tag{3.6}$$

One expects (B_c^{peak}, B_c^{open}) < B_c^{valley} from Eqs. 3.4, 3.5, and 3.6 since (Δ, Γ_{tot}) < E $\sim$ U. Furthermore, Eq. 3.4 implies that B_c^{valley} will have a maximum at mid-valley, where E = U/2, and decreases to match B_c^{peak} as the peak is approached and E $\rightarrow$ 0. If we make the approximation (from Eq. 3.2) that $\langle G_{el} \rangle \propto \left(E_e^{-1} + E_h^{-1}\right) \propto \sim E^{-1}$ and noting that $B_c^{valley} \propto \sqrt{E}$ further implies that $B_c^2 \langle G_{el} \rangle \sim$ constant.

3.3   Cotunneling in quantum dots: Experiment

We report measurements for three quantum dots defined using Cr/Au electrostatic gates on GaAs/AlGaAs heterostructures. The dots use similar designs with adjustable point contacts and two or three shape-distorting gates as shown in Fig. 3-3a. The shape-distorting gates allow ensemble statistics to be gathered on a single device. The "chaotic" shape and size of the dots (within the ballistic transport regime) permits comparison to a universal theory [122]. Important parameters for the dots are given in the table of Fig. 3-3b. Measurements were made in a dilution refrigerator using a 2-wire ac voltage bias set-up with V_{rms} ~ 5 μV (< Δ, kT) at 13Hz. The base electron temperature, T ~ 100 mK, measured from CB peak widths, easily satisfies the requirement $kT < \sqrt{U\Delta}$ ~ 600 mK, so elastic cotunneling is the dominant transport process in CB valleys.

Conductance fluctuation statistics were measured by rastering over gate voltage, V_g, and perpendicular magnetic field, B, to yield a 2D scan of conductance, as seen in Fig. 3-4a. Here, two CB peaks and one CB valley in between are seen as a function of magnetic field with the conductance, G, shown in a colorscale. The white traces labeled 1 and 4 follow the tops of the CB peaks, determined from $cosh^{-2}$ fits [102]. Trace 2 follows the minima of the valley from parabolic fits. Trace 3 follows a path partway up the peak at a position linearly interpolated (at each B) between the peak and valley. Random conductance fluctuations are seen in the peaks, valleys, and all interpolated paths (see Fig. 3-4b,e,f).

(a)   1 μm   (b)

parameter	dot 1	dot 2	dot 3
l (μm)	8.4	8.4	4.3
A (μm²)	0.81	0.45	0.57
Δ (μeV)	8.8	15.8	12.4
U (μeV)	330	410	250
E_T (μeV)	140	180	200
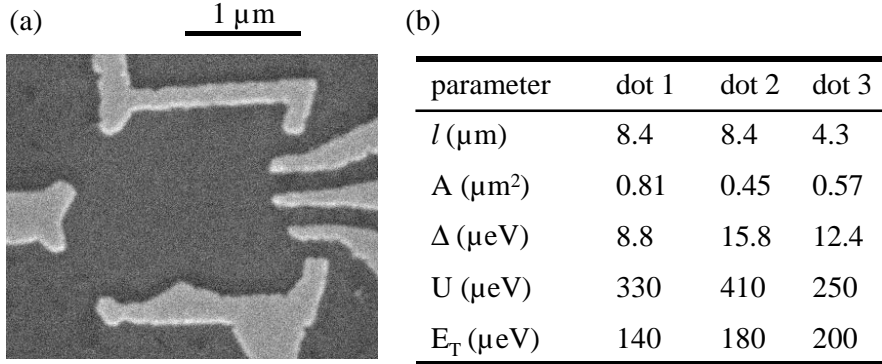
Figure 3-3. Quantum dot SEM and device parameters. **(a)** Scanning electron micrograph (SEM) image of dot 1. The other devices share the same chaotic design with either two or three shape-distorting gates. **(b)** Device parameters for the three dots measured in this experiment: mean free path (l), area (A) based on ~ 150 nm depletion around gates, mean level spacing ($\Delta = 2\pi\hbar^2/m^*A$), charging energy ($U = e^2/C$), and Thouless energy ($E_T = \hbar v_F/A^{1/2}$).
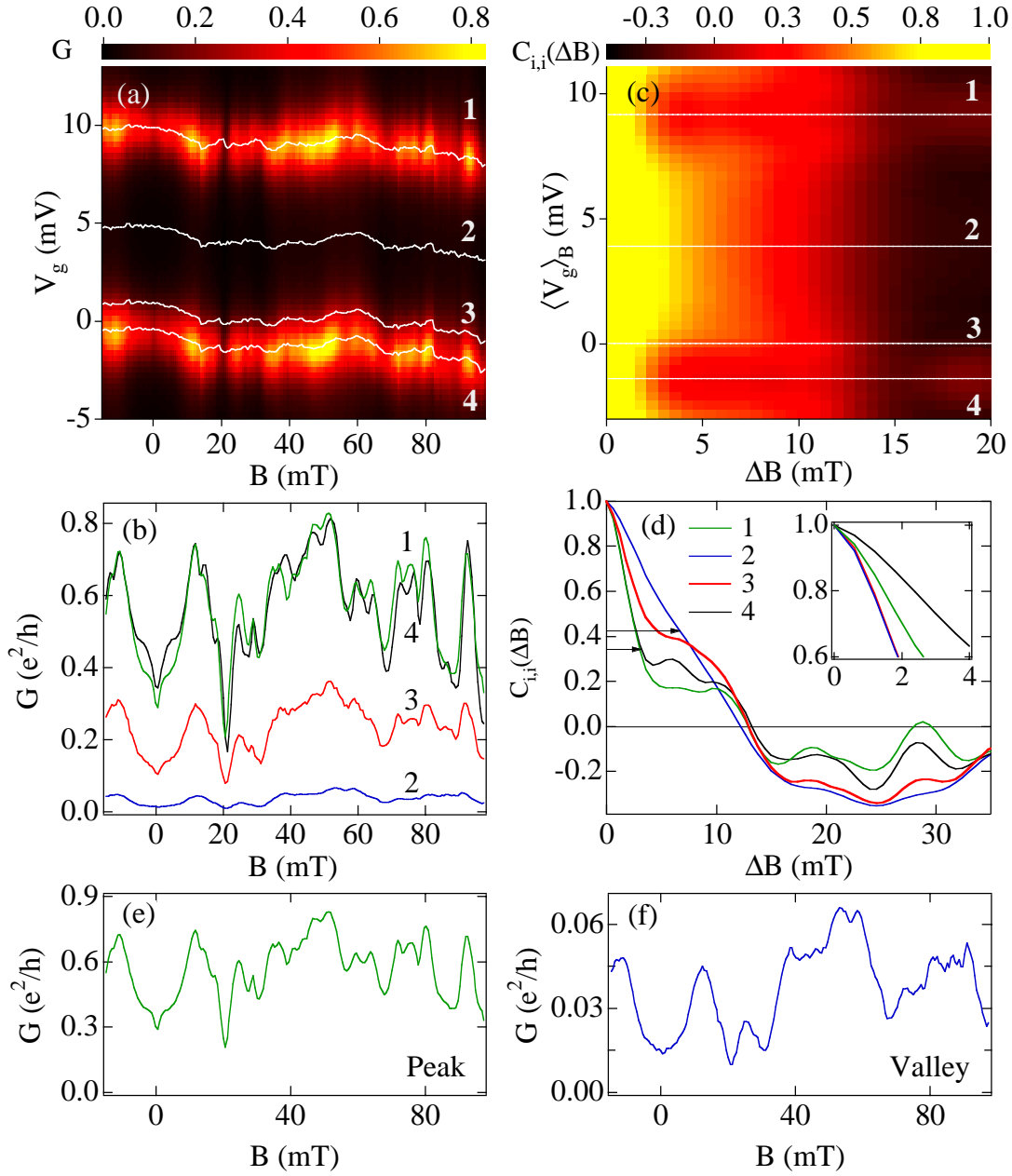
Figure 3-4. Conductance fluctuations and autocorrelations of CB peaks and valleys. **(a)** Differential conductance G (colorscale) as a function of V_g and perpendicular magnetic field B for dot 1 (same data as Fig. 3-2). **(b)** Conductance as a function of B for the four paths shown as labeled white traces in (a): a CB peak (green), a CB valley (blue), an interpolated path between (red), a second CB peak (black). **(c, d)** Autocorrelations $C_{i,i}(\Delta B)$ of the conductance fluctuations for (c) all interpolated paths as a function of average gate voltage along the path $\langle V_g \rangle_B$ and (d) for the four labeled traces. The valley autocorrelation function is wider than the peak, indicating a larger characteristic field scale. Inset: $C_{i,i}(\Delta B)$ near $\Delta B = 0$. **(e,f)** Conductance fluctuations of a peak and valley (each on its own scale). Note that the characteristic scale of fluctuations for the valley is longer than the peak.

The autocorrelation of G(B) along the peak tops, valley bottoms, and interpolated paths in between is shown in the colorscale of Fig. 3-4c as a function of ΔB and the average gate voltage along the path, $\langle V_g \rangle_B$. The specific autocorrelations of the labeled paths are shown in Fig. 3-4d. The field scale of fluctuations is defined by the condition $C_{i,i}(0.325B_c) = 0.82$. This somewhat awkward definition was chosen to coincide with Ref. [122] while allowing B_c to be measured in the universal region $C_{i,i}(\Delta B \sim 0) \sim 1$, where presumably nonuniversal features of the dot geometry such as short trajectories are not important. In qualitative agreement with the expectations discussed above, the periodic change in B_c from a maximum in the valley to a minimum on peak is easily seen in the width of the $C_{i,i}(\Delta B)$ colorscale, Fig. 3-4c, or directly from the autocorrelations shown in Fig. 3-4d. We note that a theoretically expected difference in the functional forms of $C_{i,i}(\Delta B)$ for peaks versus valleys [103, 104, 122] is not resolvable in the data.

The striking oscillation of B_c from a minimum on CB peaks to a maximum in CB valleys is shown in Fig. 3-5a for a series of five CB peaks. To determine a quantitative estimate of the field scale in the valleys compared to the peaks, the ensemble-averaged[6] field scale, $\overline{B_c}$, and conductance, $\overline{\langle G \rangle_B}$, were obtained from statistically independent peak–valley–peak data sets, sampled by changing the voltage applied to one of the shape-distorting gates. Figure 3-5b shows $\overline{B_c}$ and $\overline{\langle G \rangle_B}$ for 31 peaks and 22 valleys from dot 1, estimated to contain ~14 statistically independent data sets. The measured values, $\overline{B_c}^{valley} = 6.3 \pm 0.3$ mT and $\overline{B_c}^{peak} = 4.0 \pm 0.2$ mT, give a ratio $\overline{B_c}^{valley} / \overline{B_c}^{peak} \sim 1.6$, consistent with ratios of $1.4 - 1.8$ for the other dots. While the general behavior of B_c in valleys compared to peaks agrees with theoretical expectations, the ratio is smaller than expected from Eqs. 3.4 and 3.5. In particular, one would expect $\overline{B_c}^{valley} / \overline{B_c}^{peak} \sim (18\text{mT} /4.6 \text{ mT}) \sim 4$ for dot 1. This discrepancy is found in all of the dots and is not understood at present. Figure 3-5c shows the approximately linear dependence of $\overline{B_c}^{-2}$ on $\overline{\langle G \rangle_B}$ for the data in Fig. 3-5b. We note, however, that this relation assumes only a single carrier—either electrons or holes—and so can only be applied near the valley bottom or peak top.

To show that B_c^{valley} is enhanced due to charging effects, it is useful to compare B_c for both peaks and valleys to the characteristic field B_c^{open} for open dots ($G_{dot} > e^2/h$). Ensemble-averaged field scales, $\overline{B_c}^{open}$ (using the definitions of $C_{i,i}(\Delta B)$ and B_c above), obtained from ~30 statistically independent traces of conductance fluctuations at three different lead conductances in dot 1 are shown in Fig. 3-5d along with $\overline{B_c}^{peak}$ (at $\overline{\langle G \rangle_B} \sim 0.4$ e^2/h) and $\overline{B_c}^{valley}$ (at $\overline{\langle G \rangle_B} \sim 0.05$ e^2/h) for the strong-tunneling regime. These data

---

[6] We use an overbar (i.e. $\overline{B_c}$) to indicate an ensemble average obtained by averaging data from several different dot configurations. The average over magnetic field is indicated by angle brackets. (So $\overline{\langle G \rangle_B}$ is the ensemble-averaged magnetic field averaged conductance).
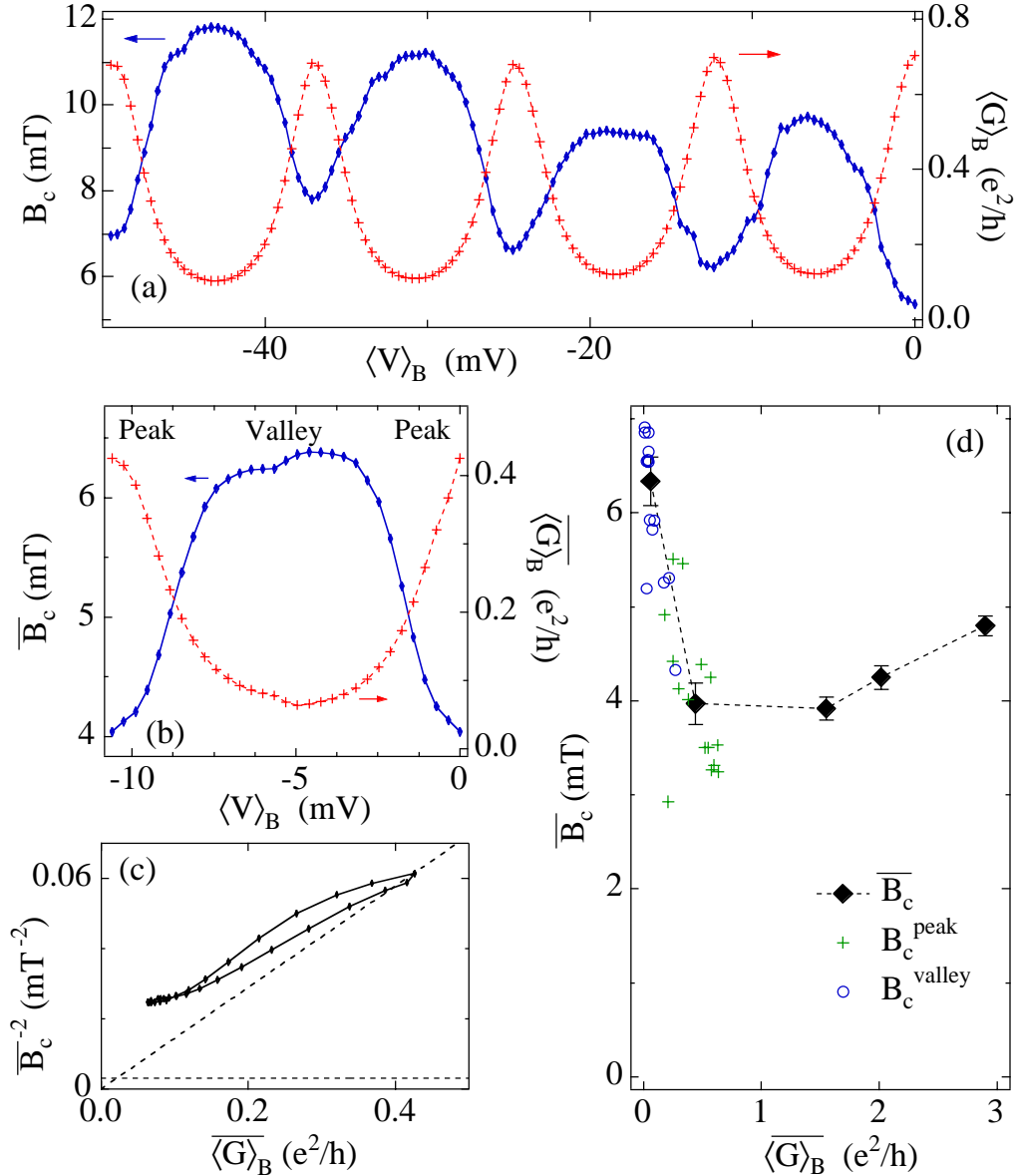
Figure 3-5. Oscillation of the characteristic field scale B_c. (**a**) Characteristic field B_c (left axis) and average conductance $\langle G \rangle_B$ versus average gate voltage $\langle V_g \rangle_B$ for several CB peaks and valleys in dot 2. (**b**) Ensemble-averaged characteristic field $\overline{B_c}$ (blue) and average conductance $\overline{\langle G \rangle}_B$ (red) across peak–valley–peak for ~14 independent data sets (dot 1), showing modulation of $\overline{B_c}$. (**c**) $\overline{B_c}^{-2}$ vs. $\overline{\langle G \rangle}_B$ for the same data. Diagonal line indicates $B_c^2 \langle G \rangle = $ constant; horizontal line is saturation $\overline{B_c}^{-2} = (\kappa \phi_0 / A)^{-2} = 0.003$ mT^{-2} for $E_T < E$. (**d**) Average $\overline{B_c}$ for three open dot configurations and peak and valley conductances (black diamonds), from data in (b). Unaveraged B_c values for peaks (green crosses) and valleys (blue circles) show spread in data. The open-dot $\overline{B_c}$ is modified (by ~ 5-15 %) to reflect changes in dot area upon opening leads.

show that $\overline{B}_c^{\,open}$ converges to $\overline{B}_c^{\,peak}$ as the dot becomes isolated, while $\overline{B}_c^{\,valley}$ is considerably larger than either. This supports the observation that the characteristic (single-particle) energy scales for transport though open dots and for resonant tunneling, Γ and Δ respectively, coincide at the onset of blockade ($\Gamma \sim \Delta$), and that both are smaller than E (set by classical charging) which determines $\overline{B}_c^{\,valley}$.

As mentioned above, it is known theoretically [99, 115] and from recent experiments [100, 101] that the ensemble-averaged normalized on-peak conductance, $\overline{g}(B) = \overline{G(B)/\langle G \rangle}_{B \neq 0}$, is lower when time-reversal symmetry is obeyed (i.e. at B = 0), in analogy to weak localization. In contrast, elastic cotunneling in the valleys is not expected to show weak localization—that is, $\overline{g}_{valley}$ should not be suppressed at B = 0 [122]. We have investigated the change in average conductance, $\delta g = (\overline{g}(B > B_c) - \overline{g}(B = 0))$, for 81 independent pairs of peaks and valleys measured in dot 3. As shown in Fig. 3-6a, we find $\delta g_{peak} = 0.14$ for the peaks, somewhat smaller than the RMT result, $\delta g_{peak} = 1/4$ [114, 115]. Since the RMT calculation assumes $\Gamma \ll kT \ll \Delta$ while the measurement has $\Gamma \sim 0.7\Delta$ and $kT \sim \Delta$, it is reasonable that theory should overestimate the measured value somewhat. For the valleys, we find that $\overline{g}_{valley}$ lacks any significant dip on a field scale of B_c (~ 8 mT for dot 3) around B = 0 (Fig. 3-6b), in agreement with theory [122]. We note that averages such as $\overline{g}(B)$ are difficult to measure in the CB regime because, unlike in open dots, fluctuations in the unaveraged normalized conductance g are on the order of g itself [114, 115, 122], as illustrated in Fig. 3-6 (dashed lines).

Finally, we investigate correlations between neighboring peaks and valleys as a function of separation (in units of peak spacing), ΔN. Ensemble-averaged cross-correlations[7], $\overline{C(\Delta B, \Delta N)} \equiv \overline{C_{i,i+\Delta N}(\Delta B)}$, for five peaks and valleys are shown in Fig. 3-7. The maximum of $\overline{C(\Delta B, \Delta N)}$ at $\Delta B = 0$ gives a measure of the similarity between the conductance fluctuations of pairs of peaks or valleys separated by ΔN. This value is seen to decrease to ~ 0 for $\Delta N > 2$ for the peaks, whereas for valleys the correlation remains high, $\overline{C(0,3)} \sim 0.5$. This is also seen in Fig. 3-7c for $\overline{C(0,\Delta N)}$ versus ΔN where peak-peak cross-correlations are seen to decrease faster than both valley-valley and peak-valley cross-correlations. The enhanced cross-correlation for valleys reflects the fact that, unlike resonant tunneling on peaks, elastic cotunneling relies on contributions from $\sim E/\Delta$ levels. In moving from one valley to the next, only one of the E/Δ levels is different, hence the similarity among neighbors.

---

[7] The cross-correlation $C_{ij}(\Delta B)$ is calculated for pairs of peak-peak, valley-valley, or peak-valley conductance fluctuations. Each pair can be assigned a separation ΔN (in units of the peak spacing). The ensemble average $\overline{C(\Delta B, \Delta N)}$ is an average over all peak-peak (or valley-valley, or peak-valley) pairs that are separated by ΔN.
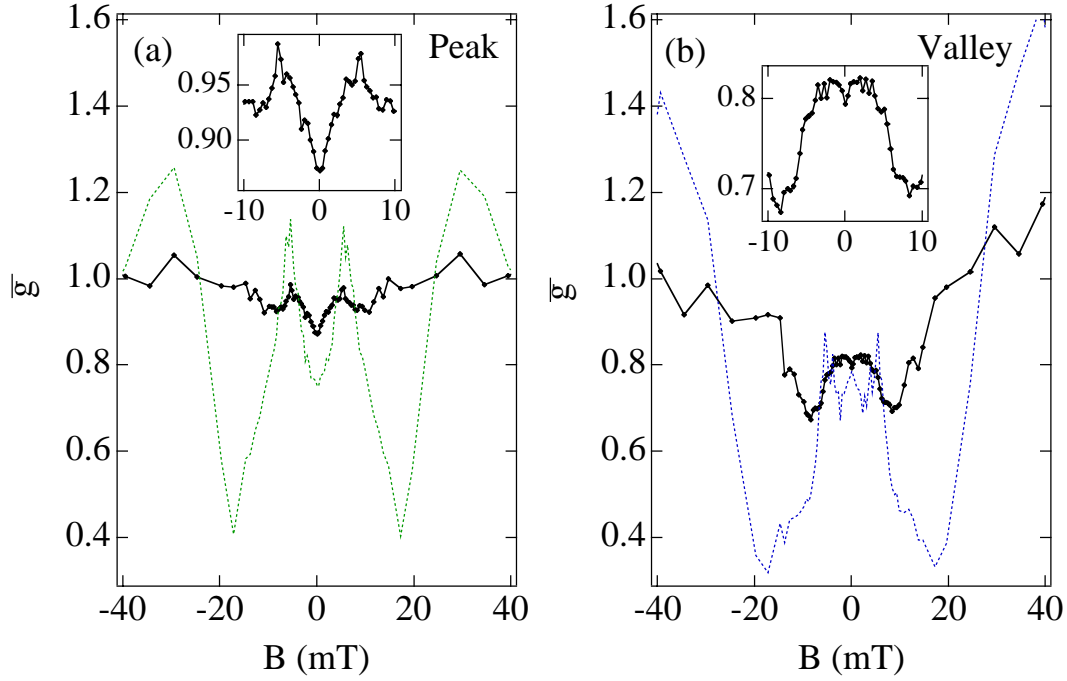
Figure 3-6. Weak localization of CB peaks and valleys. Ensemble-averaged normalized conductance, $\overline{g}$, (solid) for 81 statistically independent **(a)** peaks and **(b)** valleys as a function magnetic field for dot 3. Peak conductance $\overline{g}_{peak}$ has a dip around $B = 0$ with a width $\sim B_c$ associated with the breaking of time-reversal symmetry. No dip around $B = 0$ is seen in $\overline{g}_{valley}$ (on the scale of $B_c \sim 8$ mT). Insets show the regions around $B = 0$. Unaveraged normalized conductance (dashed) shows large fluctuations around average values for both peaks and valleys.
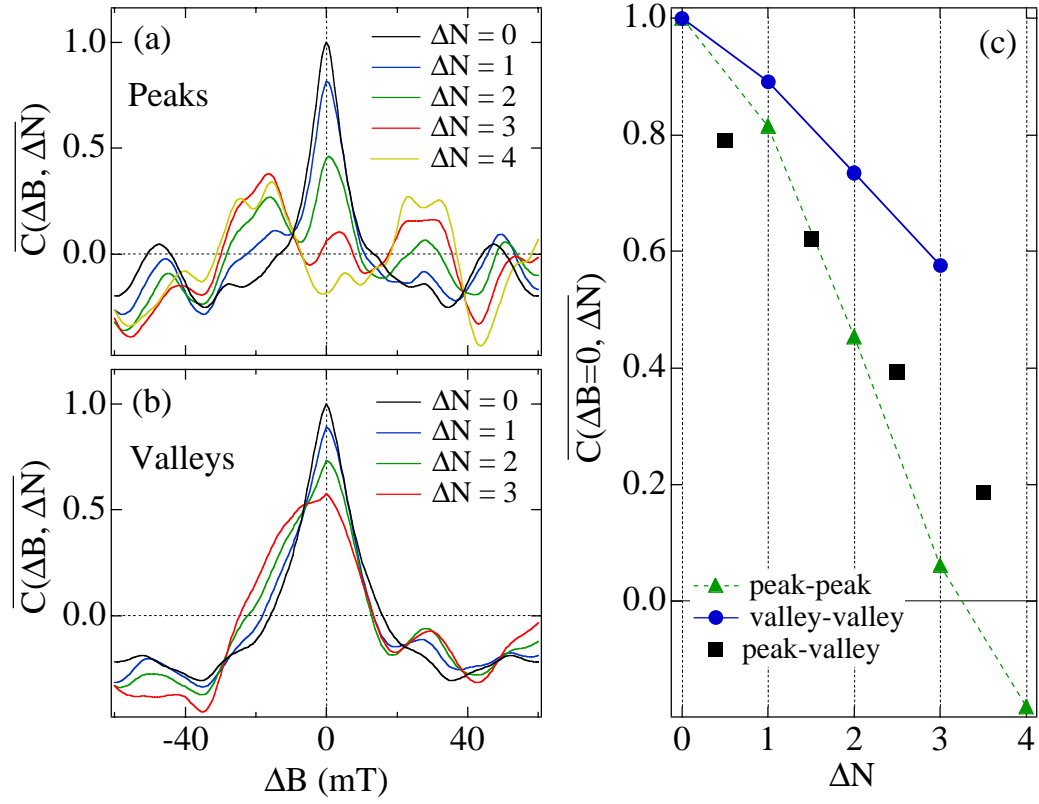
Figure 3-7. Cross-correlation between neighboring peaks & valleys. Average cross-correlation of conductance fluctuations, $\overline{C(\Delta B, \Delta N)}$, for **(a)** peaks and **(b)** valleys. **(c)** Maximum cross-correlation at $\Delta B = 0$, $\overline{C(0, \Delta N)}$, for peak-peak (green triangles), valley-valley (blue circles) and peak-valley (black squares), showing peak-peak correlations decrease more quickly than the others.

3.4   Conclusion

We have presented measurements of mesoscopic fluctuations of elastic cotunneling in the valleys of Coulomb blockaded quantum dots. Unlike resonant tunneling on CB peaks, cotunneling in the valleys is sensitive to charging effects. We observe a larger magnetic field scale for the cotunneling (valley) fluctuations compared to the peaks, as well as an absence of "weak localization" in valleys. Additionally cotunneling fluctuations remain correlated over several valleys while peak-peak conductance correlations decreases quickly—a direct result of the many levels participating in cotunneling processes. This investigation of cotunneling in CB quantum dots has nicely illustrated a system where both coherence and charging effects play an important role in transport, but one where the effects of interactions can be easily identified through dependence on the charging energy.

The devices measured in this chapter were fabricated by Sam Patel on wafers grown by Ken Campman in Art Gossard's group at UCSB (see Appendix C, Insomnia 2a Dot #21, Insomnia 1 Dot #10, Dante 1 Dot # 11). In addition, Sam Patel contributed significantly to the measurements. This experiment is published in Ref. [49].

Chapter 4

Mesoscopic Coulomb Blockade in One-Channel Quantum Dots

4.1 Introduction

The study of mesoscopic effects in confined electron systems often focuses on experimental situations where the two important effects of quantum coherence and interactions between particles can be cleanly separated. Investigations of conductance fluctuations due to quantum interference in open quantum dots is one example. In these systems, electron-electron interactions slightly modify the properties of the device, for instance through dephasing, but the overall character is not changed [55, 72]. Another example is the case of Coulomb blockade (CB), the dramatic result of electron charging effects in confined systems with tunneling contacts to the reservoirs. Quantum interference modifies some properties of the CB, such as inducing random fluctuations of peak heights, but does not change its essential features [99-101]. The previous chapter took this example one step further, identifying signatures of interaction effects on the quantum interference of elastic cotunneling in the CB valleys [49]. Put another way, we investigated the manner in which interactions affect the quantum interference which affects the overall large signature of charging (the Coulomb blockade). The effects of interference and interactions were still considered separately. There are situations, however, when the convenient but artificial separation of coherence and interactions causes entire phenomena to be missed. This Chapter concerns one such case, in which the experimental signature of interactions (the Coulomb blockade itself) appears only because of the presence of quantum interference [125].

4.2   One-Channel Quantum Dots

The system we study in this experiment is again a quantum dot connected to two reservoirs with adjustable quantum point contacts leads. We set one point contact exactly at the first quantized plateau ($2e^2/h$) where there is one and only one fully transmitting spin-degenerate mode. The second point contact we set to the weak-tunneling regime, such that the conductance $G_2 \ll e^2/h$.[8] In terms of the transmission coefficient of each point contact, $T_1 = 1$ and $T_2 \ll 1$. This regime is similar to the strong-tunneling regime considered in the previous chapter, in that the dot is well coupled to one of the reservoirs. However, the condition of unity transmission means there is no tunnel barrier, the dot is no longer "isolated", and electrons (or even partial charge) can slosh back and forth between the reservoir and the dot. The number of electrons on the dot is no longer a good quantum number for "one-channel" quantum dots. At this point, one might reasonably conclude that the Coulomb blockade will disappear. Indeed, this was the prevailing theoretical belief until 1998 [126, 127].

In metallic dots, it is known both theoretically [128-130] and experimentally [131] that the CB begins to be exponentially suppressed in the strong-tunneling regime as the conductance of the dot becomes larger than $\sim e^2/h$. In semiconductor quantum dots coupled to two reservoirs via point contact leads, measurements of the CB in the strong-tunneling regime have yielded varying results. Kouwenhoven *et al.* [132] found that the CB disappears when the transmission T_1 through one point contact reaches unity. However, Pasquier *et al.* [133] report small CB oscillations up to $T_1 + T_2 \sim 3$, and Crouch *et al.* [134] observed CB which decreased near $T_1 = 1$, $T_2 \ll 1$, but then increased again above $T_1 > 1$. Flensburg [126] and Matveev [127] have shown theoretically that the CB disappears at unity transmission when only inelastic processes are taken into account, appropriate in the limit $kT/\Delta \gg 1$, where Δ is the quantum level spacing. Then, in 1998, Aleiner and Glazman [125] extended the analysis to include elastic (coherent) processes, finding for the particular case of "one-channel" transport ($T_1 = 1$, $T_2 \ll 1$) that although one-channel CB would vanish for purely inelastic transport, it persists due to coherent mechanisms for temperatures comparable to the quantum level spacing.

In this chapter, we investigate several novel features of one-channel CB which illustrate the interplay between quantum interference and electron-electron interactions. These are as follows: (i) an enhancement of the CB at zero magnetic field which, like coherent backscattering in open structures, can be understood in terms of time-reversal symmetry at zero field; (ii) a strong temperature dependence of the CB on the scale of the quantum level spacing; (iii) an enhanced correlation (although less than predicted theoretically) of conductance as a function of gate voltage, compared to the weak-tunneling regime, which results from cotunneling through many levels both on and off the CB peak; (iv) peak motion as a function

---

[8] The second point contact is used to experimentally measure transport through the dot. For theoretical purposes it is (essentially) sufficient to consider a dot with a single fully transmitting lead [125].

of perpendicular magnetic field that is several times larger than in the weak-tunneling regime, though still small compared to the charging energy U.

4.3   One-Channel Coulomb Blockade: Effective scattering

The existence of CB in the one-channel regime can be understood in terms of an effective scatterer at the location of the open lead that arises due to coherent trajectories reflected from the walls of the dot [125]. It is known that a real scatterer in a nearly open lead will cause classical CB [126, 127]. Sketched in Fig. 4-1a, this case of $T_1 < \sim 1$ (reflection coefficient $R_1 > 0$) is considered the strong-tunneling regime, as described in Chapters 2 and 3. In the one-channel quantum dot, there is no real scatterer to produce the CB. However, the coherent interference of backscattered electrons—electrons that enter the dot from the open lead, scatter off the walls, and leave the dot back through the open lead again—create a standing wave which acts as an *effective scatterer* in the open lead and gives rise to the CB [125]. This process is shown in Fig. 4-1b. We emphasize that without coherence, the CB should disappear in the fully transmitting one-channel case. Only the coherent interference of backscatter electrons causes the CB to occur.

At zero magnetic field, backscattering increases due to constructive interference of time-reversed paths (Fig. 4-1c). This phenomena leads to the weak localization effect observed in open quantum dots (described in Chapter 2) [70, 83-85]. In the one-channel regime, enhanced backscattering creates a larger effective scatterer which gives stronger CB oscillations. As the perpendicular magnetic field B is increased beyond a characteristic scale B_c (where B_c puts of order one flux quantum through the backscattered trajectories, analogous to the last experiment), time-reversal symmetry is broken and the strength of the CB oscillations should decrease. To quantify the strength of the CB we evaluate the spectral power of the CB oscillations, P_{CB}. With application of a perpendicular field sufficient to break time-reversal symmetry, P_{CB} is predicted to decrease by a factor of 4 [125]. The requirement of coherence for CB in the one-channel dot implies a strong temperature dependence of P_{CB} on the scale of the quantum level spacing Δ (relevant for quantum interference) rather than the classical charging energy U (relevant for classical CB). Detailed calculations yield

$$P_{CB}(B,T) = \frac{G_2^2}{4} \Lambda(B) \alpha \frac{\Delta}{T} \left(\frac{\Delta}{U} \right)^2 \ln^3 \left(\frac{U}{2\pi kT} \right), \qquad (4.1)$$

where $\Lambda(B << B_c) = 4$ and $\Lambda(B >> B_c) = 1$, $\alpha \approx 0.207$ is a numerical factor, and G_2 is the conductance of the tunneling point contact [125]. Another consequence of the coherent nature of one-channel CB is that small changes in parameters such as device shape or magnetic field, which alter the interference pattern in the dot, can shift the position in gate voltage where the CB peak appears. Experimentally this appears as a strongly B-dependent peak position, with excursions predicted to be on the scale of the peak spacing.

Figure 4-1. One-channel Coulomb blockade: Schematics. (**a**) A quantum dot with one tunneling point contact (right) and the other point contact nearly open (transmission coefficient T ~ 1). A scatterer (X) at the open point contact gives a finite reflection coefficient, R > 0, and leads to Coulomb blockade in the strong-tunneling regime. (**b**) The one-channel regime, where the open point contact has exactly unity transmission (T = 1, R = 0). Coherent interference of backscattered trajectories, like the one shown, produce a standing wave at the point contact which acts as an effective scatterer—also giving rise to Coulomb blockade. (**c**) At zero perpendicular field B, time-reversed trajectory pairs interfere constructively, enhancing the backscattered conductance and leading to stronger CB oscillations. (**d**) An SEM micrograph of dot 1 with an estimated area of 0.5 μm^2 after depletion.

(a)

$T \sim 1$
$R > 0$

(b)

$T = 1$
$R = 0$

(c)

$B = 0$

$T = 1$
$R = 0$

(d)

500 nm
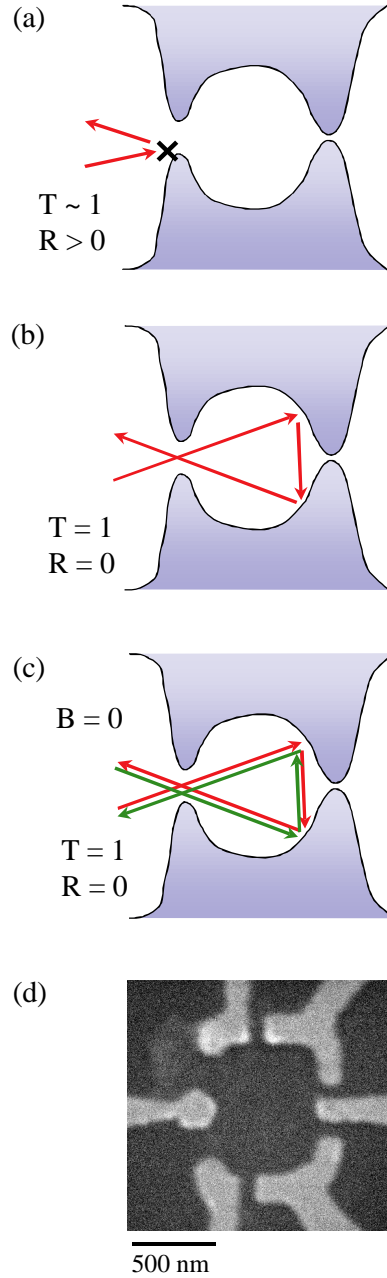
4.4   Experimental Results

We report measurements of two quantum dots (micrograph in Fig. 4-1d) fabricated using CrAu electrostatic gates 900 Å above a two-dimensional electron gas on a GaAs/AlGaAs heterostructure. A multiple-gate design allows independent control of point contact conductances and dot shape via several shape-distorting gates. Both dots have an area of 0.5 μm^2 giving a level spacing[9] $\Delta = 2\pi\hbar^2/m^*A = 14$ μeV (m* is the effective electron mass, and A is the dot area assuming a 100 nm depletion width). Measurements were made in a dilution refrigerator in a 2-wire configuration with an ac voltage bias of ~ 5 μV at 13.5 Hz. The experimental temperature T used throughout the chapter refers to the electron temperature measured from the widths of CB peaks in the weak-tunneling regime. At fridge base, T = 100 mK. Gate voltages can be related to dot energy through the ratio η, measured from the linear temperature dependence of the full width at half maximum of CB peaks in the weak-tunneling regime at T > Δ, where eη(FWHM) = 4.3kT (as noted in Chapter 2). This ratio then converts peak spacing to charging energy, giving eη(peak spacing) = U = 260 μeV for dot 1 and 320 μeV for dot 2.

A number of novel features of one-channel transport are illustrated in Fig. 4-2. The rapid oscillations in conductance as a function of gate voltage are the CB oscillations. Comparing Figs. 4-2a and 4-2b shows that the CB oscillations in the one-channel regime are considerably stronger at B = 0 mT (<< B$_c$) compared to 100 mT (>> B$_c$ ~ 20 mT). In contrast, the strength of the CB does not appear to depend on magnetic field in the weak-tunneling regime (Figs. 4-2c and 4-2d). One-channel CB also shows large fluctuations of valley conductance due to large cotunneling contributions which are suppressed in the weak-tunneling regime.

The B dependence of one-channel CB arising from the breaking of time-reversal symmetry can be studied quantitatively by evaluating the power spectral density P$_g$(f) of the conductance, g(V$_g$), at a number of different perpendicular magnetic fields. The argument f is the gate-voltage frequency in units of cycles/mV.[10] In both the one-channel and weak-tunneling regimes, P$_g$(f) shows a clear peak around the CB frequency, f$_{CB}$ = η/U , as seen in Figs. 4-3a,b. In the one-channel regime, the CB peak in P$_g$(f) has a clear maximum around B = 0, whereas CB in the weak-tunneling regime is essentially independent of B. We define the CB power, P$_{CB}$, as the power in a window around the CB frequency in P$_g$(f) (bracketed regions in Figs. 4-3a,b). The enhanced CB power around B = 0 in the one-channel regime now appears as a peak at

---

[9] We use the spin-non-degenerate form of the level spacing for these dots because experiments on dots of similar size and design do not show a spin-degenerate filling of the single particle states [105].

[10] Power spectra are computed from half-overlapping segments of 256 points with Hanning windowing, normalized for each magnetic field so that the one-sided sum over frequencies equals var(g). See *Numerical Recipes in C* [135].
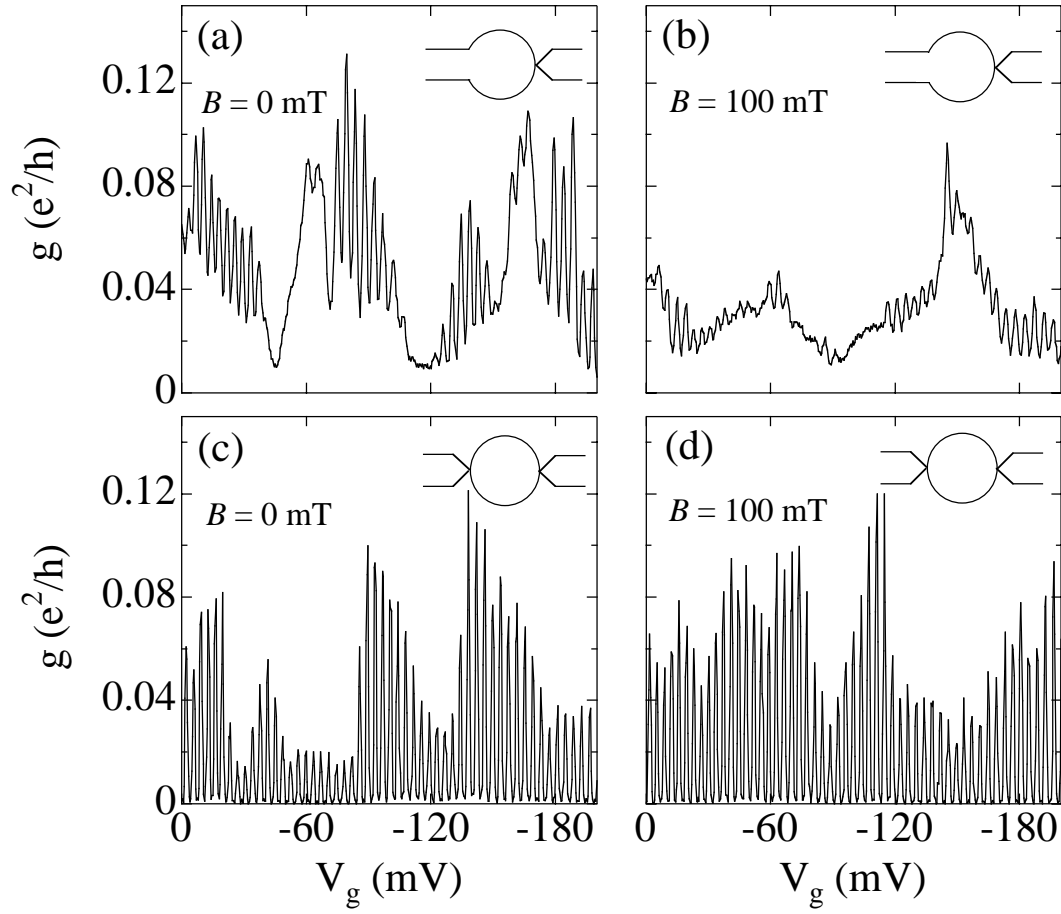
Figure 4-2. CB oscillations in the one-channel regime. Differential conductance, g, showing CB oscillations as a function of gate voltage, V_g, in the one channel regime **(a,b)** and weak-tunneling regime **(c,d)** at perpendicular field B = 0 mT (< B_c ~ 20 mT) and B = 100 mT (> B_c). One-channel CB is stronger at B = 0 mT compared to B = 100 mT, unlike weak-tunneling CB. The icons represent quantum dots in the one-channel regime (a,b) and weak-tunneling regime (c,d).
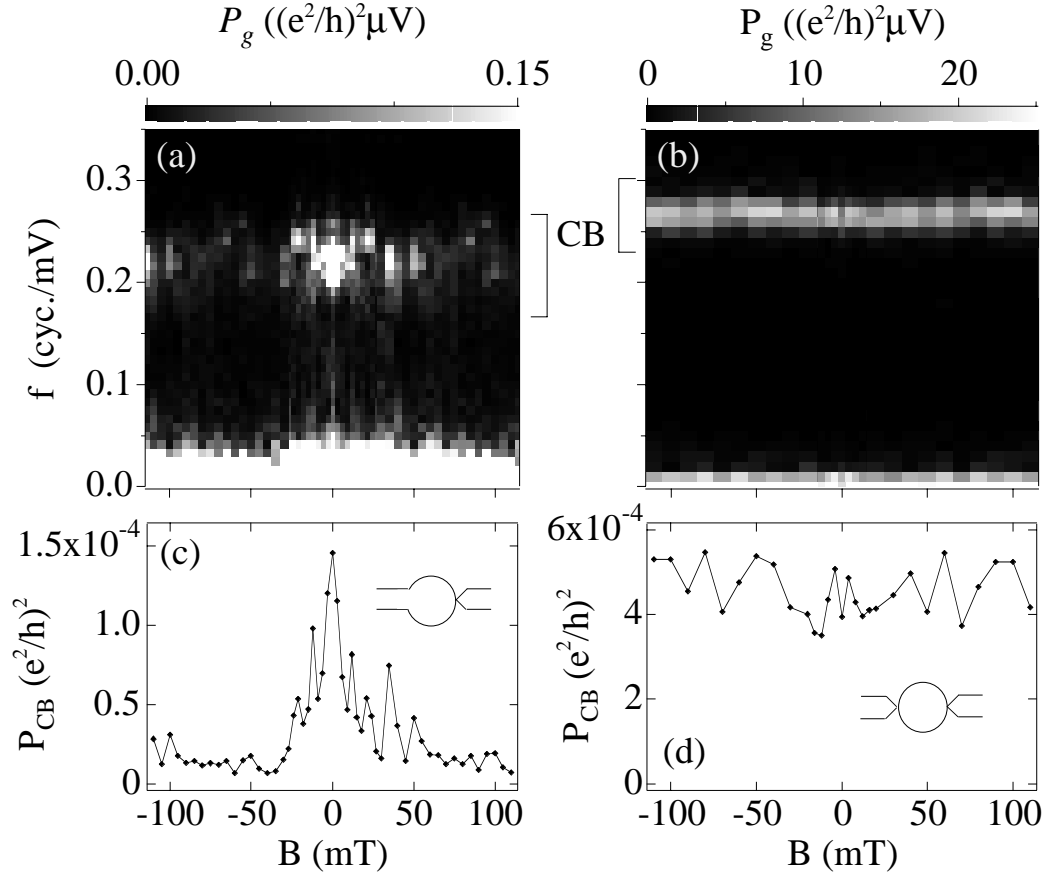
Figure 4-3. One-channel CB power spectral density. **(a,b)** Grayscale plots of the power spectral density, P_g, as a function of gate-voltage frequency f (cycles/mV) and perpendicular magnetic field B for **(a)** one-channel CB and **(b)** weak-tunneling CB (dot 1). The dominant frequency of CB oscillations is within the bracketed region marked "CB" in each plot. In the one-channel regime (a), the bright structure at B ~ 0 at the CB frequency indicates stronger CB at zero field. No corresponding field dependence of CB is seen for weak-tunneling (b). At each magnetic field, the power within the bracketed region defines $P_{CB}(B)$, the CB power. **(c,d)** $P_{CB}(B)$ for data in (a) and (b). Again, the zero-field enhancement of the CB in the one-channel regime is seen as a peak in $P_{CB}(B)$ around B = 0.
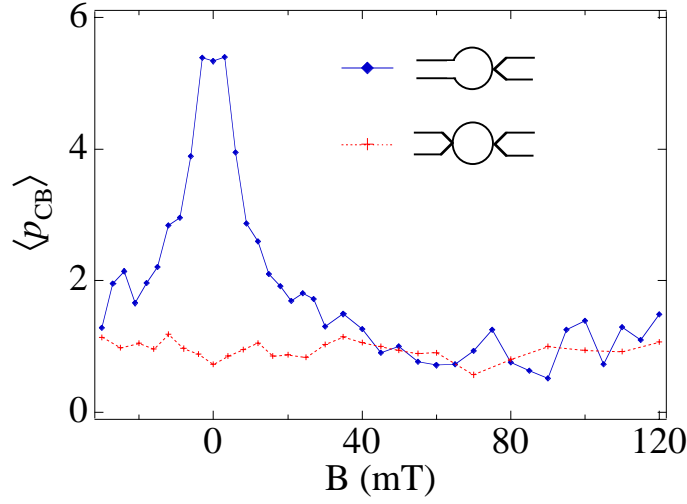
Figure 4-4. Average CB power. Magnetic field dependence of CB oscillations for the one-channel (blue) and weak-tunneling (red) regimes given by the CB power normalized to its B >> B_C value and averaged over shape configurations, $\langle p_{CB}(B) \rangle$ (dot 1). Uncertainties are ~ 10% for the one-channel regime and ~ 30% for the weak-tunneling regime.

B = 0 in the function $P_{CB}(B)$ (Fig. 4-3c), while $P_{CB}(B)$ is flat for weak tunneling (Fig. 4-3d). We note that the width of the CB peak in $P_g(f)$ around f_{CB} is broader and shows greater fluctuations in frequency in one-channel CB compared to the weak-tunneling regime (Fig. 4-3a vs. Fig 4-3b). This implies a broader distribution of peak spacings in the one-channel regime, contrary to the predictions of Ref. [125], and remains an interesting open problem.

CB power normalized by its large-B average, $p_{CB}(B) = P_{CB}(B) / \langle P_{CB}(B) \rangle_{B>>B_c}$, and averaged over an ensemble of several dot shapes provides a useful quantity for comparing the B dependence of CB in the one-channel and weak-tunneling regimes (Fig. 4-4). To compute these data, $P_{CB}(B)$ traces from seven data sets in the one-channel regime and three data sets in the weak-tunneling regime were normalized by the average value over 27 mT < B < 130 mT [for two of the one-channel sets: 21 mT < B < 60 mT] and then averaged. The zero-field value, $\langle p_{CB}(0) \rangle$ ~ 5.3 ± 0.5, is somewhat larger than the predicted factor of 4 for reasons not understood. In the weak-tunneling regime $\langle p_{CB}(0) \rangle$ ~ 0.7 ± 0.2, somewhat closer to unity than the zero-temperature theoretical value of 9/16 [99], presumably due to decoherence [136]. We note that a B-dependent real reflection in the point contact with maximum reflection at B = 0 could lead to a spurious enhancement of CB power at B = 0. To rule out this possibility, we have measured (in a separate device) the field dependence of the open point contact with the rest of the dot undepleted and find only very slight B dependence with no distinct features on the 10 - 40 mT scale (Fig. 4-5).
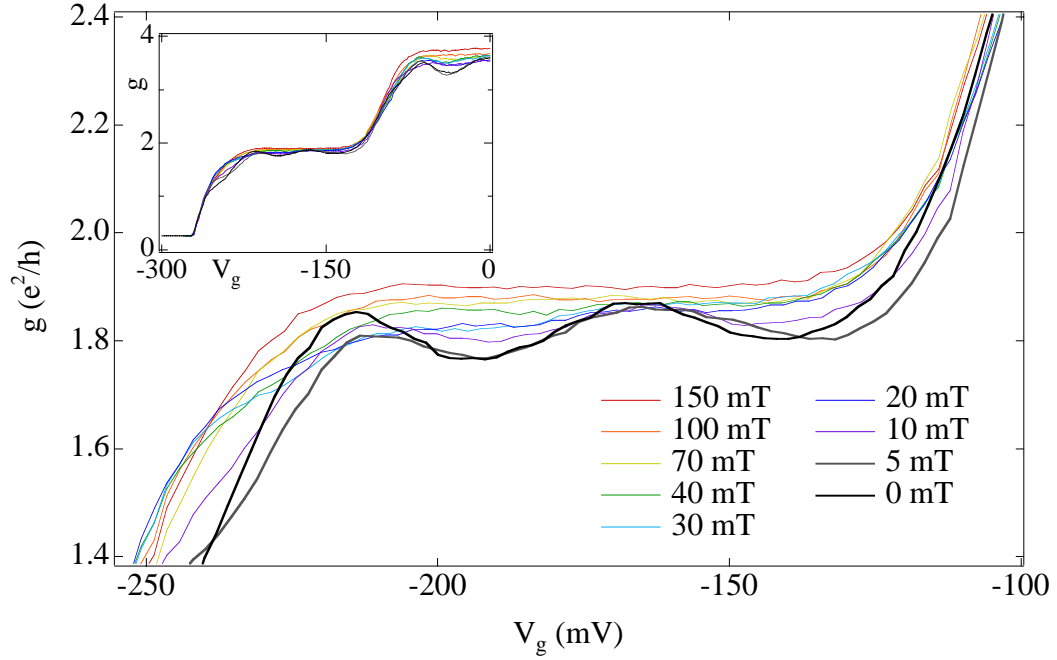
Figure 4-5. B-dependence of a quantum point contact. The first quantized plateau of a point contact is shown for perpendicular fields B = 0 to 150 mT. The conductance change, ~ 5% at most in the field range (40 mT), is not enough to account for the observed CB power increase shown in Fig. 4-4, above. The inset shows the first two plateaus. The data has not been corrected for any series resistance, so the plateau value is slightly below $2e^2/h$.

The temperature dependence of one-channel CB power is shown in Fig. 4-6a along with the no-free-parameters theory, Eq. 4.1, for both B $<<$ B_c (open squares) and B $>>$ B_c (filled squares). Experiment and theory are roughly consistent up to T ~ 300 mK (kT ~ 2.5 Δ), with good agreement in slope and the T independence of the ratio P_{CB}(B $<<$ B_c)/ P_{CB}(B $>>$ B_c), and reasonable agreement in absolute magnitude given the lack of free parameters. Note the log scale on the vertical axes and that CB powers range over a factor of ~ 100. At temperatures above ~ 400 mK, one-channel CB is strongly suppressed and the enhancement around B = 0 disappears, as seen in both Figs. 4-6a and 4-6b.

We have also investigated correlations in conductance as a function of V_g, $C(\delta V_g) = \left\langle g(V_g)g(V_g + \delta V_g) \right\rangle_{V_g}$ (average is over gate voltage) in the one-channel regime. Long correlations are expected in one-channel CB due to the significant contributions of cotunneling via many levels (of order U/Δ) [50, 122], as discussed in the previous chapter. Figure 4-7 shows the discrete correlation
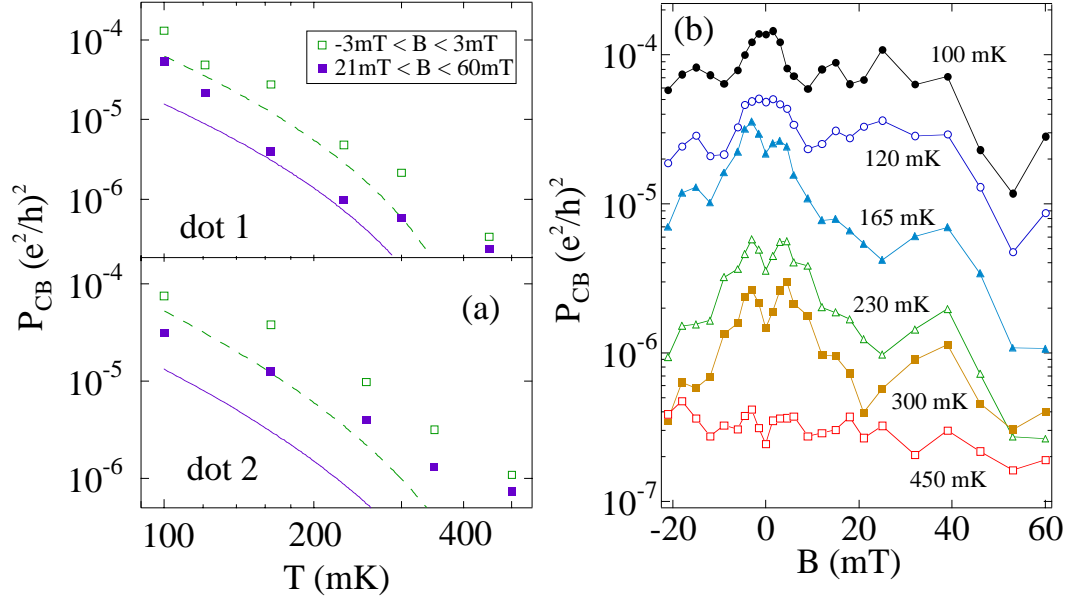
Figure 4-6. Temperature dependence of the CB power. **(a)** CB power, $P_{CB}(B)$, as a function of temperature, averaged over field ranges -3 mT $< B < 3$ mT (open squares) and 21 mT $< B < 60$ mT (solid squares), along with theory (Eq. 4.1) for $B \ll B_c$ (dashed curve) and $B \gg B_c$ (solid curve). **(b)** $P_{CB}(B)$ decreases strongly with increasing temperature from 100 mK (top curve) to 450 mK (bottom curve) in dot 1. The zero-field peak in $P_{CB}(B)$ persists up to ~ 400 mK.
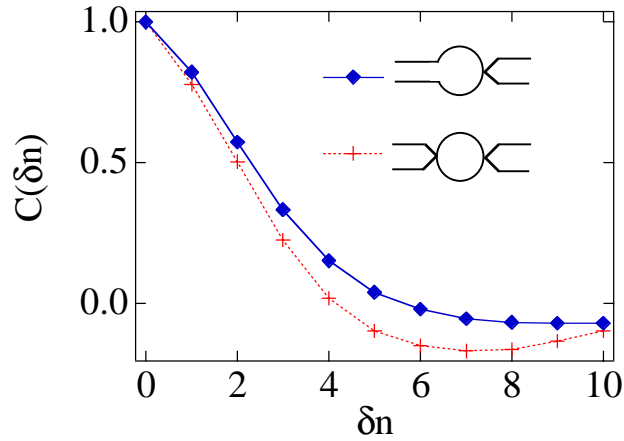
Figure 4-7. Autocorrelation of CB oscillations. Averaged (magnetic field and dot shape ensemble) autocorrelation function, $C(\delta n)$, of CB conductance oscillations in gate voltage V_g in units of peak number δn, where $\delta V_g = \delta n (U/\eta)$ for dot 1. The correlation length, given by the width of a gaussian fit, for one-channel CB (diamonds) is 2.8 peaks, slightly larger, but comparable to the weak-tunneling regime (crosses), 2.4 peaks, and much smaller than the length of $\sim U/\Delta \sim 15$ peaks expected theoretically.

function[11] $C(\delta n)$, where $\delta n = 0,1,2,\ldots$ acts as a peak index, defined for the one-channel CB regime as $C(\delta V_g)$ evaluated at the CB period, $\delta V_g = \delta n(U/\eta)$. In the weak-tunneling regime, $C(\delta n)$ is directly evaluated using sets of discrete peaks heights, $C(\delta n) = \langle g_{max}(n) g_{max}(n+\delta n) \rangle_n$, to avoid spurious correlations in $C(\delta V_g)$ caused by uniformly low valley conductance. As seen in Fig. 4-7, the correlation length in the one-channel CB (2.8 peaks) is considerably shorter than the theoretical value of $U/\Delta \sim 15$ peaks, and not significantly different than that of the weak-tunneling regime (2.4 peaks). This short correlation length may be caused by changes in the energy spectrum of the dot as electrons are added with each successive CB peak. This suggests that the number of added electrons sufficient to scramble the dot spectrum is less than U/Δ, consistent with similar conclusions based on the temperature dependence of peak correlations in the weak-tunneling regime [71, 137].

Finally, we have investigated the predicted large-scale peak motion as a function of magnetic field in the one-channel CB regime. Whereas the weak-tunneling regime exhibits CB peak motion on the scale of the level spacing[12] (once scaled to dot energy by η) [90, 91, 100, 137, 138], peak motion in the one-channel regime is expected to be of order U [125]. An enhanced peak motion in B for one-channel CB compared to weak-tunneling CB is seen in Fig. 4-8, although the effect is not as large as predicted theoretically. The standard deviation of peak motion about its average position is $0.09 \, U \, (\sim 2 \, \Delta)$ for one-channel CB (Fig. 4-8a), compared to $0.02 \, U \, (\sim 0.5 \, \Delta)$ in the weak-tunneling regime (Fig. 4-8b), the latter consistent with other measurements [90, 100, 137]. For a subsequent investigation of large-scale peak motion in the strong-tunneling regime see Ref. [137].

4.5   Conclusions

In summary, we have presented measurements of mesoscopic Coulomb blockade which arises due to quantum coherence in a quantum dot with one fully transmitting channel ($T_1 = 1$, $T_2 \ll 1$). One-channel CB is enhanced in the presence time-reversal symmetry and has a strong temperature dependence on the

---

[11] The correlation functions $C(\delta n)$ are calculated for each magnetic field B, then averaged over B to give $\langle C(\delta n) \rangle_B$ for a given data set (one dot shape). The ensemble average is computed by averaging $\langle C(\delta n) \rangle_B$ for several dot shapes. The final 'averaged' correlation function shown in Fig. 4-7 is the 'ensemble-averaged magnetic-field-averaged autocorrelation function in peak number δn', $\overline{\langle C(\delta n) \rangle_B}$, where the overbar represents the ensemble average (as in Chpt. 3). Note that the notation of the figure is simply $C(\delta n)$ to avoid mass confusion.

[12] There has been some debate as to whether the fluctuations of peak spacings (equivalently, peak motion) in the weak-tunneling regime should be controlled by Δ or U. Two experiments [87, 88] have found peak spacing fluctuations larger than predicted by RMT and suggested [87] that fluctuations in the classical charging energy U dominate peak spacing fluctuations. Other theoretical predictions [91, 138] give fluctuations of order Δ, consistent with this work and a number of other experiments from our group [90, 100, 137].

scale of the quantum level spacing, consistent with theory [125]. Correlation of conductance in gate voltage appears limited to ~ 3 peaks, smaller than expected, perhaps as a result of changes in the energy spectrum of the dot upon adding electrons. The motion of mesoscopic CB peaks with magnetic field is significantly greater than in the weak-tunneling regime, but smaller than expected theoretically.

The devices measured in this chapter were fabricated by Sam Patel on a wafer grown by Cem Duroz in Jim Harris' group at Stanford (see Appendix C, CEM2385-SRP1 Dots #10, #13). Sebastian Maurer and Sam Patel contributed to the measurements. This experiment is published in Ref. [50].
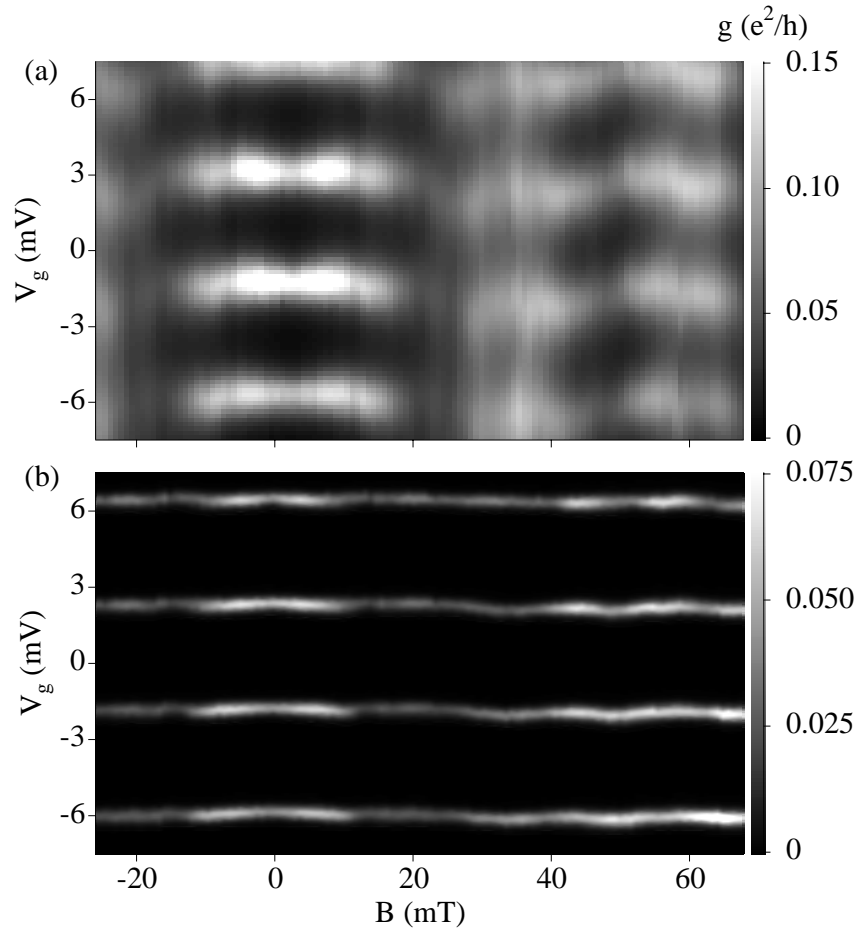
Figure 4-8. Enhanced peak motion in the one-channel regime. Grayscale plots of conductance versus gate voltage V_g and perpendicular magnetic field B shows larger fluctuations of CB peak position as a function of B in the one-channel regime **(a)** than in the weak-tunneling regime **(b)**. Note symmetry in B of CB peak height and position (dot 1). Fluctuations in the one-channel regime are ~ 0.09U ~ 2Δ, less than expected theoretically.

Chapter 5

A Tunable Kondo Effect in Quantum Dots

5.1   Introduction

This chapter addresses the Kondo effect in quantum dots, a third regime where both quantum coherence and electron-electron interactions play crucial, non-trivial roles. We investigate this classic many-body effect again using strongly coupled quantum dots in the Coulomb Blockade (CB) regime with particular interest in the CB valleys. In a small, cold quantum dot, the cotunneling processes between electrons in the leads and an unpaired electron in the dot can form a "macroscopic coherent spin-singlet state". The basis of this state involves spin-flip scattering events between electrons in the dot and electrons in the leads. Unlike the two experiments described in the previous chapters, the effects of quantum coherence and electron-electron interactions (now with spin) cannot be separated for the Kondo effect.

5.2   Background

The observations in the 1930s [139] of an anomalous increase in the low temperature resistivity of some metals began the decades long process of understanding what has become known as the Kondo effect [51, 140]. At that point, it was understood that the resistivity of a conductor, dominated by electron-phonon scattering, decreases with decreasing temperature as T^5 before saturating at a finite value (due to scattering from lattice impurities) as $T \rightarrow 0$ [141]; that is, $\rho \sim \rho_0 + aT^5$. The new anomalous behavior was a logarithmic divergence in ρ as $T \rightarrow 0$, making the resistivity $\rho \sim \rho_0 + aT^5 - b\log(T)$ as seen in Fig. 5-1.
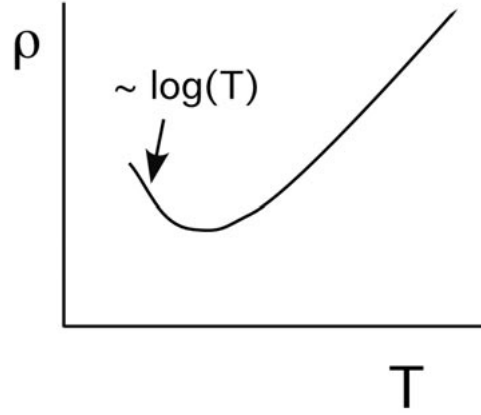
Figure 5-1. Temperature dependence of the resistivity, ρ. The resistivity decreases as T^5 for high temperature, due to electron-phonon scattering then reaches a minimum at ρ_0 before increasing roughly logarithmically with decreasing T.

This unusual phenomena remained unexplained for several decades. Finally in the late '50s and early '60s theoretical models began to associate the anomalous temperature dependence with scattering from magnetic impurities [142, 143]. Experimentalists began purposely adding magnetic impurities to metallic crystals and, in 1964, conclusively demonstrated that the anomalous temperature dependence was related to the presence of these impurities [144]. Soon thereafter, Jun Kondo made the first theoretical explanation of this elusive question [145], and for his contributions, the effect bears his name.

The key to unraveling the Kondo effect was the magnetic impurities imbedded in a metallic host. The requirements for an atomic impurity to retain a finite magnetic moment while imbedded in a metallic host were outlined by Anderson in 1961 [143] using a model Hamiltonian, now known as the Anderson Hamiltonian:

$$H_A = \sum_{\sigma;k<k_f}\varepsilon_{k\sigma}c_{k\sigma}^{\dagger}c_{k\sigma} + \sum_{\sigma}\varepsilon_{\sigma}d_{\sigma}^{\dagger}d_{\sigma} + \frac{1}{2}Un_{\sigma}n_{\sigma'} + \sum_{\sigma;k<k_f}t_{k\sigma}c_{k\sigma}^{\dagger}d_{\sigma} + H.c.. \tag{5.1}$$

The first term in the Anderson Hamiltonian is the energy of the free electron system—all the conduction electrons in the host metal—represented by the creation and annihilation operators $c_{k\sigma}^{\dagger}$ and $c_{k\sigma}$. The index σ indicates the spin of an electron, and k indicates the momentum. The second term represents the energy of localized electrons on the impurity state, with creation operator $d_{\sigma}^{\dagger}$. In this model, only a single "d-orbital"
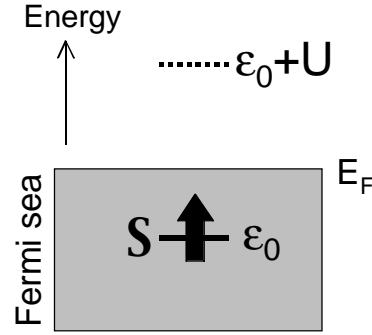
Figure 5-2. The Anderson model. Delocalized conduction electrons fill the states of a Fermi sea up the Fermi energy, E_F. A spin-degenerate state ε_0 lies below E_F, occupied by one electron. Due to Coulomb repulsion, the next available state (double-occupation) is above the Fermi energy at $\varepsilon_0 + U$, and so is not filled.

state which can hold zero, one or two electrons is considered.[13] The third term in Eq. 5.1 describes the charging energy between the localized electrons on the single impurity state and is parameterized by U. Finally, the fourth term represents transitions between the localized impurity state and the delocalized states in the bulk metal.

The model described by the Anderson Hamiltonian is drawn schematically in Fig. 5-2. Here, delocalized electrons fill up the Fermi sea of a bulk metal host up to the Fermi energy, E_F. A localized spin-degenerate impurity state sits at an energy ε_0 below E_F and is filled by one electron (in this case, spin-up). Double occupation is prevented by the Coulomb interaction energy U which lifts the energy of the doubly occupied state to $\varepsilon_0 + U$, well above the Fermi energy. Anderson determined that an atomic impurity with sufficiently large Coulomb repulsion U, and sufficiently weak hybridization, t, between the localized state and the leads would retain a finite magnetic moment in such a model [143]. The Anderson Hamiltonian is one starting point for describing magnetic impurities, including quantum dots, which lead to the Kondo effect.

---

[13] The state is considered a d-orbital because the outer shell of many magnetic impurity atoms are partially filled d-shells. A single state can be considered for simplicity without changing any of the important physics [143, 146].
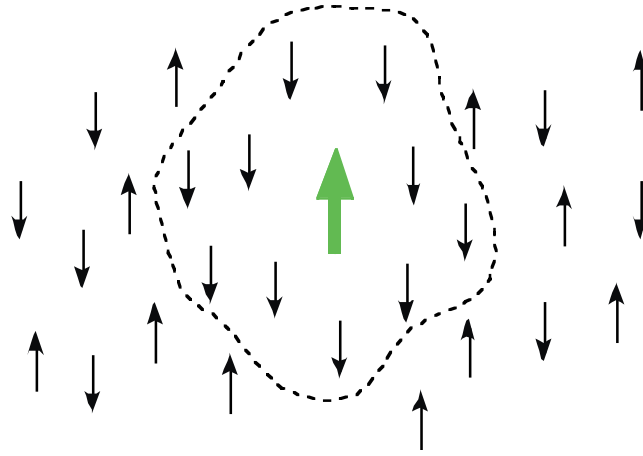
Figure 5-3. Schematic picture of a spin-singlet bound state between the localized impurity spin (green) and the spins of conduction electrons in the host metal.

Now that we have a model for a localized spin within a bulk metal system, we can consider interactions between the localized and delocalized states. The electron in the localized state can lower its kinetic energy by virtually hopping up to an unoccupied state at the Fermi surface (hence spreading out its wavefunction) [147, 148]. This can only occur if there is an available state of the *same* spin at the Fermi energy—that is, there must be an *excess* of electrons with the *opposite* spin at the Fermi energy of the bulk metal to allow this virtual transition to take place (due to the Pauli exclusion principle). To create a local excess of one spin species in the vicinity of the impurity essentially means a number of free electrons become semi-localized, a process which costs energy. So, we have a competition between the energy gained by *delocalizing* the impurity electron (by letting it virtually hop on/off the impurity site) and the energy cost of *localizing* free electrons of the opposite spin around the impurity site. At low enough temperatures, delocalizing the impurity electron wins [148]. The conduction electrons in the bulk metal try to screen the impurity spin forming a spin-singlet state with the impurity electron [51, 149], illustrated schematically in Fig. 5-3. This antiferromagnetic bond between the impurity state and the conduction electrons has a characteristic energy scale kT_K, where T_K is known as the Kondo temperature.

Another useful picture which describes the build-up of the bond between the impurity electron and the free conduction electrons in shown in Fig. 5-4. The interactions depicted involve scattering events which can flip the spins of both the conduction electron and the impurity spin. This is equivalent to the impurity electron hopping off the localized state and another electron of opposite spin hopping back on. Suppose the impurity electron begins in a spin-up state (Fig. 5-4a). A conduction electron scatters off the impurity and may or may not flip the spins of both particles. This leaves the two particles entangled (Fig. 5-4b). A second scattering event between the localized impurity and another conduction electron adds that
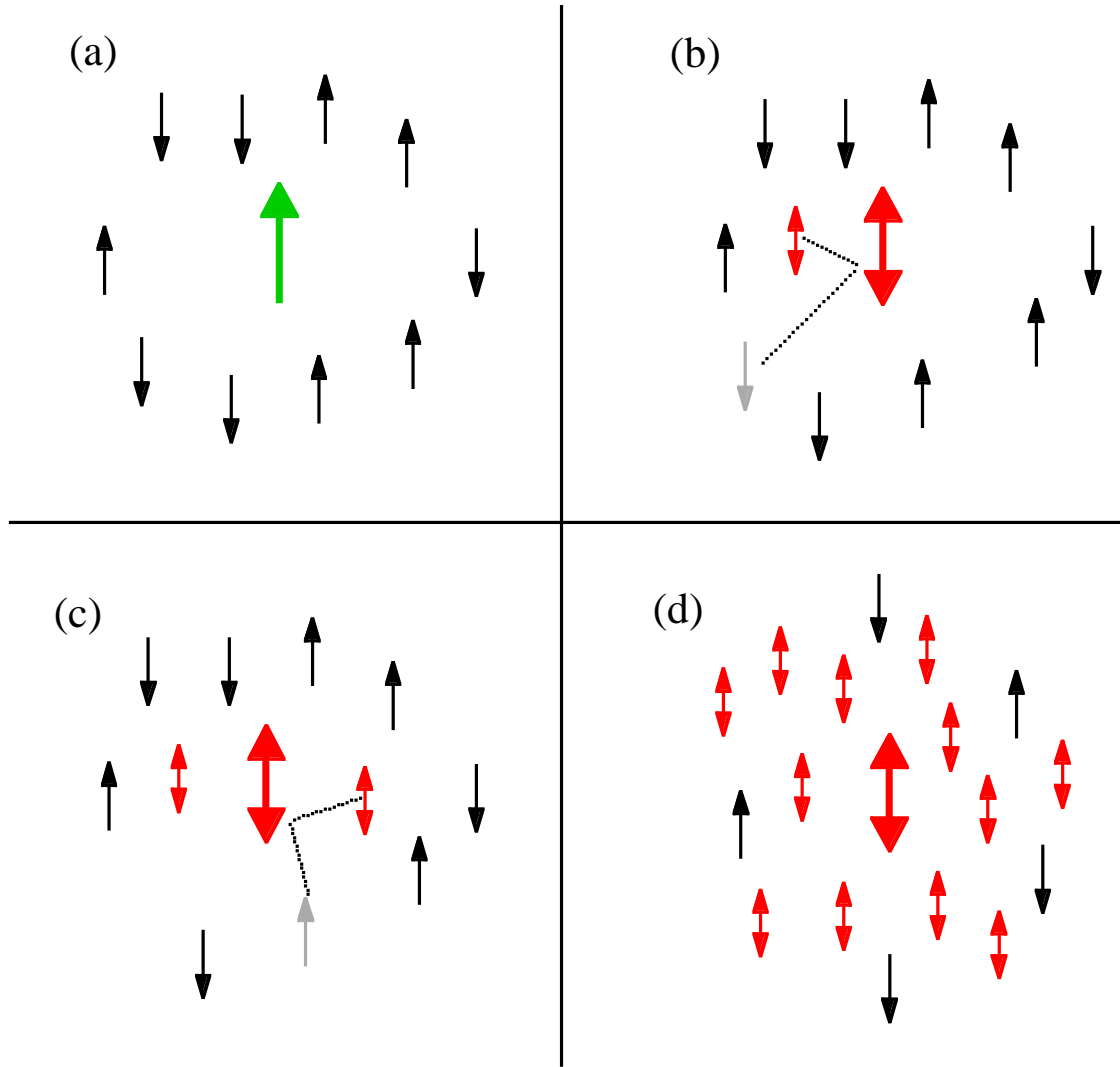
Figure 5-4. Simple picture of Kondo cloud formation. **(a)** A single magnetic impurity (large green arrow) is surrounded by conduction electrons (black). **(b)** One electron scatters off the impurity with the possibility of flipping its spin and that of the impurity. These two particles are now entangled (shown in red). **(c)** A second electron scatters off the impurity, also with the possibility of a spin-flip, thus becoming entangled with both the impurity and the previous scattered electron. **(d)** Continued scattering events build up a state where a large number of conduction electrons are correlated with the localized impurity. This bound state is known as the Kondo cloud.

electron to the entangled state (Fig. 5-4c). Continued scattering events build up a "cloud" of conduction electrons which are correlated with the each other and the localized impurity forming a macroscopic coherent state (Fig. 5-4d). This is the spin-singlet state described above and is often called the "Kondo cloud".

The Kondo singlet state is relatively extended in size and, therefore, acts as a more effective scatterer than the impurity itself. This leads to the observed increase in resistivity observed at low temperature. At temperatures $T >> T_K$, the singlet state has not formed (not energetically favorable) and the resistivity of the host metal shows the typical T^5 dependence due to phonon scattering. As the temperature approaches T_K, the resistivity bottoms out, then increases logarithmically with decreasing temperature in what has become a hallmark of the Kondo effect.

Kondo's initial success in explaining the resistivity minimum has led, over the years, to a much fuller understanding of the many-body physics underlying this magnetic impurity system [51, 140, 150-152]. A substantial review of the theoretical work on the Kondo effect from the 1960's through the 1980's as well as some comparison to experiments of the time is presented in Ref. [51]. Predictions can now be made for the resistivity dependence of many parameters of the impurity-host system (such as bias voltage, magnetic field, and the depth of the magnetic impurity state below the Fermi sea), in addition to a full non-perturbative solution to the temperature dependence from $T = 0$ to $T >> T_K$ [153]. Unfortunately, these predictions are not easily tested in metallic systems because the parameters involved are difficult or impossible to change. For instance, it is not possible to change the energy of the magnetic impurity relative to the Fermi energy, nor to create a large bias voltage across an impurity which is surrounded by a metallic crystal. Furthermore, it is very difficult to study the effects of a single magnetic impurity imbedded in a metallic host. Rather, experimental measurements are an ensemble average over a number of impurity atoms in the crystal lattice.

With the advent of quantum dots in the late 1980's and early '90's, a new system emerged for studying the Kondo effect. A quantum dot with an unpaired spin strongly coupled to the elections in the leads can be described by the same physics as a magnetic impurity in a metal [58-60, 154, 155]. Using an Anderson model description (Fig. 5-5a), the unpaired electron on the dot is the localized magnetic impurity state, the Coulomb charging energy of the dot pushes the next available state up (by U) above the Fermi energy, and the electrons in the source and drain leads are the delocalized conduction electrons. This system allows one to study an individual, artificial magnetic impurity and tune *in situ* many of the parameters in the Kondo problem: temperature, voltage bias, magnetic field, the coupling between the impurity and conduction electrons, and the depth of the impurity state below the Fermi energy of the leads.

The first experimental demonstration of the Kondo effect in quantum dots was reported by Goldhaber-Gordon *et al.* in 1998 [156]. The work in this chapter includes more extensive measurements of the temperature dependence of the equilibrium and non-equilibrium Kondo effect in quantum dots that
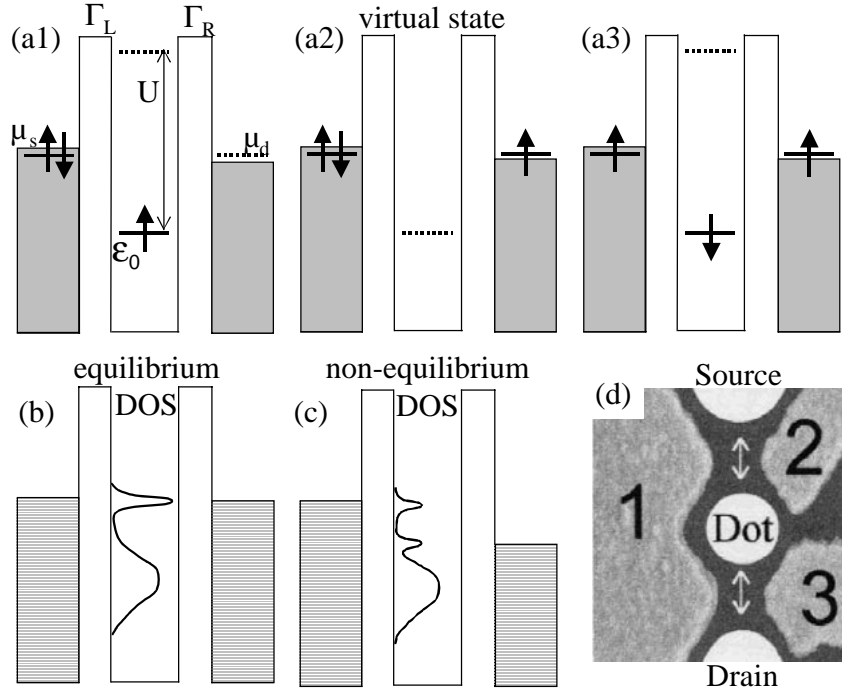
Figure 5-5. (a) Schematic energy diagram (Anderson model) of a dot with one spin-degenerate energy level ε_0 occupied by a single electron. U is the single-electron charging energy, and Γ_L and Γ_R give the tunnel couplings to the left and right leads. The parameters ε_0, Γ_L, and Γ_R can be tuned by the gate voltages. The states in the source and drain leads are continuously filled up to the electrochemical potentials, μ_L and μ_R. The series **(a1, a2, a3)** depicts a possible virtual tunnel event in which the spin-up electron tunnels off the dot and a spin-down electron tunnels on the dot. Such virtual tunnel events which involve spin-flips build up a macroscopically correlated state (the Kondo cloud) with properties that are known as the Kondo effect. **(b)** The Kondo effect can be pictured as a narrow resonance in the density-of-states (DOS) of the dot at the Fermi energies of the leads, $\mu_L = \mu_R$. The lower energy bump in the DOS is the broadened single particle state ε_0. **(c)** A source-drain voltage V results in the difference: $e\mathrm{V} = \mu_L - \mu_R$. For finite V, the DOS peak splits in two; one peak located at each chemical potential. **(d)** SEM photo of the gate structure which defines our quantum dots (dot 1).

agree well the results of Ref. [156]. In addition, we present data using a parallel magnetic field that identifies the Kondo physics, and we demonstrate the tunability of the Kondo temperature with an applied gate voltage. Subsequent work in the field, since the time of this experiment, will be discussed at the end of the chapter.

5.3   Quantum Dot as a Tunable Kondo Impurity

The important parameters for the Kondo effect in quantum dots are illustrated in the energy diagrams of Fig. 5-5. We treat the dot as an electron box separated from the leads by tunable tunnel barriers with a single spin-degenerate energy state ε_o occupied by one electron of either spin up or spin down. The tunnel couplings to the left and right lead are given by Γ_L and Γ_R. The parameters ε_0, Γ_L, and Γ_R can all be tuned by the gate voltages. The addition of a second electron to the state ε_0 costs an on-site Coulomb energy $U = e^2/C$. The diagrams of Fig. 5-5a shows the dot in the Coulomb Blockade. An electron cannot tunnel onto the dot since the two electron energy $\varepsilon_o + U$ exceeds the Fermi energies of the leads, μ_L and μ_R. Also, the electron on the dot cannot tunnel off because $\varepsilon_0 < \mu_L$, μ_R. However, higher-order cotunneling processes in which the intermediate state costs an energy of order U are allowed for short time-scales [108], limited by the Heisenberg uncertainty relation for time and energy. In particular, we are interested in virtual tunneling events which effectively flip the spin on the dot. One such example is depicted in Fig. 5-5 (a1 - a3) in which the spin-up electron tunnels off the dot and a spin-down electron tunnels on the dot. The sum of all successive spin-flip processes effectively screen the local spin on the dot such that the electrons in the leads and on the dot together form a spin-singlet state. Analogous to the singlet state formed by the magnetic impurity in a metal, this macroscopically correlated state gives rise to the Kondo effect. In a quantum dot, the Kondo effect can be described as a narrow peak in the density-of-states (DOS) at the electrochemical potentials of the leads, $\mu_L = \mu_R$, as shown in Fig. 5-5b [60, 157-159]. This DOS Kondo resonance gives rise to enhanced conductance through the dot. The enhanced conductance and DOS resonance is analogous to the low-temperature increased resistivity in metals. The Kondo cloud increases scattering which, in metals, increases the resistivity. In dots, however, these scattering events are exactly the mechanism for transport through the blockaded dot, so they increase conductance. Out of equilibrium, when a bias voltage V is applied between the source and drain, $e\mathrm{V} = \mu_L - \mu_R$, the Kondo peak in the DOS splits into two peaks, each pinned to one chemical potential (Fig. 5-5c) [60, 158]. This splitting leads to two specific features in transport. First, at zero magnetic field, the differential conductance dI/dV versus V mimics the Kondo resonance in the DOS, so a peak in dI/dV is expected around zero voltage. Second, a parallel magnetic field lifts spin degeneracy resulting in a dI/dV versus V showing two peaks at $e\mathrm{V} = \pm g^* \mu_B B_\parallel$ [60, 160, 161], where g^* is the effective Landé factor and μ_B is the Bohr magneton, and $B_\parallel$ is the *parallel* magnetic field.

In our GaAs/AlGaAs quantum dot devices (Fig. 5-5d), negative voltages applied to the gates control the parameters ε_0, the electron number N, and Γ_L, Γ_R, the energy broadening of the discrete states caused by the coupling to the left and right leads. The conductance shows CB oscillations on varying the gate voltage V_g (for example, Fig. 5-6a). Although the exact number of electrons N is not known, each period corresponds to a change of one electron on the dot. N should thus oscillate between an even and an

odd number. If we assume spin-degenerate filling of the single-particle states[14], the total spin on the dot is zero when N = even (all states are double-occupied with antiparallel spins), and for N = odd, the total spin is ± 1/2 (the topmost state is singly occupied with either spin up or down). In other words, for even N the dot is nonmagnetic, whereas for odd N the dot has a net spin magnetic moment [162]. This property allows quantum dots to be tuned between a Kondo and a non-Kondo systems as we vary N with the gate voltage.

Measurements were made on two quantum dots of similar shape (Fig 5-5d) fabricated on a GaAs/AlGaAs heterostructure with a two-dimensional electron gas (2DEG) about 100 nm below the surface. Dot 1 has an estimated size of 170 nm x 170 nm and confines ~ 60 electrons while dot 2 is about 130 nm x 130 nm containing ~ 35 electrons. The two dots form the double dot structure fabricated by N.C. van der Vaart and discussed in detail in Ref. [163]. Each dot was measured independently, by biasing only the gate voltages that define a single dot, in a dilution refrigerator with an effective electron base temperature $T_{base} \approx 45$ mK (measured from the widths of CB peaks in the weak-tunneling regime). During measurements of CB oscillations, the voltages on gates 1 and 3 are swept simultaneously. The *dc conductance*, G = I/V, was measured in a 2-wire voltage bias configuration. Recall that for small bias voltage V, the differential and dc conductance are equivalent. For example, CB peaks in linear response (V ~ 0) dc conductance look the same as the linear response differential conductance CB shown in the previous experiments. The measurements of the differential conductance, g = dI/dV, presented in this chapter, use standard ac lockin techniques with a small ac bias voltage of 1μV at 13.5 Hz.

The spin coupling interactions which give rise to Kondo physics contribute significantly only for temperatures comparable to or lower than the Kondo temperature

$$T_K \sim [U\Gamma]^{1/2}\exp[\pi\varepsilon_0/2\Gamma], \tag{5.2}$$

where $\Gamma = \Gamma_L + \Gamma_R$, and ε_0, the energy of the localized state measured from the Fermi energy of the leads, is negative [164, 165]. To make this regime accessible experimentally, Γ is made as large as possible by setting the gate voltages V_g such that the broadened CB oscillations in Fig. 5-6a slightly overlap. This implies that $\Gamma \sim \Delta$ where Δ is the single-particle level spacing measured as 0.1 meV and 0.15 meV in dots 1 and 2 respectively. The existence of more than one spin-degenerate level in our dots is expected to further enhance the Kondo temperature. For a review of the Kondo effect in multi-level systems, see Refs. [166-168]. The respective Coulomb energies of the two dots in the weak-tunneling regime were measured as U = 1 meV and 1.3 meV. The Coulomb energy U decreases by a factor of ~2 in the strong-tunneling regime of our measurements [169].

---

[14] In measurements of the evolution of the CB peaks versus perpendicular magnetic field, we observe pairing in the motion between adjacent peaks. This indicates spin-degenerate filling of the energy states, in contrast to the results of Ref. [105], who reported non-spin-degenerate filling of the energy states.
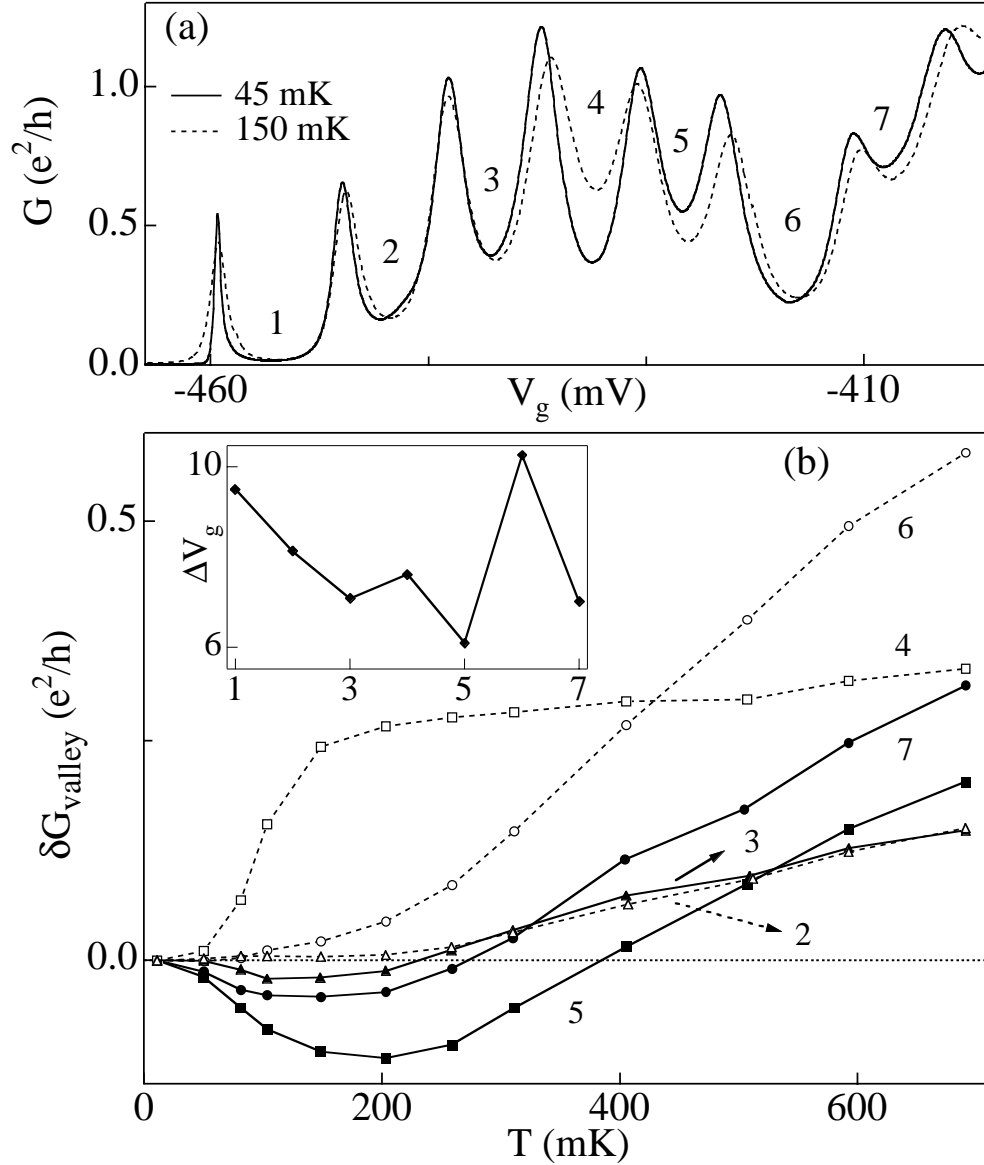
Figure 5-6. Conductance minima in temperature dependence of alternate CB valleys **(a)** Linear response dc conductance $G = I/V$ versus gate voltage V_g measured in dot 1 at $B = 0$ for $V = 7.9$ µV at 45 mK (solid) and 150 mK (dashed). The parity of the valley numbering is indicated by an odd or even number N. From left to right, the CB peaks become broader (i.e. Γ is increasing) because the tunnel barrier induced by gates 1 and 2 decreases when increasing the voltage on gate 1. Increasing T from 45 to 150 mK increases the conductance of the even numbered valleys but decreases the conductance of valleys 3, 5 and 7. The detailed temperature dependence is shown in **(b)** where we plot the change in valley conductance $\delta G_{valley}(T) = G_{valley}(T) - G_{valley}(T_{base})$ with $T_{base} \approx 45$ mK. The inset to (b) shows the spacings ΔV_g between adjacent peaks. We observe a larger (smaller) peak spacing for even (odd) N.

The dc conductance $G = I/V$ from dot 1 is shown in Fig. 5-6a for electron temperatures of 45 and 150 mK. The base temperature ($T_{base} \approx 45$ mK) measurement shows even-odd peak spacings (Fig. 5-6a, inset) which arise from the filling of spin-degenerate energy states. The energy cost to add an odd numbered electron onto an unoccupied energy state of the dot is the Coulomb energy plus the single particle spacing, $U + \Delta$, whereas adding an even-numbered electron costs only U. Although the absolute value of N is not exactly known, we obtain the parity of the electron number for the valleys in Fig. 5-6a from the even-odd spacings together with magnetic field measurements (not shown). Valleys with smaller peak spacings (N = odd) also have a larger base temperature conductance than their neighbors, a result of the Kondo peak in the DOS enhancing the valley conductance when N = odd. Comparing the valley conductances, we see that valleys 3, 5 and 7, decrease when T is increased to 150 mK, while the even numbered valleys increase. This even-odd effect is illustrated in more detail in Fig. 5-6b where we plot the change in valley conductance with temperature, $\delta G_{valley}(T) = G_{valley}(T) - G_{valley}(T_{base})$. Whereas all the valley conductances for N = even increase with T, for N = odd the spin-correlated Kondo state is destroyed by an increasing T such that G_{valley} first decreases. The minimum in δG_{valley} strongly resembles the resistance minimum in metallic Kondo systems [140, 144].

Measurements on dot 2 also show agreement with expectations of the Kondo effect. The middle valley in Fig. 5-7a is identified as a "Kondo" valley because it shows a larger base temperature conductance than the neighboring valleys. The detailed T dependence in Fig. 5-7b shows that this Kondo valley also has a conductance minimum around 200 mK. Furthermore, the conductance peaks on either side of the Kondo valley decrease and move apart with increasing T (see also Fig. 5-7b), in qualitative agreement with theory [60]. The motion of the peak position, which had not been previously reported, is attributed to a renormalization of the non-interacting energy state ε_0 due to fluctuations in N.

To investigate the non-equilibrium Kondo effect we measure the differential conductance dI/dV in the center of the Kondo valley of Fig. 5-7a. At base temperature, dI/dV has a peak at V = 0 (Fig. 5-7c, bold curve). The peak has a width ~ 50 μV which is narrow compared to the energy scales of U, Δ, and Γ. Increasing T broadens the dI/dV peak until it completely disappears at ~ 300 mK. The insets to Fig. 5-7c give the temperature dependence of the dI/dV peak maximum on a logarithmic scale and the peak width (the full-width at three-quarters max) on a linear scale. A classic Kondo signature, the logarithmic T dependence of the maximum is expected for $T_K <\sim T$ [58]. The width is expected to saturate at ~ T_K at low temperatures. We do not observe such saturation which suggests that $T_K <\sim 45$ mK in the middle of the Kondo valley.

In order to increase $T_K \sim [U\Gamma]^{1/2}\exp[\pi\varepsilon_0)/2\Gamma]$, we decrease the distance ε_0 between the localized state and the Fermi energy by moving away from the Kondo valley in Fig. 5-8a towards a neighboring CB peak. The zero-bias dI/dV peak is seen to increase in both height and width when tuning ε_0 towards the Fermi energy (Fig. 5-8b). The width of the dI/dV peak, shown in Fig. 5-8c, is determined by the larger of
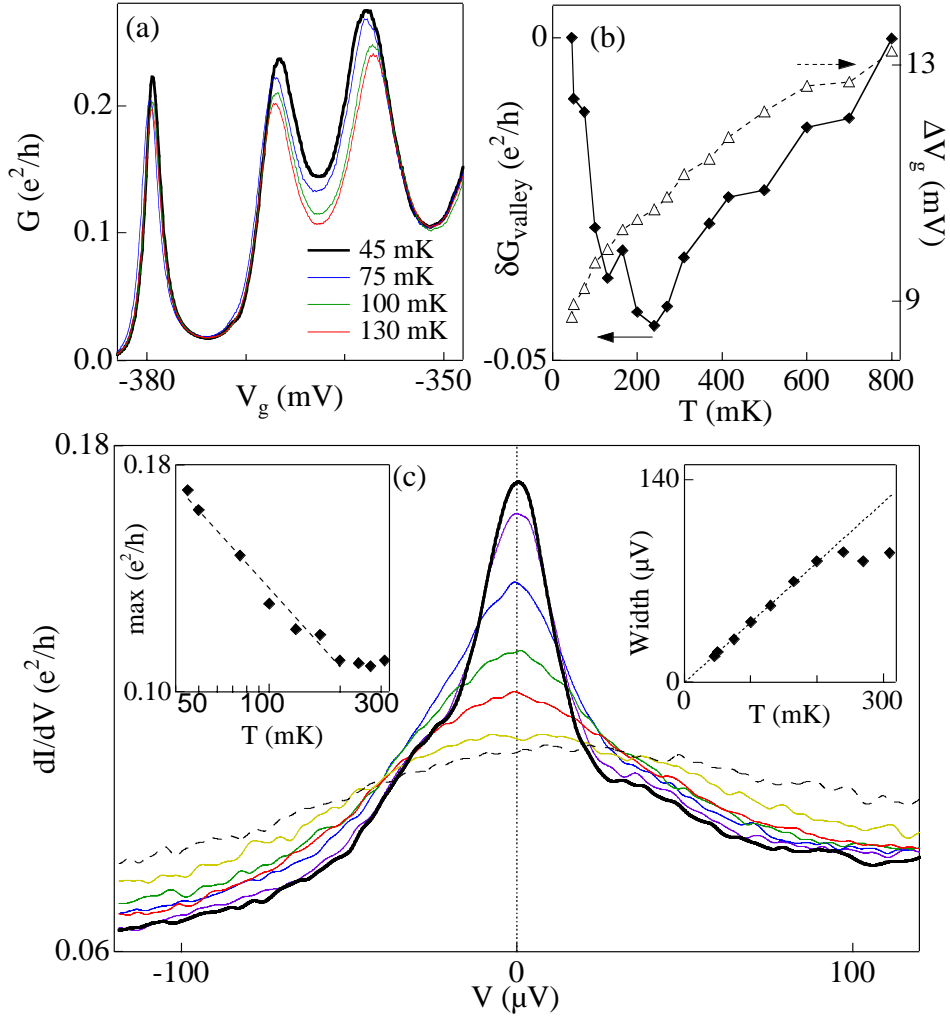
Figure 5-7. (a) Conductance G for B = 0 and V = 5.9 μV at 45 (bold curve), 75, 100 and 130 mK in dot 2. Because dot 2 is smaller, the tunnel barriers increase more rapidly with negative gate voltage, and we observe only three consecutive valleys in the Kondo regime. The middle valley shows pronounced Kondo behavior. **(b)** Left axis: $\delta G_{valley}(T)$ (♦) for the center of the middle, Kondo valley in (a). Right axis: gate voltage spacing $\Delta V_g(T)$ (□) of the peaks bordering the Kondo valley. Increasing T results both in a Kondo minimum in δG_{valley}, and an increasing peak spacing that we ascribe to a renormalization of the energy level ε_0. **(c)** Differential conductance dI/dV versus source-drain bias voltage V for T = 45 (bold), 50, 75, 100, 130, 200, and 270 (dashed) mK. The gate voltage is set in the center of the middle valley. The asymmetry in the zero-bias peak is probably because $\Gamma_L \neq \Gamma_R$. Left inset: The peak maximum is logarithmic in T. Right inset: The peak width (the full-width at three-quarter maximum) is linear in T with a slope of 4.8k_B (dotted line).
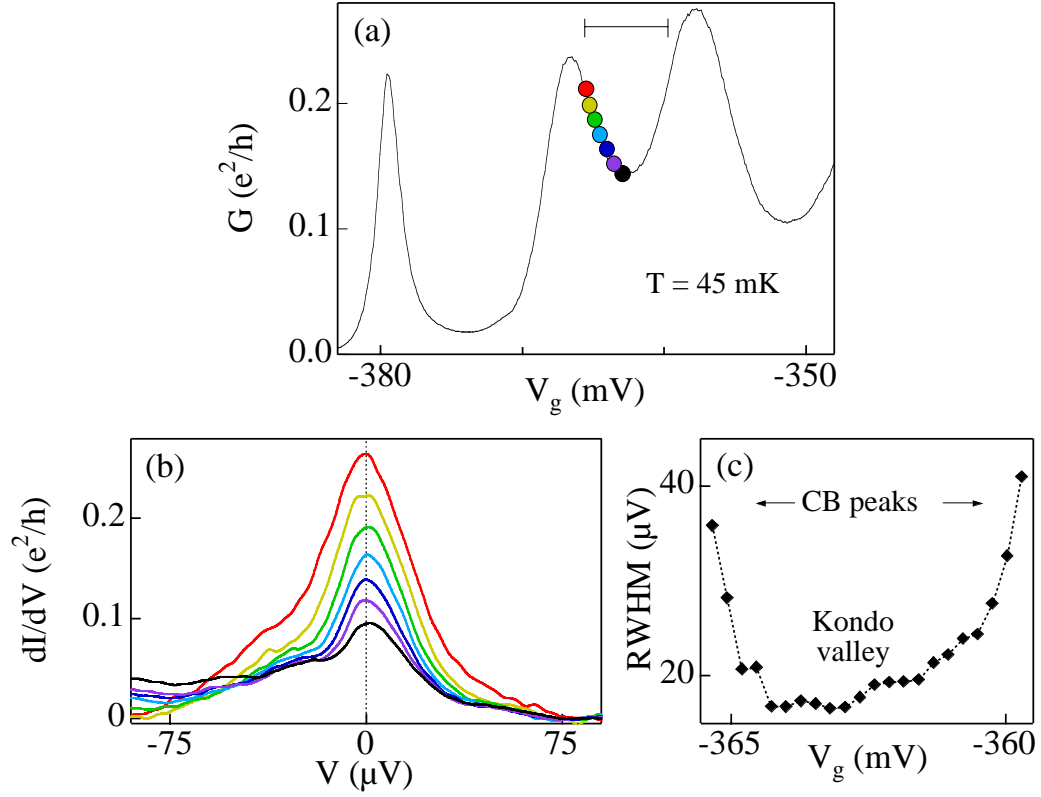
Figure 5-8. Controlling the Kondo temperature **(a)** The same series of three CB peaks from dot 2, as shown in Fig. 5-7. The middle valley is the Kondo valley. The colored dots indicate the gate voltages for the traces in (b). The horizontal bar marks the gate voltage range of (c). **(b)** Zero-bias peak in dI/dV at 45 mK for different gate voltages stepping from the center of the Kondo valley in (a) (bottom black curve, V_g = -363 mV) up the left side of the CB peak (top red curve, V_g = -366 mV). The curves have been shifted so the background values align at ~ 75 μV. The amplitude of the zero-bias peak increases as the conductance G increases moving up the flank of the CB peak. **(c)** We measure the right half-width at half-max (RWHM) of the zero-bias peak (relative to the baseline dI/dV at ~ 75 μV) which begins to increase halfway up the CB peak on either side The increasing width follows the increase of the Kondo temperature T_K above T_{base}. The increase in T_K results from bringing ε_0 towards the Fermi energies $\mu_L = \mu_R$ by tuning the gate voltages.
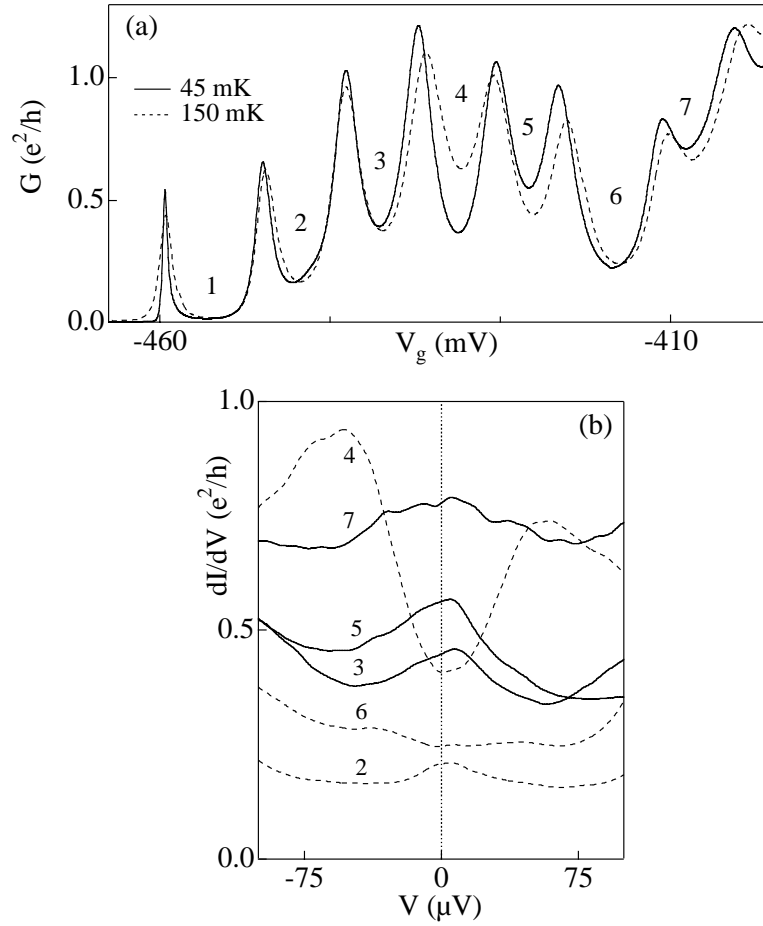
Figure 5-9. Zero-bias peak in alternate valleys **(a)** The same series of CB peaks from dot 1 shown previously in Fig. 5-6a. **(b)** Differential conductance, dI/dV, as a function of V for the center of each CB valley in (a). The odd valleys (solid lines) have a pronounced zero-bias maximum.

T_K or T. As the measurements in Fig. 5-8b were all taken at 45 mK, the increase in width of the dI/dV peak when approaching the CB peaks on either side of the Kondo valley indicates that here T_K exceeds T—that is, T_K is increasing. Figure 5-8c demonstrates the first control of T_K in a Kondo system. The largest value we obtain for T_K can be estimated from the largest dI/dV peak in Fig. 5-8b; the width of ≈ 80 μV implies $T_K \sim 1$ K.[15]

---

[15] Subsequent experiments which extract a value for the Kondo temperature based on the functional form of the temperature dependence of the conductance have found the width of the dI/dV peak to follow $\sim 2kT_K$ [30, 170]. This would suggest $T_K \sim 0.5$ K for the largest dI/dV peaks reported here.
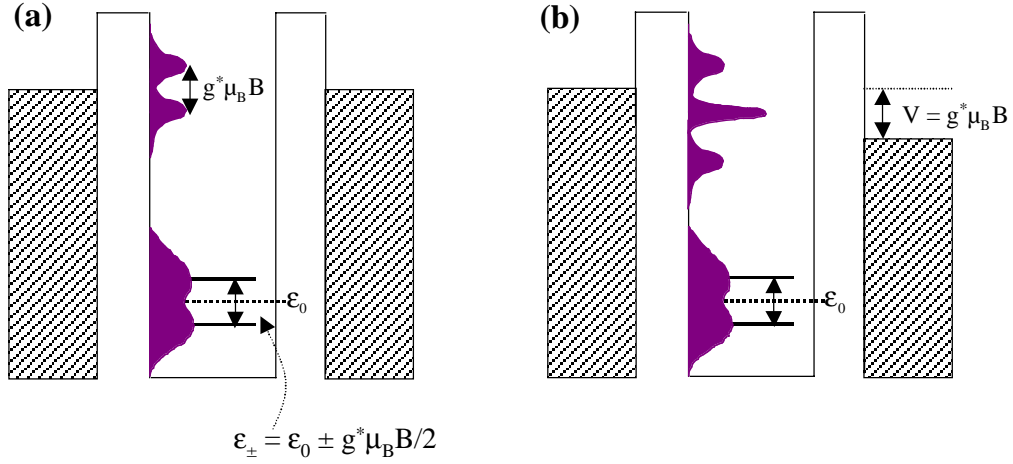
Figure 5-10. Density of states in a parallel magnetic field **(a)** The density of states (DOS), shown in purple, for a Kondo impurity in a parallel magnetic field $B_\parallel$ at $V = 0$. The spin-degenerate state ε_0, which contains an unpaired electron, splits into two spin-resolved states with energies $\varepsilon_0 \pm g^*\mu_B B/2$. The Kondo peak in the DOS also splits into two smaller peaks at $E_F \pm g^*\mu_B B$. At zero source-drain bias voltage ($V = 0$), the enhanced conductance from the Kondo resonance is lost. **(b)** When finite bias V is applied across the dot, each of the spin-resolved DOS peaks in (a) form around each chemical potential resulting in 4 peaks in the DOS. When $V = \pm g^*\mu_B B$, a Kondo resonance associated with each chemical potential aligns within the conduction window, re-establishing the enhanced conductance of the Kondo effect. Experimentally, the effect of a finite magnetic field is to split the zero-bias peak in the differential conductance into two peaks at $V = \pm g^*\mu_B B$.

The absence and presence of a zero-bias peak for N = even or odd, respectively can be seen in the dI/dV measurements for the valleys of dot 1 in Fig. 5-9c. Valleys 3, 5 and 7 indeed have a narrow zero-bias peak. Valley 6 has a flat dI/dV, while valley 4 has a minimum in the dI/dV, which resembles the form predicted by Ref. [171] for a quantum dot with N = even. Valley 2 shows a slight maximum at $V = 0$. This could arise from a dot with a net spin of ± 1 instead of 0. Occasionally we observe small shoulders on the sides of peaks in dI/dV. It is unclear whether these shoulders are related to the fact that our dots have multiple levels [166-168].

A magnetic field $B_\parallel$ in the plane of the 2DEG splits the spin-degenerate states of the quantum dot by the Zeeman splitting, $\varepsilon_\pm = \varepsilon_0 \pm g^*\mu_B B_\parallel/2$, as shown in Fig. 5-10a. When the dot has an unpaired electron, the Kondo peak in the DOS at *each* chemical potential is expected to split by *twice* the Zeeman energy, $2g^*\mu_B B_\parallel$ [60]. In equilibrium, there is no longer a peak in the DOS at $\mu_L = \mu_R$, and the zero-bias conductance is not enhanced. Instead, one expects the peak in dI/dV to be shifted to a finite bias (Fig. 5-10b): $V = \pm g^*\mu_B B_\parallel/e = \pm 25\ \mu V/T$, where $g^* = -0.44$ for bulk GaAs. In Fig. 5-11a we show that indeed the
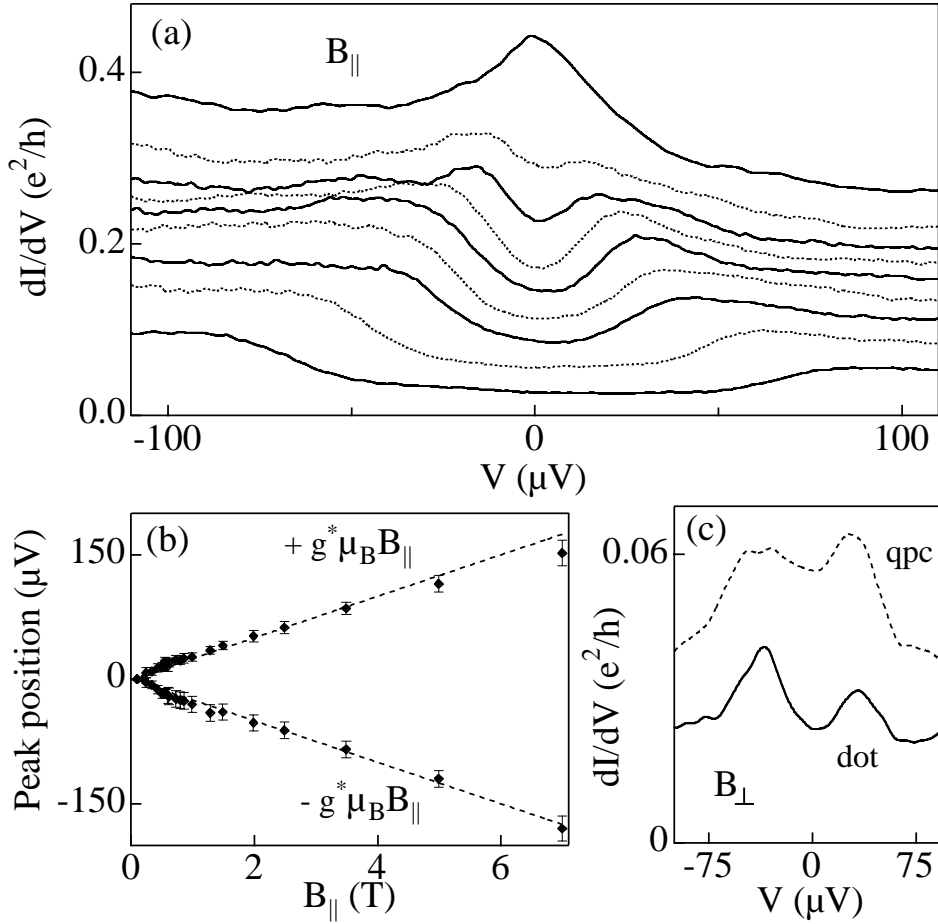
Figure 5-11. Split zero-bias peak in parallel magnetic field **(a)** The splitting of the zero-bias peak in the differential conductance dI/dV with a magnetic field $B_{\parallel}$ in the plane of the 2DEG. From top to bottom: $B_{\parallel}$ = 0.10, 0.43, 0.56, 0.80, 0.98, 1.28, 1.48, 2.49, and 3.49 T. The curves are offset by 0.02 e^2/h. Above ~0.5 T we resolve a splitting which increases linearly with $B_{\parallel}$. The data are from the Kondo valley of Fig. 5-7. **(b)** Position, in bias voltage, of the dI/dV maxima as a function of $B_{\parallel}$ up to 7 T. The dashed line indicates the theoretical splitting of $\pm g^*\mu_B B/e = \pm 25$ µV/T with $g^* = -0.44$ for GaAs. **(c)** Split peaks at 36 µV/T are observed in the dI/dV of the quantum dot and also in a single quantum point contact (qpc) (formed by a negative voltage on gates 1 and 3 only) in a perpendicular magnetic field $B_{\perp} = 1.89$ T. The Landau level filling factor is 4 at this field in the bulk 2DEG. Measurements at other $B_{\perp}$ and in other qpc's also showed similar structure. In contrast, the dI/dV of a qpc in high $B_{\parallel}$ is flat.
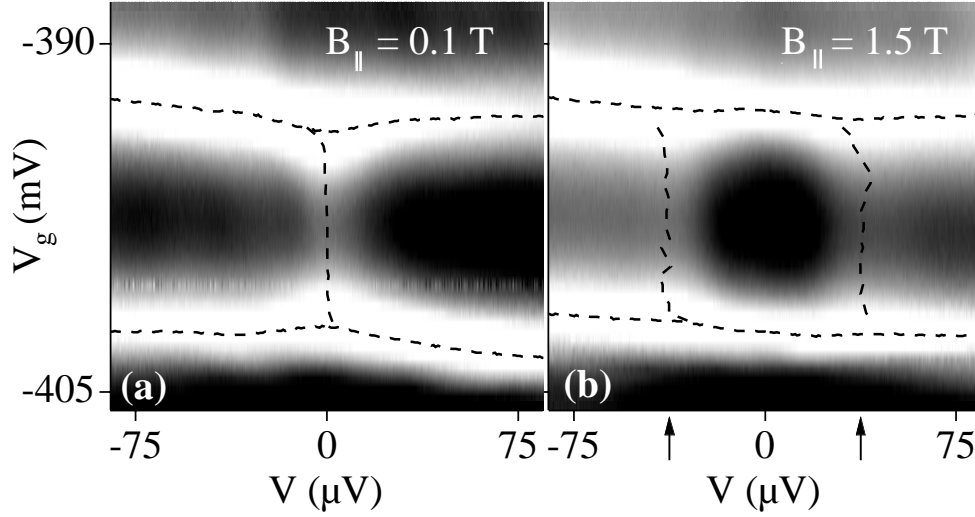
Figure 5-12. Split zero-bias peak independent of gate voltage **(a, b)** Grayscale plots of dI/dV as a function of V_g and V show the zero-bias peak for $B_{\parallel} = 0.1$ T split into two shoulder peaks at $B_{\parallel} = 1.5$ T. White regions mark large dI/dV while black regions indicate low conductance. This valley is the Kondo valley from Fig. 5-7(a). The contour of the CB peaks (horizontal) and the maxima in the dI/dV (vertical) are indicated by dashed lines. The valleys on either side of the Kondo valley do not show a zero-bias or split dI/dV peak. The arrows on the bottom axis of (b) indicate the theoretical splitting, which should be independent of V_g, with a value of ± 37.5 µV at $B_{\parallel} = 1.5$ T. The arrows matches the experimental results very well.

experimental zero-bias peak splits into two peaks when we increase $B_{\parallel}$ from 0 to 7 T. The peak positions, shown in Fig. 5-11b, fall directly on top of the theoretical prediction, ± 25 µV/T (dashed lines).[16]

The correct splitting of the dI/dV peak with magnetic field is considered the most distinct sign of Kondo physics [60]. Probing the Zeeman doublet single-particle states ($\varepsilon_{\pm}$) with the differential conductance could also reveal a peak split linear in $B_{\parallel}$. However, in this case, the splitting would be gate voltage dependent. A gate voltage-independent peak split by $2g^*\mu_B B_{\parallel}$ distinctively identifies the Kondo effect with no free parameters. Figures 5-12a and 5-12b show grayscale plots of the differential conductance, dI/dV, as a function of V and V_g over two CB peaks (white horizontal regions) and a Kondo valley (dark region between) at $B_{\parallel} = 0.1$ T and $B_{\parallel} = 1.5$ T. The Kondo valley shows a zero-bias peak in dI/dV at B = 0.1 T (brighter vertical strip), which splits into two dI/dV peaks at 1.5 T. The maxima of the

---

[16] It is not necessarily expected that our data match the theoretical splitting using the bulk GaAs g-factor because the effective g-factor in the 2DEG of a typical GaAs/AlGaAs heterostructure has been experimentally determined to be less than in the bulk [172].

CB peaks (horizontal) and the Kondo dI/dV peak(s) (vertical) are indicated by dashed lines. In both Fig. 5-12a and 5-12b, the maxima in dI/dV occur only for the Kondo valley and not for the neighboring valleys. Note that the location of the split maxima for $B_{\parallel} = 1.5$ T are independent of V_g throughout the valley.

Peaks in dI/dV reported in [156] were split by 33 µV/T in a magnetic field $B_{\perp}$ perpendicular to the plane of the 2DEG. This value, significantly smaller than the 50 µV/T measured here, could result from quantum Hall states in the leads. Figure 5-11c shows the dI/dV at $B_{\perp}$= 1.89 T for both our quantum dot (solid) and a single quantum point contact (dashed). Each curve shows split peaks in dI/dV at 36 µV/T. The point contacts of both our dots showed significant structure around ~ 35 µV/T in a perpendicular magnetic field. What might cause a field dependent splitting in the dI/dV of a quantum point contact is unclear.[17] However, the orbital changes caused by $B_{\perp}$ severely complicate the identification of Kondo physics in a perpendicular magnetic field. Furthermore, with the formation of spin-polarized Landau levels in the leads, a single electron on the dot cannot equally couple to both spin states in the leads which should suppress the Kondo resonance.

In summary, we have realized a tunable Kondo effect in small quantum dots. The dots can be switched from a Kondo to a non-Kondo system as the number of electrons on the dot is changed from odd to even. The Kondo temperature can be tuned by means of the gate voltage as the single-particle energy state nears the Fermi energy. Measurements of the temperature and magnetic field dependence of a Coulomb-blockaded dot show good agreement with predictions of both equilibrium and non-equilibrium Kondo effects.

5.4   Related Work

In the three years since this experiment was completed, a number of subsequent experiments on the Kondo effect in quantum dots and other novel systems have been carried out by other groups. In particular, Goldhaber-Gordon and collaborators [173] completed the first quantitative analysis of the Kondo effect in quantum dots. This work included a comparison of experimental results with the predicted temperature dependence, derived by Costi, Hewson and Zlatic [153] using numerical renormalization group theory, which permitted extraction of the Kondo temperature. The experiment matched theoretical predictions very well. Other groups have also observed the Kondo effect in semiconductor quantum dots. Schmid *et al.* [174, 175] reported initial observations in 1998 and subsequently reported a Kondo resonance observed in two consecutive CB valleys. Simmel *et al.* [176] observed a Kondo resonance which was shifted slightly off zero-bias, perhaps because their device was tuned such that dot was coupled much more strongly to one

---

[17] It is somewhat interesting to consider this data in light of the measurements presented on single quantum point contacts in Chapter 6 which appear to show an analogous type of Kondo effect.

lead then the other. They attribute the observed shift in the "zero-bias" peak to the pinning of the Kondo peak in the DOS to the more open lead.

Two subsequent experiments have also been performed at TUDelft under the continued supervision of Leo Kouwenhoven. In one, van der Wiel *et al.* [170] report the first observation of the conductance in a Kondo valley reaching the unitary limit of $2e^2/h$. They are also able to quantitatively fit their temperature dependent data and extract Kondo temperatures as a function of V_g (or equivalently ε_0) with good theoretical agreement. Furthermore, because their device was imbedded in one arm of an Aharonov-Bohm ring, they were able to demonstrate that conductance through the Kondo impurity is at least partially phase coherent. The second experiment, by Sasaki *et al.* [177] demonstrates the Kondo effect at a singlet-triplet state degeneracy point in a finite perpendicular magnetic field. In this case, it is the degeneracy of the singlet and triplet states, not a single spin-degenerate level, which allows the magnetic exchange coupling with the leads to form a Kondo state.

The Kondo effect has also been studied in other systems over the past several years. Using carbon nanotubes, Nygard *et al.* [30] have seen all of the same Kondo signatures that have been observed in semiconductor dots including the temperature dependence of the linear conductance, the zero-bias peak in alternating valleys, the splitting of the zero-bias peak with magnetic field, and even the singlet-triplet Kondo state. The many advances of nanotechnology have also enabled scientists to study the original Kondo system, a single magnetic atom in a bulk magnetic host, for the first time. Scanning tunneling microscopy (STM) measurements allow the identification and investigation of a single magnetic atom such as cobalt on the surface of non-magnetic metallic crystals such as gold, silver or copper. Two successful experiments of this kind were reported simultaneously in 1998 by Madhavan *et al.* [178] and Li *et al.* [179]. In both, a narrow resonance with a fano lineshape was observed centered on the magnetic impurity and not elsewhere. More recently, Manoharan *et al.* [180] reported a spectacular experiment in which a single cobalt atom was placed at one focal point of an ellipse corral formed by other cobalt atoms on a copper surface. In addition to the Kondo resonance observed at the location of the single cobalt atom, they were able to see a smaller Kondo resonance at the other focal point—even though there was no magnetic impurity at that location. An additional recent observation of Kondo physics using STM techniques was done by Odom *et al.* [181] measuring small magnetic clusters on carbon nanotubes. With our increased ability to manipulate particles on the atomic scale, there are certain to be other intriguing experiments of this type in the future.

Finally, it goes without saying that the volume of theoretical work on the Kondo effect in quantum dots has increased tremendously in the past decade. A complete review of the recent developments in the field is beyond the scope of this thesis. However, a number of the theoretical developments relate directly to the experimental observations of the Kondo effect in a singlet-triplet state and in nanotubes so I refer the reader to references within those papers.

Quantum dots have proven to be versatile systems in which to study the Kondo effect. They have contributed to the current status of the Kondo effect as one of the few true many-body problems which has been tackled with relative theoretical and experimental success. Even so, there continues to be a seemingly unending list of new theoretical and experimental developments in this topic—one of which is the subject of the next chapter.

Chapter 6

"0.7 Structure" and Kondo Physics in a Quantum Point Contact

6.1   Introduction

This last experimental chapter is devoted to transport measurements on quantum point contacts, narrow constrictions formed in the 2DEG by two split surface gates. As described in Chapter 2, the conductance through a quantum point contact (QPC) is quantized in units of $2e^2/h$ as the width of the constriction is decreased by the confining potential. The quantization indicates the full transmission of one-dimensional (1D) modes through the constriction, with the factor of two reflecting the spin-degeneracy of those modes. This interpretation, based on a non-interacting Fermi-liquid picture, successfully describes most of the initial experiments on QPCs. For a overall review of QPCs within a non-interacting framework, see Ref. [62].

The past several years have seen a number of experiments which reveal deviations from the simple QPC quantization [182-184]. One particularly robust deviation is an extra plateau or shoulder-like feature on the low-density side of the first quantized plateau (see Fig. 6-4a) which typically occurs at a conductance of $\sim 0.7(2e^2/h)$ and becomes more prominent with increasing temperature. This feature, termed the "0.7 structure", is visible in even the earliest experimental data on QPCs [63, 185, 186], though it was not studied itself until 1996 [184]. Since then, the 0.7 structure has been observed in by a number of groups using different materials and device geometries [187-196].

In the first investigation of the 0.7 structure, Thomas *et al.* suggested that this feature arises from a spontaneous spin polarization, presumably due to electron-electron interactions [184]. A number of subsequent experiments on QPCs [187-194] and clean quantum wires [194-196] have provided further evidence connecting the 0.7 structure at zero magnetic field with known effects of spin polarization at higher magnetic field. At the same time, several theoretical models have found a breaking of spin degeneracy in QPCs at low electron density [197-208], though no microscopic model has yet shown the 0.7 structure emerging directly from electron-electron interactions. It is worth noting that the ground state of a strictly 1D system cannot display spontaneous spin polarization at zero magnetic field, according to the Lieb-Mattis theorem [209]. However, QPCs are short quasi-1D channels which continuously evolve into large 2D reservoirs and, as such, may not be subject to the prohibitions of the Lieb-Mattis theorem.

The fact that the 0.7 structure becomes stronger at higher temperature (see Fig. 6-4a) suggests that the feature is not a ground-state property at all. Instead, the 0.7 feature appears as a crossover from perfect quantized conductance at low temperature to a reduced conductance at high temperature, with an anomalously small crossover temperature. This crossover, in a system with a spin degree of freedom, is the hallmark of the Kondo effect. The Anderson model [143] which describes the Kondo effect provides an interesting alternative to explanations of the 0.7 structure invoking spin polarization. Namely, within the Anderson model, the spin degree of freedom is split *dynamically* by a Coulomb charging energy, U, but there is no *static* ferromagnetic polarization. An important distinction between the Kondo effect described in Chapter 5 for quantum dots or impurities in bulk metals and the present situation is that the QPC is an *open* system with no obvious localized state. A speculation was made recently about the possibility of a Kondo state in a QPC [210], but at this writing, no concrete theory of such an effect has yet been formulated.

In this chapter, we present experimental evidence that at low-temperatures the unpaired spin degree of freedom associated with the 0.7 structure forms a Kondo-like correlated many-body state. We find a number of remarkable similarities between the present QPC system and the Kondo effect seen in quantum dots [30, 53, 156, 170, 173, 174, 176]. The similar features include: (i) a narrow conductance peak at zero source-drain bias that forms at low temperature, (ii) collapse of conductance data onto a single universal function over a range of gate voltages in the vicinity of the 0.7 feature using a single scaling parameter (which we designate the Kondo temperature), (iii) correspondence between the Kondo scaling factor and the width of the zero-bias peak, and (iv) splitting of the zero bias peak in a magnetic field.

The outline for the remainder of the chapter is as follows. Details of the five QPC devices and the measurement set-up will be described in Section 6.2. In Sec. 6.3, we present linear and nonlinear differential conductance measurements of a QPC including the temperature and magnetic field dependence of the 0.7 structure. The nonlinear data highlight the similarity between the 0.7 feature at zero magnetic field and the spin-resolved plateaus at high magnetic field. In Sec. 6.4, we discuss various methods for

estimating the effective g-factor in this system. Section 6.5 contains the measurements of the zero-bias-anomaly (ZBA) that occurs at low temperature and low magnetic field in the region between zero and one fully transmitted mode. In Sec. 6.6, we introduce the specific Kondo signatures in the QPC transport data. In particular, we scale the temperature-dependence of the conductance using both a modified form of the Kondo conductance in QDs and an activated form (previously used in Ref. [190]). The width of the ZBA is consistent with the Kondo temperatures extracted from the scaling, and the ZBA splits with application of a parallel magnetic field. Finally, in Sec. 6.7, we present measurements on other devices and show a range of behaviors. A short conclusion is given in Sec. 6.8.

6.2   QPC Devices and Measurement Set-up

The quantum point contacts are formed in the two-dimensional electron gas (2DEG) of a high-mobility delta-doped GaAs/AlGaAs heterostructure. From bottom to top, the layer sequence is: 250 nm GaAs/AlGaAs superlattice, 1.2 μm GaAs, 68 nm AlGaAs (x = 0.36), 2.5 x 10^{12} cm^{-2} delta doping, 26 nm AlGaAs (x = 0.36), 8 nm GaAs cap. The 2DEG has a bulk electron density of 1.2 x 10^{11} cm^{-2} and mobility of 4.1 x 10^{6} cm^{2}/Vs measured in the dark at 4.2 K. Ohmic contacts made of Ni-Au-Ge, annealed into the wafer, are used to make electrical contact to the 2DEG.

Eight QPCs are patterned in two sets on a single hourglass-shaped mesa using ebeam-defined Cr/Au surface gates. The gate patterns which create each set, seen in Fig. 6-1a, are comprised of one four-fingered gate opposite four individual gates. In any given measurement, only *one* "finger" gate and *one* of the matching individual gates is energized. This creates a single narrow constriction in the 2DEG. Measurements were made on the five QPCs shown in Fig. 6-1b, each with a slightly different channel width, W, and length, L (Fig. 6-1c). The size of all QPCs is much less than the mean free path of 23 μm, so transport through the devices is ballistic. The data presented in Secs. 6.3 to 6.6 were measured using QPC 4, though all devices displayed qualitatively similar behavior. Measurements from QPCs 1, 2, and 3, including examples of less pristine-looking data, are shown in Sec. 6.7.

All measurements were performed in a ^{3}He/^{4}He dilution refrigerator with an estimated base electron temperature of 80 mK. The differential conductance, g = dI/dV, was measured as a function of *parallel* magnetic field, B, temperature T, and dc source-drain bias voltage, V_{sd}, using a 4-wire voltage bias set-up in a crossed geometry, shown in Fig. 6-2. A small ac voltage bias, $|V_{rms}| < 10$ μV, is applied between the ohmics labeled V+ and V- in the source and drain electron reservoirs, respectively. The differential current in the circuit is measured using standard ac lockin techniques at 275 Hz. Because the QPC resistance varies significantly compared to the other in-line resistances (roughly 1 kΩ from the ohmics and 4 kΩ from the cryostat wiring), it is necessary to explicitly measure the voltage drop across the device, ΔV_{ac}, using a second pair of ohmics to ensure an accurate measure of the conductance. This is

(a)

(b)

(c)

QPC size	1	2	3	4	5
W (μm)	0.4	0.3	0.3	0.3	0.7
L (μm)	0.5	0.2	0.3	0.4	0.4
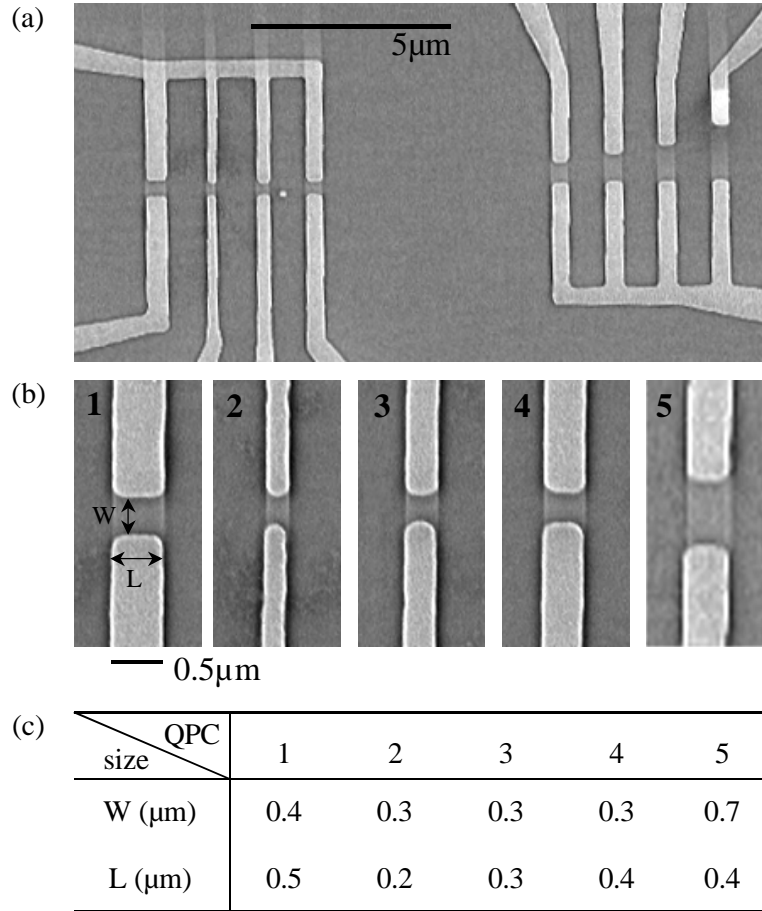
Figure 6-1. Quantum Point Contact SEMs. **(a)** Scanning electron micrograph (SEM) image of eight QPCs fabricated on a GaAs/AlGaAs heterostructure. A single point contact is formed by negatively biasing one of the large 4-fingered gates and one of the opposite individual gates. **(b)** Close-up views of the five QPCs measured. (c) Dimensions of the five QPCs measured.

accomplished with a second lockin, phase-locked to the first. The crossed geometry of this 4-wire measurement is used in conjunction with a small perpendicular magnetic field to ensure voltage equilibration near the sensing leads. Given the orientation of the schematic shown in Fig. 6-2, we apply a field of 25 mT into the page during most of the measurements. A discussion of the crossed 4-wire measurement geometry can be found in Ref. [62]. Even with this geometry, a series resistance of ~ 350 Ω at B = 0 to ~ 2 kΩ at B = 8 T has been subtracted from all data using the plateaus at multiples of $2e^2/h$ to infer the series resistance.
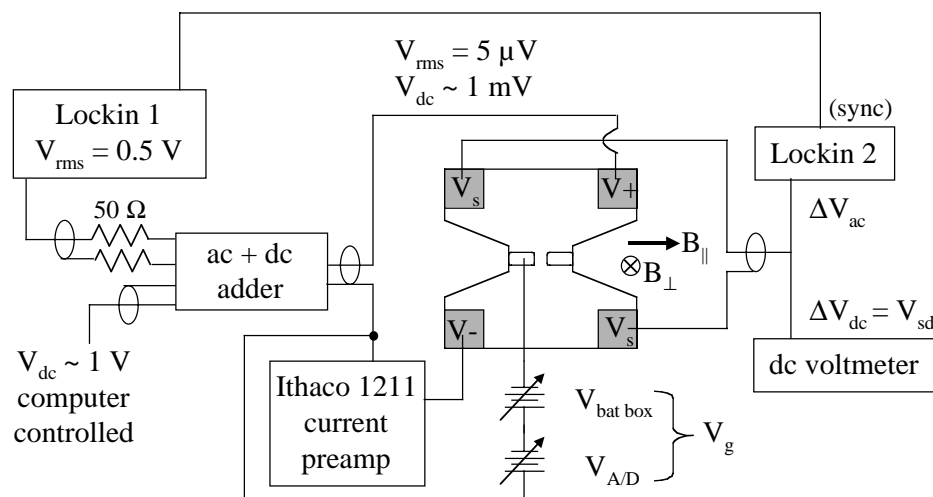
Figure 6-2. Crossed 4-wire voltage bias measurement set-up. The QPCs are biased with a small ac voltage (and optionally a dc voltage from a computer controlled analog/digital converter) and the current measured using standard ac lockin techniques. The ac + dc adder box contains voltage dividers of roughly 10^5:1 for ac signals and 1000:1 for dc signals. Additional voltage sensing lines are measured with a second lockin (and optional dc voltmeter). The QPC gates are biased relative to a drain ohmic using a potentiometer controlled battery box in series with a voltage from the computer controlled A/D converter. The orientations of the parallel and perpendicular magnetic fields are shown.

The width of the QPC is controlled with negative voltages applied to the two surface gates which form the constriction. Unless otherwise indicated, the same voltage, V_g, was applied to both gates simultaneously. The gate voltage consists of a computer-controlled voltage from an analog/digital (A/D) converter in series with a potentiometer-controlled battery box and is referenced to one of the ohmic contacts in the drain. A computer-controlled dc source-drain voltage, V_{sd}, may be applied across the QPC using another channel of the A/D converter, as seen in Fig. 6-2. The values of V_{sd} reported in the data are explicitly measured across the sample. We note that the dc source-drain voltage is not applied symmetrically across the device. Though this can produce slight asymmetries in the data, the small biases used in these measurements do not contribute to significant "self-gating" [190] around the features of interest.

The sample was mounted parallel to a 9 Tesla solenoid magnet and aligned to ~ 0.5 degrees, measured in a Van der Pauw configuration. The parallel magnetic field was oriented perpendicular to the current direction in the sample. A second magnet, made of two superconducting coils wrapped around the inner vacuum can of the dilution refrigerator, provided up to 150 mT of perpendicular field to allow independent control of both the parallel and perpendicular fields. A picture of the homemade perpendicular field magnet can be found in Appendix D.
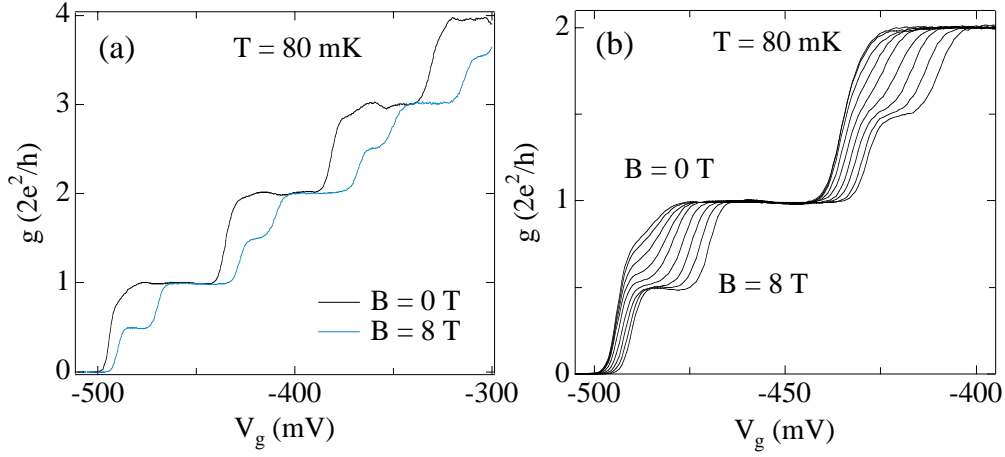
Figure 6-3. Magnetic field dependence of the QPC linear conductance. **(a)** The linear response ($V_{sd} \sim 0$) conductance g = dI/dV of QPC 4 as a function of gate voltage, V_g, shows four spin-degenerate plateaus quantized in units of $2e^2/h$ at B = 0 and T = 80 mK (black trace) which split into twice as many spin-resolved plateaus at parallel magnet field B = 8 T (blue trace). **(b)** Conductance, g, for the first two subbands versus V_g for parallel magnetic fields of B = 0 to 8 T in 1 T steps. The 0.7 structure, visible as the slight shoulder below the $2e^2/h$ plateau at B = 0, appears to be a zero-field remnant of the first spin-resolved plateau e^2/h.
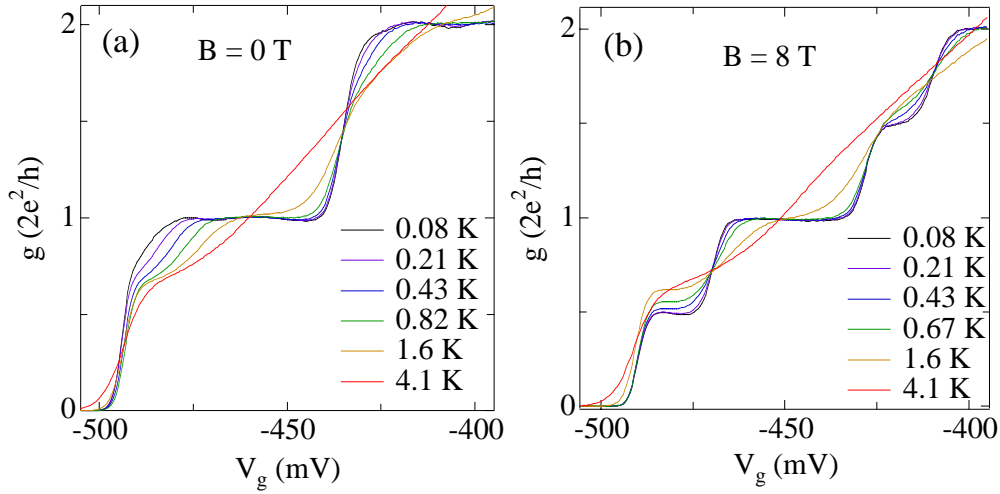
Figure 6-4. Temperature dependence of the QPC linear conductance. **(a)** Conductance, g, versus gate voltage, V_g, measured at B = 0 at several temperatures, T. At the lowest T, the 0.7 structure is barely visible as a shoulder on the left of the plateau at $2e^2/h$. With increasing temperature, conductance on the shoulder is reduced, forming an extra plateau at $\sim 0.7(2e^2/h)$. Over the same range of T, the spin-degenerate plateaus at multiples of $2e^2/h$ become less visible with increasing temperature due to thermal smearing. **(b)** Temperature dependence of the conductance for B = 8 T. The spin-resolved plateaus at both e^2/h and $3e^2/h$ increase in conductance with increasing temperature up to 1.6 K over their whole range in V_g. The plateaus at $2e^2/h$ and $4e^2/h$, in contrast, become thermally smeared at both the falling and rising edge simultaneously with temperature.

6.3   0.7 Structure in a QPC

The linear response conductance (i.e. around $V_{sd} \sim 0$) of the first 4 quantized plateaus of QPC 4 at B = 0 is shown in Fig. 6-3a. At high parallel magnetic field, the spin-degenerate plateaus at multiples of $2e^2/h$ split into spin-resolved plateaus at multiples of e^2/h, as expected within the standard non-interacting picture. Figure 6-3b shows the evolution of the plateaus as the magnetic field is decreased from 8 T to 0 in steps of 1 T. A remnant of the first spin-resolved plateau seems to persist down to B = 0 at T = 80 mK as the shoulder-like feature just below the quantized plateau at $2e^2/h$. This is the "0.7 structure". As the temperature is increased, this shoulder becomes more pronounced and a clear plateau near $0.7(2e^2/h)$ forms (Fig. 6-4a). In contrast, the spin-degenerate plateaus become more washed out. Stated another way, as the temperature is lowered, the spin-degenerate plateaus at $2e^2/h$ sharpen up, while the plateau at $0.7(2e^2/h)$ rises to the "unitary limit" value of $2e^2/h$, and thus disappears. The temperature dependence of the spin-resolved plateaus at B = 8 T is shown in Fig. 6-4b. Note that the conductance of the first spin resolved plateau increases from $0.5(2e^2/h)$ to roughly $0.7(2e^2/h)$ and is the last remaining feature at the highest temperature.

Nonlinear transport data is shown in Fig. 6-5 as a series of traces of conductance, g, versus source-drain bias voltage, V_{sd}, measured at sequential steps in gate voltage, V_g (not offset). In this representation, the plateaus in $g(V_g)$ appear as dense regions where many lines accumulate. Figure 6-5a shows data at B = 0 and T = 80 mK, with the integer plateaus around $V_{sd} \sim 0$ at 1 and 2 ($2e^2/h$), as well as the high-bias "half-plateaus" ($V_{sd} > \sim 0.5$ mV) at g ~ 1/2, 3/2, and 5/2 (in units of $2e^2/h$) labeled. The half-plateaus are well-understood, arising when the number of transport modes available for left-going and right-going electrons differs by one [211-213], (see the energy diagram of Fig. 6-7c). The plateau at 0.8 ($2e^2/h$) in the B = 0 data is not expected in a non-interacting picture. At a magnetic field of 8 T (Fig. 6-5c), the spin-resolved plateaus are visible at odd multiples of e^2/h and extend up into high-bias plateaus at ~ 0.8 times the distance between spin-degenerate plateaus for each subband. These high-bias plateaus at 0.8, 1.8 and 2.8 ($2e^2/h$) are essentially the half-plateaus of a spin-resolved system, occurring when the number of spin-resolved modes available to left- and right-going electrons differs by one.

Within the first subband ($g < 2e^2/h$), the nonlinear data at T = 600 mK and B = 0, (lower region of Fig. 6-5b), bear a striking resemblance to the same conductance region at B = 8 T. In particular, the slight accumulation of lines which denote the 0.7 structure at B = 0 merges with a high-bias plateau at ~ $0.8(2e^2/h)$ exactly as the first spin-resolved plateau does in high field. Note that the QPC does not show any extra plateaus in higher subbands at zero magnetic field. The overall impression given by comparing Figs. 6-5b and 6-5c is consistent with the linear transport data of Fig. 6-3b: The extra plateau that starts at ~ $0.7(2e^2/h)$ and extends up to ~ $0.8(2e^2/h)$ at high-bias appears to result from a splitting of spin bands,
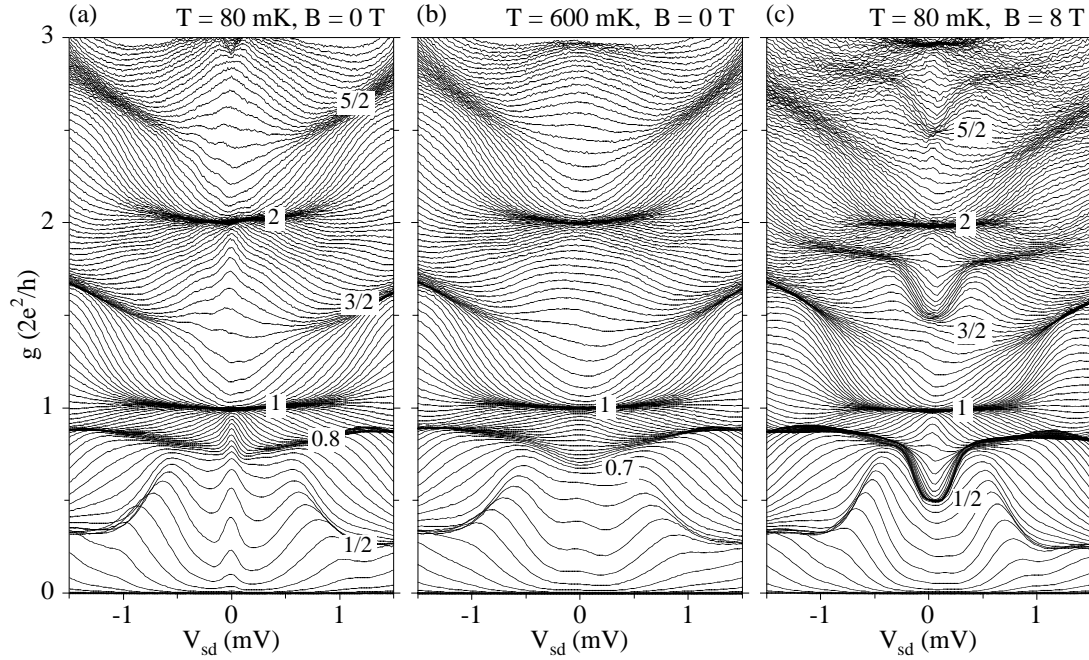
Figure 6-5. QPC nonlinear conductance. Nonlinear transport, showing differential conductance g = dI/dV as a function of dc source-drain bias voltage, V_{sd}, at many different gate voltages, V_g. Plateaus in g(V_g) appear as dense regions where many traces accumulate. **(a)** Nonlinear data at low temperature (T = 80 mK) and B = 0, at intervals of 1.25 mV in V_g. The usual plateaus at integer values of $2e^2/h$ around $V_{sd} \sim 0$ and "half-plateaus" at odd multiples of e^2/h at high bias are clearly visible as dark regions where many lines come together (as labeled, in units of $2e^2/h$). Note the conductance peak around $V_{sd} \sim 0$ for $g < 2e^2/h$. This zero-bias anomaly (ZBA) is present only at low magnetic field and low temperatures. At high bias, an extra plateau (not expected within a noninteracting electron pictures) appears at $g \sim 0.8(2e^2/h)$. **(b)** Nonlinear transport for higher temperature (T = 600 mK) at B = 0, in steps of 1.0 mV in V_g. Data appear similar to the 80 mK data except for the absence of a ZBA. Instead, an accumulation of lines (weak plateau) at $g \sim 0.7(2e^2/h)$ around $V_{sd} \sim 0$ indicates the 0.7 structure at higher temperature. The plateau at $0.7(2e^2/h)$ merges with the high-bias plateau at $0.8(2e^2/h)$. **(c)** Nonlinear data at large parallel field, B = 8 T, and T = 80 mK at intervals of 1.2 mV in V_g. Additional spin-resolved plateaus at odd multiples of e^2/h appear around $V_{sd} \sim 0$. The spin-resolved plateaus in each subband merge with corresponding high-bias plateaus at 0.8, 1.8, and $2.8(2e^2/h)$. Note that within the first subband, the high-bias feature at $0.8(2e^2/h)$ connected with the first spin-split mode looks strikingly similar to the data at B = 0. leading to transport signatures in the lowest mode at B = 0 which greatly resemble the situation at 8 T for all modes, where spin degeneracy is explicitly lifted by the applied field.
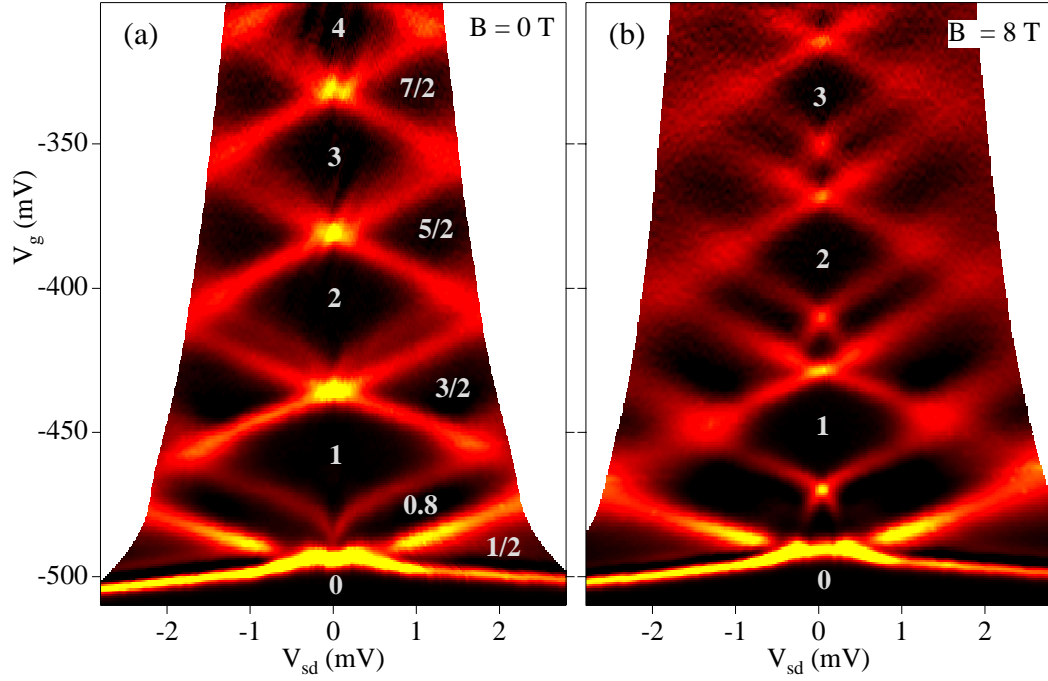
Figure 6-6. Nonlinear transconductance colorscales. Transconductance, the derivative of conductance with respect to gate voltage, dg/dV_g, in colorscale as a function of V_{sd} and V_g at $T = 80$ mK for **(a)** $B = 0$ and **(b)** $B = 8$ T. Black regions ($dg/dV_g \sim 0$) correspond to plateaus in $g(V_g)$. Red and yellow regions ($dg/dV_g > 0$) mark transitions between plateaus in $g(V_g)$. **(a)** The central black diamonds of the integer plateaus (labeled in units of $2e^2/h$) and the high-bias half-plateaus fit within a noninteracting electron model for the QPC. The extra transition lines that form the bottom edge of the first integer plateau are not expected in a simple model. The extra plateaus (black regions) on the other side of theses transitions are the high-bias $0.8(2e^2/h)$ features seen in Fig. 6-5a. **(b)** The high magnetic field data show small diamonds centered around $V_{sd} \sim 0$ in between the larger labeled diamonds. These are the spin-resolved plateaus. The transition lines which form the boundary between the first integer plateau and the spin-resolved plateau below are similar to the extra transitions in the $B = 0$ data.

Another way of viewing the nonlinear transport data is the transconductance—the derivative of g with respect to gate voltage, dg/dV_g (obtained by numerically differentiating the experimental conductance data) [187]. The transconductance emphasizes transitions between plateaus in $g(V_g)$ (seen as red/yellow bands) while the plateaus appear black. Figure 6-6 shows the transconductance in colorscale as a function of V_{sd} and V_g for (a) $B = 0$ T and (b) $B = 8$ T at $T = 80$ mK.

A line drawing of the transconductance for a non-interacting spin-degenerate QPC is shown in Fig. 6-7 with energy diagrams corresponding to the marked locations in the central plot. In this simple model, the transconductance shows a series of X's, one atop the next as a function of V_g, which form diamonds centered around $V_{sd} = 0$. The crossing point of each "X" sits at the gate voltage where a new
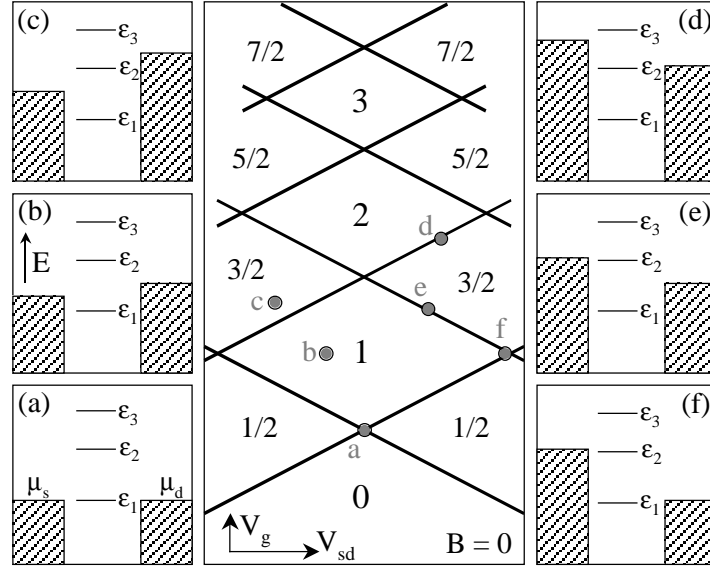
Figure 6-7. Schematic transconductance for a noninteracting QPC. The central line drawing represents the transconductance at B = 0, with the black lines corresponding to the red/yellow transition lines in the experimental data (Fig. 6-6). The integer and half-plateaus are labeled with their conductance, in units of $2e^2/h$. The surrounding energy diagrams show the relative locations of the first three one-dimensional (1D) subbands (ε_1, ε_2, ε_3) and the source and drain chemical potentials (μ_s, μ_d) for the locations in V_g and V_{sd} marked with blue circles. **(a)** The crossing points of two lines at $V_{sd} = 0$ occur when μ_s and μ_d are both aligned with a 1D subband. **(b)** Within the first integer plateau, $\varepsilon_1 < \mu_s$, $\mu_d < \varepsilon_2$. **(c)** The half-plateaus occur when a transport band lies between μ_s and μ_d. **(d)** Transition lines with positive slopes indicate that μ_d is exactly aligned with an energy band. **(e)** Transition lines with negative slopes indicate that μ_s is exactly aligned with an energy band. **(f)** Points where two lines cross occur when both μ_s and μ_d are exactly aligned with either different ($V_{sd} \neq 0$) or the same ($V_{sd} = 0$) energy states.

transport band (ε_n) is exactly aligned with the source and drain chemical potentials, $\mu_{s,d}$ (illustrated by Fig. 6-7a). Each centered diamond represents a quantized plateau in $g(V_g)$, where μ_s and μ_d both lie between the same two energy bands (Fig. 6-7b). The regions immediately outside the central diamonds are the half-plateaus, where a single energy band lies between μ_s and μ_d (Fig. 6-7c). Lines which run diagonally upwards from left to right in the transconductance plot indicate that a band is exactly aligned with μ_d (Fig. 6-7d and 6-7f), while those running diagonally downwards have a band aligned with μ_s (Fig. 6-7e and 6-7f). Note that the point marked (f) in the schematic gives a direct measure, in V_{sd}, of the subband spacing between consecutive energy levels. At high field, where each spin-degenerate band splits in two, the corresponding transition lines in the transconductance will also each split in two, resulting in twice as many stacked X's.

Returning to the experimental data of Fig. 6-6, the overall character of the transconductance at both low and high field is consistent with the simple model of the QPC. The central black diamonds are the quantized plateaus, marked in units of $2e^2/h$. At high field (Fig. 6-6b), additional small diamonds—the spin-resolved plateaus at odd multiples of e^2/h—can be seen below each large (labeled) diamond. The 0.7 structure is visible in the $B = 0$ data as an extra pair of transition lines, symmetric in V_{sd}, with a distinctive downward curvature as they approach the "origin" at $V_{sd} = 0$ and $V_g \sim -500$ mV. Crossing these features into the central diamond (labeled '1') marks the transition from the extra high-bias plateaus at $\sim 0.8(2e^2/h)$ (seen in Figs. 6-5a-c) to the $2e^2/h$ plateau. These extra transitions are greatly diminished or absent in higher subbands[187, 190]. Comparing the data at $B = 0$ to that at 8 T, we again note that the extra plateaus and transitions associated with the 0.7 structure are very similar to those attributed to the first spin-resolved plateau at high field.

6.4 Effective g-factor measurements

The transconductance at $V_{sd} = 0$ has previously been used to measure the effective g-factor, g^*, of the QPC system [184]. This is done by measuring the separation of the transconductance peaks which correspond to transitions from conductance $g = 0$ to $g = e^2/h$ and from $g = e^2/h$ to $g = 2e^2/h$, as shown in Fig. 6-8 for temperatures of $T = 80$ mK, 670 mK, 1.3 K, and 3.1 K. The transconductance traces shown on the right (offset vertically for clarity) are obtained by differentiating the linear response conductance for $B = 0$ to 8 T in steps of 0.5 T shown on the left (offset horizontally for clarity) at each temperature. At $B = 0$ and $T = 80$ mK (Fig. 6-8b), the transconductance peak associated with the first plateau shows a small side peak—evidence of the 0.7 structure. As the magnetic field is increased, this side peak grows and splits from the main peak. The separation between peaks, ΔV_g (blue squares in Fig. 6-9a), is linear in magnetic field. Similar behavior occurs at each temperature, with the results shown in Fig. 6-9a. The splitting of the $B = 0$ transconductance peaks (though not the original side peak at $B = 0$) is a result of the evolution from spin-degenerate to spin-resolved plateaus (seen in conductance, Fig. 6-8a,d), with the separation given by the Zeeman energy, $g^*\mu_B B$.

The effective g-factor can be determined from the slope of ΔV_g vs. B (Fig. 6-9a) if the gate voltage can be scaled to energy. To determine the scaling factor, a finite source-drain bias voltage is applied which splits the transconductance peak of each plateau (Fig. 6-9b). The splitting in gate voltage, δV_g, is equated to the applied V_{sd} as $\eta \delta V_g = eV_{sd}$, where η is the conversion factor between gate voltage and energy. For better accuracy, one can use the slopes of transitions corresponding to the two lines of a transconductance X instead of a single value of V_{sd}. Then, g^* is determined from the equation: η(slope of ΔV_g vs. B) = $g^*\mu_B$. The values of η and g^* measured in this way, are shown in the table of Fig. 6-9c. These measurements give
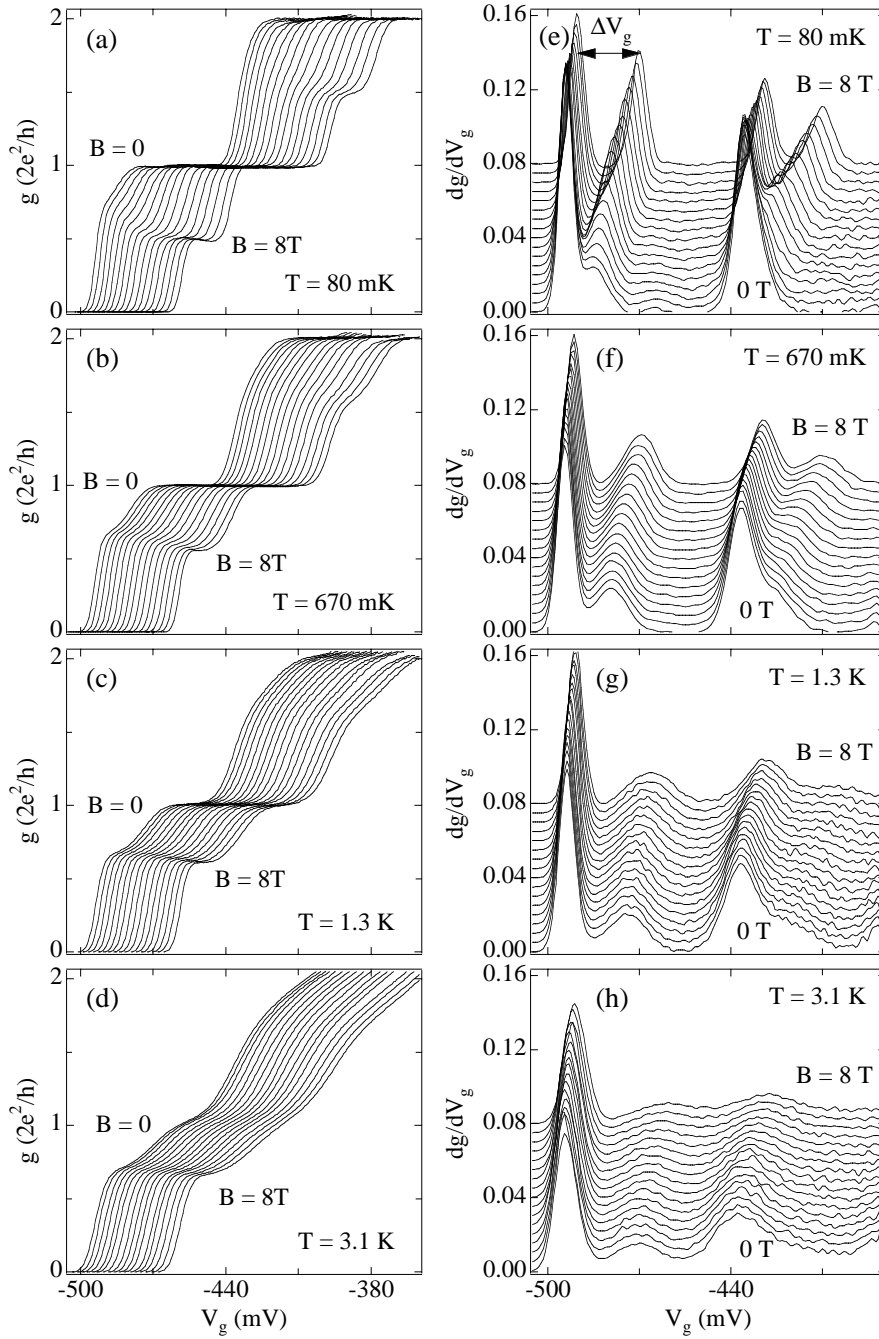
Figure 6-8. Linear transconductance, temperature and magnetic field dependence. **(a-d)** Linear response conductance, g, vs. gate voltage for parallel magnetic fields B = 0 to 8 T in 0.5 T steps at temperatures **(a)** T = 80 mK, **(b)** 660 mK, **(c)** 1.3 K, **(d)** 3.1 K. Traces in V_g are offset by 2mV for clarity. **(e-h)** Linear response transconductance, dg/dV_g, for B = 0 to 8 T in 0.5 T steps obtained by numerically differentiating the conductance data in (a-d) with respect to V_g. Traces are offset vertically by 0.005 for clarity. **(e)** At T = 80 mK, the B = 0 transconductance shows two prominent peaks corresponding to the conductance rise up
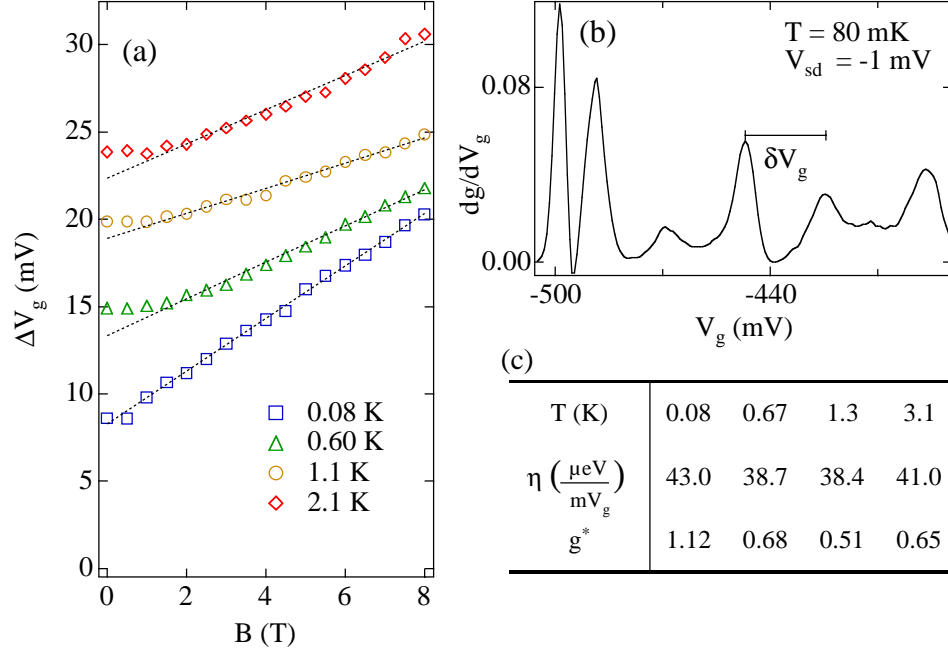
Figure 6-9. Effective g-factor measured from transconductance peak splitting. **(a)** The gate voltage splitting of the first subband transconductance peaks, ΔV_g, as a function of parallel magnetic field, B, at temperatures T = 80 mK (blue squares), 660 mK (green triangles), 1.3 K (yellow circles) and 3.1 K (red diamonds) from the data in Fig. 6-8 (e-h). Solid lines show linear fits to ΔV_g for B > ~ 1 T. **(b)** The transconductance, dg/dV_g, at V_{sd} = -1 mV and B = 0. (This trace is a vertical line through the colorscale in Fig. 6-6a at V_{sd} = -1 mV). The distance δV_g measures the splitting of the second subband transconductance peak due to the finite V_{sd}. The conversion between gate voltage and energy $\eta = eV_{sd}/\delta V_g$. **(c)** The effective g-factor, g^*, is determined from the slope of ΔV_g vs. B as $\eta(\text{slope}) = g^*\mu_B$. Values for η and g^* are given for each of the temperatures measured. At the lowest temperature, T = 80 mK, the effective g-factor appears enhanced by ~ 3 times the bare GaAs g-factor, $|g^*| = 0.44$.

to the first integer plateau and up to the second plateau. The transconductance peak of the first plateau has a small side peak (at less negative V_g) due to the 0.7 structure. As the spin-resolved plateaus begin to form with increasing parallel magnetic field, the side peak grows and splits from the main transconductance peak of the first plateau. The gate voltage splitting of the two peaks of the first plateau is ΔV_g. In the second subband, the single transconductance peak at B = 0 splits into two as the spin-resolved plateau at $3e^2/h$ develops. **(f)** At T = 660 mK, the side transconductance peak associated with the 0.7 is more resolved at B = 0 (because the 0.7 structure is more prominent in the linear conductance at higher T) and continues to split smoothly from the main peak with increasing field. The same behavior is seen at **(g)** T = 1.3 K and **(h)** T = 3.1 K.

an effective g-factor at T = 80 mK which is enhanced by a factor of ~ 3 compared to the bulk GaAs value, $|g^*| = 0.44$, consistent with the results of Ref. [184].

The method for determining the effective g-factor described above assumes that the conversion factor η, measured for a given V_g and V_{sd} range, can be used in the linear response region where the conductance increases from 0 to $2e^2/h$ at $V_{sd} = 0$. This assumption is valid when the transition lines in the transconductance colorscale are all straight. However, as noted above, the transition lines associated with the extra high-bias plateau at ~ $0.8(2e^2/h)$ are noticeably curved as they approach the relevant region at V_{sd} ~ 0. Therefore, we cannot be sure that the value of η—and thus g^*—measured in our case using the straight lines between the first and second integer plateau, is accurate for the linear response region around the 0.7 structure.

Another method for determining the effective g-factor is to directly measure the spin splitting, $\delta = g^*\mu_B B$, from the tips of the transconductance diamonds corresponding to the spin-resolved plateaus at high parallel magnetic field. The transconductance data at B = 8 T is shown again in Fig. 6-10a with the tip of the first spin-resolved plateau indicated by 'b'. From the corresponding energy diagram in Fig. 6-10b, it is clear that $eV_{sd} = \mu_s - \mu_d = \delta$ at this point. Note that a dashed line at this value of V_{sd} also intersects the diamond tips of the spin-resolved plateaus of the second and third subband, as expected. The value of g^* obtained from this direct measurement is ~ 1.5 times the bare g-factor, somewhat less than the value reported for the method above.

The difficulty in accurately estimating g^* can be seen in yet a third measurement, also obtained from the transconductance colorscale. Points 'c' and 'd' in Fig. 6-10a mark the transitions where $eV_{sd} = \Delta$, the spacing between the first spin mode of two subsequent subbands ($\Delta = \varepsilon_2 - \varepsilon_1$), and $eV_{sd} = \Delta - \delta$, respectively. This difference in source-drain bias gives another measurement of the spin splitting $e(V_{sd}(c) - V_{sd}(d)) = \delta_h = g^*\mu_B B$. Clearly δ_h, indicated by the thick bar on the bottom axis, is larger than δ_l so the g-factor obtained from this measurement is larger as well. This is, again, a direct consequence of the change in slope of the transition lines associated with the extra plateaus at ~ $0.8(2e^2/h)$ (marked by '*') as they pass through $V_{sd} = 0$. Besides highlighting the need to be especially precise when reporting an estimate of the g-factor in these systems, the measurements described here seem to indicate a bias-dependence of the spin-splitting even at B = 8 T where we expected a simple spin-polarized system.

6.5   Zero-Bias Anomaly

The low temperature nonlinear data shown in Fig. 6-5a have a significant additional feature compared to the higher temperature data (Fig. 6-5b): a narrow peak in conductance around $V_{sd} = 0$ for the whole range $0 < g < 2e^2/h$. This zero-bias anomaly forms as the temperature is lowered, as seen in Fig. 6-11b. The ZBA is closely linked to the disappearance of the 0.7 structure at low temperature: comparing Figs. 6-5a and 6-5b,
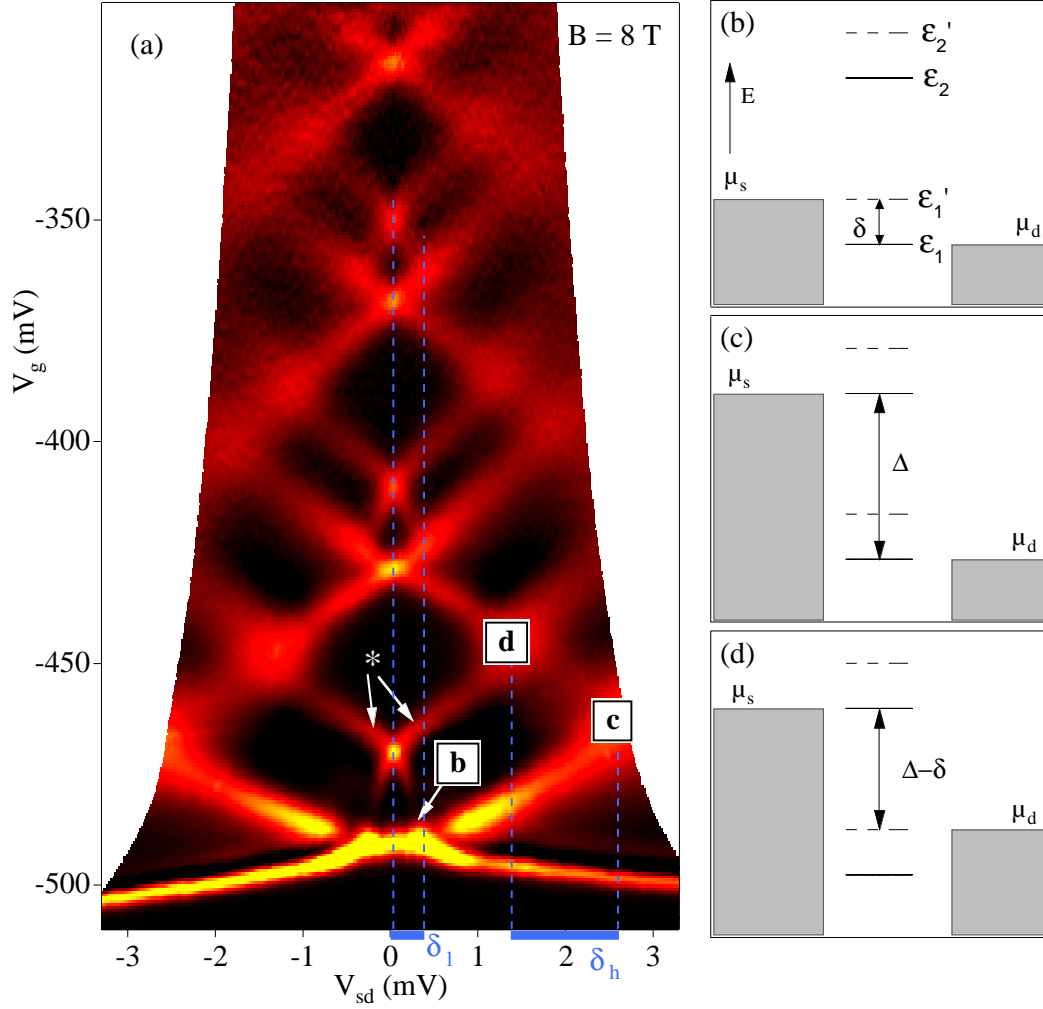
Figure 6-10. Additional g-factor measurements. **(a)** The transconductance colorscale at B = 8 T provides two additional methods for measuring the effective g-factor in the QPC system. At the location in (V_{sd}, V_g) marked **(b)**, the drain chemical potential, μ_d, is aligned with the state ε_1 of the spin-resolved first subband and the source chemical potential, μ_s, is aligned with the second spin state, ε_1'. Therefore the bias voltage $eV_{sd} = (\mu_s - \mu_d)$ precisely determines the spin-splitting $\delta = g^*\mu_B B$ (indicated by the thick blue bar labeled δ_l along the V_{sd} axis), and so also g^*. Another measure of g^* from the transconductance at high field is the difference in V_{sd} at the points labeled (c) and (d). In **(c)**, the source and drain align with the first spin state of consecutive subbands; their difference measures the subband spacing Δ. In **(d)**, μ_d is aligned with the second spin state of the first subband, so $eV_{sd} = \Delta - \delta$. The difference of V_{sd} between points (c) and (d) is a second measure of the spin splitting δ, indicated by the thick blue bar labeled δ_h at the bottom of (a). Note that the spin splitting measured at high-bias (c,d) is larger than that measured at low-bias (b), $\delta_h > \delta_l$. These two values give different measures of the effective g-factor.
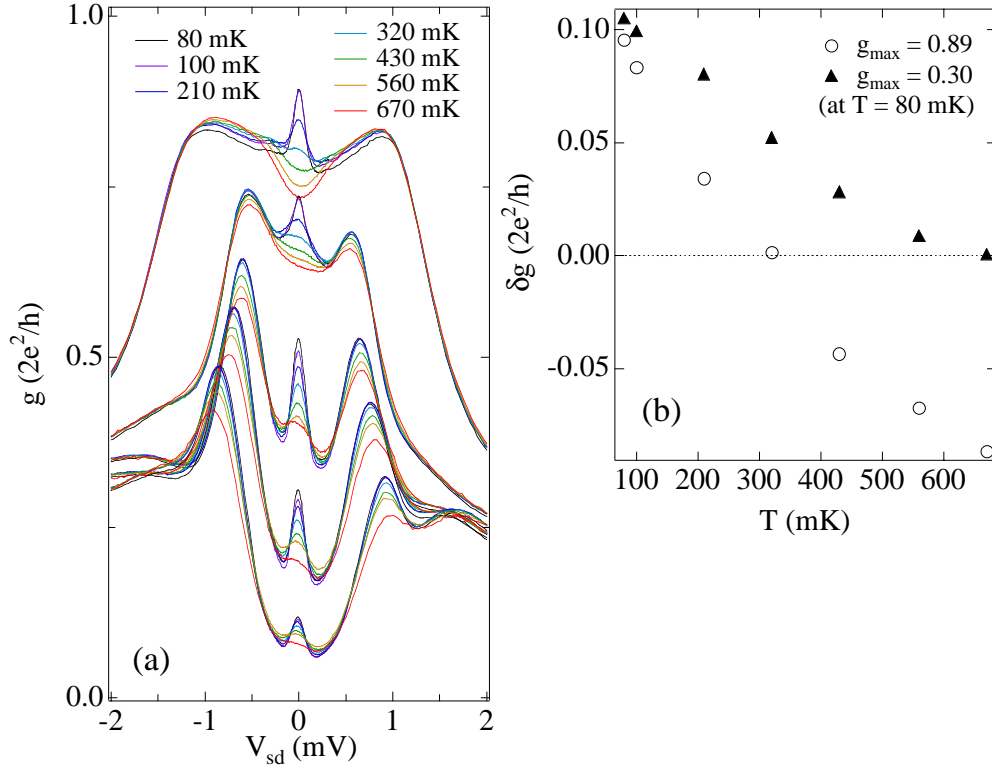
Figure 6-11. Temperature dependence of the zero-bias anomaly. **(a)** Conductance vs. source-drain bias voltage shows a narrow peak around $V_{sd} \sim 0$. The temperature dependence of this zero-bias anomaly (ZBA) from 80 mK to 670 mK shows the ZBA disappearing at high temperature. **(b)** The height of the ZBA peak, δg, defined as the difference between the peak max, g_{max}, and the local minimum on the left-hand side, as a function of T for the first set of curves where $g_{max} = 0.89(2e^2/h)$ at T = 80 mK (open circles) and fourth set of curves where $g_{max} = 0.30(2e^2/h)$ at T = 80 mK. Note that the peak height for the high conductance ZBA drops off much faster with increasing T than the ZBA at low conductance. (Where the peak turns into a local minimum in the high conductance ZBA around Vsd ~ 0 by 430 mK, the "height" is taken as the difference between the local minimum and the shoulder of the curve where it drops off the high-bias plateau at ~ $0.8(2e^2/h)$).

one sees that it is precisely this ZBA peak that lifts the 0.7 plateau toward $2e^2/h$. In contrast, the high-bias region remains largely unaffected by temperature.

The temperature dependence of the ZBA peak height, δg, defined as the difference between peak maximum, g_{max}, and the local minimum on the left-hand side, is shown in Fig. 6-11b for the gate voltages corresponding to the first (highest) set of curves and the fourth set of curves from Fig. 6-11a. Note that the ZBA height diminishes more quickly with increasing T at high g than at low g. The existence of a narrow ZBA with significant temperature dependence underscores the importance of staying precisely on top of the ZBA peak when measuring the temperature dependence of the linear response conductance (as in Fig. 6-4a).
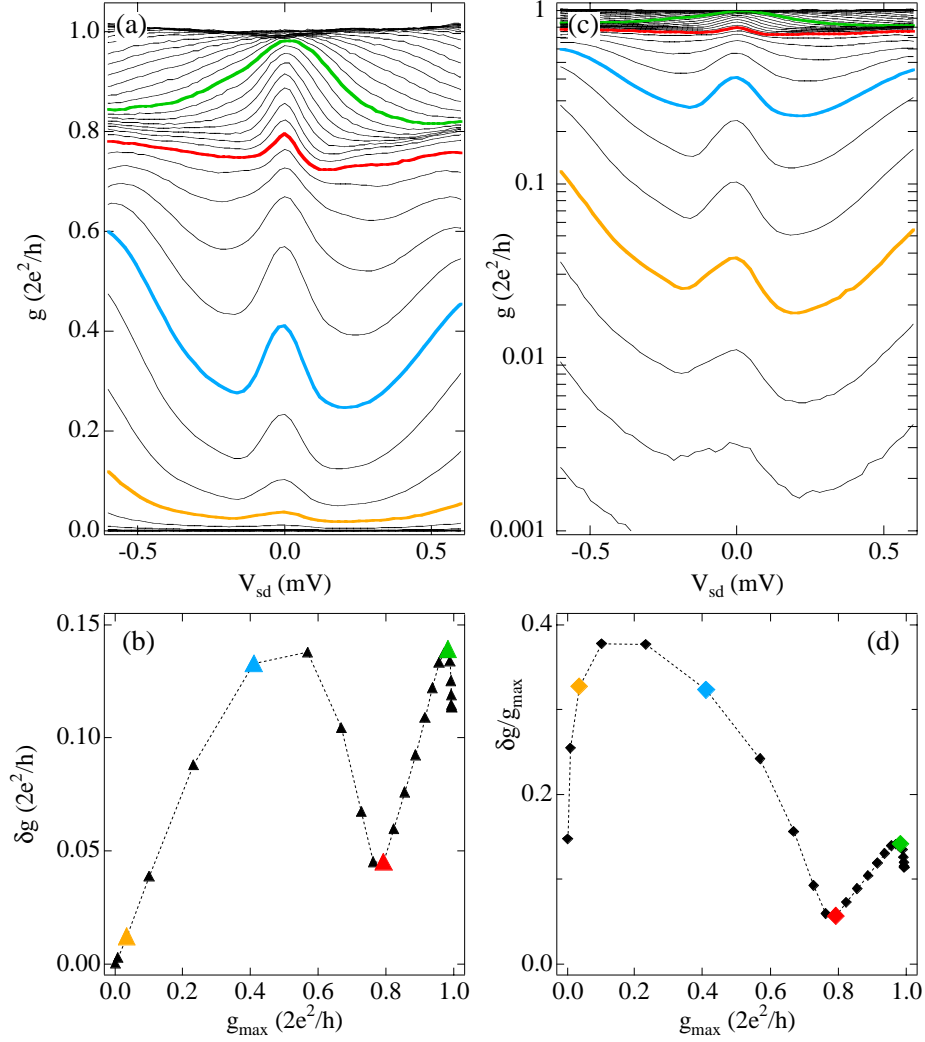
Figure 6-12. ZBA peak height. **(a)** Nonlinear transport data from Fig. 6-5a showing the ZBA peak around $V_{sd} \sim 0$. Conductance traces at four values of V_g are colored to correspond to colored markers in the following graphs. **(b)** The ZBA peak height, δg, (the difference between the peak max and the local minimum on the left-hand side) versus the peak max, g_{max}. **(c)** The nonlinear transport data with conductance on a logarithmic scale shows that the ZBA peak persists down to very low conductance. **(d)** The relative height of the ZBA peak, $\delta g/g_{max}$, versus g_{max}.

Further information about the height of the ZBA is given in Fig. 6-12. The ZBA peak height, δg, versus peak max, g_{max}, shows oscillations over the range $0 < g_{max} < 2e^2/h$ (Fig. 6-12b), with a local minimum occurring near $g \sim 0.8(2e^2/h)$. The colored markers correspond to the colored traces in Figs. 6-12a,c. The ZBA persists down to very low conductance, as seen in Fig. 6-12c where conductance is shown on a logarithmic axis. The relative height of the ZBA, $\delta g/g_{max}$ (Fig. 6-12d), also shows a pronounced local minimum around $g \sim 0.8(2e^2/h)$.

6.6   Kondo Effect Signatures

The formation of a zero-bias conductance peak and the associated enhancement of the linear conductance up the unitary limit ($2e^2/h$) at low temperature is reminiscent of the Kondo effect seen in quantum dots containing an odd number of electrons [30, 53, 58-60, 156, 170, 173, 174, 176]. Guided by this similarity, we investigate the temperature dependence of the QPC conductance for the type of scaling seen in quantum dots [30, 170, 173]. In the Kondo regime, the conductance through a quantum dot saturates at the unitary limit of $2e^2/h$ as the temperature goes to zero. At higher temperature the dependence is given by a universal form derived by numerical renormalization group methods[153] and well approximated by the empirical function[173]

$$g(T) = G_0[f(T/T_K)] \sim G_0\,[1 + (2^{1/S} - 1)\,(T/T_K)^2]^{-S} \tag{6.1}$$

where T_K, the Kondo temperature, and G_0, the saturation conductance, are typically fit parameters and s = 0.22 for a spin 1/2 on the dot. For QPCs, we consider a scaling of the temperature dependence of the conductance using a slightly modified form of Eq. 6.1:

$$g(T) = e^2/h\,[f(T/T_K) + 1], \tag{6.2}$$

with the Kondo temperature, T_K, as the only scaling parameter. Equation 6.2 differs from the form used for quantum dots (Eq. 6.1) by the addition of a constant e^2/h term and by fixing the prefactor of $f(T/T_K)$ to e^2/h. The motivation for adding the constant term of e^2/h to the usual dot form is primarily empirical—allowing the prefactor and the added constant to be adjustable fit parameters along with T_K consistently gave values that were very close to these, and fixing both values at 1 had essentially no effect on the fit values for T_K (compare $T_K(1)$ and $T_K(3)$ in Fig. 6-14f). Examples of fits to g(T) using Eq. 6.2 with T_K the only fit parameter are shown in Fig. 6-13a and using Eq. 6.1 with both T_K and G_0 as fit parameters in Fig. 6-13b.

Experimentally, we find that the single parameter T_K extracted from the above fits allows data from a broad range of gate voltages (raw data shown in Fig. 6-14a) to be scaled onto a single curve as a function of scaled temperature T/T_K (Fig. 6-14b). The scaled curve is well-described by the modified Kondo form of Eq. 6.2. The values of T_K increase exponentially with gate voltage (Fig. 6-14c, right axis). A best line fit to $\ln(T_K) \sim a(V_g - V_g^0)$ gives a = 0.18 (for T_K in Kelvin and V_g in mV).
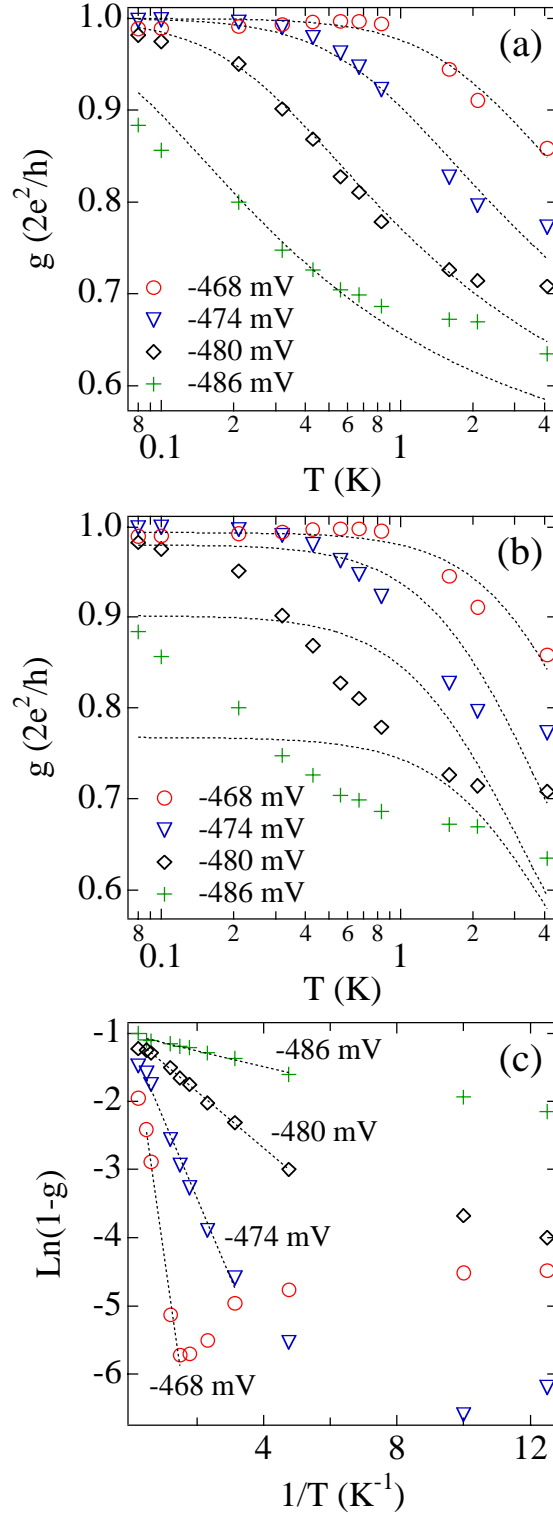
Figure 6-13. Example fits of g(T) to various functional forms. **(a)** The linear response conductance, g, versus temperature, T, for four different gate voltages. The dotted lines, least-squared-fits to the modified Kondo form of Eq. 6.2 with a single fit parameter T_K, show relatively good agreement with the experimental data. The shape and color of the markers at these V_g are the same used in Fig. 6-14. **(b)** Least-squared-fits to the usual Kondo form in quantum dots, Eq. 6.1, with both G_0 and T_K as fit parameters. The fits do not match the data well. **(c)** The same experimental data shown in an Arrhenius plot: $\ln(1-g(T))$, with g in units of $2e^2/h$, versus the inverse temperature, 1/T. The slope of a least-squared line fit over a limited range of data gives the activation temperature T_A from Eq. 6.3.
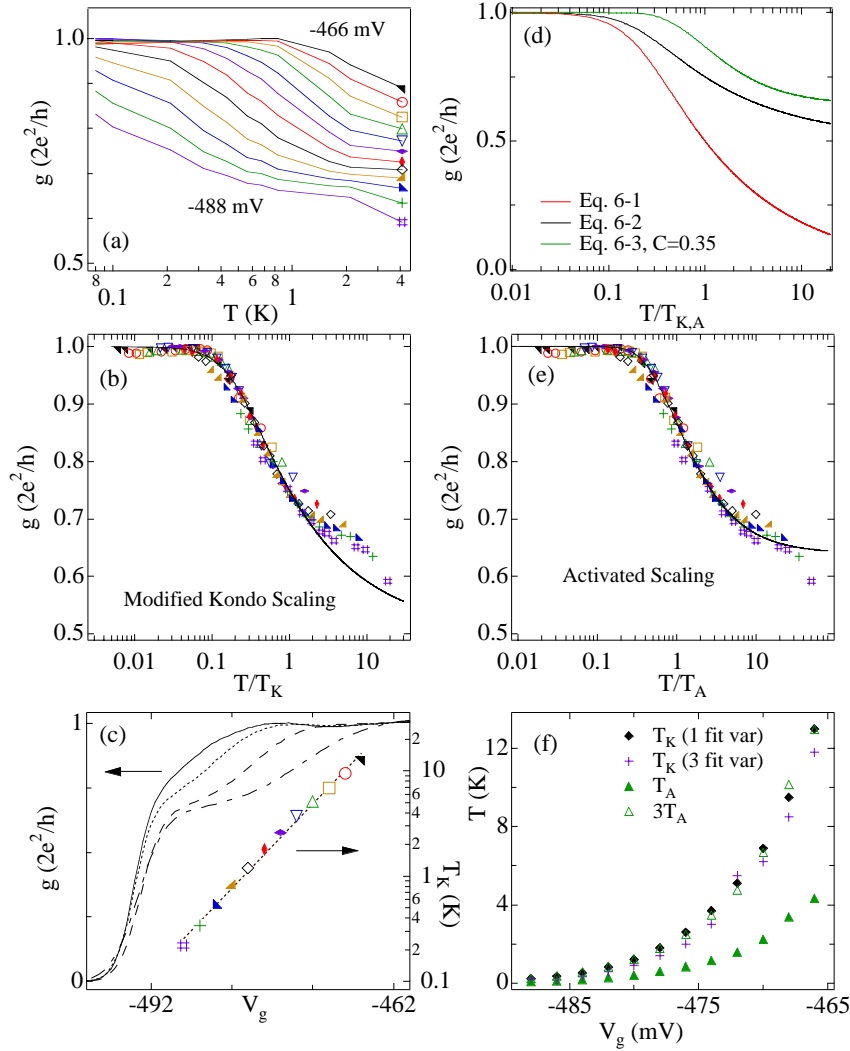
Figure 6-14. g(T) scaled by a T_K and T_A. **(a)** Raw conductance data g(T) from V_g = -466 mV to -488 mV in 2mV steps. Marker shape and color are kept the same throughout the figure. **(b)** Linear conductance, g, as a function of scaled temperature T/T_K where T_K is the single fit parameter in Eq. 6.2. When scaled this way, $g(T/T_K)$ collapses to a single curve that agrees well with the modified Kondo form, Eq. 6.2 (solid curve). **(c)** The values of T_K (markers, right axis) obtained from fits of g(T) to Eq. 6.2. The Kondo temperature, T_K, depends exponentially on V_g; a line fit to $\ln(T_K)$ vs. V_g (dotted line) gives a slope of 0.18. Several conductance curves (left axis; as in Fig. 6-4a) at temperatures of 80 mK (solid line), 210 mK (dotted), 560 mK (dashed) and 1.6 K (dot-dashed) show the range of gate voltages where scaling was applied. **(d)** The functional forms of the scaled conductance for Eq. 6.1 with $G_0 = 2e^2/h$ (red), Eq. 6.2 (black), and Eq. 6.3 with C = 0.35 (green) versus the scaled temperature T/T_K or T/T_A. Note the similarity between the modified Kondo form (Eq. 6.2) and the activated form (Eq. 6.3). **(e)** Linear conductance, g, as a function of scaled temperature T/T_A, where T_A is the activation temperature from the Arrhenius plots, also collapses to a single curve now well-described by the activated form of Eq. 6.3 (solid curve). **(f)** The values of T_K (diamonds) and T_A (filled triangles) used in the scaling plots above. The values of T_K from the single-parameter fits to Eq. 6.2 (diamonds) are nearly identical to the T_K values (crosses) extracted from Eq. 6.2 when both the prefactor and added constant are also used as fit variables. The values of T_A depend exponentially on V_g and are very close to 1/3 the Kondo temperatures (open triangles show $3T_A$).

Overall, the exponential dependence of T_K on V_g is not surprising given the known dependence of T_K for quantum dots [164], $T_K \sim \exp[\pi\varepsilon_0(\varepsilon_0+U)/(\Gamma U)]$ (neglecting nonexponential prefactors), which depends exponentially on ε_0, the energy of the localized spin relative to the Fermi energy of the leads, on (ε_0+U), the energy of the next available state (split from ε_0 by the Coulomb charging energy U), and on Γ, the level width due to coupling of the localized state to the external electron reservoirs. However, in the *open* QPC system, it is not immediately clear what energy should be associated with ε_0. An obvious first guess is to consider the bottom of the first spin-degenerate subband. If, in fact, the first subband is dynamically split by a Coulomb energy U, then we might be able to associate the lower energy spin band with ε_0 and the higher energy spin band with $\varepsilon_0 + U$ in a typical Anderson model. We emphasize again that the spin splitting is dynamic, not static. We hypothesize that the first band (ε_0) lies below the Fermi energy of the leads, E_F, and the second band ($\varepsilon_0 + U$), lies above E_F. As the plateau at $2e^2/h$ is approached, the second band at $\varepsilon_0 + U$ reaches and then crosses below E_F. This hypothesis is based on the fact that $g > e^2/h$ for the region where we are able to extract T_K, suggesting that one spin mode is fully transmitting, and on the increasing dependence of T_K as the first plateau is approached from below. Within a standard Anderson model, as the second band approaches E_F, the term $\varepsilon_0 + U$ goes to zero and T_K increases. If, instead, the first band were close to E_F, ε_0 would increase with increasing V_g, so T_K would decrease, the opposite of the experimental results seen in Fig. 6-14c. Another possible explanation for the exponential dependence of T_K on V_g may lie in the gate voltage dependence of Γ. This possibility is currently under theoretical investigation [214].

Previously, the temperature dependence of the QPC conductance around the 0.7 structure was shown to have an activated form,

$$g(T) = 1 - C\exp[-T_A/T] \tag{6.3}$$

where T_A, the activation temperature, and C are both used as fit parameters [190]. By plotting the conductance data in an Arrhenius plot (Fig. 6-13c), $\ln(1-g)$ vs. $1/T$ (g in units of $2e^2/h$), the slope of the linear region gives the activation temperature, T_A. Note that the data at the lowest temperatures (large $1/T$) do not follow the activated behavior. Interestingly, the values of T_A extracted from the Arrhenius plots depend exponentially on V_g and, in fact, are almost exactly 1/3 of the values of T_K above (Fig. 6-14f). Furthermore, when scaled by T_A, the conductance over the same range of gate voltage again collapses to a single curve, now well-described by Eq. 6.3 with $C \sim 0.35$, as shown in Fig. 6-14e. The remarkable similarity between the two fitting functions is less surprising when one notes that the two functional forms are nearly identical (Fig. 6-14d). Though the forms of both the Kondo and activation temperature

dependence scale the conductance over a wide range of V_g, the values of T_K (and not T_A) correspond well to the source-drain bias features of the ZBA and the transconductance, as discussed next.

Continuing to explore the analogy to the Kondo effect in quantum dots, a characteristic feature of the low-temperature Kondo regime ($T < T_K$) is that the width of the ZBA is set by T_K, rather than other (larger) level-broadening energy scales (i.e. Γ) [170]. We examine the ZBA of the point contact for analogous behavior by plotting the width of the zero-bias conductance peak as a function of gate voltage over the range $0 < g < 1$ (in units of $2e^2/h$). Figure 6-15a shows that the width of the ZBA is roughly constant for $g < 0.7$, ($V_g < \sim 490$ mV). At $g \sim 0.7$, the ZBA first narrows significantly, by $\sim 35\%$, and then broadens as g approaches $2e^2/h$. Compared to T_K, we see that the ZBA peak width is very close to $2kT_K/e$ for $g > 0.7$ where values of T_K can be extracted. Relations between the ZBA width and the values of kT_K/e with a similar prefactor of ~ 2 have been observed previously in experiments on quantum dots [170] and nanotubes [30].

A similar correspondence between the Kondo temperature and the applied bias voltage is seen in the $B = 0$ transconductance plot of Fig. 6-15b (same data as Fig. 6-6a). The first integer plateau, half-plateaus at 1/2 and 3/2 and the anomalous plateaus at 0.8 (all in units of $2e^2/h$) are labeled. Superimposed on the color plot are the Kondo temperatures (white crosses), each plotted at an equivalent "Kondo bias voltage" $V^K_{sd} = kT_K/e$ and at the V_g where that T_K was measured. The alignment of these points with the extra transitions suggest that an applied bias exceeding V^K_{sd} destroys the correlated, Kondo-like, state causing the conductance to drop to the high-bias value of the extra plateau, ~ 0.8 ($2e^2/h$). For comparison, the activation temperatures are also included in the color plot (white diamonds) at equivalent bias voltages, kT_A/e. In contrast to Ref. [190], we find that the values of T_K—not T_A—trace out the extra transition lines in the transconductance.

Another feature we have investigated based on the analogy to the Kondo effect in dots is the splitting of the zero-bias peak by twice the Zeeman energy upon application of an in-plane magnetic field [30, 53, 59]. In the QPC, we find a somewhat more complicated evolution than in dots, as seen in Fig. 6-16a. In particular, the ZBA does not split uniformly over the full range $0 < g < 2e^2/h$. At intermediate conductances—in the general vicinity of the 0.7 feature—a splitting is seen that is reasonably consistent with $2g^*\mu_B B$, (i.e. the splitting is roughly linear in field up to ~ 3 T with a g-factor that is ~ 1.5 times the bulk GaAs g-factor). However, at both higher and lower conductances, the peak is not split by an in-plane field, but merely collapses. The surface plots in Figs. 6-16b-d provide a broader overview of the effect of an in-plane magnetic field. The surfaces represent the nonlinear conductance as a function of V_{sd} and V_g at $B = 0$, 3, and 6.5 T. The ZBA is seen as the spine running down the $B = 0$ surface centered around $V_{sd} = 0$. At $B = 3$ T, a small crevice has developed in the intermediate conductance range. Finally, at $B = 6.5$ T, the spin-resolved plateau at $0.5(2e^2/h)$ is well-formed and the ZBA has disappeared except at the highest conductances.
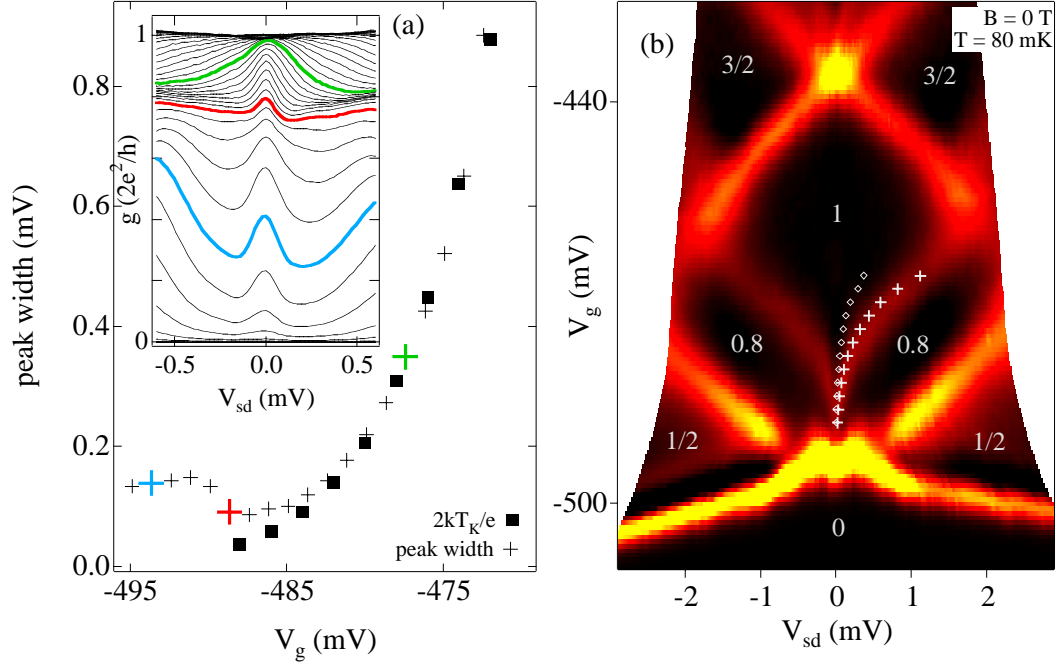
Figure 6-15. Correspondence between T_K and ZBA width. **(a)** Widths of the zero-bias peak (cross symbols), defined as the full-width at half-max (from the local minimum on the left side of the peak), for gate voltages corresponding to $0 < g < 2e^2/h$. Peak width is roughly constant up to $g \sim 0.7(2e^2/h)$ ($V_g \sim -490$ mV) at which point it decreases significantly then increases as g approaches $2e^2/h$. Also plotted are the values of $2kT_K/e$ (squares) from the scaling fits (Fig. 6-14) over the range of gate voltage where T_K could be extracted, $0.7(2e^2/h) < g < 2e^2/h$. The ZBA peak matches $2kT_K/e$ well in this region. Three colored crosses indicate peak widths for the corresponding colored traces in the inset. Inset: Nonlinear transport data from Fig. 6-5a showing the ZBA in $g(V_{sd})$ at several gate voltages. **(b)** The transconductance colorscale at $B = 0$ (same data as Fig. 6-6a) with the plateau at $2e^2/h$, high-bias half-plateaus at 1/2 and 3/2, and the extra plateaus associated with the 0.7 structure that rise to $0.8(2e^2/h)$ at high bias labeled (in units of $2e^2/h$). The Kondo temperatures from the scaling fits to Eq. 6.2, in units of voltage, kT_K/e (white crosses), are superimposed on the colorscale plot at several values of V_g with no adjustment. Note that the position of the transition from the extra plateau to the $2e^2/h$ plateau agrees will with the Kondo temperature. For comparison, the activation temperatures from fits to Eq. 6.3, in units of voltage, kT_A/e (white diamonds), are also shown and do not trace out the extra transition line.
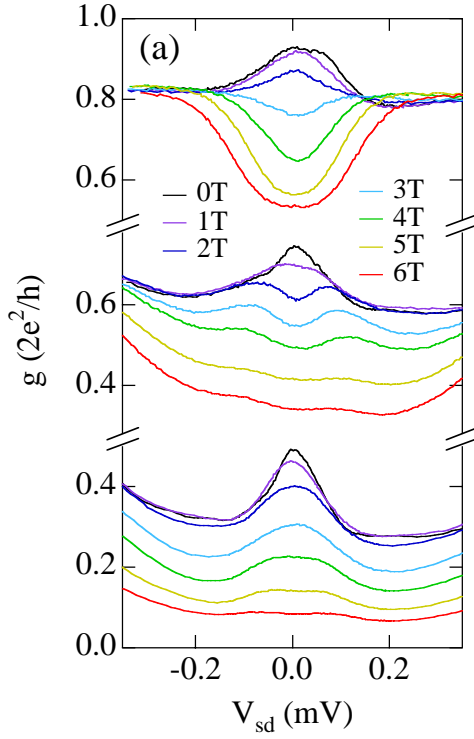
Figure 6-16. Evolution of the ZBA in parallel field. **(a)** Conductance $g(V_{sd})$ shows the zero-bias anomaly in parallel magnetic fields B = 0 to 6 T in 1 T steps at three gate voltages corresponding to high, intermediate and low conductance. In all cases, the ZBA disappears with increasing B. For high conductance, a wide zero-bias minimum develops at high field, corresponding to the formation of the spin resolved plateau at e^2/h. For intermediate conductance, the ZBA peak splits as well as diminishes. At low conductance, the ZBA is suppressed without splitting or forming a minimum up to B = 6 T. **(b-d)** Surface plots of the conductance below the $2e^2/h$ plateau as a function of V_{sd} and V_g for **(b)** B = 0 T, **(c)** 3 T, and **(d)** 6.5 T. The ZBA is the spine running down the surface at $V_{sd} = 0$ at B = 0. A small crevice forms at intermediate conductances at 3 T corresponding to the split ZBA seen in (a). By B = 6.5 T, the spin-resolved plateau at e^2/h is well formed. The data in this figure were measured in zero perpendicular magnetic field.
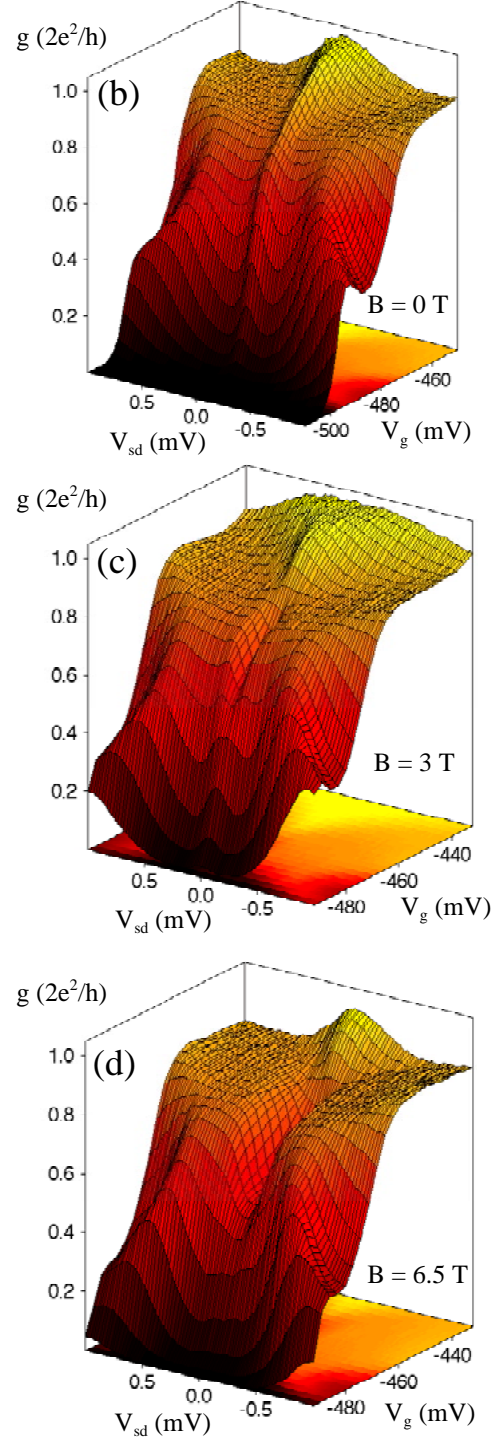
The absence of splitting in the ZBA peak at higher conductances is reasonable given the high T_K in this region. That is, for $T_K > 2g^*\mu_B B$ no splitting is expected within a conventional Kondo interpretation. The absence of splitting for low conductance (bottom traces of Fig. 6-16a) may be evidence that the ZBA in this region does not have a Kondo like origin. The possibility that different mechanisms lead to a ZBA in low and high conductance regions is supported by the nonmonotonic width of the ZBA as a function of the gate voltage (Fig. 6-15a). It is worth recalling the temperature dependence of the ZBA height (Fig. 6-11a) at this point. The complete suppression of the ZBA with increasing T should occur at $\sim T_K$ for a given gate voltage. We observe that the ZBA at high conductance, where T_K is relatively high, is suppressed more quickly with T than at low conductance. Though we cannot extract a value for T_K at $g < \sim 0.7(2e^2/h)$, extrapolating T_K to lower conductance yields a smaller T_K, predicting faster suppression of the ZBA with T. That we see the opposite may imply something about T_K—perhaps there is a change in the monotonic dependence we have measured—or that a different mechanism is responsible for transport behavior at low conductance.

 It is important to emphasize that the Kondo effect provides an explanation for two major mysteries associated with the extra conductance plateau in a QPC, namely (i) the apparent spontaneous spin splitting and (ii) the noninteger value, 0.7, for the "spin-split" plateau. In the Kondo effect, there is a splitting between spin bands due to the Coulomb interaction between electrons. However, this splitting is purely dynamic and does not lead to a static spin polarization. The origin of the conductance value $0.7(2e^2/h)$ is apparent from the scaling plot (Fig.6-14b)—the true high-temperature limit of the plateau is $0.5(2e^2/h)$, consistent with an ordinary spin-split plateau. However, the Kondo contribution to the conductance decays slowly with increasing temperature, always leaving a small residual enhancement of the conductance above 0.5. Moreover, the recovery of the conductance to the full unitary limit with decreasing temperature is a necessary feature of the Kondo effect.

6.7   Other Devices

In addition to the in-depth measurements presented so far, it is useful to see the range of behavior exhibited by various QPC devices. In Fig. 6-17a-d, the quantized plateaus in the linear response conductance at parallel magnetic field B = 0 are shown for QPCs 1 to 4. For these measurements, the two gates which form a QPC are biased independently with the "finger" gate voltage, V_{fg}, held constant while the voltage on the small single gate, V_g, is swept. QPC 1 (Fig. 6-17a) shows significant resonances for some V_{fg} at perpendicular magnetic field $B_{perp} = 0$. A small perpendicular field $B_{perp} = 25$ mT (or temperature T = 300 mK, not shown) significantly suppresses these resonances. QPC 2 also shows resonances at less negative V_{fg} which are reduced by a finite perpendicular field (Fig. 6-17b,d). QPC 3 and QPC 4 are, overall, cleaner than the previous point contacts, with relatively consistent looking plateaus for the entire range of V_{fg} (Fig.

6-17c,d). The affect of a small perpendicular magnetic field on QPC 3 is shown in Fig. 6-17f, where both gate voltages are swept together.

The low temperature nonlinear conductance data for QPC 3 (Fig. 6-18) at parallel magnetic field B = 0 and B = 8 T are nearly identical to that of QPC 4 (Fig. 6-5), including the narrow ZBA for $0 < g < 2e^2/h$ and the extra high-bias plateau at $0.8(2e^2/h)$ at B = 0. In QPC 2, the nonlinear conductance at T = 80 mK and B = 0 shows additional structure as a function of V_{sd} besides the zero-bias peak. These features may be related to resonances in the linear response conductance of QPC 2, though they have not been investigated further. Even with the extra features, the nonlinear data of QPC 2 are qualitatively the same as discussed previously for QPC 4: a ZBA and an extra high-bias plateau appear at B = 0. In the intermediate conductance regime, the ZBA seems to split with a parallel magnetic field of 3 T. By B = 6.5 T, the spin-resolved plateau at $0.5(2e^2/h)$ is starting to form.

6.8   Conclusions

We have presented measurements of the temperature, parallel magnetic field, and dc source-drain bias voltage dependence of several quantum point contacts, with a detailed look at the 0.7 structure and the zero-bias anomaly in both linear and nonlinear conductance. Additionally, we discussed three non-equivalent methods for measuring the effective g-factor, and compared two different forms for the temperature dependence of the conductance. Overall, we find a number of similarities between the low-temperature behavior of QPCs and the Kondo effect in quantum dots. These include (i) a narrow zero-bias conductance peak which forms at low temperature, (ii) the scaling of conductance using the Kondo temperature extracted from a modified form of the universal Kondo conductance in dots, (iii) correspondence between the Kondo scaling factor and the width of the zero-bias peak, and (iv) splitting of the zero-bias peak with a parallel magnetic field. We note that the Kondo effect helps explain the apparent spin-splitting in the QPC at zero-magnetic field: the spin bands are split *dynamically* by the Coulomb charging energy but there is no *static* ferromagnetic polarization. Though no microscopic theory yet exists for the Kondo effect in an *open* QPC system, the experimental data strongly suggest a many-body correlated state analogous to the Kondo effect in quantum dots.

Figure 6-17. Quantized plateaus of other QPCs. **(a-e)** Linear response ($V_{sd} \sim 0$) conductance, g, versus the gate voltage V_g on one of the two surface gates forming the QPC constriction. The gate voltage on the large "finger gate", V_{fg}, is held constant at different values. Data is shown for perpendicular magnetic fields of 0 and 25 mT as indicated. **(a)** QPC 1 has significant resonances in the quantized plateaus. **(b,e)** QPC 2 show resonances for some values of V_{fg} but not for others. A small perpendicular field suppresses the resonances significantly. **(c,d,f)** QPC 3 and QPC 4 are overall much cleaner than devices 1 and 2.
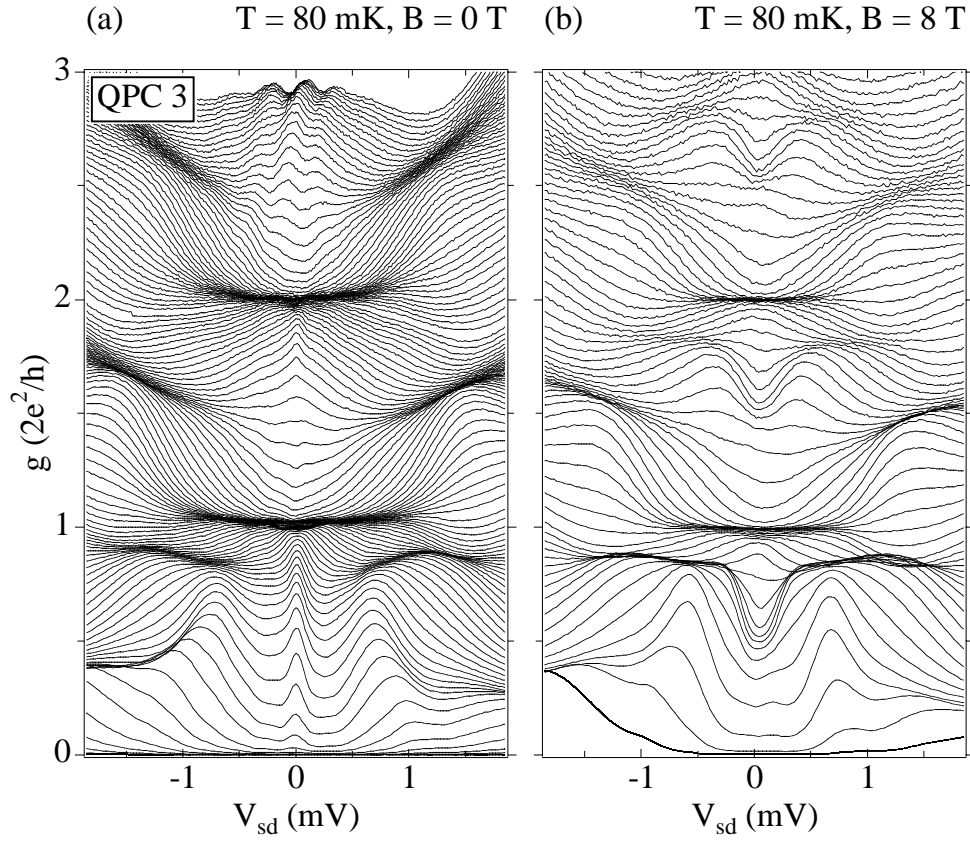
Figure 6-18. Nonlinear transport data for QPC 3. **(a,b)** Nonlinear conductance $g(V_{sd})$ at T = 80 mK and parallel fields **(a)** B = 0 and **(b)** B = 8 T for different gate voltages in steps of 1.24 mV and 2.64 mV, respectively. The data are qualitatively the same as for QPC 4 (shown in Fig. 6-5a,c) including a zero-bias conductance peak for $g < 2e^2/h$ and the extra high-bias plateaus at $\sim 0.8(2e^2/h)$ at B = 0. A perpendicular field of 25 mT was applied during these measurements.
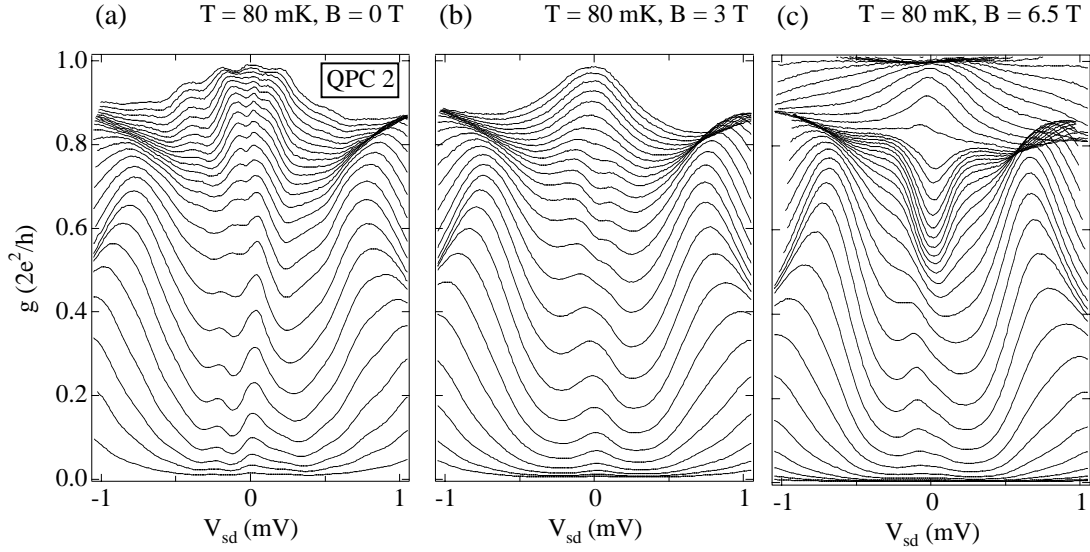
Figure 6-19. Nonlinear transport data for QPC 2. **(a)** Nonlinear conductance $g(V_{sd})$ at T = 80 mK and B = 0 for gate voltages in steps of 3 mV. There is a conductance peak around $V_{sd} \sim 0$ but also several additional peaks at finite V_{sd}. The extra high-bias plateaus at $\sim 0.8(2e^2/h)$ are very similar to those found in the other devices. **(b)** At B = 3 T, the extra resonant features have died out, and the zero-bias peak appears split for an intermediate conductance regime—similar to the behavior of QPC 4. **(c)** By 6.5 T (with 4mV steps in V_g), the spin-resolved plateau at e^2/h is becoming well-formed for a small range of V_g. An asymmetric conductance peak is observed at $V_{sd} \sim$ -0.1 mV for $g < 0.5$ ($2e^2/h$) in this data. A perpendicular field of 25 mT was applied during all these measurements, and the finger gate was held constant at V_{fg} = -600 mV.

Chapter 7

Conclusion

7.1   Summary

This thesis presents a series of experiments which show significant contributions of both electron-electron interactions and quantum coherence to transport through mesoscopic systems. Devices fabricated in a two-dimensional electron gas (2DEG) are well suited to investigate these effects because the electron mean free path is long, leading to long coherence times at low temperatures, and modern lithographic techniques can produce small structures where the quantized nature of electron charge is important. Quantum dots (QDs), which confine electrons to an effective zero-dimensional box, and quantum point contacts (QPCs), which constrict electrons through a narrow one-dimensional channel, are the two types of devices considered in this work.

In the first experiment (Chapter 3), transport measurements are presented for quantum dots in the strong-tunneling Coulomb blockade (CB) regime. Coherent electron transport through the device shows fluctuations of the conductance, evidence of quantum interference, that is sensitive to charging effects in the CB valleys where elastic cotunneling is the dominant transport mechanism. The effects of interactions can be accounted for using a single parameter—the charging energy—and are measured using the magnetic field correlation length of conductance fluctuations in CB valleys compared to CB peaks.

The second experiment (Chapter 4) shows Coulomb blockade in a quantum dot with one fully-transmitting lead and one weak-tunneling lead. In this system, the CB appears only due to coherent interference of backscattered trajectories, with increased strength at zero magnetic field where time-

reversed backscattered pairs interfere constructively. This is a remarkable illustration of the interplay between interactions and coherence: the predominant effect of interactions, namely the Coulomb blockade, is turned on and off by quantum interference.

The third and fourth experiments described in this thesis both investigate the Kondo effect, a classic many-body problem where the effects of coherence and interactions (now including spin) cannot be trivially separated. Quantum dots are well suited to study the Kondo effect because a number of relevant parameters can be varied using quantum dots but cannot be changed in the traditional bulk metal systems. We present the second observation of the Kondo effect in dots including the first demonstration of a gate-voltage-controlled Kondo temperature (Chapter 5).

The last experiment introduces new data on quantum point contacts which show a number of remarkable similarities to the Kondo effect in quantum dots (Chapter 6). Linear and non-linear transport measurements of the "0.7 structure", a robust extra plateau or shoulder-like feature in the lowest mode of a QPC, show evidence for a lifted spin-degeneracy. The formation of a zero-bias peak at low temperature, the collapse of the temperature-dependent conductance to a single curve when scaled by one parameter (the Kondo temperature), and the correspondence of this temperature scaling parameter to the source-drain bias voltage width of the zero-bias peak strongly suggest that a Kondo-like correlated many-electron state forms in the QPC at low temperatures. This idea was somewhat surprising because the QPC is an open system while the Kondo effect typically requires a localized spin state. A Kondo-like QPC state remains, at this point, unexplained theoretically.

7.2   Future Directions

The investigation of mesoscopic systems with significant coherence, charging, and spin effects is far from over. A fundamental desire to understand the physics which governs small (but not too small) systems has brought us a remarkable way over the past decades. Combined with the recent fervor that quantum computing has created, the outlook for research in the mesoscopic arena seems secure for many years.

One direction of mesoscopic physics that I feel is worth noting in particular is that of integrated-multi-device systems. Coupled lateral quantum dots, where a two-level charge state develops, have been measured by many groups already [163, 215-220]. A system of coupled vertical dots, which have the advantage of precisely controlling the electron number all the way down to zero, seems right around the corner [221, 222]. Aharonov-Bohm rings with devices imbedded in the arms have proven extremely valuable tools to investigate the phase relationship of transport through devices [223-225]. Further application of such "two-path" interferometers may help determine the potential of both QDs and QPCs as electron spin filters. Systems of QPCs in series or a QD and a QPC in series are also under study to gauge the effectiveness of either device as a filter of electron spin [226] (described briefly in Appendix A).

Finally, the integration of many devices into actual circuit systems is at the heart of many proposals to use semiconductor solid state devices as the qubits of a quantum computer [34, 227].

The timescales of these goals range from the next month to the next century. Creating isolated systems with very long coherence times (compared to today's standards) and mediating the interactions between devices should provide sufficient challenge for the next several generations of Ph.D. students. The work presented in this thesis is just the beginning of what will likely be many decades of experiments involving small electronic systems where coherence, charging and spin play important and intertwined roles.

Appendix A

Switching Ferromagnetic Point Contacts

A.1 Motivation & History

Two years of my Ph.D. research were spent trying to make an electron spin filter out of quantum point contact (QPC) devices. Though not (yet) successful in this ultimate goal, for reasons that will be described below, we were able to show a "proof of concept" of a switching ferromagnetic gate implementation. This appendix will briefly describe the motivation and history behind this experimental attempt, the approach we were using to create a spin filter, measurements of practice samples, and a short discussion of the problems encountered.

The goal of this research was to create a filter for electron spin that could be operated without a large external magnetic field. This goal was motivated, in part, by quantum computing proposals that suggest using spin in quantum dot systems as the fundamental qubit [34]. A spin filter would be useful, for instance, to set known initial states and read out final states. A QPC which preferentially transmits spin up or spin down electrons operates as a spin filter and could easily be integrated into a system of quantum dot qubits. A spin filter can turn a difficult measurement of electron spin into a much easier measurement of electron charge—measuring whether an electron passed through the filter gives a measure of its spin.

It is well known that a QPC will act as a spin filter in a large external magnetic field if the gate voltages are set so that transmission occurs only through the first spin-resolved mode. The species of transmitted spins (up or down) will depend on the direction of the external field. Flipping the filtered spin requires changing the direction of the external field. Considering the typical fields involved (several tesla) and the high-inductance superconducting magnets employed, the timescale to flip the spin filter would be,

at best, several minutes. Additionally, with a large external magnetic field, every spin filter in a system would transmit the same spin—they could not be operated independently.

We sought a spin filter implementation that would allow independent control of multiple filters. Our idea consisted of two parts. First, we hoped to use the 0.7 structure of a QPC. At the time, the experimental data of Ref. [184, 187] reported an enhanced g-factor at the lowest spin-degenerate mode. Additionally, there was speculation the 0.7 structure itself was a spontaneous spin polarization at zero magnetic field. Our spin filter proposal involved setting the gate voltages of a QPC to the 0.7 structure, taking advantage of the spontaneous polarization or enhanced g-factor to more easily create a spin polarized current through the QPC. The second feature of our proposal was the use of ferromagnetic material as the gates of the QPC. The field produced by the ferromagnetic gates would set the axis of the spin polarization for the filter. By switching the magnetization of the ferromagnetic material, we hoped to easily flip the filtered spin. Additionally, because each QPC spin filter would have its own ferromagnetic gates, each could be operated independently.

To test our proposed filters, we designed devices with two QPCs in series to perform a focusing experiment as in Ref. [228]. Because each QPC filter could be independently controlled, we could measure the current transmitted through both QPC spin filters aligned parallel and antiparallel to each other. A larger transmission for filters aligned together than for anti-aligned filters would indicate successful filter mechanism.

A.2   Design & Fabrication

The first generation spin filter devices are shown in Fig. A-1. The design consists of two QPCs in series (to test the filters, as mentioned above). The QPC split-gates (false-colored pink) are made of permalloy (NiFe). We chose permalloy because it is a soft ferromagnet, meaning it has a small coercive field (of order 1 mT) so the polarization direction should be easy to flip. The gates are long and thin to take advantage of shape anisotropy and to determine the easy-axis of polarization. To flip the ferromagnets we run a small current through the wide gold wires (false-colored yellow) running over top the QPC gates. The small magnetic field created by the current in the wire will polarize the ferromagnet beneath, the polarization direction (left/right) set by the current direction (up/down) according to the right-hand rule. The wires are designed with three terminals so the current above each ferromagnetic gate can be controlled independently. A square of silicon oxide (Si0, false-colored blue) insulates the QPC gate metal from the current-carrying wires.

Fabrication of the devices shown in Fig. A-1 requires seven major processing steps. Details of the fabrication steps are given in Appendix B. First, the two-dimensional electron gas (2DEG) for each device must be electrically isolated from the others by etching separate mesas (photolithography and wet-etching).
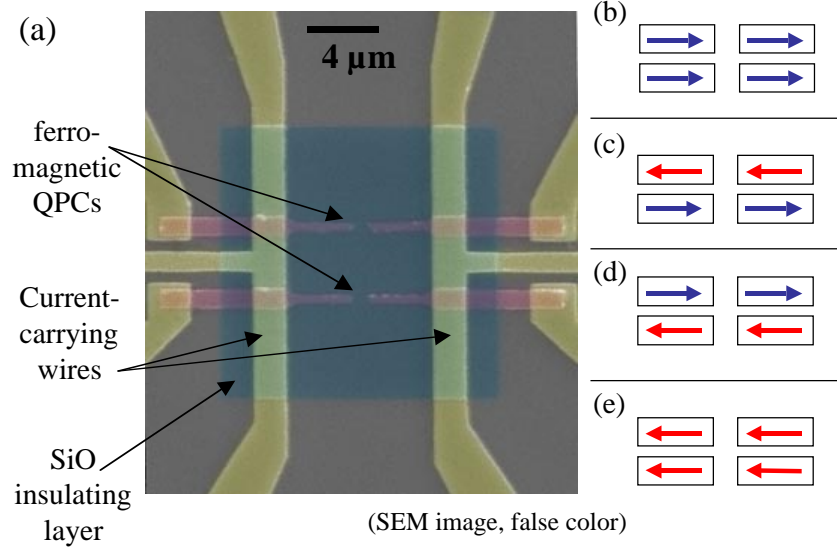
Figure A-1. Spin filter device, SEM colorized image. **(a)** False-color SEM image shows the first generation spin filter test devices comprised of two QPCs in series. The QPCs are made with ferromagnetic gate material (colored pink) whose polarizations can be set independently with the current-carrying gold wires above. The arrows on the right **(b-e)** show the aligned (b and e) and anti-aligned (c and d) polarizations for the series QPCs. A square of SiO insulates the gate metal of the QPCs from the current-carrying wires above.

Second, the ohmic contacts to the 2DEG are deposited and annealed (photolithography, metal deposition, anneal). Third, the small ferromagnetic gates are defined using ebeam lithography with a permalloy evaporation. Fourth, the larger gold patterns which extend the permalloy gates out towards the edge of the mesa are made (ebeam lithography and Cr/Au evaporation). Fifth, the insulating square of SiO is patterned (ebeam lithography and SiO evaporation). Sixth, the current-carrying wires are made (ebeam lithography and Cr/Au evaporation). Finally, the bondpads and connecting metal are deposited (optical lithography and Cr/Au evaporation). In the best of circumstances (with each step working the first time), this process takes at least two weeks to complete. Unfortunately, "the best of circumstances" seemed few and far between.

A.3   Testing

The first step in testing the spin filter devices was to determine the maximum current through the current-carrying wires. At 4.2 K in a liquid helium dunker, we measured the voltage across two terminals of a wire with increasing current bias (the third terminal is floating). We found the maximum current possible

(before blowing up the wires)[18] was 150 - 170 mA. Modeling the wires with the numerical magnetic field simulator "Biot-Savart" (by Meritt Reynolds, © Reynolds Software, 1993) and using 120 mA, the maximum field along the long axis of the QPC gates is ~ 30 mT. The field drops off quickly outside the region of the wire. Given the low coercivity of permalloy (a few mT), we expect this current should be sufficient to set the polarization of the QPC ferromagnetic gates. In the z-direction (perpendicular to the surface), there is also an appreciable field of ~ 30 mT with 120 mA of current, but due to the shape anisotropy of the ferromagnetic gates, we did not expect this field to significantly affect the polarization.

The second test performed on the spin filter devices was a measurement of the polarized ferromagnetic gates to ascertain that we could, in fact, flip the polarizations independently using the current-carrying wires. Several attempts to detect the magnetic polarization using magnetic force microscopy (MFM) were unsuccessful, likely due to a rough surface left from the metal lift-off processes. The next efforts, using a scanning Hall probe system led to the successful "proof of concept" of the ferromagnetic gates. The scanning Hall probe measurements were done in collaboration with Janice Wynn in Kathryn Moler's lab at Stanford. The system consists of a variable temperature (4.2 K to room temperature) scanning probe with a small (2 μm x 2 μm) Hall bar mounted to the piezo scanners. The piezo scanner has a range of motion of ~ 70 μm x 70 μm at 4.2 K and ~ 120 μm x 120 μm at 80 K (where our measurements were taken). The sample to be scanned is mounted opposite the Hall probe. The Hall probe is operated in a four-wire current bias measurement set-up with a bias of 11.8 μA at 4.2 K.[19] The voltage across the Hall probe, given by $V_H = (B_z I)/(n_e e)$, where n_e is the electron sheet density in the 2DEG, is a direct measure of the average perpendicular magnetic field B_z over the area of the Hall bar. A description of scanning Hall probe systems can be found in Ref. [229].

For our spin filter devices, the magnetic field measured is due to the ferromagnetic gates and/or current flow through the current-carrying wires. Figure A-2a shows the image from the Hall probe at 80 K with a (dc) current of 10 mA flowing from the top terminal to the middle terminal of the right hand wire (current direction indicated by orange arrows). Similarly, Fig. A-2b shows the Hall probe image with 10 mA current running from the bottom to the middle terminal of the right hand wire. The image in Fig. A-2c was taken with 10 mA of current running from the top to bottom terminals. The grayscale of the Hall probe images, shown on the right, indicates the magnetic field detected in the z-direction (out of the sample plane). The current carrying wires create a magnetic field around the wire according to the right-hand-rule; the field out of the page (white) is defined positive and into the page (black) defined negative. A schematic of the wire/device orientation is shown in Fig. A-2e. In Fig. A-2d, the measured field B_z is shown (in green) as a function of position along the short green line in the middle of Fig. A-2c. The calculated field in the

---

[18] Seldom do you get the chance to intentionally blow up devices—it's quite a treat.

[19] The bias current is probably slightly larger at 80 K, where our measurements were taken, but had not been calibrated.
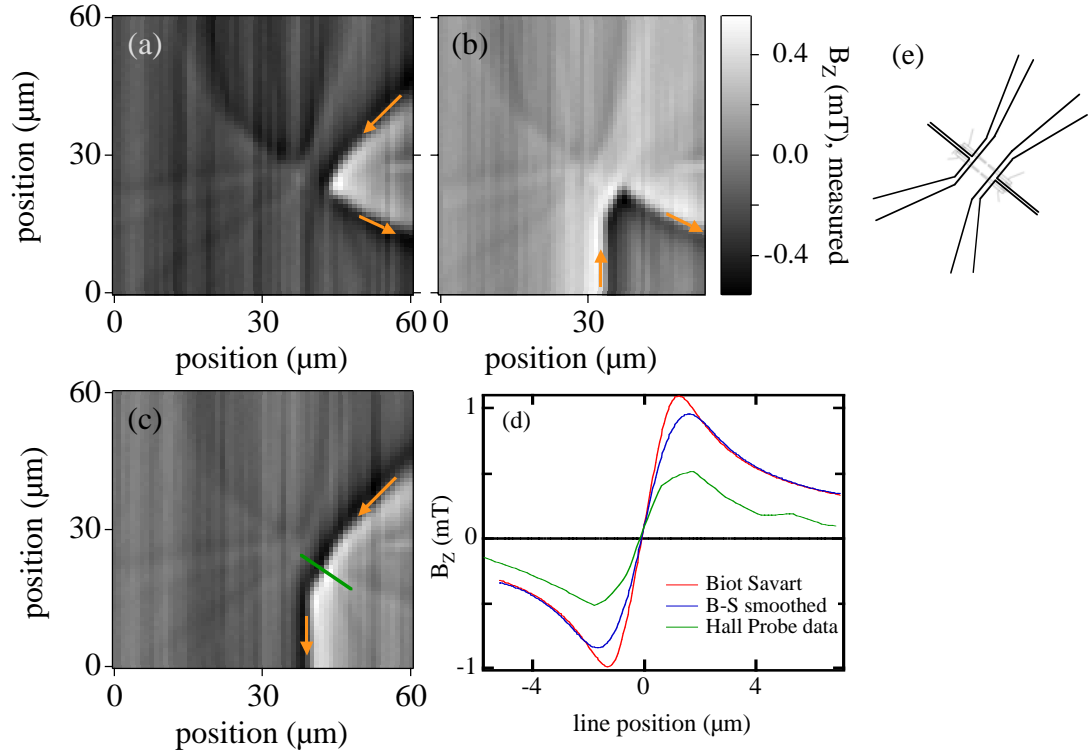
Figure A-2. Hall probe images of current-carrying wire. **(a-c)** Scanning Hall probe images (taken in collaboration with Janice Wynn and Kathryn Moler) of a 10 mA dc current flowing through the right hand wire of a spin filter device. The orange arrows indicate the direction of current flow in each case. The grayscale, shown to the right of (b), measures the magnetic field (averaged over the are of the Hall bar) in the z-direction (out of the page, defined as positive, is white). Current flow through the wire produces fields according to the right-hand-rule, so the field is positive/negative on opposite sides of the wire. **(d)** The measured B_z field taken from the green line shown in (c) is shown in green. The calculated field from the Biot-Savart modeling program with 10 mA of current through the given wire geometry is shown in red. The calculated field after being smoothed over 2 μm (the size of the Hall probe) is shown in blue. **(e)** Line drawing of the shape of the spin filter device in the orientation of the Hall probe images. The current-carrying wires with three terminals are the dark sets of lines.

z-direction from the same position in the Biot-Savart model is shown in red, and in blue after being smoothed over 2 μm (the size of the Hall probe). The calculated field overestimates the measured field by a factor of ~ 2.

The Hall probe images of the current-carrying wire served as confirmation that the Hall probe system was working. We next performed a series of images without any current flowing through the wires in order to detect the ferromagnetic QPC gates. Between consecutive images we applied a current through
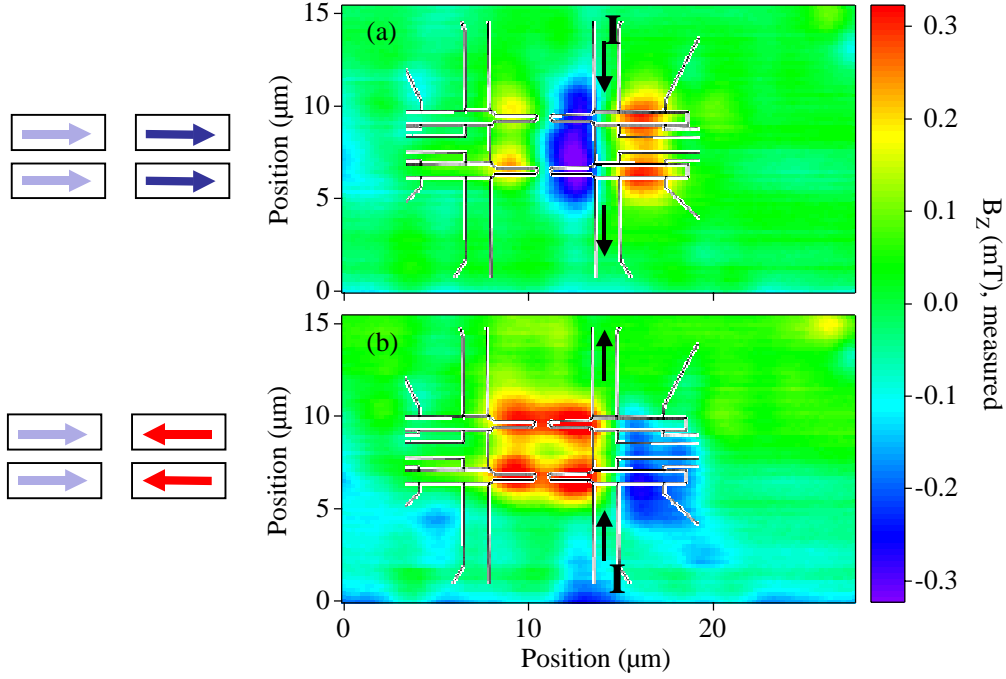
Figure A-3. Hall probe image of aligned ferromagnets. The scanning hall probe image shows the B_z field of the ferromagnetic QPC gates when no current is flowing through the wire above. Each image was taken after a current I = 100 mA was applied through the wire (in the direction indicated) and then turned off. The polarization of each gate is shown with the arrows on the left. By reversing the applied current direction, the polarization of the ferromagnets is successfully flipped from right (a) to left (b).

the wires to change the polarization of the ferromagnets. Figure A-3a,b shows two consecutive images taken (a) after a current I = 100 mA was applied from the top to the bottom wire terminal polarizing both of the right hand QPC gates to the right, and (b) after I = 100 mA was applied from the bottom to the top terminal, polarizing both gates to the left. It should be emphasized that no current was flowing through the wire during the scan which produced the images in Fig. A-3 or Fig. A-4. Also note that we applied current only through the right hand wire of the device, so only the ferromagnetic gates on the right side of each QPC were flipped; gates on the left of both QPCs remained unchanged. Subsequent tests on this device showed that a current of 40 mA was required to fully flip the polarization direction of the ferromagnetic gates.[20]

---

[20] A current of 20 mA seemed sufficient to flip the polarization, but the field detected by the Hall probe after the flip was not at full strength (compared to using 40 mA).
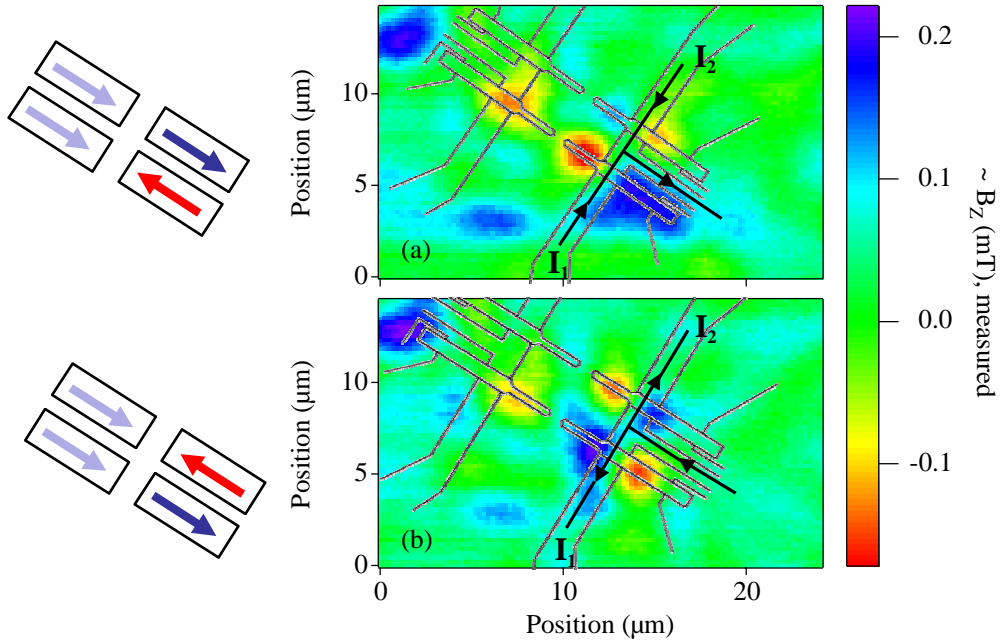
Figure A-4. Hall probe images of anti-aligned ferromagnets. Scanning Hall probe images taken after sequential currents of $I_1 = 80$ mA then $I_2 = 40$ mA were applied through the current-carrying wire in the directions indicated. These directions of current flow leave the ferromagnets beneath polarized in opposite directions, as seen in the alternating colored regions beneath the gates (and in the arrow diagrams on the left).

The final test of the ferromagnetic gates involved polarizing the neighboring gates opposite each other. The results are shown in Fig. A-4a,b. In each case, a current $I_1 = 80$ mA was applied first, followed by a current $I_2 = 40$ mA in the directions indicated. We found this system worked well as one of the ferromagnetic gates seemed to flip more easily (less current required) than the other. The Hall probe images in Fig. A-4a,b show the neighboring ferromagnetic gates are indeed polarized in opposite directions. The schematic arrows on the left shown the interpreted polarization.

The Hall probe measurements of the ferromagnetic gates gave an excellent and essential "proof of concept" for our switching spin filter design. We showed that the polarization direction of each ferromagnetic gate could be set by a current passing through an overlying wire. In addition, we showed that each gate could be independently controlled. However, we also noticed that the ferromagnetic gates did not appear to be single domains. This is visible in the images in Figs. A-3 and A-4 where the overlaid diagram of the wire and QPCs shows the tips of the QPC gates much closer together than the colored regions which indicate the fields from the polarized metal. We expect that the magnetic field in the z-direction is detected where the dominant left/right domain ends. To maximize the field in the region of the QPC constriction

where electrons flow through, we needed to ensure that the ferromagnetic gates were polarized to their tips. Subsequent generations of devices addressed this issue by making the ferromagnetic gates diamond shaped,[21] and by moving the current-carrying wire closer to the constriction to ensure polarization of the tips.

Though the flipping ferromagnetic gates boded well for this spin filter implementation, we were not able to successfully measure electron transport through the system despite several generations of devices and attempts. A number of problems and many unfortunate coincidences contributed to this lack of success. On the bright side, the measurements never indicated that this implementation failed—we simply were not able to make a reliable set of transport measurements. Before briefly mentioning some of the problems we encountered, it is worth remembering one feature of this QPC spin filter implementation which might prove an obstacle. As mentioned in the beginning of this section, we hoped to use the enhanced g-factor or spontaneous polarization possibly associated with the 0.7 structure in order to produce a spin filter with preferential transmission of one spin species. Given the discussion in Chapter 6, where we hypothesize that the 0.7 structure results from a *dynamic* lifting of degeneracy between the spin bands due to Coulomb interactions, the suggestion to use the 0.7 structure to produce a *static* preferential spin transmission seems unlikely to succeed. However, without a full theoretical explanation of the 0.7 structure, we still don't know whether there is a spin effect which could be used to help implement a spin filter. There may be other ways around this obstacle as well, for instance by creating magnetic fields with ferromagnetic gates or electromagnetic wires that are large enough to create preferential spin transmission through the lowest mode of a QPC themselves.

Finally, I want to briefly summarize some of the (known) difficulties that occurred in our attempted measurements of the spin filter systems. One problem resulted from the new Pt-Au-Ge ohmic contacts being used on the devices. These devices were among our first attempts to switch from Ni-Au-Ge ohmic material to Pt-Au-Ge and required different evaporation methods as well as new recipe development. Overall, the Pt-Au-Ge ohmics seemed to give significantly lower yield and less consistent ohmic behavior than we were accustomed to with Ni-Au-Ge. This rendered a good number of devices unmeasurable (though often only after testing them in the ^{3}He cryostat). The inclusion of permalloy, a new material for our lab, also led to numerous difficulties during the course of this research. It is possible (though difficult) to thermally evaporate permalloy and even more difficult (though possible) to get the permalloy to adhere to the GaAs surface. At different points I tried several techniques including a Cr sticking layer, evaporating without cooling the sample, and evaporating while cooling the sample with liquid nitrogen. In the end, it

---

[21] The energy required for a domain wall depends on its length. If a domain wall can become shorter by moving slightly, it will do so to save energy. Thus, domain walls shouldn't form in a diamond-shaped gate because a lower energy state is always available by moving the domain wall towards the tips until the entire gate is single domain.

seemed that the permalloy would adhere to the GaAs (without a sticking layer) most consistently when evaporated without cooling. I also experimented with capping the permalloy with gold to prevent oxidation. We believed oxidation of the permalloy might be a problem after the many unsuccessful attempts to image the material with the MFM. In retrospect, I don't think the failure of the MFM to image anything clearly magnetic was due to the absence of magnetic material on the sample, but instead due to surface roughness or general inexperience with the MFM. We also hypothesized that oxidation of the permalloy might be a problem because the QPCs made of permalloy gates consistently behaved worse than QPCs on the same chip made of standard Cr/Au gates. The permalloy QPCs never showed quantized plateaus and often would not pinch off the conductance to g = 0 even with up to 6 V applied to the gates. This behavior suggested that the effective electrical gates were much farther apart than the lithographic metal appeared, perhaps because the permalloy had completely oxidized? To avoid worsening a potential oxidation problem, we took to testing the spin filter devices in either a 1.2 K dunk stick with a vacuum can, or the ^{3}He system (also with a vacuum can) so the samples would not be exposed to water vapor when warmed. This significantly extended the time required to test individual devices. We have not determined why the permalloy QPCs did not work as well as those made of Cr/Au. The final significant obstacle encountered during the efforts to measure the spin filter devices was an unrelated, but just as frustrating, problem with the cryostat wiring. Before, during, or after a number of measurements, I discovered that one of more of the wires connecting the sample at low temperature to the outside of the cryostat were faulty. In some cases, the wires would only become disconnected (or very high resistance) at low temperature, making it extremely difficult to find and fix the problems.

The unfortunate series of wiring problems, on top of questionable ohmic contacts and unusual behavior of the ferromagnetic QPCs, led to two years of fabrication and measurements of spin filter devices without any conclusive results. I believe the idea of a QPC spin filter is still a valuable effort, and possibly the inclusion of ferromagnetic gates a viable candidate for successful implementation. However, the difficulty of integrating new materials onto devices should not be underestimated, and the likelihood of success given the expected magnetic fields and the implementation scheme should be carefully considered before embarking on many years of further work.

Appendix B

Device Fabrication

B.1 Overview

The devices presented this thesis, with the exception of the dots measured in Chapter 5, were fabricated in the cleanrooms of Ginzton Laboratories and the Center for Integrated Systems (CIS) at Stanford University. The fabrication processes used in our group are continually evolving as new equipment becomes available, new locations require certain changes, and other properties (such as resist thickness and wire-bond adhesion) slowly change over time. In this appendix, I will describe the processing methods that were used to fabricate the quantum dots in Chapters 3 and 4 as well as the QPCs in Chapter 6 and the spin filter devices in Appendix A. Most of the credit for developing these processes goes to former Marcus group students Andy Huibers, Sam Patel, Sandra Godijn, Duncan Stewart and Mike Switkes.

We are fortunate to have collaborations with several groups that grow GaAs/AlGaAs heterostructures using molecular beam epitaxy, namely the Gossard group at UCSB, the Harris group at Stanford, the Shayegan group at Princeton, and the Heiblum group at the Wiezman Institute in Israel. Beginning from an MBE-grown wafer, the outline of the fabrication process is as follows:

1. Cleave a small chip (~ 6 mm x 6 mm) from the wafer.

2. Etch mesas to provide electrical isolation between devices (photolithography).

3. Pattern, deposit and anneal ohmic contacts (photolithography).

4. Pattern and deposit gates which define the device on a 100 μm scale (ebeam lithography).

5. Pattern and deposit bondpads which connect to the small scale gates (optical lithography).

6. Glue chip into carrier and bond to devices of interest.

Figure B-1 shows a quantum dot device at several levels of magnification so that the photo and ebeam lithography steps are all visible. As the general principals of photo and ebeam lithography are relatively common in the mesoscopic community, I will not give a broad overview of these fabrication methods but instead describe the particular recipes that I have used.
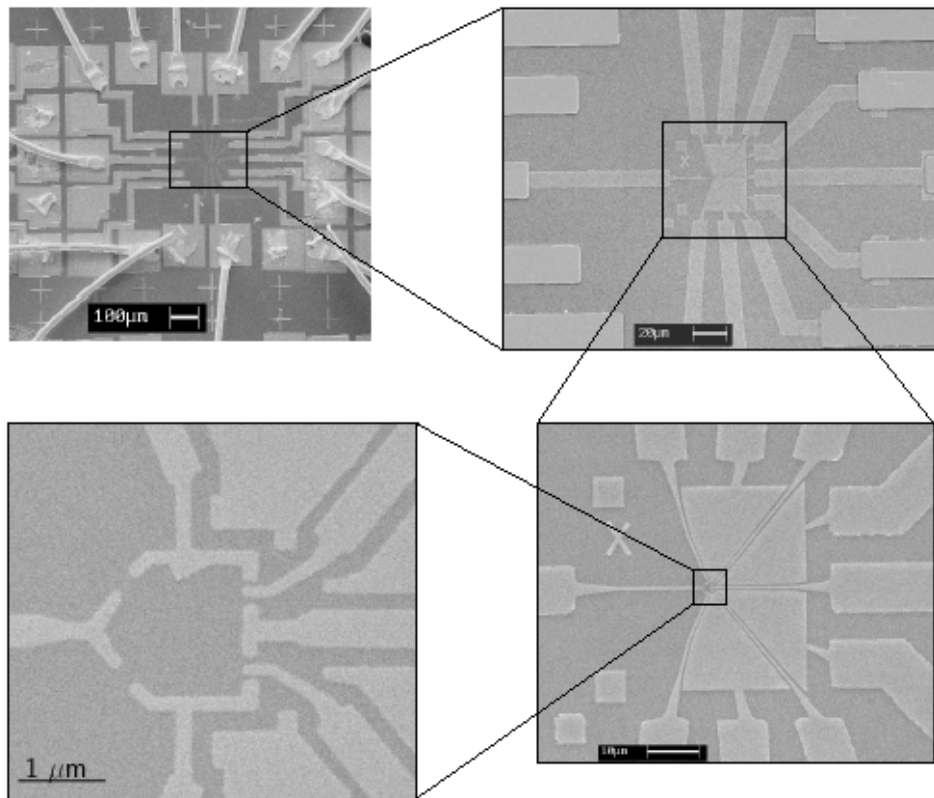
Figure B-1. SEM images of a quantum dot at increasing magnification. The upper left picture shows the ohmics and bondpads of the device with wirebonds. The other three picture show predominantly ebeam defined gates. (Dot fabrication and images courtesy of M. Switkes).
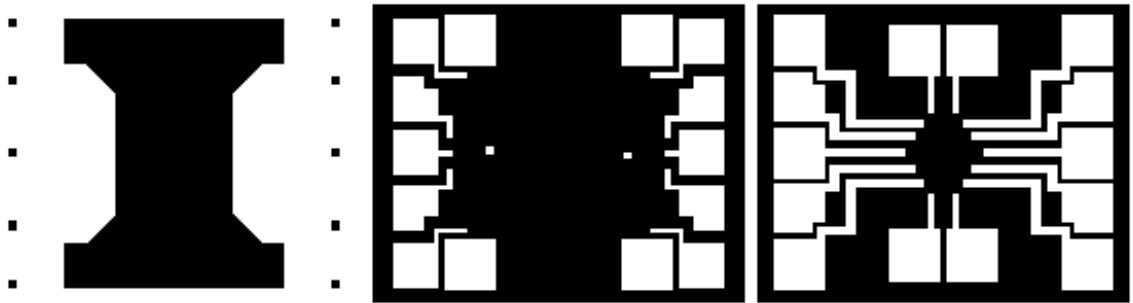
Figure B-2. Mesa, ohmic and bondpad layers of a photolithography mask. This mask, designed by M. Switkes, has been used for several generations of dots and point contacts. Dark areas represent regions of the mask covered in Cr which is opaque to ultraviolet light. The photoresist gets exposed only in the white areas. From left to right the three layers are the mesa, ohmics and bondpads for a single device. Note that only the four square ohmic pads fall on the mesa and will make electrical contact to the 2DEG.

B.2 Photolithography

Photolithography was done in the inner "Submicron Room" of the Ginzton cleanroom using a Karl Suss MB-3 photolithography machine with chrome plated glass masks. The general principle involves a photosensitive plastic "resist" that is exposed to light in the desired pattern to create a mask for either etching or metal liftoff. Over the years, a number of different masks were made for various device designs. One of the older, but often used, designs can be seen in Fig. B-2. A single 4" mask is usually made with four quadrants to incorporate multiple patterns necessary for a complete device. From left to right, Fig. B-2 shows the designs for a single device mesa, ohmics, and bondpad interconnects.

The photolithography recipe developed in our group has been optimized to be very reliable and give a large undercut to facilitate liftoff. Without doing an edge bead removal step, the resolution of this process is ~ 3 μm. With edge bead removal, I have gotten nice features down to ~1 μm. Because we use ebeam lithography for all our small features, the relatively poor resolution is not a problem. The basic photolithography recipe I have used is the following:

- Three-solvent clean for 5 min each in borothene (or TCE or other equivalent), acetone, methanol. Use ultrasound if possible (not advised after the fragile ebeam layers have been deposited).

- Hotplate bake, 120° C, 5 min. Place chips on a glass slide on the hotplate.

- Spin Shipley 1913 photoresist at 7000 rpm for 30 sec. This gives a ~ 1 μm thick layer of photoresist, with an edge bead.

- Hotplate bake, 90° C, 20 min. (I often cover the samples with an aluminum foil wrapped beaker to block any stray UV light).

- Chlorobenzene soak, 15 min. This step hardens the top of the resist so it is less soluble in the developer, leading to a large undercut for liftoff. (Can be skipped for etch processes).

- Hotplate bake, 90° C, 5 min. (to remove leftover chlorobenzene solvents).

- Optional edge bead removal for small features (can be done before or after the chlorobenzene soak/bake):

  o Expose each edge of the chip for ~ 2 min. each. The time required will depend on the lamp power and thickness of the resist. It is useful to have a separate mask with large dark rectangles in order to expose two sides of the chip simultaneously.

  o Develop the chip in equal parts deionized water (DI) : Microposit concentrated developer (Shipley) for 1 –2 minutes. Rinse chip in DI water. (Note: in the Harvard Gordon McKay 2nd floor cleanroom, the developer used is Microposit 351 Developer Concentrate and is diluted 1:5 with DI water).

  o Repeat as necessary. It often takes two exposures and develops to completely remove the edge bead. Edge bead removal is time consuming and a major pain.

- Expose desired pattern. I use 45 seconds for large patterns (ones which do not require edge bead removal), and 24.5 seconds for fine patterns. These times will depend on the lamp power and should be checked with a junk chip for every machine and fab run.

- Develop in equal parts DI and Microposit concentrated developer for 1 min. 15 sec. for large patterns, or 20 – 30 sec. for fine patterns. Rinse in DI water. It is always OK to check how the develop is progressing by rinsing the sample in DI, looking under the microscope (with a UV filter in place!!) and then continuing the develop. As with the exposure time, the develop time may change over the years, with different cleanrooms, humidity, and many more variables I'm sure. (Note: in the Harvard Gordon McKay 2nd floor cleanroom, the developer used is Microposit 351 Developer Concentrate and is diluted 1:5 with DI water).

- Oxygen plasma with 100% O_2, at ~ 150 W for 0.09 minutes (in the Ginzton Phlegmatron, 50 % power, 0.09 min) to clean the surface.

- For metal evaporation and liftoff steps, we have always done an oxide removal acid dip. At Stanford, we did a HF dip with 20:1 buffered oxide etch (BOE) for 15 seconds. At Harvard, I switched to a (much safer) 5 second dip in 30% ammonium hydroxide, with seemingly fine results. The sample should then be loaded into the evaporator as quickly as possible (5 – 10 minutes is fine).

- For the bondpad interconnect layer, evaporate 250 Å Cr, then 2250 Å Au using processed cooling water to cool the sample during and after the evaporation. Liftoff in acetone, using ultrasound only as a last resort (as the thinner ebeam metal could come off as well).

- The wet etch and ohmic recipes are described in the following sections.

It is strongly advised to process at least one, preferably two, practice (junk) chips along with any real 2DEG sample. This is particularly important for the ohmic step because we believe the photoresist developer slightly etches the GaAs surface, rendering poor ohmic contacts if the ohmic photolithography has to be rinsed off and repeated after developing. In the steps above, the three-solvent clean and bake can be done simultaneously on the real and junk chips. Then spin the junk chips first, and, if they look good, go ahead and spin the real chip. If the junk chips don't turn out for whatever reason, do not proceed with the real 2DEG. The chips may all be baked together, soaked in chlorobenzene and baked again. All exposures, including edge bead removal, should be done on the practice chips first. If the exposure and develop look good (good undercut for metal liftoff processes), then the real chip can be processed in exactly the same manner. Otherwise, cut your loses, rinse off the photoresist in acetone and start again. This is OK even on the ohmic step provided you have not exposed the real 2DEG yet. After exposing and developing the patterns, the chips (real and junk) can be stored, away from solvent fumes and in the dark, for several days with no ill effects. For metal liftoff steps, process the junk chips through the plasma etch, oxide acid etch, metal evaporation, and liftoff before following with the real 2DEG. If the first junk chip does not liftoff, try the second. If it looks risky and this is the final bondpads step, your time is better spent redoing the whole process than ruining a set of nearly completed devices. If this is the ohmic step, it's a 50-50 decision. As mentioned previously, I have had bad luck with ohmic contacts that were processed a second time. We believe this may be due to damage to the surface during the first processing attempt. Because the ohmics rely on metal diffusing into the substrate, the condition of the surface could play a role in successful ohmic contact. Your best bet is to make sure the undercut on an ohmic layer looks good on the junk chips before processing the real 2DEG. Then pray.

B.3   Wet Etching

Etching of the mesas is done in a solution of dilute sulfuric acid. The mixture is 1:8:240 of hydrogen peroxide : sulfuric acid : DI water. Always add the hydrogen peroxide to the acid in a graduated cylinder to measure, then pour into the DI water. Mix well. Because an etch step can take several hours, I recommend leaving the etch mixture covered with a cover glass when not in use to prevent nonuniform evaporation which will change the etch rate. Every etch mixture should be calibrated using a patterned junk chip made of good GaAs (not a 2DEG heterostructure, but not unknown junk either). I have always used an Alpha

Step profilometer to measure the etch profile. We generally etch all of the AlGaAs layer to the depth of the 2DEG, though a shallower etch is sufficient to isolate devices in most cases.

I have used a second etch recipe for smaller patterns, namely ebeam defined "trenches" which can also be used to isolate devices if there isn't an appropriate mesa mask available. This recipe was developed by Duncan Stewart in our group to give vertical walls for smaller features. The recipe is 2:6:100 of hydrogen peroxide : phosphoric acid : *isopropanol*. **Note that the dilutant is isopropanol, a solvent, instead of water. Be very careful** with this etch as it is easy to forget you are using isopropanol and the tendency to dispose of the etch into a general acid waste bottle is strong. From experience, this leads to explosive results. Make sure you have a proper, unique waste disposal bottle for this etch, and again, always add the small amount of acid + hydrogen peroxide to the larger solvent quantity.

B.4   Ohmic Contacts

Following the photolithography step for the ohmic contacts, metal is evaporated using either a thermal or ebeam evaporator (or both). I have used two recipes to make ohmic contact to the 2DEG. The first is 50 Å Ni, 1200 Å AuGe eutectic, 250 Å Ni, and 1500 Å Au, and should be done in a single thermal evaporator step. Cool with chilled water during the evaporation. Liftoff in acetone (should be relatively easy with a large undercut, but ultrasound can be used if needed). After liftoff, the ohmic metal must be annealed into the heterostructure to make contact to the 2DEG. The optimum annealing time and temperature will vary from one heterostructure to the next and should be determined separately for each one. Remember to process a little extra material if using a new wafer so you can cleave a couple rows into small pieces to use for ohmic development. In general, we have found that this Ni-Au-Ge ohmic recipe yields good electrical contact (< 1 kΩ) when annealed at $410°$ C for $20 - 50$ seconds. Compared to the Pt-Au-Ge recipe below, this recipe has given consistently good results over many years.

The advantage of the second ohmic recipe, Pt-Au-Ge, is the elimination of Ni (ferromagnetic) from the chip. Depending on the evaporators available (Pt requires an ebeam evaporator), I have tried slightly different versions of Pt-Au-Ge ohmics. None have yielded the same consistently good results I find with Ni-Au-Ge, though I suspect it is simply a matter of developing the "right" recipe. At best, I have learned to expect ohmic contact of < 5 kΩ using Pt-Au-Ge, and would consider using ohmics up to $15 - 20$ kΩ if necessary (and possible). At Stanford, I used a recipe developed by John Stockton in our group which required two separate evaporations (by Tom Carver in the Ginzton cleanroom): first 350 Å Ge and 20 Å Au, followed by 300 Å Pt and 650 Å Au. At Harvard, I used the old ebeam evaporator in the McKay 2nd floor cleanroom and could do the entire recipe in one pump down: 350 Å Ge, 300 Å Pt, 650 Å Au. Generally speaking, I found that Pt-Au-Ge ohmics needed to be annealed at a higher temperature than Ni-Au-Ge. Again, the exact time and temperature should be determined for each chip using small expendable

pieces of the 2DEG. The most successful chip I processed with Pt-Au-Ge ohmic contacts was annealed using the homemade annealer in the Westervelt group as follows: 1 min. at 110° C, 20 sec. at 250° C, then 75 sec. at 450° C. This was repeated a second time after rotating the chip 180°.

Ohmic contacts on the real 2DEG chip should be tested in a dunker at 4.2 K after annealing to ascertain that they are satisfactory before proceeding with further processing. I would generally test one or two pairs of ohmics on devices near the edge of the chip as well as one set of four ohmics on a single device (to do a 4-wire measurement of the 2DEG as well). If the ohmics seem questionable, keep checking more until you can decide whether the chip is useable or not. Re-annealing ohmic contacts on a chip is a possible last resort.

B.5   Electron Beam Lithography

Electron beam (ebeam) lithography is used to pattern the fine metal structures that define the gates of the quantum dots and point contacts as well as the larger gate material that connects out to the features of the bondpad photo layer. The lithography process is similar to that used for photolithography: a plastic resist is spun onto the chips, the desired patterns exposed with an electron beam microscope (ebeam), then developed. At Stanford I have use the converted Leica Leo Stereoscan 440 electron microscope in the Ginzton cleanroom. Also at Stanford I have used (and prefer) the Hitachi ebeam writer located at CIS. At Harvard I used the converted Joel ebeam microscope in Gordon McKay. Each machine requires different design files and different operation, so I will not discuss details that relate to a particular ebeam system.

Over the years, there have been a number of ebeam resist recipes used by our group. For some of the older recipes, see the theses of Andy Huibers, Duncan Stewart, and Mike Switkes [106, 230, 231]. I used a double layer PMMA (polymethyl methacrylate) recipe with a light-weight bottom layer and heavy-weight top layer. The light-weight bottom layer is more soluble in the developer, so gives an undercut. My ebeam lithography process is as follows:

- Three-solvent clean, 5 min. each in borothene (or TCE or equivalent), acetone, methanol. Use ultrasound unless thin metal gates have already been deposited.

- Hotplate bake, 2 min. at 180° C.

- Spin a 5% solution of 200k molecular weight PMMA in chlorobenzene at 3000 rpm for 40 sec.

- Hotplate bake, 20 min. at 180° C. (It is likely that this bake time can be reduced, though I have never done so).

- Spin a 2% solution of 950k PMMA in MIBK (methyl isobutyl ketone) at 5000 rpm for 40 sec. MIBK is a less aggressive solvent than chlorobenzene, so should create a more well-defined layer interface than another solution of PMMA in chlorobenzene would. It's not always possible to get

PMMA dissolved in MIBK however, and at times I have used the second layer in a chlorobenzene solution with fine results.

- Hotplate bake, 20 min. at 180° C.

- Expose with the ebeam system, at the dose determined during a practice exposure matrix (discussed below).

- Develop in a solution of 3:1, isopropanol : MIBK with 1.3% methyl ethyl ketone (MEK) added. For all ebeam processing using the Stanford Hitachi and Harvard Joel systems, I developed for 2 minutes. The developing process used on the old Ginzton Leica machine was more complicated and can be found in Andy Huibers' thesis [230].

- The developed chip is now ready to be loaded into the evaporator for gate metal deposition. For standard Cr/Au gates, we typically use 25 Å Cr and 120 Å Au. Other evaporations (SiO, NiFe, or thicker Cr/Au) can be used as desired. Liftoff in acetone. Use ultrasound as a last resort.

As with the photolithography process described above, I strongly advise the parallel processing of at least one junk chip with every real 2DEG sample. After the resist is spun and baked, the junk chip is used to write an exposure matrix with the ebeam. The exposure matrix should be written at a 4 – 6 doses that span the range you would expect to yield good results given the machine being used. For the Stanford Hitachi system, my exposure matrices typically ran from 160 to 260 $\mu C/cm^2$. On the Harvard Joel system I used doses of 300 – 420 $\mu C/cm^2$ (at a magnification of 1000x or 5000x) Sometimes an ebeam system gives nearly the same results even after several months, while other times you may find exposures change from week to week or worse, day to day. The exposure matrix is also a good opportunity to test all of your device designs to make sure they write as expected. Keep at least one device that you write at every exposure to pick the correct dose. To select the proper exposure, develop the junk chip, evaporate the gates, and view the chip in the SEM. If none of the exposures look good, or devices have not written as expected, repeat the exposure matrix on a second (or third or fourth) junk chip if you have one. If not, clean the PMMA off the real sample and start again, processing more junk chips in parallel. Once a good exposure dose is found, the real chip should be written as soon as possible.

Most ebeam metal layers consist of very small features which define the dot or point contact, as well as larger metal strips which extend the small gates out to the photolithography bondpad layer. These two (or more) sets of gates are typically written at successively lower magnification and, correspondingly, successively higher dosages. Usually, only the resolution and precision of the smallest features are important, so larger gate sets can be overexposed to ensure they turn out. In my experience with the Stanford Hitachi and Harvard Joel ebeam systems I have had good luck when I pick the exposure dose that

turns out correctly after using a standard 2 minute develop, instead of varying the develop time to fit the dose.

B.6   Packaging and Wire Bonding

We use PMMA to glue chips to our 28 or 32 pin non-magnetic ceramic chip carriers. An advantage of using PMMA as glue means that chips can be easily removed from the carriers by soaking in acetone. I have used an ultrasonic wedge bonder (an old West-Bond model 5416) with 25 μm Au wire to connect the bond pads on the device to the chip carrier pads. I often use a little heat, ~ 70° C, on the sample chuck during wire-bonding. Too much heat (for instance due to a faulty, unpredictable heater!) can anneal the gold gates into the sample resulting in leaky gates. A SEM image of two bonded chips glued in a chip carrier is shown in Fig. B-3. Many years ago we found that it was easier to bond to annealed ohmic material than to the thick Cr/Au bondpads alone. For this reason, the ohmic layer on subsequent masks includes ohmic material underneath the bondpads (which sit off the mesa, so the ohmic metal does not make contact to the 2DEG). In the past two years, I have found that wire-bonding to the ohmic material is more difficult than the plain Cr/Au gates—the exact opposite of the conclusions from 4 – 5 years ago. This may be due, in part, to the use of Pt-Au-Ge instead of Ni-Au-Ge ohmics. Nonetheless, it exemplifies why wire-bonding, like most other fabrication steps, is somewhat of a black art.
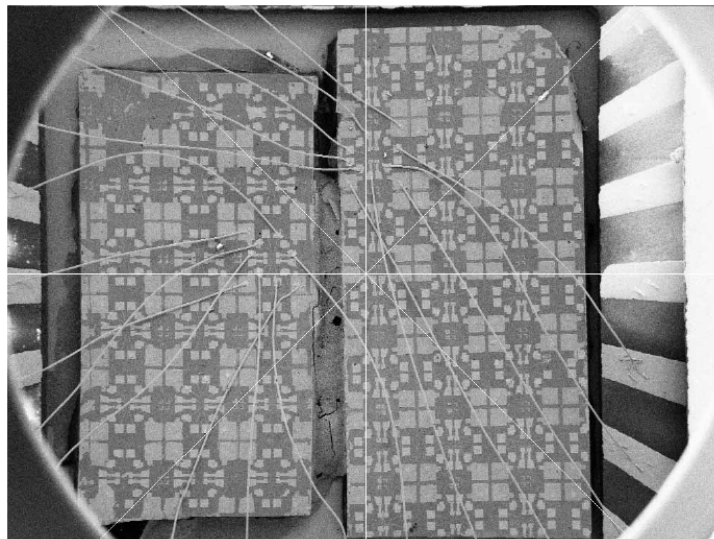
Figure B-3. SEM image of two chips in a chip carrier. The circular rim is the final aperture of the electron microscope. The two devices were bonded by Sam Patel, the wire-bonding champion of the world. (Image courtesy of A. Huibers).

Appendix C

Device Inventory

C.1   Heterostructures

C.1.1   Wafer 940708A

This wafer was grown by Art Gossard's group at UCSB. Devices from this wafer were used in the elastic cotunneling experiment (Chpt. 2). Within our group, this wafer is known as "Insomnia".

2DEG Depth: 1600 Å

Sheet density, $n_s = 1.8 \times 10^{11}$ cm^{-2}

Mobility, $\mu = 1.0 \times 10^6$ cm^2/Vs

Growth Profile: 10 nm GaAs

100 nm AlGaAs, x = 0.3

delta doping layer, Si, 2.5 x 10^{12} cm^{-2}

50 nm AlGaAs, x = 0.3

800 nm GaAs

300 nm superlattice (AlGaAs/GaAs, x = 0.3)

substrate of semi-insulating GaAs

C.1.2   Wafer 950113A

This wafer was grown by Art Gossard's group at UCSB. Devices from this wafer were used in the elastic cotunneling experiment (Chpt. 2).

2DEG Depth: 1000 Å

Sheet density, $n_s = 2.8 \times 10^{11}$ cm^{-2}

Mobility, $\mu = 500,000$ cm^2/Vs

Growth Profile not available.

C.1.3   Wafer CEM2385A

This wafer was grown by Cem Duroz in Jim Harris' group at Stanford. Devices from this wafer were used in the mesoscopic CB experiment (Chpt. 3). Quantum dots from this wafer were among the quietest and most useful our group has ever measured.

2DEG Depth: 900 Å

Sheet density, $n_s = 2 \times 10^{11}$ cm^{-2}

Mobility, $\mu = 140,000$ cm^2/Vs

Growth Profile: 10 nm GaAs

40 nm AlGaAs, x = 0.34, with uniform Si doping 1.0×10^{18} cm^{-3}

40 nm AlGaAs, x = 0.34

1000 nm GaAs

50 nm AlGaAs, x = 0.34

1300 nm superlattice (10 nm AlGaAs, x = 0.34, 3 nm GaAs; 100 periods)

substrate of semi-insulating GaAs

C.1.4   C.T. Foxon, Philips Laboratories Wafer

This wafer was grown by C. T. Foxon at Philips Laboratories in the Netherlands. The two dots measured in the Kondo experiment (Chpt. 5) were made from this heterostructure.

2DEG Depth: 1000 Å

Sheet density, $n_s = 1.9$ x 10^{11} cm^{-2}

Mobility, $\mu = 2.3$ x 10^6 cm^2/Vs

Growth Profile not available.

C.1.5   Wafer MBE 4-105

This wafer was grown by Vladimir Umansky in Moty Heiblum's group at the Wiezman Institute in Israel. The point contact devices measured for the Kondo in QPCs experiment (Chpt. 6) were fabricated from this wafer.

2DEG Depth: 1020 Å

Sheet density, $n_s = 1.2$ x 10^{11} cm^{-2}

Mobility, $\mu = 4.1$ x 10^6 cm^2/Vs

Growth Profile: 8 nm GaAs

26 nm AlGaAs, x = 0.36,

delta doping layer, Si, 2.5 x 10^{12} cm^{-2}

68 nm AlGaAs, x = 0.36

1600 nm GaAs

250 nm superlattice (AlGaAs/GaAs)

substrate of semi-insulating GaAs

C.2   Devices

The following devices produced published data. Areas estimated with depletion regions of ~ 100 nm.

C.2.1   Insomnia 2a, Dot #21
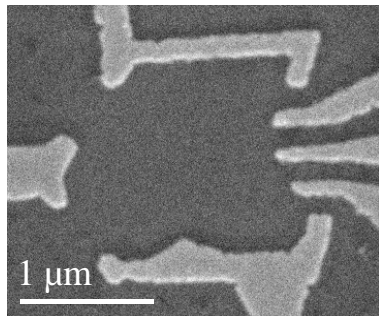
Area = 0.81 μm^2
2DEG: 940708A
Fabricated by: Sam Patel
Experiment: Elastic cotunneling, "dot 1"

C.2.2   Insomnia 1, Dot #10
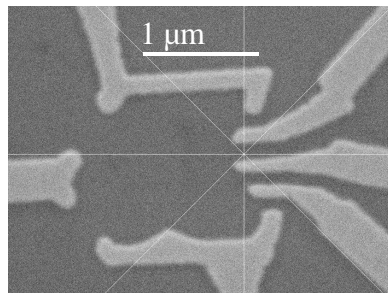
Area = 0.45 μm^2
2DEG: 940708A
Fabricated by: Sam Patel
Experiment: Elastic cotunneling, "dot 2"
AKA: Rain

C.2.3   Dante 1, Dot #11

Design: as Insomnia 2a, Dot #21 and Insomnia 1, Dot #10 above
Area = 0.57 μm^2
2DEG: 950113A
Fabricated by: Sam Patel
Experiment: Elastic cotunneling, "dot 3"
AKA: Inferno

C.2.4   CEM2385-SRP1, Dot #68, Dot #14
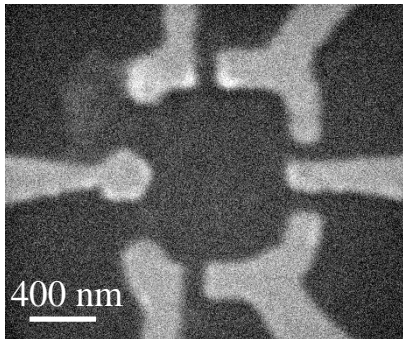
Area = 0.5 μm^2
2DEG: CEM2385A
Fabricated by: Sam Patel
Experiment: Dot #68 = Mesoscopic Coulomb blockade, "dot 1"
            Dot #14 = Mesoscopic Coulomb blockade, "dot 2"

C.2.5   van der Vaart Double Dot
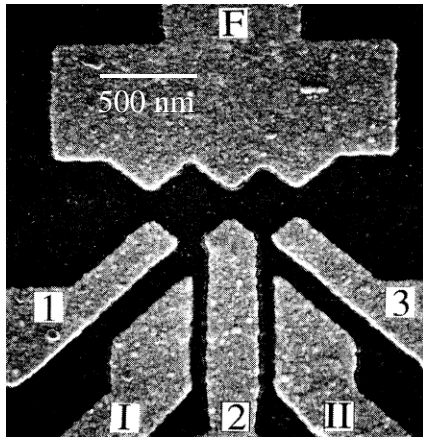
Dot 1 (left) Area = 170 nm x 170 nm = 0.029 μm^2
Dot 2 (right) Area = 130 nm x 130 nm = 0.017 μm^2
2DEG: C.T. Foxon, Philips Laboratories
Fabricated by: N. C. van der Vaart
Experiment: Kondo effect in quantum dots

C.2.6   Weizman 5, QPCs Device #8
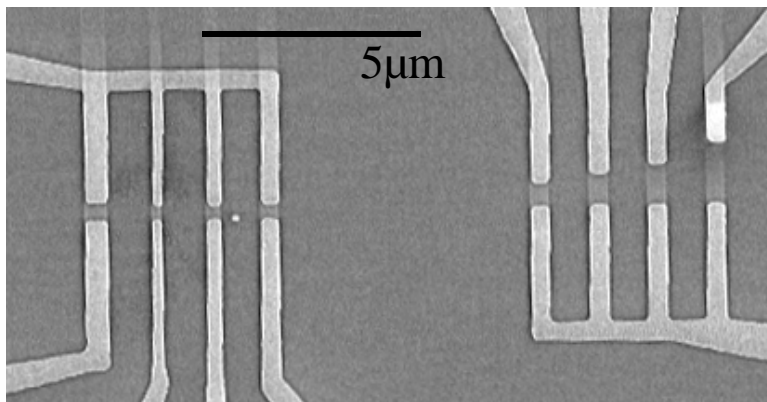
QPC channel width x length
QPC1: 400 nm x 500 nm
QPC2: 300 nm x 200 nm
QPC3: 300 nm x 300 nm
QPC4: 300 nm x 400 nm
QPC6: 700 nm x 400 nm (= QPC "5" in Chapter 6).
2DEG: MBE 4-105
Fabricated by: Sara Cronenwett
Experiment: Kondo effect in quantum point contacts

Appendix D

Useful Measurement Information

D.1   ac + dc Adder Box Circuit Diagram
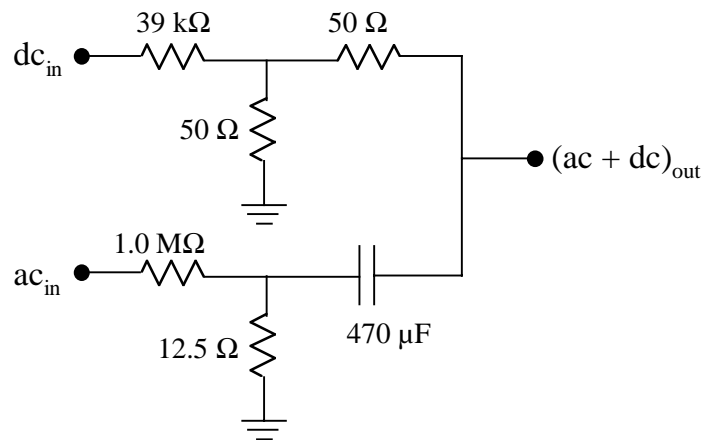
Figure D-1. The ac + dc adder box circuit constructed to passively add a small ac lockin signal to a large dc voltage bias. The circuit was designed by D. Stewart and optimized for use at 13 Hz where the dc voltage divider has a ratio of 1000:1 and the ac voltage divider has a ratio of 10^5:1.

D.2   Battery Box Circuit Diagram
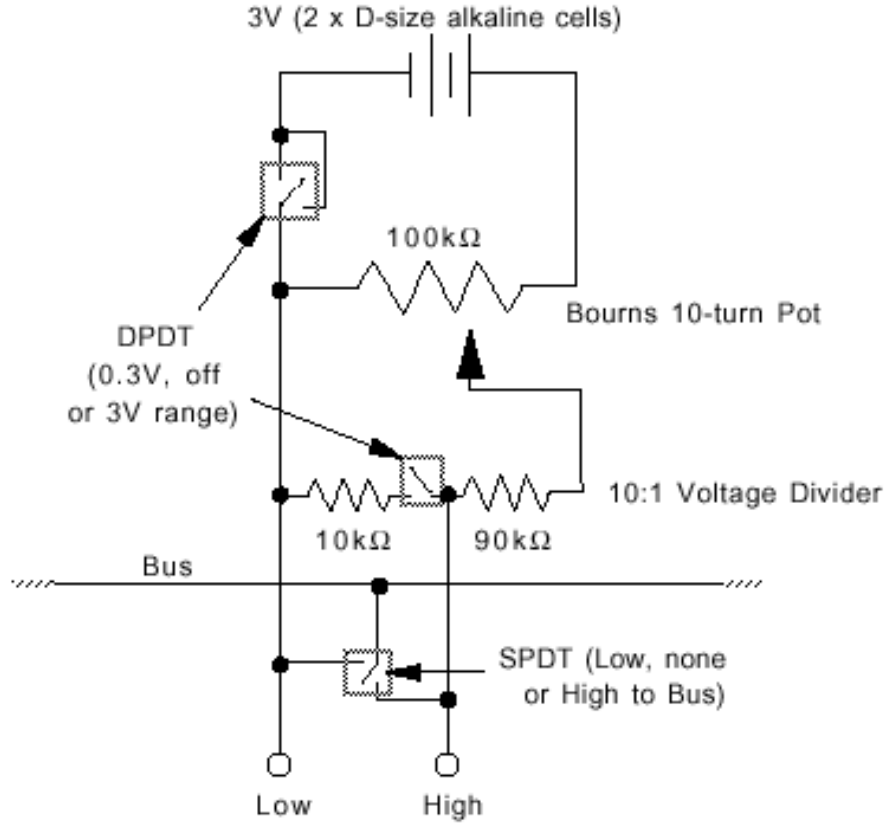
Figure D-2. Battery Box Circuit. One channel of the battery boxes used by the Marcus group to bias the depletion gates on quantum dots and point contacts. In a typical set-up, the gates are connected to the "Low" terminal, a computer controlled voltage is connected to the "High" terminal, and the SPDT switch is set in the middle (the Bus disconnected). If no computer controlled voltage is used, the SPDT is set to High to Bus. Schematic by Ian Chan.

D.3   Cryostats

The measurements reported in this thesis were all taken in an Oxford Instruments Kelvinox 100 ^{3}He-^{4}He dilution refrigerator, either in the Marcus group (at Stanford and later Harvard) or in the Quantum Transport group at TUDelft. The Marcus group fridge had no special electrical filtering during the time of the first two experiments (Chapters 3 and 4) except for inline "π" filters ($\sim$ 50 MHz roll-off). The base

electron temperature was consistently ~ 90 – 100 mK while the mixing chamber temperature was ~ 15 – 25 mK. Following those experiments, the fridge was fitted with a low-temperature RC filter attached to the mixing chamber, designed and built by Andy Huibers. The wires were shielded in a metal can from the output of the filter to the sample. This significantly reduced the electron base temperature to ~ 45 mK. A description of this filter, made from ultra-fine high-resistive wire, can be found in Appendix C of Andy Huibers' thesis [230]. Unfortunately, the Huibers filter has not aged gracefully. Over the years, the sample wires have become disconnected, presumably due to contraction and expansion of the epoxy filled filter during thermal cycling. Therefore, by the time of the QPC experiment described in Chapter 6, we replaced the Huibers filter with a rudimentary "cold resistor box". Wires connected to ohmics had resistors of 1 kΩ in the resistor box, while depletion gate wires had 100 kΩ resistors. Because we did not have a quantum dot in the fridge during those measurements, we were not able to precisely measure the base electron temperature with our make-shift filter box. A similar cold resistor filter box has recently been carefully designed and built by Susan Watson for the new dilution fridge in our lab with outstanding results—the electron base temperature has been measured as low as 40 mK.

The dilution fridge I used at Delft had a homemade copper powder filter with additional resistors and capacitors that could be added to each wire individually for additional filtering. I measured the base temperature of electrons in that cryostat to be 45 mK.

In addition to the dilution fridges, I have made many (unpublished) measurements on an Oxford Instruments Heliox 2$^{\text{VL}}$ ^{3}He sorption-pumped insert with a base temperature of ~ 300 mK. The turnaround time of the ^{3}He system (~ 4 hours) is much shorter than that of the dilution fridge (> 12 hours), so it is very useful for testing samples quickly. The single-shot sorption design holds a base temperature for 5 – 10 hours, depending on the magnetic fields, temperature control, and the quality of the initial ^{3}He condense. I have also made use of a 1.2 K pumped ^{4}He insert built by Desert Cryogenics. This system also has the advantage of quick turnaround (< 1 hour) and a vacuum can.

Before measuring (almost) any device in the ^{3}He or dilution cryostats, they are tested in a simple 4.2 K dunk stick. Our dunkers are homemade and among the most valuable equipment in the lab. They provide a quick and easy test system for ohmic development as well as quantum dots and point contacts. It is well worth the time to test the 2DEG and all the gates of a device before cooling it down in one of the more involved cryostats. A series of measurements for dunk testing is given in Sec. D.5.

The dilution fridges in the Marcus lab are housed inside metal shielded rooms. Though we have never noticed a difference between data taken with the door open or shut, the shielded rooms provide a great service simply as a large ground. Invariably you touch the door or wall of the shielded room before touching any wires leading into the cryostat, thereby discharging any static electricity to the room instead of your device.

D.4   Perpendicular IVC Magnet

To make measurements in a large parallel magnetic field, we mount the sample vertically in the cryostat, parallel to the axis of the superconducting solenoid magnet. The sample mount, designed by Joshua Folk, allows the device to be aligned to within a degree of vertical (Fig. D-3b). Remnant perpendicular fields created by the external magnetic due to imperfect sample alignment are canceled out by a split-coil hand-wound superconducting magnet mounted to the outside of the fridge inner vacuum can (IVC), as seen in Fig. D-4a,c. In addition to trimming out any unwanted fields, the IVC magnet provides up to ~ 150 mT of perpendicular field (at 10 mT/A with a critical current of ~ 15 Amps in zero external field). When the parallel magnetic field is high, remember that the critical current of the small IVC magnet decreases! The maximum field of the IVC magnet is limited by the critical current of the superconducting wire and the space available (which determines the number of coils possible).

D.5   Dunk Testing

There are a number of measurements that should be performed when first testing a device (at 4.2 K in a dunker), before cooling down a major cryostat. These are the series of measurements that I perform:

- 2-wire measurement of the ohmics using a Keithley K2400. Source $\pm$ 1, 10, 20, 40 mV and measure the current. Check for the overall resistance (ideally $R < 1$ kΩ; OK if $R < 5$ kΩ; might be useable if $5\Omega < R < 20$ kΩ; no good if $R > 20$ kΩ), ohmic behavior ($V = IR$; the resistance should stay ~ constant), and symmetric results at both positive and negative voltages (i.e. no diodic behavior).

- 2-wire measurement of the ohmics using a lockin. This ensures that the ohmic behavior is still good for very low currents and voltages. Source 0.5, 1, and 2 nA using 0.5, 1, and 2 V outputs through a 1 GΩ resistor (after splitting the high and low lockin output). The high and low current lines are T'd together with the high and low voltage BNC cables respectively to make a 2-wire measurement. Check for overall resistance and ohmic behavior.

- 4-wire lockin measurement of the 2DEG resistance. A standard 4-wire current bias measurement, using 1 – 100 nA of current to measure the resistance of the 2DEG. R_{2DEG} should be relatively low in most of the mesa designs we use, often < 100 Ω.

- Check for gate leakage. There are many methods; this one seems relatively safe. Ground the ohmics on the break-out box. Ground the bus of the battery box. (Make sure these are the same ground). Split the input of the Ithaco 1211 current pre-amp, connecting the low (shield) to ground (battery box bus). Connect the high side of the Ithaco input to the high side of a battery on the battery box. Connect the low side of the battery to the gate to be tested. Read the output of the
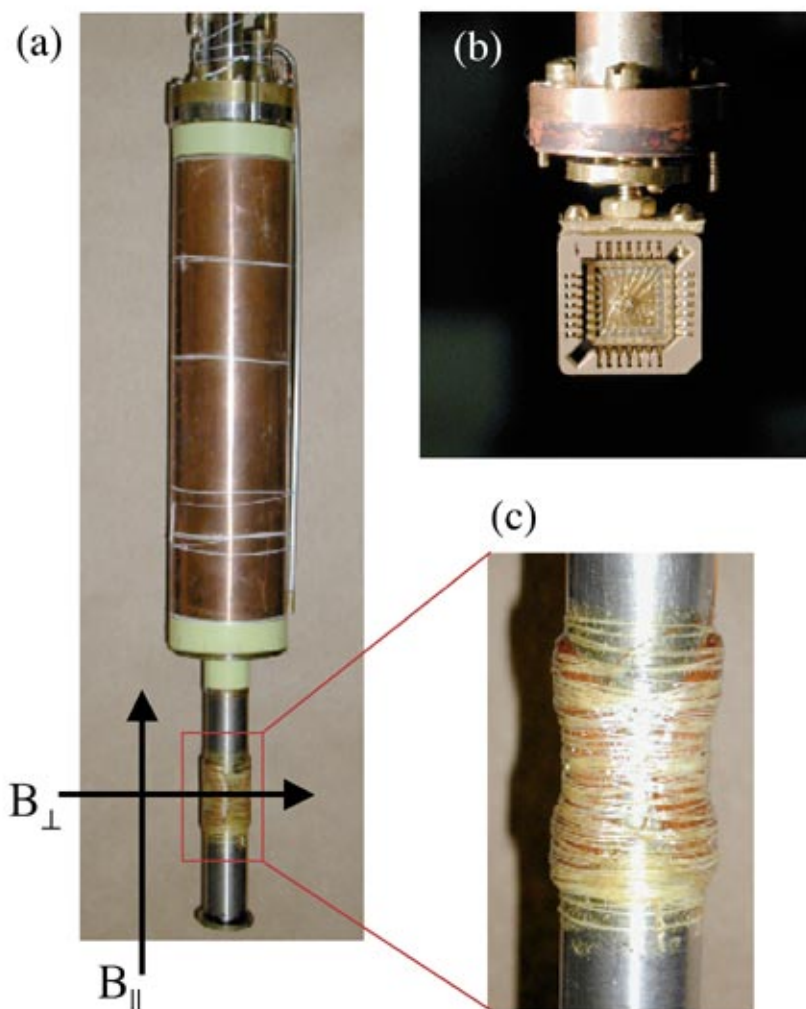
Figure D-3. IVC magnet and parallel sample mount. **(a)** ^{3}He-^{4}He dilution refrigerator inner vacuum can (IVC) shown with the homemade split-coil magnet attached near the bottom (at the location of the sample mount inside). The direction of the parallel and perpendicular fields are indicated. **(b)** The parallel sample mount designed by Joshua Folk. Three set screws between the bottom of the cold finger and the circular plate to which the sample holder connects allow the sample to be aligned within 0.5°. **(c)** Close-up view of the IVC magnet. The magnet has a maximum field of about 150 mT. The magnet is attached to the IVC can with GE varnish and dental floss. (Note: for larger magnets, capable of ~ 1 T, we have found that GE varnish and dental floss is NOT sufficient to hold the magnet to the IVC can).

Ithaco on a DMM. Take readings of the Ithaco with the battery at zero and several other increasing voltages (up to 1 V should be sufficient). Any current flow between the gate and the 2DEG returns via the grounded ohmic and is read on the Ithaco. Because the Ithaco has an offset, it is important to take the change in current read on the Ithaco along with the change in voltage on the battery to determine the resistance between the gates and the 2DEG. If this resistance is less than 1 GΩ, you will likely have problems. Ideally, the gate-2DEG resistance will be > 10 GΩ. You shouldn't have to check all gates, just one or two. If they leak, they'll all leak, and if they don't, none should. Generally, gate leakage is a function of the heterostructure and usually indicates a worthless wafer (unless something strange happened in processing; extra high heat during wire-bonding for instance).

- Check gate operation. Using a battery box and a 2- or 4-wire measurement of the 2DEG, make sure all QPCs pinch off and that any other gates (on a dot, for instance) are working. You can often use "pins" and other gates on a dot to pinch off the transport corridor even though they are not designed to be QPCs. QPCs should pinch off with $V_g < 3$ V (that is, technically, $V_g > -3$ V) unless they are exceptionally wide. I have gone up to 6 V on various gates in desperately hopeful dunk tests, but, generally, this large a voltage should not be necessary.

If you've gotten through all of the above tests successfully, then the device should be ready to cool down!

D.6   Measurement Tricks

A few of the specific measurement tricks used in our group are worth mentioning. To reduce the switching noise of quantum dot devices (for Coulomb blockade measurements) we now routinely cool dots with a positive bias of ~ 0.4 V applied to the surface depletion gates. This process has not been rigorously tested to prove the noise reduction, but has generally seemed to help. It is not as useful with QPCs because the positive bias leaves a "ghost" image of the gate frozen into the heterostructure—an equivalent effective negative voltage will be present when the positive bias is removed—which sometimes limits the range of the QPC.

Another noise reduction technique that has shown promise on a few occasions is a roughly linear "slow cool" of the dots from 300 K to 4 K over a period of ~ 24 hours. This is accomplished by using *very* little exchange gas on the cooldown. Again, this technique has been poorly tested (due to the long time requirement to test it rigorously), but on several occasions has yielded dots which were quieter than when cooled normally (~ 6 hours from 300 K to 4 K).

To avoid blowing up devices from static discharge to the cryostats, we make sure that there is at least 1 kΩ of inline resistance on all wires leading down to the sample. Since realizing the connection of larger inline resistances to more resilient devices, we have not blown up a device in the dilution fridge for many years. It is especially important to remember to use an inline resistor pack with the 4.2 K dunkers when testing depletion gates. The inline resistors should be left out during ohmic development tests, as the ohmic material cannot be blown off the surface, and the more precise measurements of the contacts alone are desired.

Appendix E

Data Acquisition Programs

In this appendix I am including a number of the key data acquisition programs used in our lab overall, and by me personally. All of the data acquisition in the Marcus group is done using the software package Igor Pro (© 1988, WaveMetrics, Inc., www.wavemetrics.com), currently in version 4.0. Igor is capable of comminicating with all standard GPIB-compatible hardware. We have written standard device drivers (included in E.1) for the commonly used equipment in our lab. Programming in Igor is extremely easy as it contains a C type programming language. As a result, data acquisition programs are easily customized to the desires of an individual student or individual experiment. I have included in section E.2 an example 2D sweep data acquisition program. The other advantages of Igor (over other commonly used software such as Labview) are a complete data analysis package and the ability to produce publication-ready figures all within the same program. I highly recommend Igor for everything from data acquisition to publication.

E.1   Device Drivers

E.1.1   Init Procedures

The following "initialization" procedure is run at the beginning of any experiment to define the variables for whatever devices being used. The very convinent 'wait' function is also included. (May be a standard command in Igor now).

```
// ************************************************

#pragma rtGlobals=1                  // Use modern global access method.

// Init Procedures
// Michael Switkes & Randy True
// 26 May 1996

// Run this before any GPIB session
// You need to make sure all instruments you are using are commented "in".

function InitGPIB()
        // Store the GPIB indentifiers of the instruments in the corresponding variables
        variable/G gpibboard
        variable/G dmm11
        variable/G dmm20
        variable/G dmm21
        variable/G dmm22
        variable/G itc15
        variable/G K2400
        variable/G HPmaster
        variable/G HPslave
        variable/G K238

        // Get the GPIB identifiers
        execute "NI488 ibfind \"gpib0\", gpibboard"
        execute "NI488 ibfind \"dev11\", dmm11"
        execute "NI488 ibfind \"dev20\", dmm20"
        execute "NI488 ibfind \"dev21\", dmm21"
        execute "NI488 ibfind \"dev22\", dmm22"
        execute "NI488 ibfind \"dev15\", itc15"
        execute "NI488 ibfind \"dev25\", K2400"
        execute "NI488 ibfind \"dev17\", HPmaster"
        execute "NI488 ibfind \"dev18\", HPslave"
        execute "NI488 ibfind \"dev16\", K238"

        // Make sure we're talking to the right board
        execute "GPIB board gpibboard"
End

// ************************************************
```

```
function wait(seconds)
        variable seconds
        variable t
        t = ticks
        do
        while((ticks - t)/60.15 < seconds)
End
```
// **

E.1.2   AO6 Procedures

We used a National Instruments 10-bit 6-channel AO6 board as an analog-to-digital converter (for voltages applied to depletion gates as well as the dc source-drain bias voltage). The following procedures drive the AO6 board.

```
// **************************************************
#pragma rtGlobals=1                    // Use modern global access method.

// 6 Channel AO6 Procedures
// Michael Switkes
// First written 4 June 1996 as 3 Chan AO6 Procedures
// 6 Channel Procedures created 23 October 1996

// Last modified
// by:                    Michael Switkes
// on:                    23 October 1996
// machine:        Dick

// Procedures for using the AO6 board in 6 channel mode
// with external reference (note that it is an oh and not a zero)

// These procedures assume that:
// All channels 0-5 are set up in bipolar mode with external reference
// this requires setting jumpers 7-24 to BC, and setting the switch on the
// AO6 interface box to 6 channel fixed ref.

// To go back to the 3 channel feedback reference mode (for use with 3 Channel
// AO6 procedures or George), you need to set jumpers 16-17,19-20,22-23 to
// AB and the switch on the interface AO6 box to 3 channel autoscale.
```

```
// The Wave AO6 stores the current settings for each channel in mV and you
//                should think several times before modifying it by hand.
// The global variable ao6ref stores the external reference value.  The AO6 itself
//                provides a 2.5V reference, or you can provide an external one yourself.  You
//                need to reinitilize the AO6 (initao6(extref)) to change the reference
//                since it safely zeros out all the channels before it changes the limit.
//                (presumably, the external reference doesn't change instantaniously and we
//                don't want to put undefined voltages on the pins while we're changing it)
// **************************************************

function BinToVolt(chan, bin)
        variable chan, bin

        Wave AO6 = AO6
        Nvar ao6ref = ao6ref
        return(ao6ref*(1-(bin-1)/2048))
End
// **************************************************

function VoltToBin(chan, mV)
   variable chan, mV
   variable bin

   Wave AO6 = AO6
   Nvar ao6ref = ao6ref

   bin = 2048*(1-mV/ao6ref) + 1
   if(bin > 4095)
      bin = 4095
      printf "%.2fmV out of range for channel %d, outputting %.2fmV.\r", mV, chan, BinToVolt(chan, bin)
   endif
   if(bin < 0)
      bin = 0
      printf "%.2fmV out of range for channel %d, outputting %.2fmV.\r", mV, chan, BinToVolt(chan, bin)
   endif
   return bin
End
// **************************************************

function SetChanAO6(chan, mV)
        variable chan, mV
```

```
        string cmd
        Wave AO6 = AO6
        variable junk

        junk = VoltToBin(chan, mV)
        sprintf cmd "AnalogOutput %d, %d", chan, junk
        execute cmd
        AO6[chan] = BinToVolt(chan, junk) // to allow for out of range requests
End
// **************************************************
```

// chanlimit sets the initial upper limit for the first three channels
// that is, it sets channels 3, 4, &5 to this value initially

```
function InitAO6(chanlimit)
        variable chanlimit
        Variable i = 0
        variable/g ao6ref

        Make/N=6/D/O ao6 = {0,0,0,0,0,0}
        ao6ref = chanlimit
        do
                SetChanAO6(i, 0)
                i += 1
        while(i < 6)
End
// **************************************************
```

// Function ChanRamp(chan,finalval) simply ramps the specified A06 channel smoothly in steps
// set by the global variable "rampscale" times the channel resolution to it's requested destination.

```
Function ChanRamp(chan,finalval)
        variable chan
        variable finalval

        WAVE ao6 = ao6
        NVAR rampscale = rampscale
        variable presentval = ao6[chan]
        variable cdir
        silent 1;pauseupdate
```

```
            if(abs(ao6[chan]-finalval) > (ao6[chan+6]/2048*rampscale))
                    // must ramp smoothly
                    if(finalval > presentval)
                            cdir = rampscale
                    else
                            cdir = -rampscale
                    endif
                    do
                            presentval += ao6[chan+6]/2048*cdir
                            SetChanAO6(chan,presentval)
                    while((finalval-presentval)*cdir > 0)
            endif
        setchanao6(chan,finalval)
end
// ***************************************************
```

E.1.3   DMM Procedures

The following procedures are used with HP (now Agilent) 34401A digital multi-meters.

```
// ***************************************************
#pragma rtGlobals=1              // Use modern global access method.

// DMM Procedures
// Michael Switkes & Randy True
// 26 May 1996

// Last Modified
// by:              Michael Switkes
// on:              11 June 1996
// machine:     Dick

// This file contains functions for using HP34401A DMMs.
// Return Values are in mV!!


// ***************************************************
// You need to run this function once for each dmm before using it.
// The argument passed to this function should be obtained with the command:
// NI488 ibfind "dev##", X
```

```
// where ## is the GPIB address of the DMM and X is a global variable used to store it
//                (see InitGPIB())

function InitDMM(dmm)
        Variable dmm
        string cmd

        // Set the device that we're talking to
        sprintf cmd, "GPIB device %d", dmm
        execute cmd

        // Set up to read DC voltages
        execute "GPIBwrite/F=\"%s\" \"conf:volt:dc def, max\""
        execute "GPIBwrite/F=\"%s\" \"zero:auto off\""
End
// *************************************************

function InitDMMRes(dmm)
        Variable dmm
        string cmd

        // Set the device that we're talking to
        sprintf cmd, "GPIB device %d", dmm
        execute cmd

        // Set up to read DC voltages
        execute "GPIBwrite/F=\"%s\" \"conf:res\""
        //execute "GPIBwrite/F=\"%s\" \"zero:auto off\""
End
// *************************************************


// This will set the reading speed of the DMM (integration time).
// The speed argument can be one of {-2,-1, 0, 1, 2} which
// correspond to integration times of {.00033, .0033, .017, .17, 1.7} seconds

function SetSpeedDMM(dmm, speed)
    Variable dmm, speed

    Variable linecycles     // Each speed argument corresponds to a number of linecycles to integrate over
    string cmd
    sprintf cmd, "GPIB device %d", dmm
```

```
    execute cmd

    if (speed == -2)
          linecycles = .02
    endif
    if (speed == -1)
          linecycles = .2
    endif
    if (speed == 0)
          linecycles = 1
    endif
    if (speed == 1)
          linecycles = 10
    endif
    if (speed == 2)
          linecycles = 100
    endif

    sprintf cmd, "GPIBwrite/f=\"%%s\" \"volt:dc:nplc %f\"", linecycles
    execute cmd
End
// **************************************************
```

// This is mostly for diagnostic purposes. It returns the error registered by the DMM

```
function/S errorDMM(dmm)
        Variable dmm

        string cmd
        string /G junkstring        // General technique for returning string values from
                                    // execute statements without the proliferation of
                                    // global variables
        sprintf cmd, "GPIB device %d", dmm
        execute cmd
        execute "GPIBwrite/F=\"%s\" \"syst:err?\""
        execute "GPIBread/T=\"\n\" junkstring"
        return junkstring
end
// **************************************************
```

// This reads the DMM and returns the measurement in mV.
// It is up to the application to keep track of the scaling from Volts

```
// to Ohms or inverse Ohms or whatever.

function ReadDMM(dmm)
        variable dmm
        Variable/G junkvariable
        string cmd

        sprintf cmd, "GPIB device %d", dmm
        execute cmd
        execute "GPIBwrite/F=\"%s\"  \"read?\""
        execute "GPIBread/T=\"\n\" junkvariable"
        return(junkvariable * 1000)
End
// **************************************************

// Dictionary

// To tell the GPIB interface to talk to the dmm "blah" where "blah" is set in the InitGPIB function
// (Inside a macro)
// GPIB device blah
// (inside a function -- you must define cmd as a string in your function)
// sprintf cmd, "GPIB device %d", blah
// execute cmd

// To read a voltage from dmm "blah" into variable "gack" after you have told the GPIB interface
// to talk to dmm "blah"
// (Inside a Macro)
// GPIBwrite/F="read?"
// GPIBread/T="\n" gack
// (Inside a Function -- gack must be a global variable declared earlier in the function)
// execute "GPIBwrite/F=\"read?\""
//          execute "GPIBRead/T=\"\n\" gack"
// **************************************************
```

E.2   2D Sweep Data Acquisition Program

```
// ***************************************************

#pragma rtGlobals=1                    // Use modern global access method.


// This is a 2D sweep to ramp two Ao6 channels.  It uses the 4Wire voltage bias measurement config, so
// measures current and AC bias voltage, then divides them to get cond.
// Set to run on Stanford D Fridge, spring 2001 by S.Cronenwett.


Function SaraPinPin4W(suffix,xstart,xend,xpnts,xchan,ystart,yend,ypnts,ychan,delay)
    variable xstart, xend, xpnts, ystart, yend, ypnts, delay, xchan, ychan
    string suffix

    Printf
"\241SaraPinPin4W(\"%s\",%g,%g,%g,%g,%g,%g,%g,%g,%g)\r",suffix,xstart,xend,xpnts,xchan,ystart,yen
d,ypnts,ychan, delay

    silent 1; pauseupdate
    Preferences 1

    variable /d magnet_perp = 0
    variable /d magnet_par  = 0
    magnet_perp=ReadIVCMagnet()
    magnet_par = readLakeshore()

    variable t1, t2, v
    variable j = 0
    variable i = 0
    variable lockinsensitivity = 20e-3                    // LOCK-IN SENSITIVITY
    variable acSens = 20e-6
    variable excitation = 7.5e-6                          // VOLTAGE BIAS EXCITATION
    NVAR dmm = dmm19
    NVAR dmm = dmm22
    NVAR dmm = dmm21
    NVAR twodegr = twodegr

    Printf "Check LOCK-IN SENSE = %g V.\r",lockinsensitivity
```

```
printf "2DEG Resistance = %g.\r",twodegr
printf "Parallel Mag = %g mT.  Perp magnet = %g mT.\r",magnet_par,magnet_perp
printf "RuO2 = %g ohms.\r", getRuO2()
string          starttime = time()
Printf "Run start time is %s.\r",starttime

string condmat = "cond" + suffix
string acbiasmat = "vbiasAC" + suffix
string dcbiasmat = "vbiasDC" + suffix
string savename = condmat + ".ibw"
string savename2 = acbiasmat + ".ibw"
string savename3 = dcbiasmat + ".ibw"
Make/D/N=(xpnts,ypnts) $condmat, $acbiasmat, $dcbiasmat
wave cmat = $condmat
wave acmat = $acbiasmat
wave dcmat = $dcbiasmat
cmat = NaN
acmat = NaN
dcmat = NaN
setscale  /i x, xstart,xend,cmat, acmat, dcmat
//  setscale  /i y, ystart,yend,cmat, acmat, dcmat

chanramp(xchan, xstart)
chanramp(ychan, ystart)

display; appendimage cmat
SetAxis /A

t1 = ticks
variable presentx, presenty, deltax, deltay
presentx = xstart
presenty = ystart                              // have already chan ramped to starting values
if (xpnts > 1)
    deltax = (xend - xstart)/(xpnts-1)
else
    deltax = 0
endif
print deltax
if (ypnts > 1)
    deltay = (yend-ystart)/(ypnts-1)
else
    deltay = 0
```

```
    endif
    print deltay
    do                        //OUTER LOOP IN Y-CHAN!!!
        chanramp(ychan, presenty)
        j = 0
        chanramp(xchan, xstart)                    // want to ramp back at the end of each sweep in x
        presentx = xstart                          // and reset presentx to beginning
        wait(5)
        do                    // INNER LOOP IS X-CHAN
            setchanao6(xchan, presentx)
            wait(delay)                            // wait for lock-in to settle to new value
            dcmat[j][i] = getDCV()
            cmat[j][i] = getI(lockinsensitivity)   // measure current first
            acmat[j][i] = getV(acSens)
            j += 1
            presentx += deltax
        while(j < xpnts)

        cmat[][i] = acmat[p][i]/cmat[p][i]         // this is now in resistance
        cmat[][i] -= twodegr
        cmat[][i] = 12906.5/cmat[p][i]             // now in conductance

        i+=1
        doupdate                                   // updates end of every line
        save /c/o/p=homepath cmat as savename
        save /c/o/p=homepath acmat as savename2
        save /c/o/p=homepath dcmat as savename3
        presenty += deltay
    while(i<ypnts)
    t2 = ticks
    printf "Run Time = %f seconds\r", (t2-t1)/60.15
End
// *************************************************
```

Bibliography

[1]   H. W. Fink, C. Schonenberger, Electrical conduction through DNA molecules, *Nature* **398**, 407 (1999).

[2]   D. Porath, A. Bezryadin, S. de Vries, C. Dekker, Direct measurement of electrical transport through DNA molecules, *Nature* **403**, 635 (2000).

[3]   A. Y. Kasumov, M. Kociak, S. Gueron, B. Reulet, V. T. Volkov, D. V. Klinov, H. Bouchiat, Proximity-induced superconductivity in DNA, *Science* **291**, 280 (2001).

[4]   B. Giese, J. Amaudrut, A. K. Kohler, M. Spormann, S. Wessely, Direct observation of hole transfer through DNA by hopping between adenine bases and by tunneling, *Nature* **412**, 318 (2001).

[5]   A. van Oudenaarden, S. G. Boxer, Brownian ratchets: Molecular separations in lipid bilayers supported on patterned arrays, *Science* **285**, 1046 (1999).

[6]   J. Fritz, M. K. Baller, H. P. Lang, H. Rothuizen, P. Vettiger, E. Meyer, H. J. Guntherodt, C. Gerber, J. K. Gimzewski, Translating biomolecular recognition into nanomechanics, *Science* **288**, 316 (2000).

[7]   J. Han, H. G. Craighead, Separation of long DNA molecules in a microfabricated entropic trap array, *Science* **288**, 1026 (2000).

[8]   Z. Reich, R. Kapon, R. Nevo, Y. Pilpel, S. Zmora, Y. Scolnik, Scanning force microscopy in the applied biological sciences, *Biotechnol. Adv.* **19**, 451 (2001).

[9]   R. Raiteri, M. Grattarola, H. J. Butt, P. Skladal, Micromechanical cantilever-based biosensors, *Sens. Actuator B* **79**, 115 (2001).

[10]   C. P. Collier, E. W. Wong, M. Belohradsky, F. M. Raymo, J. F. Stoddart, P. J. Kuekes, R. S. Williams, J. R. Heath, Electronically configurable molecular-based logic gates, *Science* **285**, 391 (1999).

[11]   T. Rueckes, K. Kim, E. Joselevich, G. Y. Tseng, C. L. Cheung, C. M. Lieber, Carbon nanotube-based nonvolatile random access memory for molecular computing, *Science* **289**, 94 (2000).

[12]   Y. Huang, X. F. Duan, Q. Q. Wei, C. M. Lieber, Directed assembly of one-dimensional nanostructures into functional networks, *Science* **291**, 630 (2001).

[13]   C. M. Lieber, The incredible shrinking circuit - Researchers have built nanotransistors and nanowires. Now they just need to find a way to put them all together, *Sci. Am.* **285**, 58 (2001).

[14]   W. A. Schoonveld, J. Wildeman, D. Fichou, P. A. Bobbert, B. J. van Wees, T. M. Klapwijk, Coulomb-blockade transport in single-crystal organic thin-film transistors, *Nature* **404**, 977 (2000).

[15]   M. A. Nielsen, I. L. Chuang, *Quantum Computation and Quantum Information* (Cambridge University Press, Cambridge, 2000).

[16]   A. Steane, Quantum Computing, *Rep. Prog. Phys.* **61**, 117 (1998).

[17]   I. L. Chuang, L. M. K. van der Sypen, X. L. Zhou, D. W. Leung, S. Lloyd, Experimental realization of a quantum algorithm, *Nature* **393**, 143 (1998).

[18]   L. M. K. van der Sypen, M. Steffen, G. Breyta, C. S. Yannoni, R. Cleve, I. L. Chuang, Experimental realization of an order-finding algorithm with an NMR quantum computer, *Phys. Rev. Lett.* **85**, 5452 (2000).

[19]   R. Marx, A. F. Fahmy, J. M. Myers, W. Bermel, S. J. Glaser, Approaching five-bit NMR quantum computing - art. no. 012310, *Phys. Rev. A* **6201**, 2310 (2000).

[20]   E. Knill, R. Laflamme, R. Martinez, C. Negrevergne, Benchmarking quantum computers: The five-qubit error correcting code, *Phys. Rev. Lett.* **86**, 5811 (2001).

[21]   R. P. Feynman, paper presented at the Annual Meeting of the American Physical Society, California Institute of Technology, Pasadena, CA, Dec. 29, 1959.

[22]   H. G. Craighead, Nanoelectromechanical systems, *Science* **290**, 1532 (2000).

[23]   D. M. Eigler, E. K. Schweizer, Positioning Single Atoms with a Scanning Tunneling Microscope, *Nature* **344**, 524 (1990).

[24]   M. F. Crommie, C. P. Lutz, D. M. Eigler, Confinement of Electrons to Quantum Corrals on a Metal-Surface, *Science* **262**, 218 (1993).

[25]   "International Technology Roadmap for Semiconductors: 1999 Edition" (Semiconductor Industry Association, 1999).

[26]   J. Birnbaum, R. S. Williams, Physics and the Information Revolution, *Physics Today* **53**, 38 (2000).

[27]   M. Bockrath, D. H. Cobden, P. L. McEuen, N. G. Chopra, A. Zettl, A. Thess, R. E. Smalley, Single-electron transport in ropes of carbon nanotubes, *Science* **275**, 1922 (1997).

[28]   S. J. Tans, M. H. Devoret, H. J. Dai, A. Thess, R. E. Smalley, L. J. Geerligs, C. Dekker, Individual single-wall carbon nanotubes as quantum wires, *Nature* **386**, 474 (1997).

[29]   D. H. Cobden, M. Bockrath, P. L. McEuen, A. G. Rinzler, R. E. Smalley, Spin splitting and even-odd effects in carbon nanotubes, *Phys. Rev. Lett.* **81**, 681 (1998).

[30]   J. Nygard, D. H. Cobden, P. E. Lindelof, Kondo physics in carbon nanotubes, *Nature* **408**, 342 (2000).

[31]   D. Porath, O. Millo, Single electron tunneling and level spectroscopy of isolated C- 60 molecules, *J. App. Phys.* **81**, 2241 (1997).

[32]   N. A. Gershenfeld, I. L. Chuang, Bulk spin-resonance quantum computation, *Science* **275**, 350 (1997).

[33]   B. E. Kane, A silicon-based nuclear spin quantum computer, *Nature* **393**, 133 (1998).

[34]   D. Loss, D. P. DiVincenzo, Quantum computation with quantum dots, *Phys. Rev. A* **57**, 120 (1998).

[35] J. E. Mooij, T. P. Orlando, L. Levitov, L. Tian, C. H. van der Wal, S. Lloyd, Josephson persistent-current qubit, *Science* **285**, 1036 (1999).

[36] M. A. Reed, Quantum Dots, *Sci. Am.* **268**, 118 (1993).

[37] M. A. Kastner, Artificial Atoms, *Physics Today* **46**, 24 (1993).

[38] D. C. Ralph, C. T. Black, M. Tinkham, Gate-voltage studies of discrete electronic states in aluminum nanoparticles, *Phys. Rev. Lett.* **78**, 4087 (1997).

[39] D. Davidovic, M. Tinkham, Spectroscopy, interactions, and level splittings in an nanoparticles, *Phys. Rev. Lett.* **83**, 1644 (1999).

[40] P. W. Shor, paper presented at the Proceedings of the 35th Annual Symposium on Foundations of Computer Science, Santa Fe, NM 1994.

[41] L. K. Grover, Quantum mechanics helps in searching for a needle in a haystack, *Phys. Rev. Lett.* **79**, 325 (1997).

[42] W. Hansel, P. Hommelhoff, T. W. Hansch, J. Reichel, Bose-Einstein condensation on a microelectronic chip, *Nature* **413**, 498 (2001).

[43] E. Knill, R. Laflamme, G. J. Milburn, A scheme for efficient quantum computation with linear optics, *Nature* **409**, 46 (2001).

[44] C. W. J. Beenakker, H. van Houten, Quantum Transport in Semiconductor Nanostructures, in *Solid State Physics,* H. Ehrenreich, D. Turnbull, Eds. (Academic Press, San Diego, 1991), vol. 44, pp. 1-228.

[45] C. M. Marcus, S. R. Patel, A. G. Huibers, S. M. Cronenwett, M. Switkes, I. H. Chan, R. M. Clarke, J. A. Folk, S. F. Godijn, K. Campman, A. C. Gossard, Quantum chaos in open versus closed quantum dots: Signatures of interacting particles, *Chaos Solitons Fractals* **8**, 1261 (1997).

[46] H. Grabert, M. H. Devoret, Eds., *Single Charge Tunneling* (Plenum, New York, 1992).

[47] L. P. Kouwenhoven, C. M. Marcus, P. L. McEuen, S. Tarucha, R. M. Westervelt, N. S. Wingreen, Electron Transport in Quantum Dots, in *Mesoscopic Electron Transport,* L. L. Sohn, L. P. Kouwenhoven, G. Schoen, Eds. (Kluwer, Dordrecht, 1997), vol. 345.

[48] Y. Alhassid, The statistical theory of quantum dots, *Rev. Mod. Phys.* **72**, 895 (2000).

[49] S. M. Cronenwett, S. R. Patel, C. M. Marcus, K. Campman, A. C. Gossard, Mesoscopic fluctuations of elastic cotunneling in Coulomb blockaded quantum dots, *Phys. Rev. Lett.* **79**, 2312 (1997).

[50] S. M. Cronenwett, S. M. Maurer, S. R. Patel, C. M. Marcus, C. I. Duruoz, J. S. Harris, Mesoscopic Coulomb blockade in one-channel quantum dots, *Phys. Rev. Lett.* **81**, 5904 (1998).

[51] A. C. Hewson, *The Kondo Problem to Heavy Fermions*. D. Edwards, D. Melville, Eds., Cambridge Studies in Magnetism (Cambridge University Press, Cambridge, 1993), vol. 2.

[52] L. Kouwenhoven, L. Glazman, Revival of the Kondo effect, *Physics World* **14**, 33 (2001).

[53] S. M. Cronenwett, T. H. Oosterkamp, L. P. Kouwenhoven, A tunable Kondo effect in quantum dots, *Science* **281**, 540 (1998).

[54] S. M. Cronenwett, H. J. Lynch, D. Goldhaber-Gordon, L. Kouwenhoven, C. M. Marcus, K. Hirose, N. S. Wingreen, V. Umansky, The low-temperature fate of the '0.7 Structure' in a point contact: A Kondo-like correlated state in an open system, *submitted* (2001).

[55] E. Akkermans, G. Montambaux, J.-L. Pichard, J. Zinn-Justin, Eds., *Mesoscopic Quantum Physics* (North-Holland, Amsterdam, 1995).

[56]   A. G. Huibers, J. A. Folk, S. R. Patel, C. M. Marcus, C. I. Duruoz, J. J. Harris, Low-temperature saturation of the dephasing time and effects of microwave radiation on open quantum dots, *Phys. Rev. Lett.* **83**, 5090 (1999).

[57]   E. Y. Andrei, Ed., *Two-dimensional electron systems on helium and other cryogenic substrates*, vol. 19 (Kluwer Academic Publishers, Dordrecht, 1997).

[58]   L. I. Glazman, M. E. Raikh, Resonant Kondo transparency of a barrier with quasilocal impurity states, *Pis'ma Zh. Eksp. Teor. Fiz.* **47**, 378 (1988).

[59]   T. K. Ng, P. A. Lee, On-site Coulomb repulsion and resonant tunneling, *Phys. Rev. Lett.* **61**, 1768 (1988).

[60]   Y. Meir, N. S. Wingreen, P. A. Lee, Low-temperature transport through a quantum dot: the Anderson model out of equilibrium, *Phys. Rev. Lett.* **70**, 2601 (1993).

[61]   Y. Imry, *Introduction to Mesoscopic Physics* (Oxford University Press, Oxford, 1997).

[62]   H. van Houten, C. W. J. Beenakker, B. J. van Wees, Quantum point contacts, in *Nanostructured Systems,* M. A. Reed, Ed. (Academic Press, San Diego, 1992), vol. 35, pp. 9-112.

[63]   B. J. van Wees, H. van Houten, C. W. J. Beenakker, J. G. Williamson, L. P. Kouwenhoven, D. van der Marel, C. T. Foxon, Quantized conductance of point contacts in a two-dimensional electron gas, *Phys. Rev. Lett.* **60**, 848 (1988).

[64]   D. A. Wharam, T. J. Thornton, R. Newbury, M. Pepper, H. Ahmed, J. E. F. Frost, D. G. Hasko, D. C. Peacock, D. A. Ritchie, G. A. C. Jones, One-dimensional transport and the quantisation of the ballistic resistance, *J. Phys. C* **21**, L209 (1988).

[65]   L. P. Kouwenhoven, Quantum adiabatic electron transport in ballistic conductors, in *Physics of low-dimensional semiconductor structures,* P. Butcher, N. H. March, M. P. Tosi, Eds. (Plenum Press, New York, 1993).

[66]   L. I. Glazman, G. B. Lesovik, D. E. Khmel'nitskii, R. I. Shekhter, Reflectionless quantum transport and fundamental ballistic-resistance steps in microscopic constrictions., *JETP Lett.* **48**, 238 (1988).

[67]   L. I. Glazman, A. V. Khaetskii, Quantum conductance of a lateral microconstraint in a magnetic field, *J. Phys.: Condens. Matter* **1**, 5005 (1989).

[68]   K.-F. Berggren, T. J. Thornton, D. J. Newson, M. Pepper, Magnetic depopulation of 1D subbands in a narrow 2D electron gas in a GaAs:AlGaAs heterojunction, *Phys. Rev. Lett.* **57**, 1769 (1986).

[69]   S. E. Laux, D. J. Frank, F. Stern, Quasi-one-dimensional electron states in a split-gate GaAs/AlGaAs heterostructure, *Surf. Sci.* **196**, 101 (1988).

[70]   I. H. Chan, R. M. Clarke, C. M. Marcus, K. Campman, A. C. Gossard, Ballistic Conductance Fluctuations in Shape Space, *Phys. Rev. Lett.* **74**, 3876 (1995).

[71]   S. R. Patel, D. R. Stewart, C. M. Marcus, M. Gokcedag, Y. Alhassid, A. D. Stone, C. I. Duruoz, J. S. Harris, Changing the electronic spectrum of a quantum dot by adding electrons, *Phys. Rev. Lett.* **81**, 5900 (1998).

[72]   C. W. J. Beenakker, Random-matrix theory of quantum transport, *Rev. Mod. Phys.* **69**, 731 (1997).

[73]   S. Washburn, R. A. Webb, Quantum Transport in Small Disordered Samples from the Diffusive to the Ballistic Regime, *Rep. Prog. Phys.* **55**, 1311 (1992).

[74]   C. M. Marcus, A. J. Rimberg, R. M. Westervelt, P. F. Hopkins, A. C. Gossard, Conductance Fluctuations and Chaotic Scattering in Ballistic Microstructures, *Phys. Rev. Lett.* **69**, 506 (1992).

[75]   M. W. Keller, O. Millo, A. Mittal, D. E. Prober, R. N. Sacks, Magnetotransport in a Chaotic Scattering Cavity with Tunable Electron-Density, *Surf. Sci.* **305**, 501 (1994).

[76]   J. P. Bird, A. D. C. Grassie, M. Lakrimi, K. M. Hutchings, J. J. Harris, C. T. Foxon, Conductance Fluctuations and Nondiffusive Motion in GaAs/AlGaAs Heterojunction Wires, *J. Phys.:Condes. Matter* **2**, 7847 (1990).

[77]   R. A. Jalabert, J.-L. Pichard, C. W. J. Beenakker, Universal quantum signatures of chaos in ballistic transport, *Europhys. Lett.* **27**, 255 (1994).

[78]   H. U. Baranger, P. A. Mello, Mesoscopic Transport through Chaotic Cavities - a Random S-Matrix Theory Approach, *Phys. Rev. Lett.* **73**, 142 (1994).

[79]   B. L. Altshuler, B. I. Shklovskii, Repulsion of energy levels and conductivity of small metal samples, *Sov. Phys. JETP* **64**, 127 (1986).

[80]   Y. Imry, Active Transmission Channels and Universal Conductance Fluctuations, *Europhys. Lett.* **1**, 249 (1986).

[81]   T. Guhr, A. Muller-Groeling, H. A. Weidenmuller, Random-matrix theories in quantum physics: Common concepts, *Phys. Rep.-Rev. Sec. Phys. Lett.* **299**, 190 (1998).

[82]   M. J. Giannoni, A. Voros, J. Zinn-Justin, Eds., *Chaos and Quantum Physics* (Elsevier, Amsterdam, 1991).

[83]   H. U. Baranger, R. A. Jalabert, A. D. Stone, Weak-Localization and Integrability in Ballistic Cavities, *Phys. Rev. Lett.* **70**, 3876 (1993).

[84]   A. M. Chang, H. U. Baranger, L. N. Pfeiffer, K. W. West, Weak-Localization in Chaotic Versus Nonchaotic Cavities - a Striking Difference in the Line-Shape, *Phys. Rev. Lett.* **73**, 2111 (1994).

[85]   M. J. Berry, J. A. Katine, C. M. Marcus, R. M. Westervelt, A. C. Gossard, Weak-Localization and Conductance Fluctuations in a Chaotic Quantum-Dot, *Surf. Sci.* **305**, 495 (1994).

[86]   H. van Houten, C. W. J. Beenakker, A. A. M. Staring, Coulomb-blockade oscillations in semiconductor nanostructures, in *Single Charge Tunneling,* H. Grabert, M. H. Devoret, Eds. (Plenum Press, New York, 1992).

[87]   U. Sivan, R. Berkovits, Y. Aloni, O. Prus, A. Auerbach, G. BenYoseph, Mesoscopic fluctuations in the ground state energy of disordered quantum dots, *Phys. Rev. Lett.* **77**, 1123 (1996).

[88]   F. Simmel, T. Heinzel, D. A. Wharam, Statistics of conductance oscillations of a quantum dot in the Coulomb-blockade regime, *Europhys. Lett.* **38**, 123 (1997).

[89]   A. A. Koulakov, F. G. Pikus, B. I. Shklovskii, Statistics of the charging spectrum of a two-dimensional Coulomb-glass island, *Phys. Rev. B* **55**, 9223 (1997).

[90]   S. R. Patel, S. M. Cronenwett, D. R. Stewart, A. G. Huibers, C. M. Marcus, C. I. Duruoz, J. S. Harris, K. Campman, A. C. Gossard, Statistics of Coulomb blockade peak spacings, *Phys. Rev. Lett.* **80**, 4522 (1998).

[91]   Y. M. Blanter, A. D. Mirlin, B. A. Muzykantskii, Fluctuations of conductance peak spacings in the Coulomb blockade regime: Role of electron-electron interaction, *Phys. Rev. Lett.* **78**, 2449 (1997).

[92]   M. Stopa, Fluctuations in quantum dot charging energy and polarization, *Semicon. Sci. Tech.* **13**, A55 (1998).

[93]   R. O. Vallejos, C. H. Lewenkopf, E. R. Mucciolo, Coulomb blockade peak spacing fluctuations in deformable quantum dots: a further test of random matrix theory, *Phys. Rev. Lett.* **81**, 677 (1998).

[94]   I. O. Kulik, R. I. Shekhter, Kinetic phenomena and charge discreteness effects in granulated media, *Sov. Phys. JETP* **41**, 308 (1975).

[95]   D. V. Averin, K. K. Likharev, Coulomb Blockade of Single-Electron Tunneling, and Coherent Oscillations in Small Tunnel-Junctions, *J. Low Temp. Phys.* **62**, 345 (1986).

[96]   D. V. Averin, K. K. Likharev, in *Mesoscopic Phenomena in Solids,* B. L. Altshuler, P. A. Lee, R. A. Webb, Eds. (North-Holland, Amsterdam, 1991).

[97]   G. Schon, A. D. Zaikin, Quantum coherent effects, phase transitions, and the dissipative dynamics of ultra small tunnel junctions, *Phys. Rep.* **198**, 237 (1990).

[98]   G.-L. Ingold, Y. V. Nazarov, in *Single Charge Tunneling,* H. Grabert, M. H. Devoret, Eds. (Plenum Press, New York, 1991).

[99]   R. A. Jalabert, A. D. Stone, Y. Alhassid, Statistical-Theory of Coulomb Blockade Oscillations - Quantum Chaos in Quantum Dots, *Phys. Rev. Lett.* **68**, 3468 (1992).

[100] J. A. Folk, S. R. Patel, S. F. Godijn, A. G. Huibers, S. M. Cronenwett, C. M. Marcus, K. Campman, A. C. Gossard, Statistics and parametric correlations of Coulomb blockade peak fluctuations in quantum dots, *Phys. Rev. Lett.* **76**, 1699 (1996).

[101] A. M. Chang, H. U. Baranger, L. N. Pfeiffer, K. W. West, T. Y. Chang, Non-Gaussian distribution of Coulomb blockade peak heights in quantum dots, *Phys. Rev. Lett.* **76**, 1695 (1996).

[102] C. W. J. Beenakker, Theory of Coulomb-Blockade Oscillations in the Conductance of a Quantum Dot, *Phys. Rev. B* **44**, 1646 (1991).

[103] Y. Alhassid, H. Attias, Universal parametric correlations of conductance peaks in quantum dots, *Phys. Rev. Lett.* **76**, 1711 (1996).

[104] H. Bruus, C. H. Lewenkopf, E. R. Mucciolo, Parametric conductance correlation for irregularly shaped quantum dots, *Phys. Rev. B* **53**, 9968 (1996).

[105] D. R. Stewart, D. Sprinzak, C. M. Marcus, C. I. Duruoz, J. S. Harris, Correlations between ground and excited state spectra of a quantum dot, *Science* **278**, 1784 (1997).

[106] D. R. Stewart, Stanford University (1999).

[107] I. L. Aleiner, P. W. Brouwer, L. I. Glazman, Quantum effects in Coulomb blockade, *cond-mat/0103008* (2001).

[108] D. V. Averin, Y. V. Nazarov, in *Single Charge Tunneling,* H. Grabert, M. H. Devoret, Eds. (Plenum, New York, 1991), vol. 294, pp. 217-247.

[109] B. L. Altshuler, P. A. Lee, R. A. Webb, Eds., *Mesoscopic Phenomena in Solids*, vol. 30 (North-Holland, Amsterdam, 1991).

[110] U. Sivan, F. P. Milliken, K. Milkove, S. Rishton, Y. Lee, J. M. Hong, V. Boegli, D. Kern, M. Defranza, Spectroscopy, Electron-Electron Interaction, and Level Statistics in a Disordered Quantum-Dot, *Europhys. Lett.* **25**, 605 (1994).

[111] J. P. Bird, K. Ishibashi, Y. Aoyagi, T. Sugano, Y. Ochiai, Spectral Characteristics of Conductance Fluctuations in Ballistic Quantum Dots, *Phys. Rev. B* **50**, 18678 (1994).

[112] B. L. Altshuler, B. D. Simons, in *Mesoscopic Quantum Physics,* E. Akkermans, G. Montambaux, J.-L. Pichard, J. Zinn-Justin, Eds. (Elsevier, Amsterdam, 1995).

[113] C. W. J. Beenakker, Universality in the Random-Matrix Theory of Quantum Transport, *Phys. Rev. Lett.* **70**, 1155 (1993).

[114] R. A. Jalabert, H. U. Baranger, A. D. Stone, Conductance Fluctuations in the Ballistic Regime - a Probe of Quantum Chaos, *Phys. Rev. Lett.* **65**, 2442 (1990).

[115] V. N. Prigodin, K. B. Efetov, S. Iida, Statistics of Conductance Fluctuations in Quantum Dots, *Phys. Rev. Lett.* **71**, 1230 (1993).

[116]   C. W. J. Beenakker, H. Schomerus, P. G. Silvestrov, Effect of inelastic scattering on the average Coulomb-blockade peak height in quantum dots - art. no. 033307, *Phys. Rev. B* **6403**, 3307 (2001).

[117]   P. A. Lee, T. V. Ramakrishnan, Disordered Electronic Systems, *Rev. Mod. Phys.* **57**, 287 (1985).

[118]   D. V. Averin, A. A. Odintsov, Macroscopic Quantum Tunneling of the Electric Charge in Small Tunnel-Junctions, *Phys. Lett. A* **140**, 251 (1989).

[119]   L. I. Glazman, K. A. Matveev, Residual Quantum Conductivity under Coulomb-Blockade Conditions, *JETP Lett.* **51**, 484 (1990).

[120]   D. V. Averin, Y. V. Nazarov, Virtual Electron-Diffusion During Quantum Tunneling of the Electric Charge, *Phys. Rev. Lett.* **65**, 2446 (1990).

[121]   D. C. Glattli, C. Pasquier, U. Meirav, F. I. B. Williams, Y. Jin, B. Etienne, Co-Tunneling of the Charge through a 2-D Electron Island, *Z. Phys. B-Condens. Mat.* **85**, 375 (1991).

[122]   I. L. Aleiner, L. I. Glazman, Mesoscopic fluctuations of elastic cotunneling, *Phys. Rev. Lett.* **77**, 2057 (1996).

[123]   E. Doron, U. Smilansky, A. Frenkel, Chaotic Scattering and Transmission Fluctuations, *Physica D* **50**, 367 (1991).

[124]   C. M. Marcus, R. M. Westervelt, P. F. Hopkins, A. C. Gossard, Phase Breaking in Ballistic Quantum Dots - Experiment and Analysis Based on Chaotic Scattering, *Phys. Rev. B* **48**, 2460 (1993).

[125]   I. L. Aleiner, L. I. Glazman, Mesoscopic charge quantization, *Phys. Rev. B* **57**, 9608 (1998).

[126]   K. Flensberg, Capacitance and Conductance of Mesoscopic Systems Connected by Quantum Point Contacts, *Phys. Rev. B* **48**, 11156 (1993).

[127]   K. A. Matveev, Coulomb-Blockade at Almost Perfect Transmission, *Phys. Rev. B* **51**, 1743 (1995).

[128]   S. V. Panyukov, A. D. Zaikin, Coulomb Blockade and Nonperturbative Ground-State Properties of Ultrasmall Tunnel-Junctions, *Phys. Rev. Lett.* **67**, 3168 (1991).

[129]   G. Falci, G. Schon, G. T. Zimanyi, Unified Scaling Theory of the Electron Box for Arbitrary Tunneling Strength, *Phys. Rev. Lett.* **74**, 3257 (1995).

[130]   D. S. Golubev, J. Konig, H. Schoeller, G. Schon, A. D. Zaikin, Strong electron tunneling through mesoscopic metallic grains, *Phys. Rev. B* **56**, 15782 (1997).

[131]   P. Joyez, V. Bouchiat, D. Esteve, C. Urbina, M. H. Devoret, Strong tunneling in the single-electron transistor, *Phys. Rev. Lett.* **79**, 1349 (1997).

[132]   L. P. Kouwenhoven, N. C. van der Vaart, A. T. Johnson, W. Kool, C. Harmans, J. G. Williamson, A. A. M. Staring, C. T. Foxon, Single Electron Charging Effects in Semiconductor Quantum Dots, *Z. Phys. B-Condens. Mat.* **85**, 367 (1991).

[133]   C. Pasquier, U. Meirav, F. I. B. Williams, D. C. Glattli, Y. Jin, B. Etienne, Quantum Limitation on Coulomb Blockade Observed in a 2d Electron-System, *Phys. Rev. Lett.* **70**, 69 (1993).

[134]   C. H. Crouch, C. Livermore, R. M. Westervelt, K. L. Campman, A. C. Gossard, Coulomb oscillations in partially open quantum dots, *Superlattices and Microstructures* **20**, 377 (1996).

[135]   W. H. Press, S. A. Teukolsky, W. T. Vetterling, B. P. Flannery, *Numerical Recipes in C* (Cambridge University Press, Cambridge, 1992).

[136]   J. A. Folk, C. M. Marcus, J. S. Harris, Decoherence in nearly isolated quantum dots, *Phys. Rev. Lett.* **87**, 206802 (2001).

[137]   S. M. Maurer, S. R. Patel, C. M. Marcus, C. I. Duruoz, J. S. Harris, Coulomb blockade fluctuations in strongly coupled quantum dots, *Phys. Rev. Lett.* **83**, 1403 (1999).

[138]   R. Berkovits, B. L. Altshuler, Compressibility, capacitance, and ground-state energy fluctuations in a weakly interacting quantum dot, *Phys. Rev. B* **55**, 5297 (1997).

[139]   W. Meissner, G. Voigt, *Ann. Phys.-Berlin* **7**, 761 (1930).

[140]   J. Kondo, Theory of dilute magnetic alloys, in *Solid State Physics,* F. Seitz, D. Turnbull, H. Ehrenreich, Eds. (Academic Press, New York, 1969), vol. 23, pp. 183.

[141]   N. W. Ashcroft, N. D. Mermin, *Solid State Physics* (Saunders College Publishing, ed. First Edition, 1976).

[142]   J. Friedel, *Nuovo Cimento (Suppl)* **7**, 287 (1958).

[143]   P. W. Anderson, Localized magnetic states in metals, *Phys. Rev.* **124**, 41 (1961).

[144]   M. P. Sarachik, E. Corenzwit, L. D. Longinotti, Resistivity of Mo-Nb + Mo-Re Alloys Containing1(Fe, *Phys. Rev. A* **135**, 1041 (1964).

[145]   J. Kondo, Resistance Minimum in Dilute Magnetic Alloys, *Prog. Theor. Phys.* **32**, 37 (1964).

[146]   A. P. Klein, A. J. Heeger, Localized Impurity States in Metals - Dilute Alloys of Ni in Be, *Phys. Rev.* **144**, 458 (1966).

[147]   P. W. Anderson, A. M. Clogston, *Bul. Am. Phys. Soc.* **6**, 124 (1961).

[148]   A. J. Heeger, Localized moments and nonmoments in metals, in *Solid State Physics,* F. Seitz, D. Turnbull, H. Ehrenreich, Eds. (Academic Press, New York, 1969), vol. 23.

[149]   D. C. Mattis, Symmetry of ground state in a dilute magnetic metal alloy, *Phys. Rev. Lett.* **19**, 1478 (1967).

[150]   K. G. Wilson, Renormalization Group - Critical Phenomena and Kondo Problem, *Rev. Mod. Phys.* **47**, 773 (1975).

[151]   N. Andrei, Diagonalization of the Kondo-Hamiltonian, *Phys. Rev. Lett.* **45**, 379 (1980).

[152]   P. B. Wiegmann, Towards an Exact Solution of the Anderson Model, *Phys. Lett. A* **80**, 163 (1980).

[153]   T. A. Costi, A. C. Hewson, V. Zlatic, Transport coefficients of the Anderson model via the numerical renormalization group, *J. Phys.: Condens. Matter* **6**, 2519 (1994).

[154]   A. Kawabata, On the Electron-Transport through a Quantum Dot, *J. Phys. Soc. Jpn.* **60**, 3222 (1991).

[155]   N. S. Wingreen, Y. Meir, Anderson Model out of Equilibrium - Noncrossing-Approximation Approach to Transport through a Quantum-Dot, *Phys. Rev. B* **49**, 11040 (1994).

[156]   D. Goldhaber-Gordon, H. Shtrikman, D. Mahalu, D. Abusch-Magder, U. Meirav, M. A. Kastner, Kondo effect in a single-electron transistor, *Nature* **391**, 156 (1998).

[157]   S. Hershfield, J. H. Davies, J. W. Wilkins, Probing the Kondo Resonance by Resonant Tunneling through an Anderson Impurity, *Phys. Rev. Lett.* **67**, 3720 (1991).

[158]   J. Konig, J. Schmid, H. Schoeller, G. Schon, Resonant tunneling through ultrasmall quantum dots: Zero-bias anomalies, magnetic-field dependence, and boson-assisted transport, *Phys. Rev. B* **54**, 16820 (1996).

[159]   H. Schoeller, in *Mesoscopic Electron Transport,* L. L. Sohn, L. P. Kouwenhoven, G. Schon, Eds. (Kluwer, Dordrecht, Netherlands, 1997), vol. ser. E, vol. 345, pp. 291-330.

[160] D. C. Ralph, R. A. Buhrman, Kondo-Assisted and Resonant-Tunneling Via a Single Charge Trap - a Realization of the Anderson Model out of Equilibrium, *Phys. Rev. Lett.* **72**, 3401 (1994).

[161] I. K. Yanson, V. V. Fisun, R. Hesper, A. V. Khotkevich, J. M. Krans, J. A. Mydosh, J. M. van Ruitenbeek, Size Dependence of Kondo Scattering in Point Contacts, *Phys. Rev. Lett.* **74**, 302 (1995).

[162] Y. Wan, P. Phillips, Q. M. Li, Suppression of the Kondo Effect in Quantum Dots by Even-Odd Asymmetry, *Phys. Rev. B* **51**, 14782 (1995).

[163] N. C. van der Vaart, S. F. Godijn, Y. V. Nazarov, C. Harmans, J. E. Mooij, L. W. Molenkamp, C. T. Foxon, Resonant-Tunneling through 2 Discrete Energy-States, *Phys. Rev. Lett.* **74**, 4702 (1995).

[164] F. D. Haldane, Scaling theory of the asymmetric Anderson model, *Phys. Rev. Lett.* **40**, 416 (1978).

[165] N. E. Bickers, Review of Techniques in the Large-N Expansion for Dilute Magnetic-Alloys, *Rev. Mod. Phys.* **59**, 845 (1987).

[166] T. Inoshita, A. Shimizu, Y. Kuramoto, H. Sakaki, Correlated Electron-Transport through a Quantum-Dot - the Multiple-Level Effect, *Phys. Rev. B* **48**, 14725 (1993).

[167] T. Inoshita, Y. Kuramoto, H. Sakaki, Nonlinear low-temperature transport of electrons through a multilevel quantum dot, *Superlattices and Microstructures* **22**, 75 (1997).

[168] T. Pohjola, J. Konig, M. Salomaa, J. Schmid, H. Schoeller, G. Schon, Resonant tunneling through a two-level dot and double quantum dots, *Europhys. Lett.* **40**, 189 (1997).

[169] E. B. Foxman, P. L. McEuen, U. Meirav, N. S. Wingreen, Y. Meir, P. A. Belk, N. R. Belk, M. A. Kastner, S. J. Wind, Effects of Quantum Levels on Transport through a Coulomb Island, *Phys. Rev. B* **47**, 10020 (1993).

[170] W. G. van der Wiel, S. de Franceschi, T. Fujisawa, J. M. Elzerman, S. Tarucha, L. P. Kouwenhoven, The Kondo effect in the unitary limit, *Science* **289**, 2105 (2000).

[171] J. Konig, H. Schoeller, G. Schon, Zero-bias anomalies and boson-assisted tunneling through quantum dots, *Phys. Rev. Lett.* **76**, 1715 (1996).

[172] M. Dobers, K. von Klitzing, G. Weimann, Electron-Spin Resonance in the Two-Dimensional Electron-Gas of Gaas-Alxga1-Xas Heterostructures, *Phys. Rev. B* **38**, 5453 (1988).

[173] D. Goldhaber-Gordon, J. Gores, M. A. Kastner, H. Shtrikman, D. Mahalu, U. Meirav, From the Kondo regime to the mixed-valence regime in a single-electron transistor, *Phys. Rev. Lett.* **81**, 5225 (1998).

[174] J. Schmid, J. Weis, K. Eberl, K. von Klitzing, A quantum dot in the limit of strong coupling to the reservoirs., *Physica B* **256-258**, 182 (1998).

[175] J. Schmid, J. Weis, K. Eberl, K. von Klitzing, Absence of odd-even parity behavior for Kondo resonances in quantum dots, *Phys. Rev. Lett.* **84**, 5824 (2000).

[176] F. Simmel, R. H. Blick, J. P. Kotthaus, W. Wegscheider, M. Bichler, Anomalous Kondo effect in a quantum dot at nonzero bias, *Phys. Rev. Lett.* **83**, 804 (1999).

[177] S. Sasaki, S. De Franceschi, J. M. Elzerman, W. G. van Der Wiel, M. Eto, S. Tarucha, L. P. Kouwenhoven, Kondo effect in an integer-spin quantum dot, *Nature* **405**, 764 (2000).

[178] V. Madhavan, W. Chen, T. Jamneala, M. F. Crommie, N. S. Wingreen, Tunneling into a single magnetic atom: Spectroscopic evidence of the Kondo resonance, *Science* **280**, 567 (1998).

[179] J. T. Li, W. D. Schneider, R. Berndt, B. Delley, Kondo scattering observed at a single magnetic impurity, *Phys. Rev. Lett.* **80**, 2893 (1998).

[180]   H. C. Manoharan, C. P. Lutz, D. M. Eigler, Quantum mirages formed by coherent projection of electronic structure, *Nature* **403**, 512 (2000).

[181]   T. W. Odom, J. L. Huang, C. L. Cheung, C. M. Lieber, Magnetic clusters on single-walled carbon nanotubes: The Kondo effect in a one-dimensional host, *Science* **290**, 1549 (2000).

[182]   S. Tarucha, T. Honda, T. Saku, Reduction of quantized conductance at low temperatures observed in 2 to 10 μm-long quantum wires, *Sol. St. Comm.* **94**, 413 (1995).

[183]   A. Yacoby, H. L. Stormer, N. S. Wingreen, L. N. Pfeiffer, K. W. Baldwin, K. W. West, Nonuniversal conductance quantization in quantum wires, *Phys. Rev. Lett.* **77**, 4612 (1996).

[184]   K. J. Thomas, J. T. Nicholls, M. Y. Simmons, M. Pepper, D. R. Mace, D. A. Ritchie, Possible spin polarization in a one-dimensional electron gas, *Phys. Rev. Lett.* **77**, 135 (1996).

[185]   B. J. van Wees, L. P. Kouwenhoven, H. van Houten, C. W. J. Beenakker, J. E. Mooij, C. T. Foxon, J. J. Harris, Quantized conductance of magnetoelectric subbands in ballistic point contacts, *Phys. Rev. B* **38**, 3625 (1988).

[186]   B. J. van Wees, L. P. Kouwenhoven, E. M. M. Willems, C. J. P. M. Harmans, J. E. Mooij, H. van Houten, C. W. J. Beenakker, J. G. Williamson, C. T. Foxon, Quantum ballistic and adiabatic electron transport studied with quantum point contacts, *Phys. Rev. B* **43**, 12431 (1991).

[187]   K. J. Thomas, J. T. Nocholls, N. J. Appleyard, M. Y. Simmons, M. Pepper, D. R. Mace, W. R. Tribe, D. A. Ritchie, Interaction effects in a one-dimensional constriction, *Phys. Rev. B* **58**, 4846 (1998).

[188]   A. Kristensen, P. E. Lindelof, J. Bo Jensen, M. Zaffalon, J. Hollingbery, S. W. Pedersen, J. Nygard, H. Bruus, S. M. Reimann, C. B. Sorensen, M. Michel, A. Forchel, Temperature dependence of the "0.7" 2e2/h quasi-plateau in strongly confined quantum point contacts, *Physica B* **249-251**, 180 (1998).

[189]   K. J. Thomas, J. T. Nicholls, M. Pepper, W. R. Tribe, M. Y. Simmons, D. A. Ritchie, Spin properties of low-density one-dimensional wires, *Phys. Rev. B* **61**, R13365 (2000).

[190]   A. Kristensen, H. Bruus, A. F. Hansen, J. B. Jensen, P. E. Lindelof, C. J. Marckmann, J. Nygard, C. B. Sorensen, F. Beuscher, A. Forchel, M. Michel, Bias and temperature dependence of the 0.7 conductance anomaly in quantum point contacts, *Phys. Rev. B* **62**, 10950 (2000).

[191]   K. S. Pyshkin, C. J. B. Ford, R. H. Harrell, M. Pepper, E. H. Linfield, D. A. Ritchie, Spin splitting of one-dimensional subbands in high quality quantum wires at zero magnetic field, *Phys. Rev. B* **62**, 15842 (2000).

[192]   S. Nuttinck, K. Hashimoto, S. Miyashita, T. Saku, Y. Yamamoto, Y. Hirayama, Quantum point contacts in a density-tunable two-dimensional electron gas, *Jap. J. App. Phys.* **39**, L655 (2000).

[193]   A. Kristensen, H. Bruus, paper presented at the 19th Nordic Semiconductor Meeting, Copenhagen, Denmark, May 20-23 2001.

[194]   B. E. Kane, G. R. Facer, A. S. Dzurak, N. E. Lumpkin, R. G. Clark, L. N. Pfeiffer, K. W. West, Quantized conductance in quantum wires with gate-controlled width and electron density, *App. Phys. Lett.* **72**, 3506 (1998).

[195]   D. J. Reilly, G. R. Facer, A. S. Dzurak, B. E. Kane, R. G. Clark, P. J. Stiles, A. R. Hamilton, J. L. O'Brien, N. E. Lumpkin, L. N. Pfeiffer, K. W. West, Many-body spin-related phenomena in ultra low-disorder quantum wires, *Phys. Rev. B* **63**, 121311/1 (2001).

[196]   D. Kaufman, Y. Berk, B. Dwir, A. Rudra, A. Palevski, E. Kapon, Conductance quantization in V-groove quantum wires, *Phys. Rev. B* **59**, 10433 (1999).

[197] A. Gold, L. Calmels, Valley- and spin-occupancy instability in the quasi-one-dimensional electron gas, *Phil. Mag. Lett.* **74**, 33 (1996).

[198] C.-K. Wang, K.-F. Berggren, Spin splitting of subbands in quasi-one-dimensional electron quantum channels, *Phys. Rev. B* **54**, R14257 (1996).

[199] C.-K. Wang, K.-F. Berggren, Local spin polarization in ballistic quantum point contacts, *Phys. Rev. B* **57**, 4552 (1998).

[200] D. Schmeltzer, E. Kogan, R. Berkovits, M. Kaveh, Conductance in a one-dimensional spin polarized gas, *Phil. Mag. B* **77**, 1189 (1998).

[201] S. M. Reimann, M. Koskinen, M. Manninen, End states due to a spin-Peierls transition in quantum wires, *Phys. Rev. B* **59**, 1613 (1999).

[202] B. Spivak, F. Zhou, Ferromagnetic correlations in quasi-one-dimensional conducting channels, *Phys. Rev. B* **61**, 16730 (2000).

[203] H. Bruus, V. V. Cheianov, K. Flensberg, From mesoscopic magnetism to the anomalous 0.7 conductance plateau, *cond-mat/0002338* (2000).

[204] V. V. Flambaum, M. Y. Kuchiev, Possible mechanism of the fractional-conductance quantization in a one-dimensional constriction, *Phys. Rev. B* **61**, R7869 (2000).

[205] T. Rejec, A. Ramsak, Spin-dependent resonances in the conduction edge of quantum wires, *Phys. Rev. B* **62**, 12985 (2000).

[206] H. Bruus, V. V. Cheianov, K. Flensberg, The anomalous 0.5 and 0.7 conductance plateaus in quantum point contacts, *Physica E* **10**, 97 (2001).

[207] K. Hirose, S.-S. Li, N. S. Wingreen, Mechanisms for extra conductance plateaus in quantum wires, *Phys. Rev. B* **63**, 033315/1 (2001).

[208] K. Hirose, N. S. Wingreen, Temperature-dependent suppression of conductance in quantum wires: Anomalous activation energy from pinning of the band edge, *Phys. Rev. B* **64**, 073305 (2001).

[209] E. Lieb, D. Mattis, Theory of Ferromagnetism and the Ordering of Electronic Energy Levels, *Phys. Rev.* **125**, 164 (1962).

[210] P. E. Lindelof, Effect on conductance of an isomer state in a quantum point contact, *Proc. SPIE* **4415**, 77 (2001).

[211] L. I. Glazman, A. V. Khaetskii, Nonlinear quantum conductance of a point contact, *Pis'ma Zh. Eksp. Teor. Fiz.* **48**, 546 (1988).

[212] L. P. Kouwenhoven, B. J. van Wees, C. J. P. M. Harmans, J. G. Williamson, H. van Houten, C. W. J. Beenakker, C. T. Foxon, J. J. Harris, Nonlinear conductance of quantum point contacts, *Phys. Rev. B* **39**, 8040 (1989).

[213] N. K. Patel, J. T. Nicholls, L. Martin-Moreno, M. Pepper, J. E. F. Frost, D. A. Ritchie, G. A. C. Jones, Properties of a ballistic quasi-one-dimensional constriction in a parallel high magnetic field, *Phys. Rev. B* **44**, 10973 (1991).

[214] Y. Meir, N. S. Wingreen, personal communication (2001).

[215] L. P. Kouwenhoven, F. W. J. Hekking, B. J. van Wees, C. Harmans, C. E. Timmering, C. T. Foxon, Transport through a Finite One-Dimensional Crystal, *Phys. Rev. Lett.* **65**, 361 (1990).

[216] F. R. Waugh, M. J. Berry, D. J. Mar, R. M. Westervelt, K. L. Campman, A. C. Gossard, Single-Electron Charging in Double and Triple Quantum Dots with Tunable Coupling, *Phys. Rev. Lett.* **75**, 705 (1995).

[217]   C. Livermore, C. H. Crouch, R. M. Westervelt, K. L. Campman, A. C. Gossard, The Coulomb blockade in coupled quantum dots, *Science* **274**, 1332 (1996).

[218]   R. H. Blick, D. Pfannkuche, R. J. Haug, K. von Klitzing, K. Eberl, Formation of a coherent mode in a double quantum dot, *Phys. Rev. Lett.* **80**, 4032 (1998).

[219]   D. Dixon, L. P. Kouwenhoven, P. L. McEuen, Y. Nagamune, J. Motohisa, H. Sakaki, Influence of energy level alignment on tunneling between coupled quantum dots, *Phys. Rev. B* **53**, 12625 (1996).

[220]   H. Jeong, A. M. Chang, M. R. Melloch, The Kondo effect in an artificial quantum dot molecule, *Science* **293**, 2221 (2001).

[221]   Y. Tokura, S. Sasaki, D. G. Austing, S. Tarucha, Single-electron tunneling through two vertically coupled quantum dots, *Physica E* **6**, 676 (2000).

[222]   M. N. Leuenberger, D. Loss, Spintronics and quantum computing: switching mechanisms for qubits, *Physica E* **10**, 452 (2001).

[223]   A. Yacoby, M. Heiblum, D. Mahalu, H. Shtrikman, Coherence and Phase-Sensitive Measurements in a Quantum-Dot, *Phys. Rev. Lett.* **74**, 4047 (1995).

[224]   R. Schuster, E. Buks, M. Heiblum, D. Mahalu, V. Umansky, H. Shtrikman, Phase measurement in a quantum dot via a double-slit interference experiment, *Nature* **385**, 417 (1997).

[225]   Y. Ji, M. Heiblum, D. Sprinzak, D. Mahalu, H. Shtrikman, Phase evolution in a Kondo-correlated system, *Science* **290**, 779 (2000).

[226]   P. Recher, E. V. Sukhorukov, D. Loss, Quantum dot as spin filter and spin memory, *Phys. Rev. Lett.* **85**, 1962 (2000).

[227]   G. Burkard, D. Loss, D. P. DiVincenzo, Coupled quantum dots as quantum gates, *Phys. Rev. B* **59**, 2070 (1999).

[228]   L. W. Molenkamp, A. A. M. Staring, C. W. J. Beenakker, R. Eppenga, C. E. Timmering, J. G. Williamson, C. J. P. M. Harmans, C. T. Foxon, Electron-beam collimation with a quantum point contact, *Phys. Rev. B* **41**, 1274 (1990).

[229]   A. M. Chang, H. D. Hallen, L. Harriott, Scanning Hall probe microscopy, *App. Phys. Lett.* **61**, 1965 (1992).

[230]   A. G. Huibers, Stanford University (1999).

[231]   M. Switkes, Stanford University (2000).